

6 Noise and Multiple Attenuation

- **Introduction** • Coherent Linear Noise • Treatment of Coherent Linear Noise by Conventional Processing • Reverberations and Multiples • Treatment of Reverberations and Multiples by Conventional Processing • Spatially Random Noise • **Multiple Attenuation in the CMP Domain** • Periodicity of Multiples • Velocity Discrimination Between Primaries and Multiples • Karhunen-Loeve Transform • Modeling of Multiples • **Frequency-Wavenumber Filtering** • Random Noise and Frequency-Wavenumber Filtering • Statics Corrections and Frequency-Wavenumber Filtering • Dip Filtering of Coherent Linear Noise • Frequency-Wavenumber Multiple Attenuation • **The Slant-Stack Transform** • Physical Aspects of Slant Stacking • Slant-Stack Transformation • Practical Aspects of Slant Stacking • Slant-Stack Parameters • Time-Variant Dip Filtering • Slant-Stack Multiple Attenuation • **The Radon Transform** • Velocity-Stack Transformation • The Discrete Radon Transform • The Parabolic Radon Transform • Practical Considerations • Impulse Response of the Velocity-Stack Operator • Field Data Examples • Radon-Transform Multiple Attenuation • **Linear Uncorrelated Noise Attenuation** • Design of Spatial Prediction Filters • Field Data Examples • **Exercises** • **Appendix F: Multichannel Filtering Techniques for Noise and Multiple Attenuation** • Analysis of Guided Waves • Wavefield Extrapolation in the $\tau - p$ Domain • Mathematical Foundation of the Discrete Radon Transform • Free-Surface Multiple Attenuation • Water-Bottom Multiple Attenuation • Spatial Prediction Filter • **References**
-

6.0 INTRODUCTION

In Section 1.3, we examined noise and signal characteristics of seismic data from 40 common-shot gathers. Noise generally is classified into two categories — random noise and coherent noise. The random noise category includes noise in the temporal direction and spatially random noise that is uncorrelated from trace to trace. The first type of random noise usually is stronger at late times than early times in recorded data. Time-variant bandpass filtering usually is applied to attenuate much of the temporally random noise. A powerful process that attenuates much of the random noise

uncorrelated from trace to trace is conventional CMP stacking. By using multiple receivers per channel, multiple sources per record and multiple fold of coverage, signal-to-noise ratio is increased significantly. A comprehensive review of random noise and its analysis is given by Sengbush (1983). The coherent noise category includes linear noise, and reverberations and multiples. Coherent linear noise types include guided waves, which often are abundantly present in shallow marine data, ground roll and noise associated with shallow water-bottom side scatterers.

Coherent Linear Noise

Two types of coherent linear noise that deserve special attention are guided waves and side-scattered energy. Figure 6.0-1 shows field data with coherent linear noise in three different domains — common-shot gather, common-midpoint gather, and CMP stack. The dispersive waves labeled as *A* in Figure 6.0-1a are guided waves, and the linear events *B* and *C* and the events *D* with curvature are associated with side scatterers. Guided waves manifest themselves as dispersive linear noise on both common-shot and CMP gathers, but are attenuated largely by stacking.

Guided waves are trapped in a water layer or in a low-velocity near-surface layer and travel in the horizontal direction. They are dispersive — each frequency component propagates with a different phase velocity, and are best described by normal-mode propagation. Numerical modeling of guided waves using normal-mode propagation theory is presented in Section F.1. Since they do not contain any useful reflection energy, guided waves usually are muted on CMP gathers. When one mode splits away from the rest of the guided wave packet and travels at lower speeds, and thus overlaps with reflection events, then dip filtering in the $f - k$ domain is needed (Section 6.2).

An excellent example of guided waves is seen on the field record (between 1 and 4.5 s at far offset) shown in Figure 6.0-2. The first part of the wave packet between 1 and 1.5 s at far offset contains low frequencies. High frequencies ride along the direct arrival path at approximately 0.3 s at near offset and 1.8 s at far offset, followed by moderate frequencies between 1.8–2.8 s at far offset. The very-low frequency dispersed wavetrain with high amplitudes between 2.8–4.5 s at far offset corresponds to the mode that has split from the rest of the guided-wave modes. This happens when there is a shallow, soft water bottom associated with a mud layer. Also seen on this record is the backscattered guided wave (zone *B*) with reverse linear moveout, which indicates the presence of irregularities over the ocean bottom. These irregularities also cause arrivals (zone *A*) that represent point scatterers.

The dispersive nature of guided waves can vary along a seismic traverse depending on water depth and water-bottom conditions. The shallower the water depth and the softer the water bottom, the more the dispersion and splitting of modes associated with guided waves (Figure 6.0-3).

Side-scattered energy has a large moveout range depending on the position of the scatterer acting as a point source at the water bottom with respect to the position of the recording cable (events *B*, *C*, and *D* in Figure 6.0-1a). Side-scattered energy manifests itself

with varying moveout on common-shot gathers (Figure 6.0-1a), and is not apparent on CMP gathers (Figure 6.0-1b), but reappears as linear noise on stacked sections (Figure 6.0-1c) (Larner et al., 1983).

Side-scattered energy stacks at high velocities along the linear flanks of its traveltime curve. We then anticipate that the linear noise seen on a stacked section, particularly at late times, most likely is scattered energy along the flanks of its traveltime curve, stacked together with high-velocity primary energy (Figure 6.0-4).

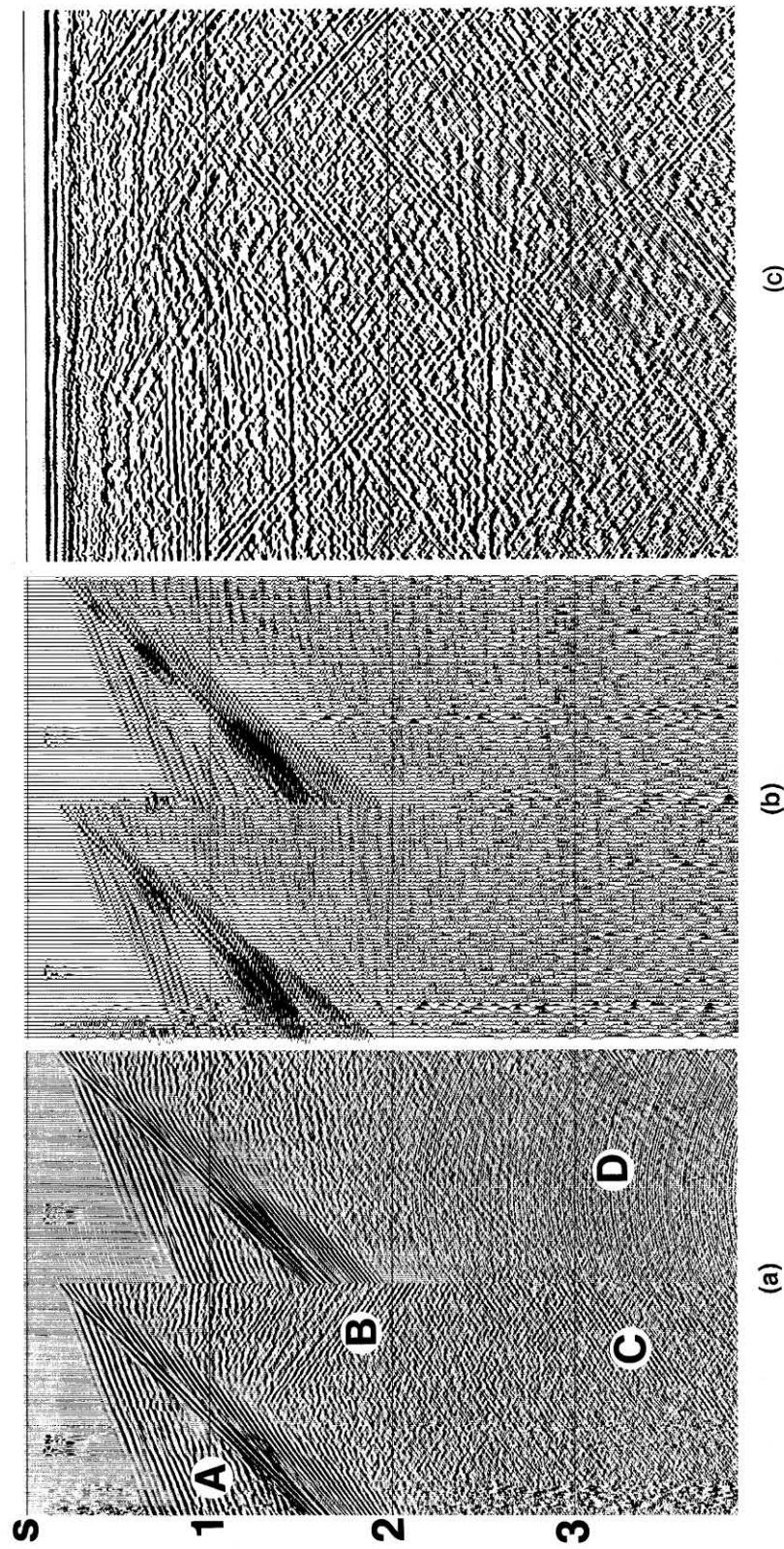
Linear noise associated with side scatterers is recognized easily on time slices from a 3-D volume of stacked data. Note in Figure 6.0-5 the circular patterns expanding out from the source of a series of point scatterers at the water bottom. In this case, certain parts of the sea-bottom pipelines act as point scatterers.

Attenuation of coherent linear noise associated with side scatterers may be achieved by $f - k$ filtering (Section 6.2), $\tau - p$ transform (Section 6.3) or Radon transform (Section 6.4) techniques. A linear event on a shot record maps onto a radial line in the $f - k$ domain, and thus can be rejected by $f - k$ dip filtering. A linear event on a shot record maps onto a point in the $\tau - p$ domain, and thus can be rejected by muting in the $\tau - p$ domain. Finally, spatially random noise and coherent linear noise are not included in the mapping from CMP domain to Radon-transform domain based on hyperbolic moveout. As a result, the reconstructed CMP gather by way of inverse transform will be free of noise.

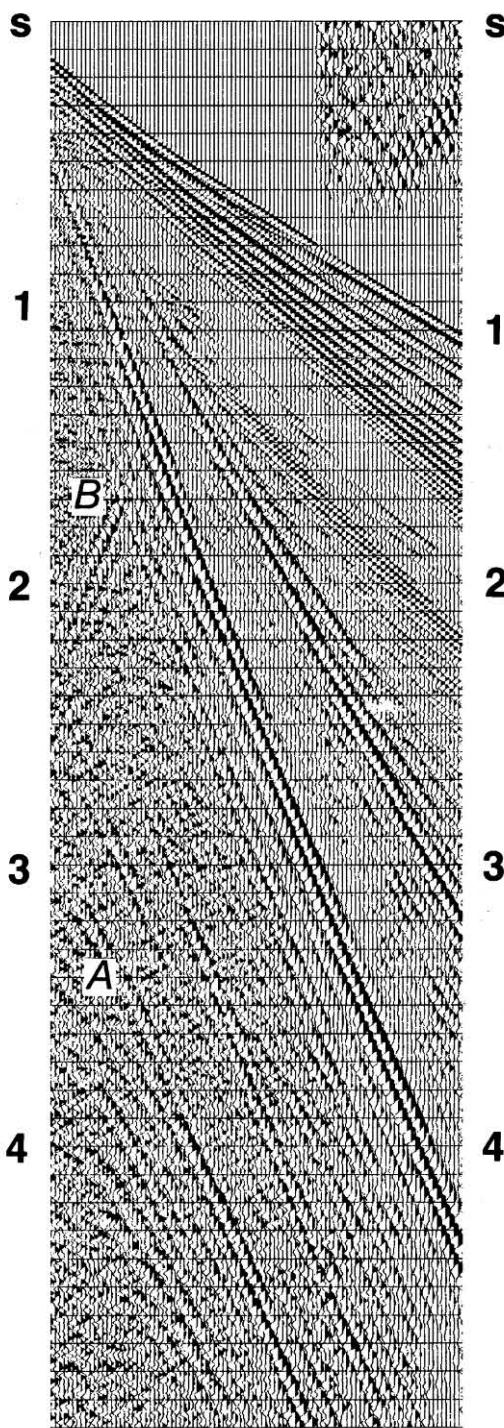
Coherent linear noise also exists in land data in the form of dispersive Rayleigh wave, commonly known as ground roll. This type of coherent noise has low group velocity and large amplitudes and is limited to low frequencies. In fact, as shown in Figure 6.0-6, ground-roll energy almost always dominates the reflection energy that may be present in the recorded data. Only after some type of amplitude scaling, reflections become visible (Figure 6.0-7). Note from the selected shot records in Figure 6.0-6 that the dispersive waves associated with the ground-roll energy change in strength and stepout (the dip of the linear noise trend) as a result of variations in the near-surface conditions.

Swell noise manifests itself on shot records in the form of low-frequency vertical streaks (Figure 6.0-8). This type of noise arises from rough weather conditions during marine seismic recordings, especially in shallow waters. A low-cut filter often removes the swell noise from shot records.

Finally, cable noise is one other type of coherent noise that manifests itself in the form of low-frequency linear events with very large stepout as seen on the shot records in Figure 6.0-9. Note the increase in the



6.0-1. (a) Two common-shot gathers and (b) two CMP gathers from the same line; (c) CMP stack. See text for details. (Data courtesy Taylor Woodrow Energy Ltd.)



6.0-2. A shot gather containing predominantly guided waves. See text for a description of the labeled events.

energy level of the cable noise as the water depth becomes shallower. As for the swell noise, a low-cut filter often removes the cable noise from shot records.

Treatment of Coherent Linear Noise by Conventional Processing

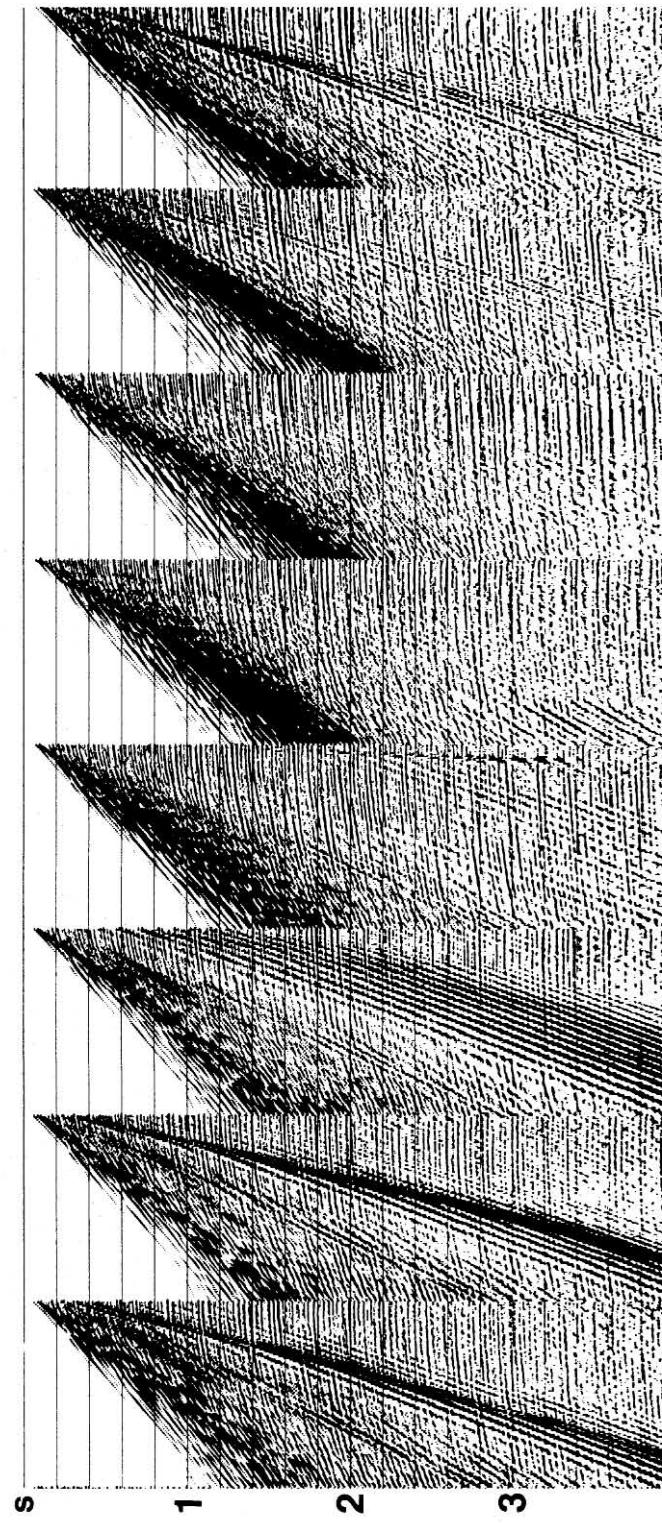
We shall apply a processing sequence to a marine 2-D data set that includes very basic steps without any special attempt to attenuate coherent linear noise. The objective is to examine the treatment of such noise by the three principal processes — deconvolution, stacking and migration.

Figure 6.0-10 shows selected raw shot records from the marine line under consideration. Note the presence of guided waves in all the records in the form of a prominent dispersive wave package. The dispersive nature of guided waves is pronounced especially in shallow water. Because of their high amplitudes, guided waves dominate recorded marine data before the correction for geometric spreading. Since they travel in the horizontal direction within the water layer, guided waves do not contribute to the useful reflection energy. Therefore, these waves are often muted in shallow records as shown in Figure 6.0-11. Unfortunately, some reflection energy at far offsets is inadvertently removed as a result of muting the guided waves.

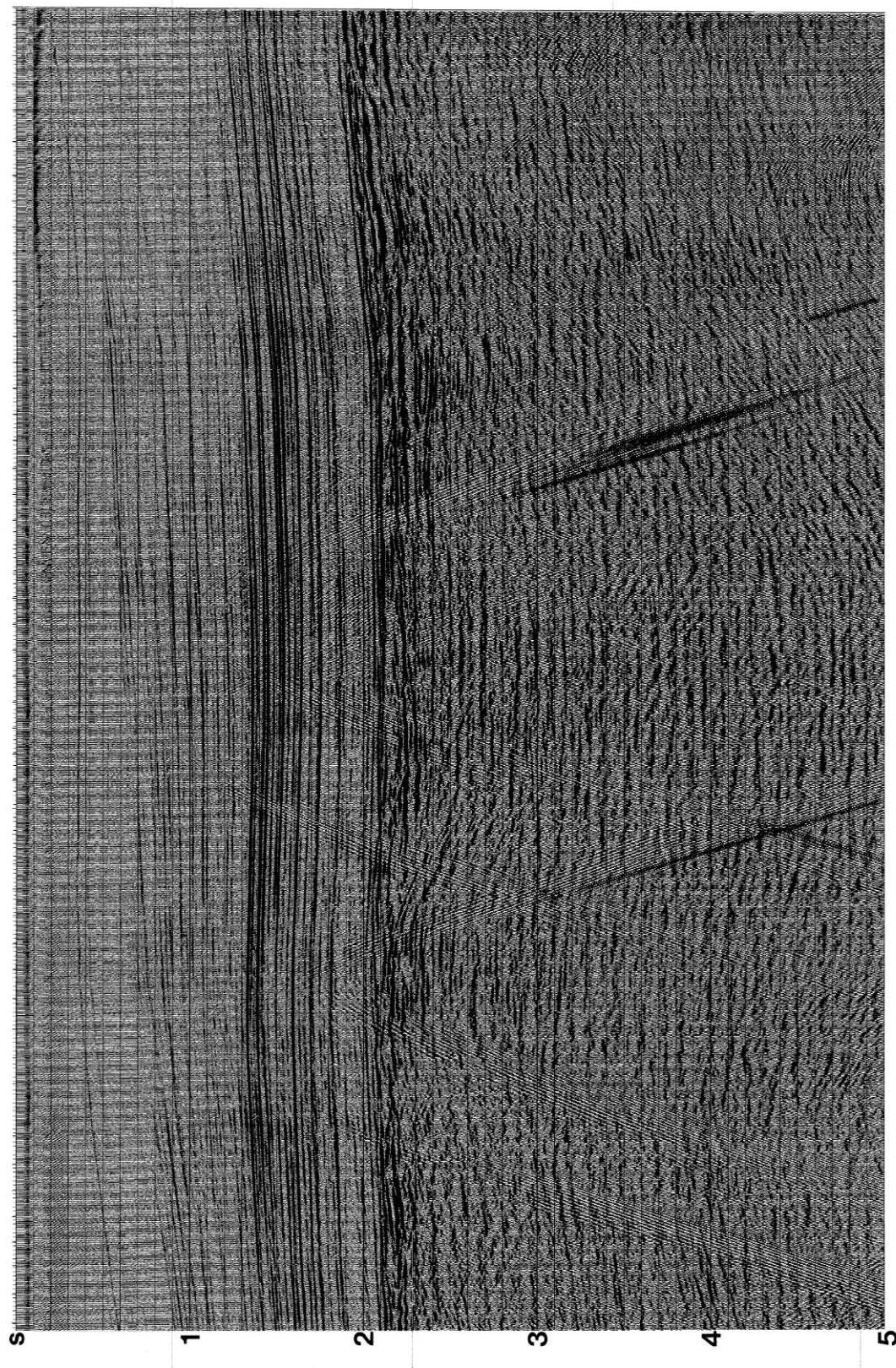
Following t^2 -scaling of amplitudes to compensate for geometric spreading, we note the enhancement of coherent noise at late times. Note in Figure 6.0-11, the records at shot points 300 and 400 contain linear noise below 2 s, and all records except at shot point 200 contain coherent noise with a curvature below 3 s, all associated with side scatterers. Additionally, observe the low-frequency cable noise with large stepout especially at near offsets below 3 s on the records at shot points 300, 400, 600, and 700.

Deconvolution flattens the spectrum and as a result enhances the low-frequency cable noise as seen in Figure 6.0-12. After the application of a wide bandpass filter, very low-frequency and very high-frequency noise components are removed. Nevertheless, the side-scattered energy with varying moveout still remains in the shot records (Figure 6.0-13).

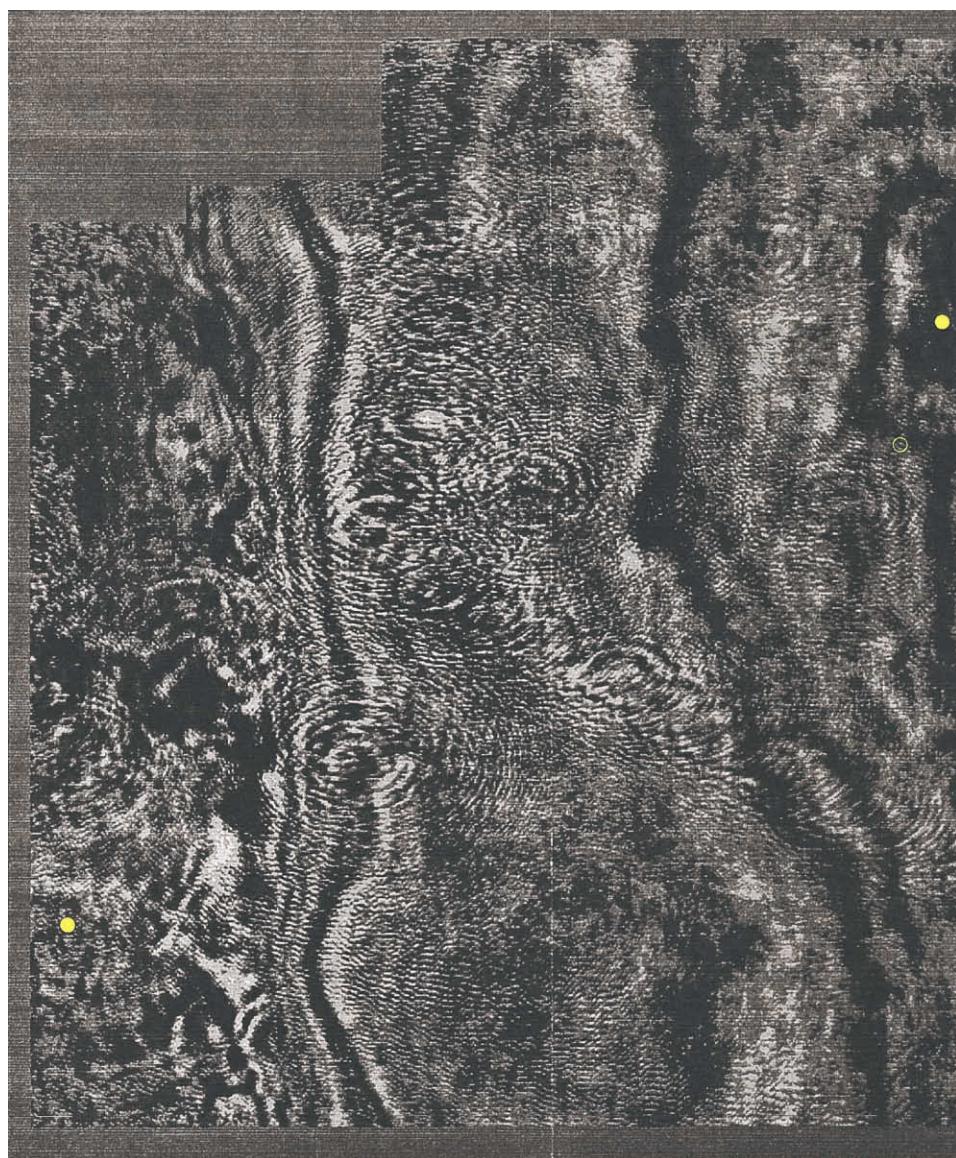
When data are sorted to CMP gathers, the linear nature of the coherent noise associated with side scatterers disappears (Figure 6.0-14). On the other hand, side-scatterer noise with curvature behaves like events with nonhyperbolic moveout. Following the normal-moveout correction and stacking, the side-scatterer energy reappears as in Figure 6.0-15. Note the dipping linear noise along the steep flanks of the diffractions associated with the side scatterers in the water bottom. The steeply dipping linear noise at water velocity should



6.0-3. Shot gathers containing guided waves with varying strength, and reverberations and short-period multiples. (Data courtesy Deminex Petroleum Company.)



6.0-4. A CMP stack that contains diffraction energy associated with side scatterers at the water bottom.



6.0-5. A time slice from an unmigrated 3-D volume of stacked data which exhibits circular patterns associated with point scatterers along sea-bottom pipelines. (Data courtesy Total Argentina.)

not be confused with the diffractions of the flanks of the salt diapirs at higher velocities.

Coherent linear noise associated with side scatterers are attenuated largely by dip-moveout correction (Section 5.2). Compare the stacked section in Figure 6.0-16 with that in Figure 6.0-15, and note that DMO correction has enhanced the diffractions associated with the salt flanks while it has attenuated the linear noise associated with the side scatterers. Any remaining side-scatterer related noise at late times is overmigrated as a result of the higher primary velocities (Figure 6.0-17).

Reverberations and Multiples

In this chapter, we shall discuss multiple attenuation techniques based on velocity discrimination between multiples and primaries, and periodicity of multiples. While these techniques seem to have a good conceptual basis, their performance on field data can be disappointing. There are several possible explanations for this.

First, for velocity discrimination techniques to be effective, significant moveout differences must exist between primaries and multiples. However, the inability

(text continues on p. 856)

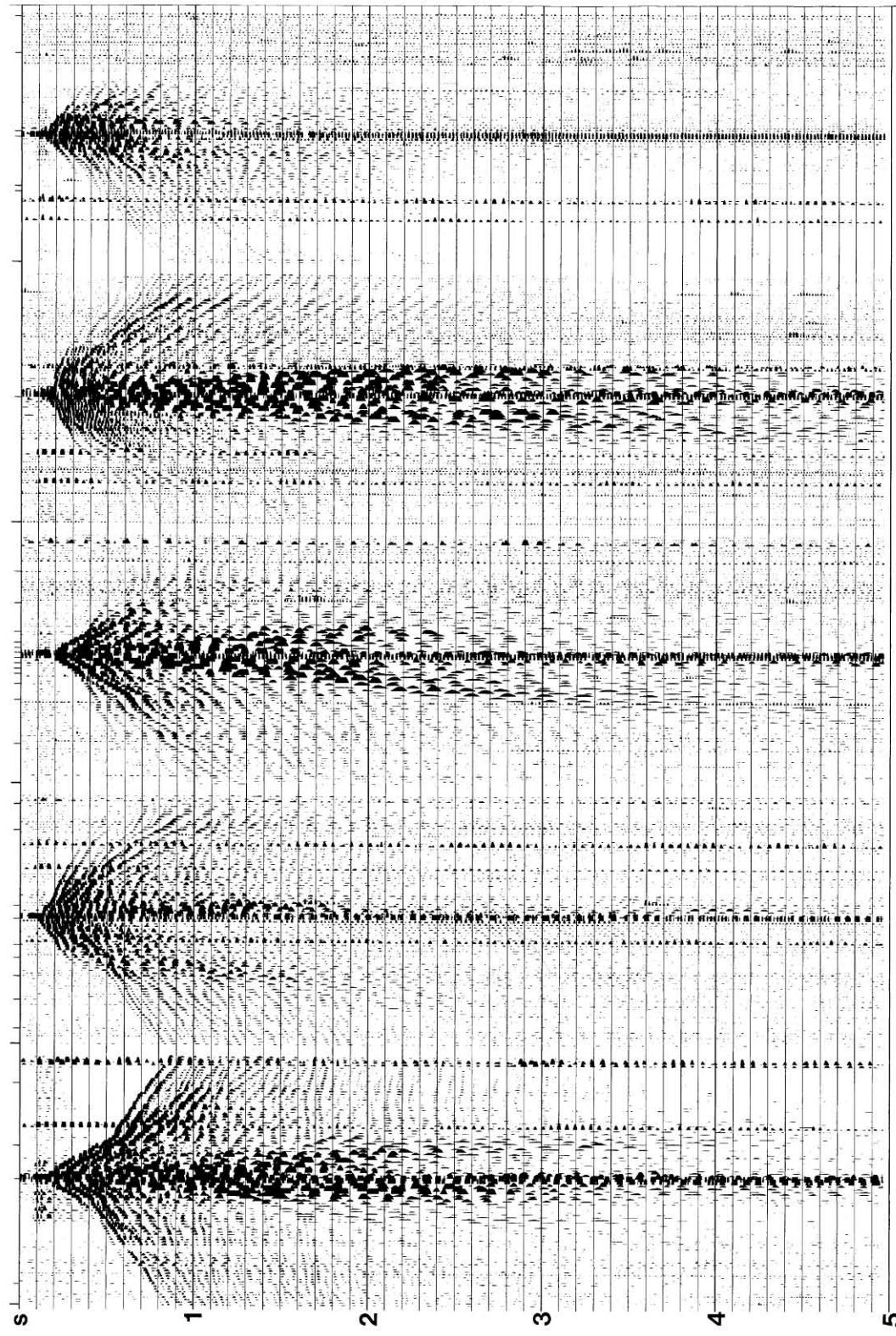


FIG. 6.0-6. Selected shot records from a land 2-D line. Note that the ground-roll energy dominates over any reflection energy that may be present in the data.

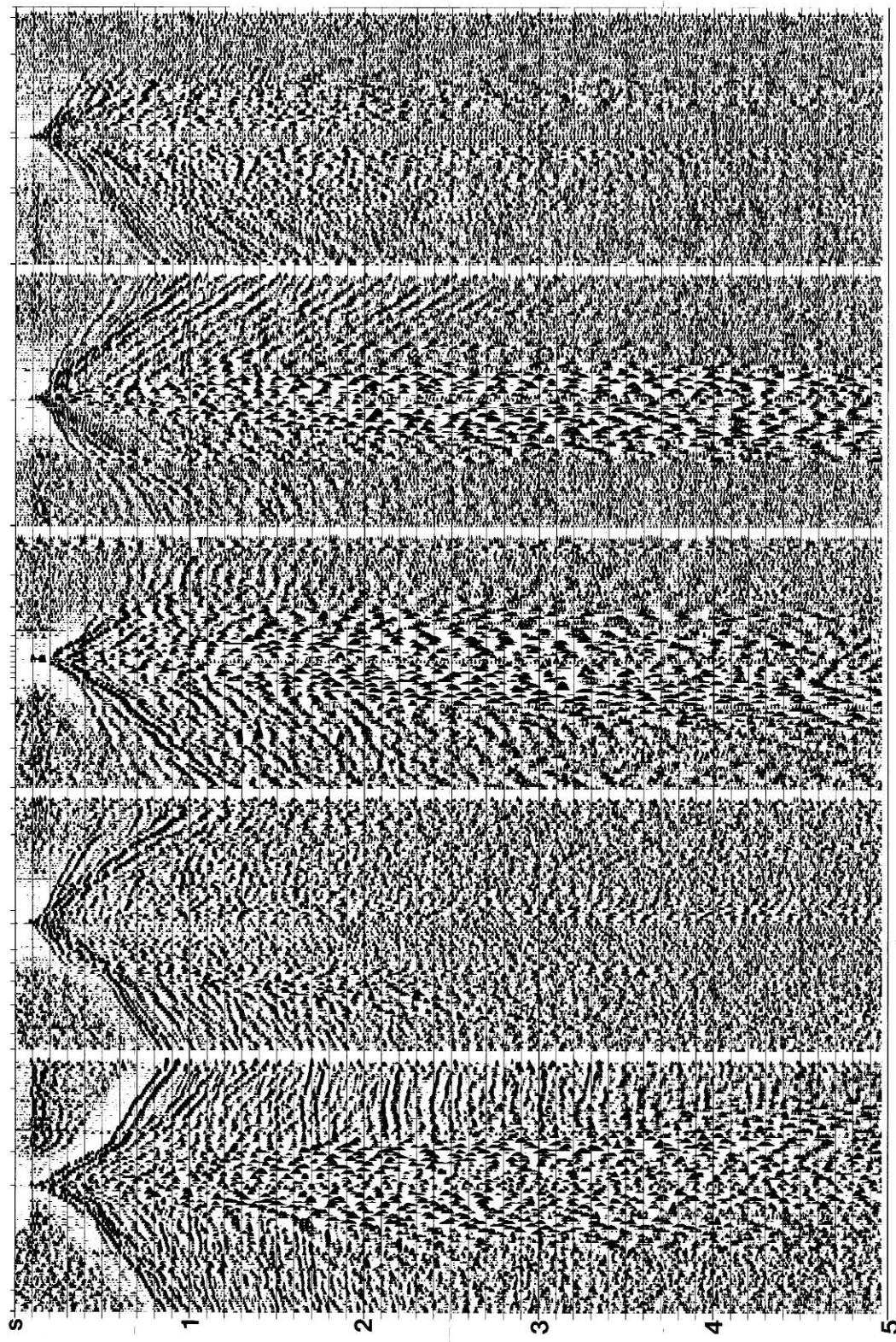


FIG. 6.0-7. Same records as in Figure 6.0-5 with AGC applied to enhance the reflection energy dominated by the ground-roll energy.

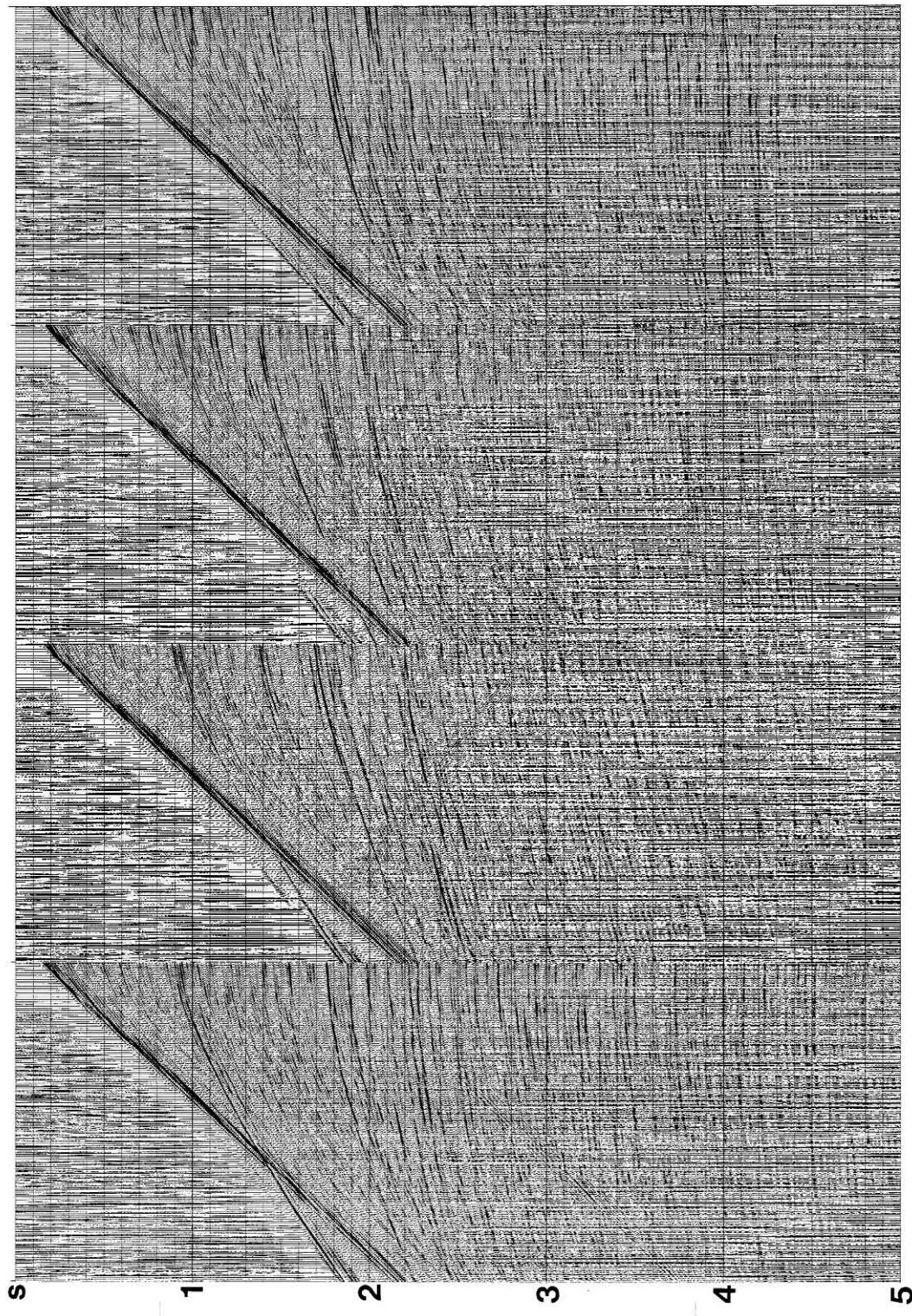


FIG. 6.0-8. Selected shot records from a marine 2-D line with swell noise.

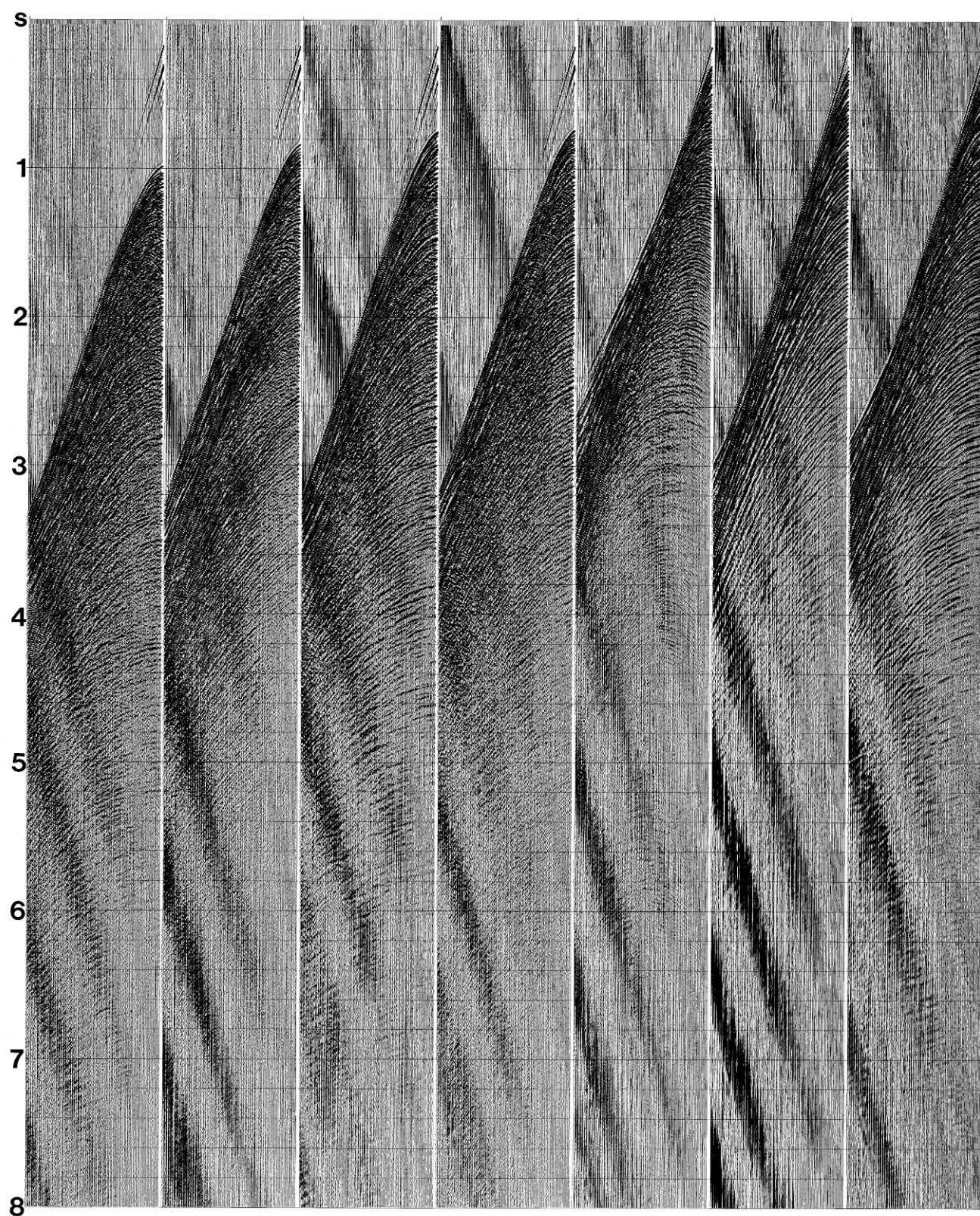


FIG. 6.0-9. Selected shot records from a marine 2-D line with swell noise.

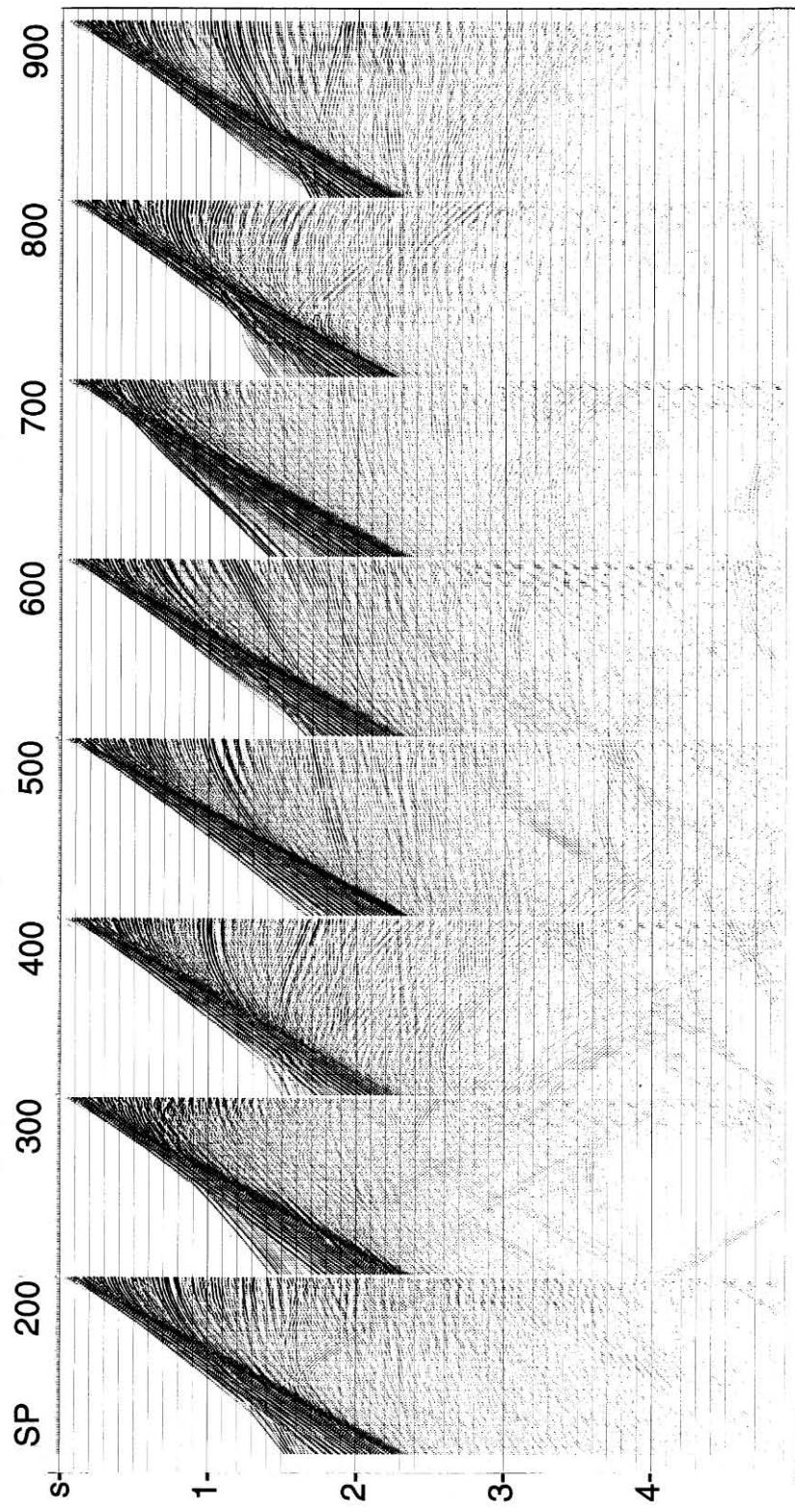


FIG. 6.0-10. Selected shot records from a marine 2-D line.

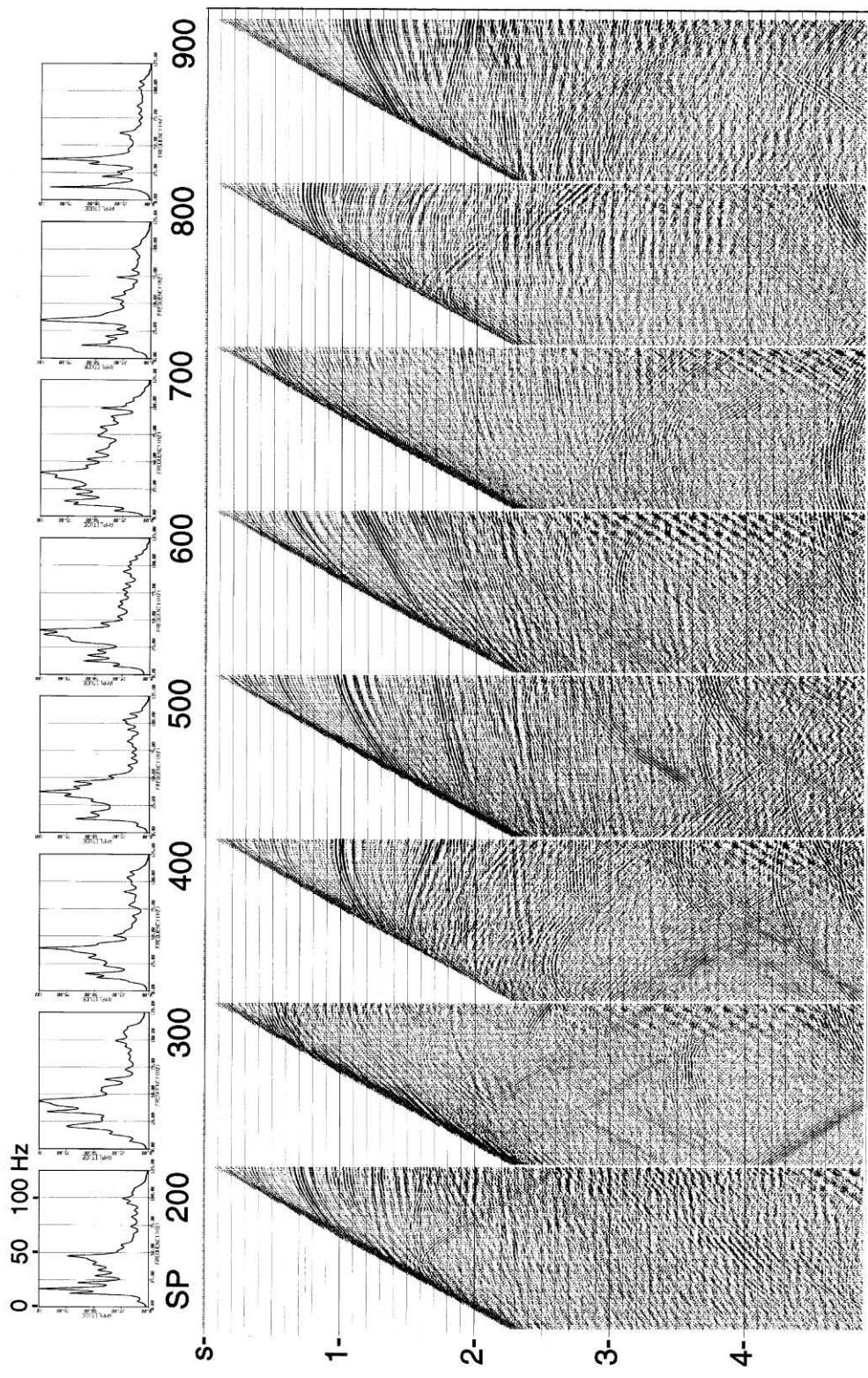


FIG. 6.0-11. The same shot records as in Figure 6.0-10 after muting the guided waves and applying t^2 -scaled scaling. Shown on top of each record is the average amplitude spectrum.

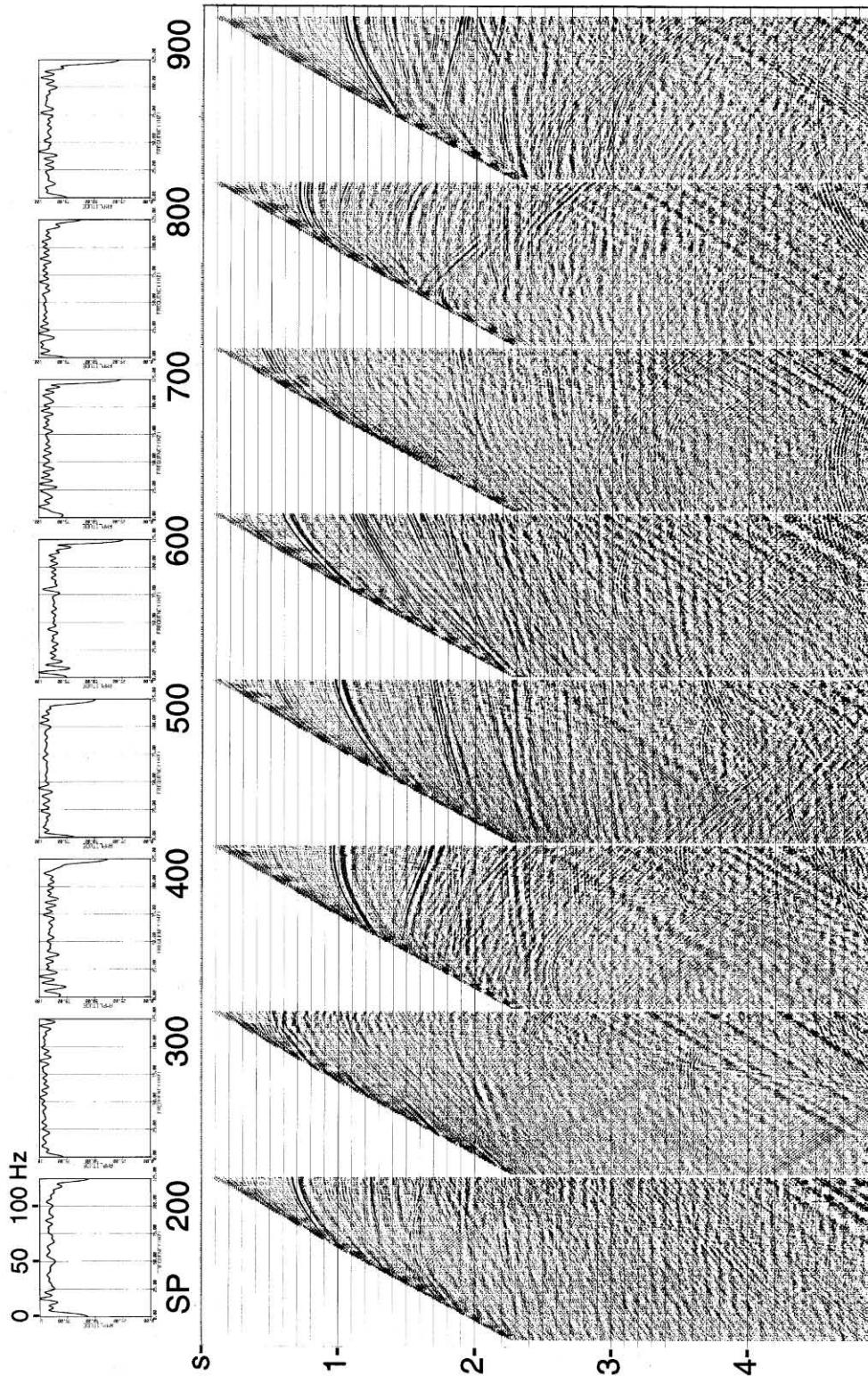


FIG. 6.0-12. The same shot records as in Figure 6.0-11 after spiking deconvolution. Shown on top of each record is the average amplitude spectrum.

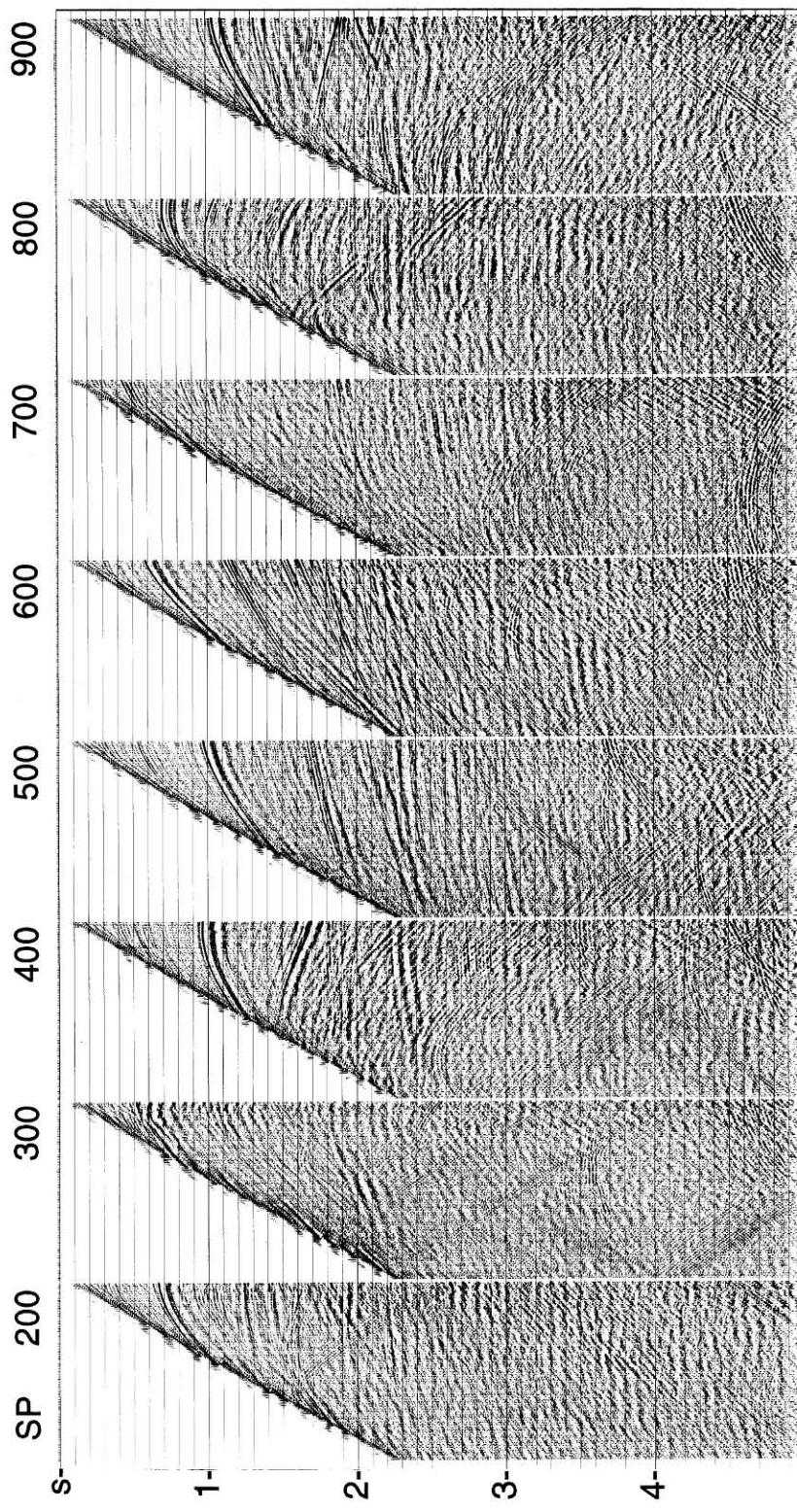
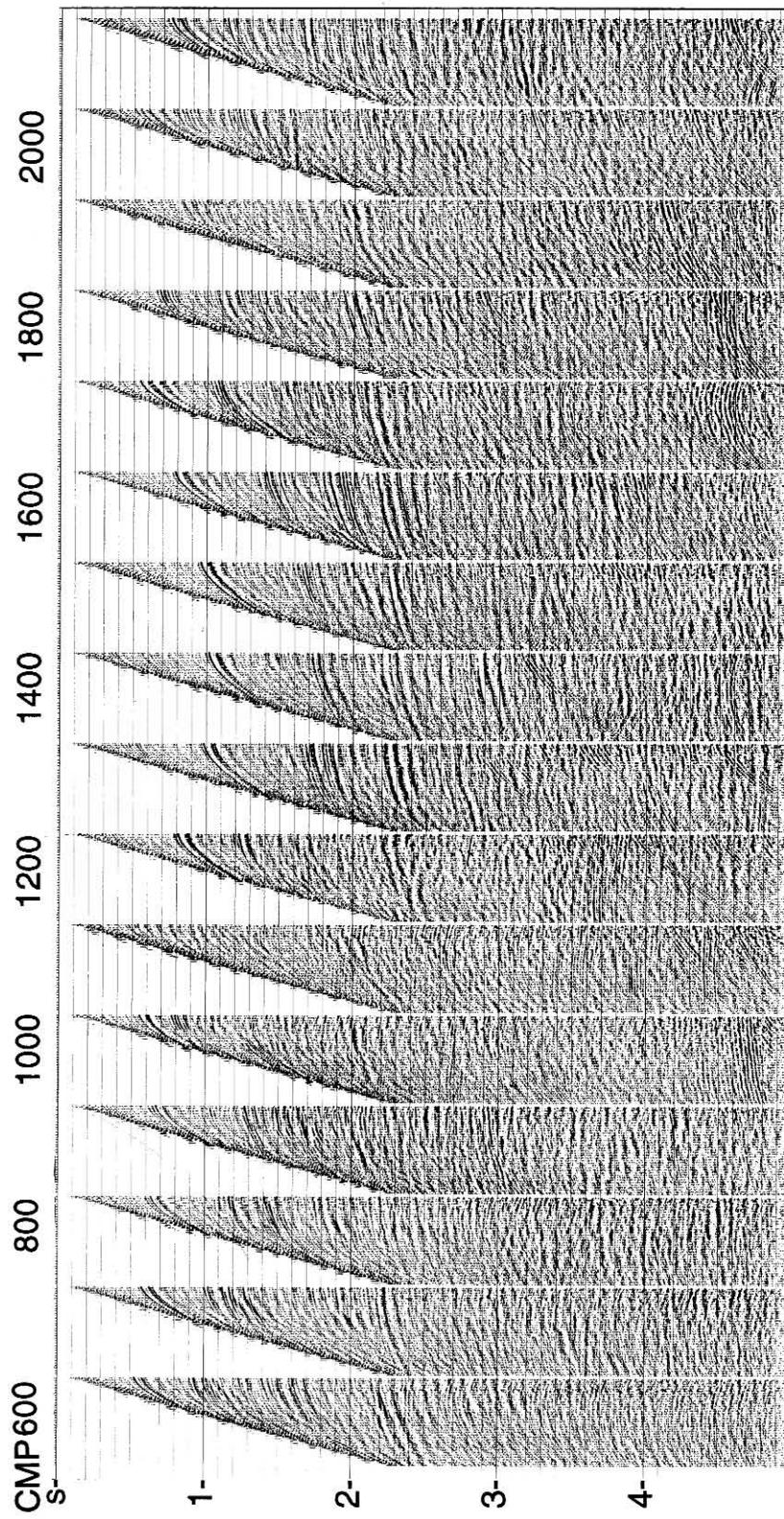


FIG. 6.0-13. The same shot records as in Figure 6.0-12 after trace balancing and wide bandpass filtering.



6.0-14. Selected CMP gathers associated with the data as in Figure 6.0-13.

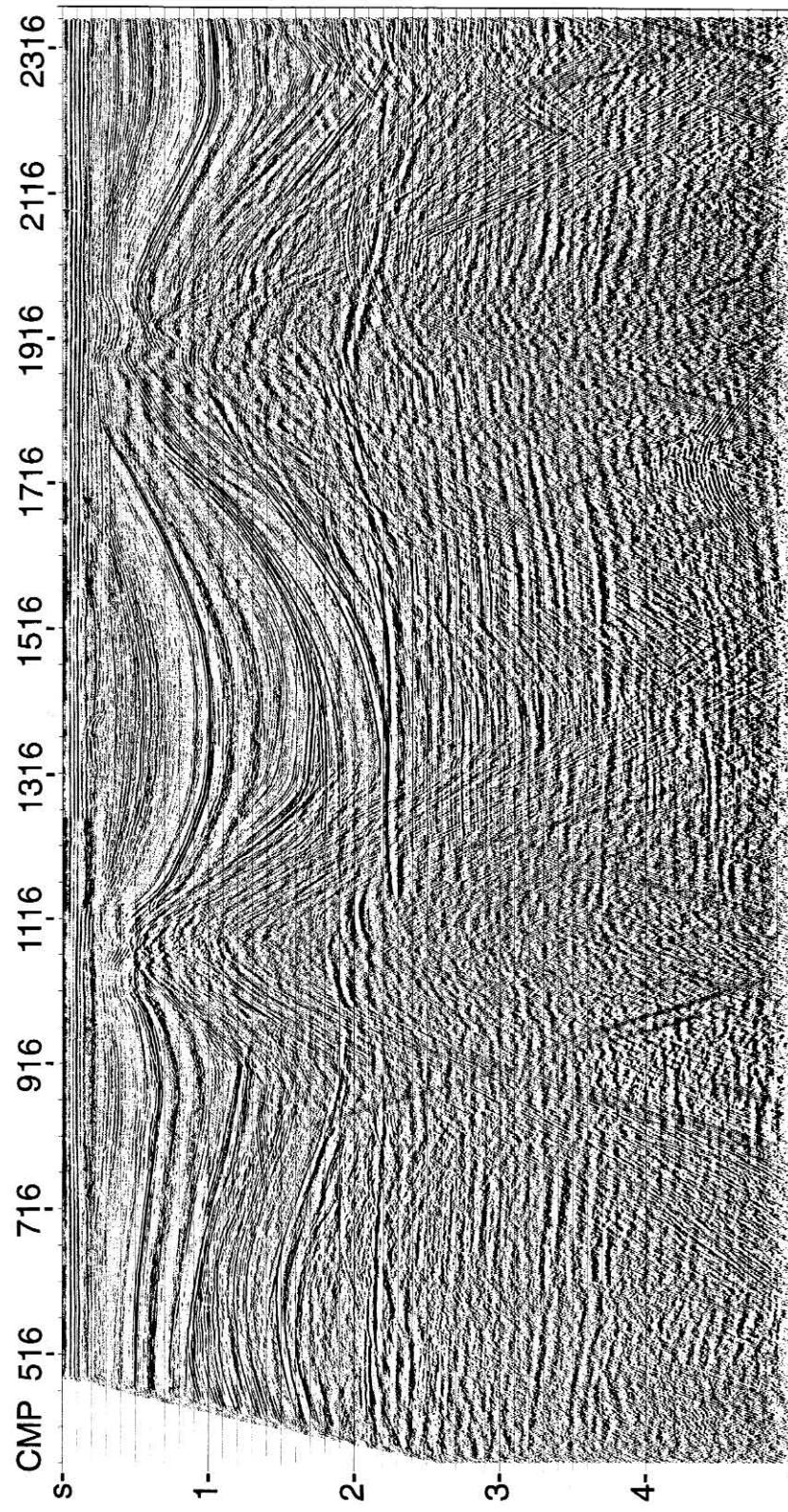


FIG. 6.0-15. CMP stack associated with the gathers as in Figure 6.0-14.

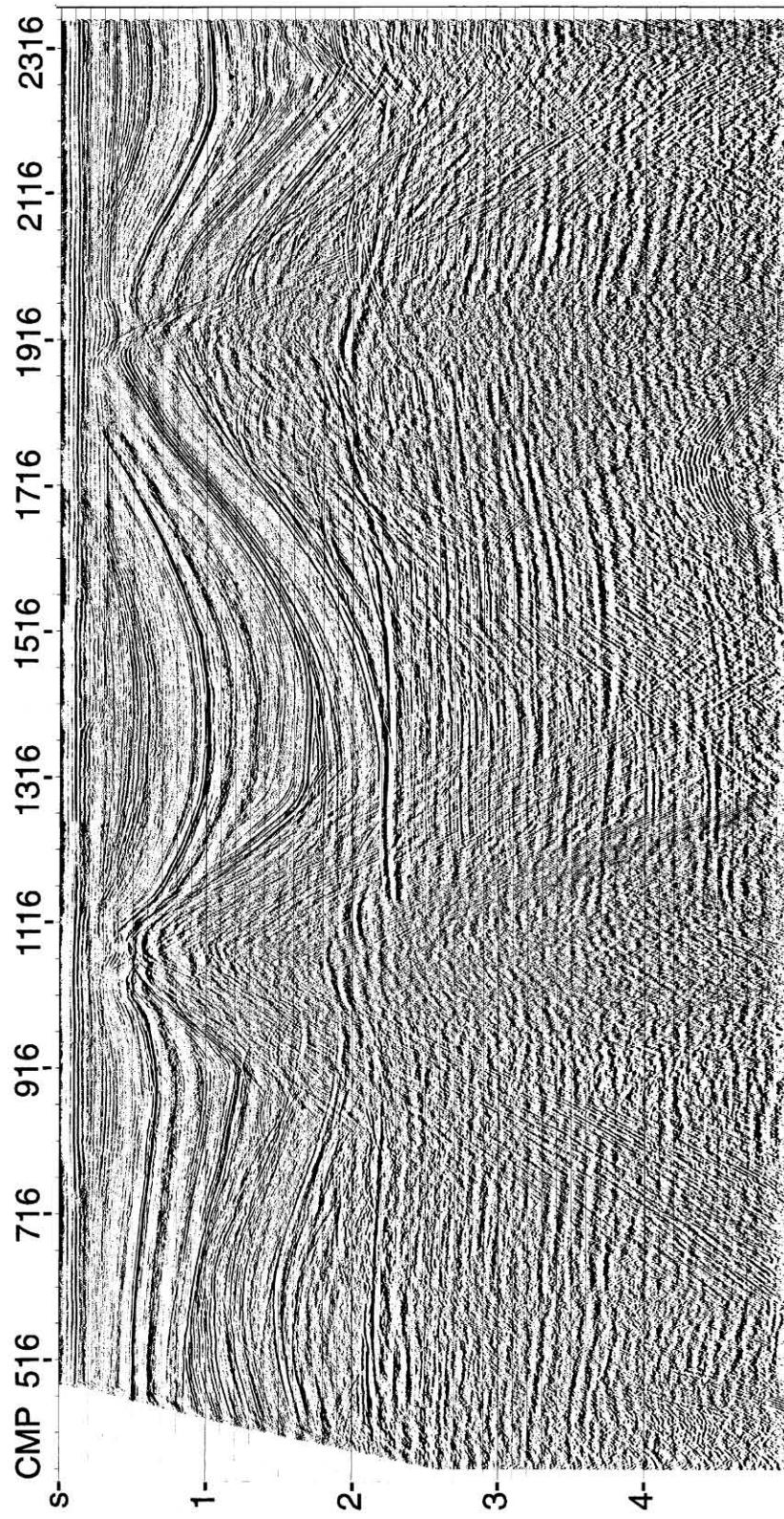
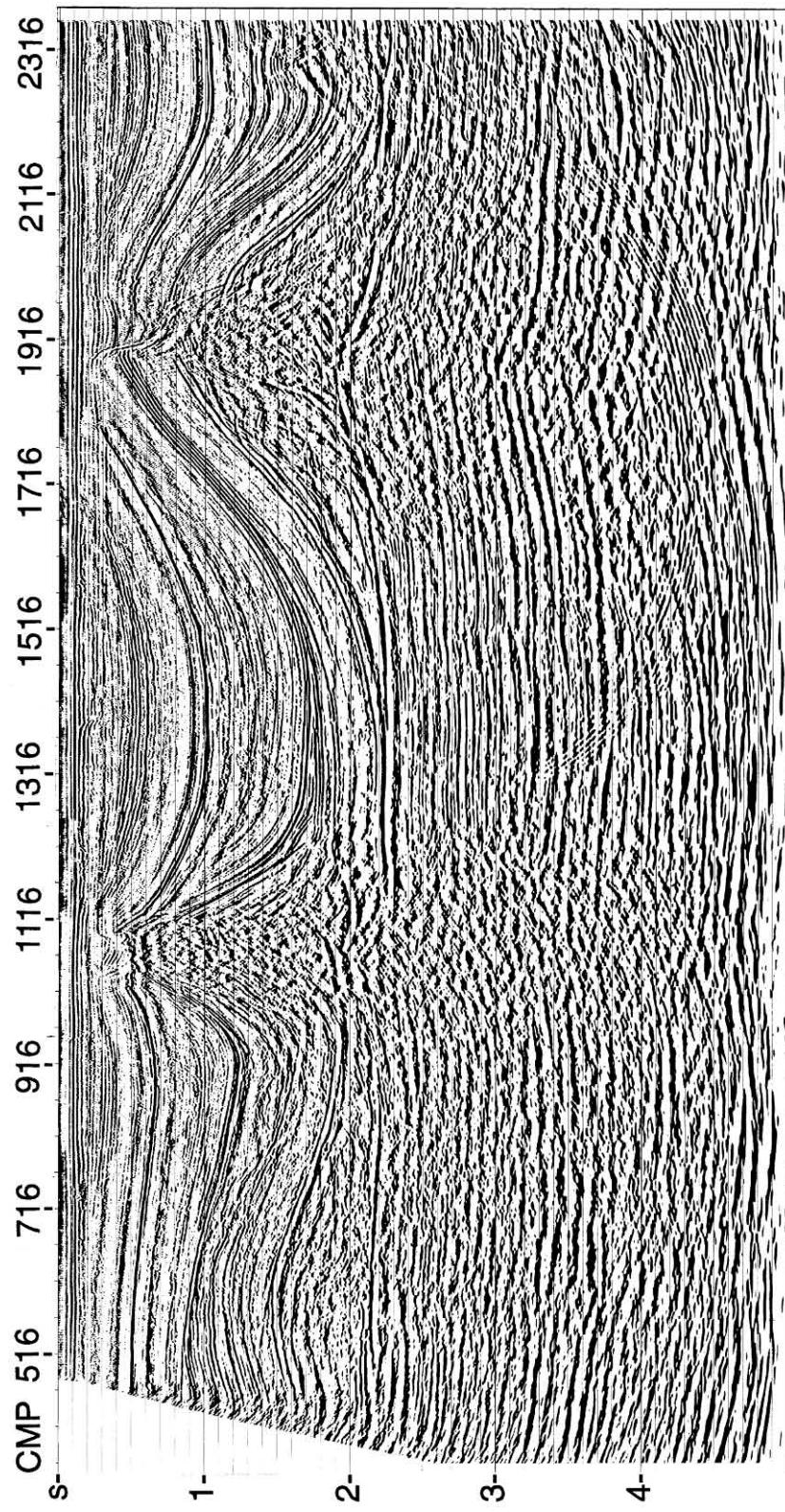
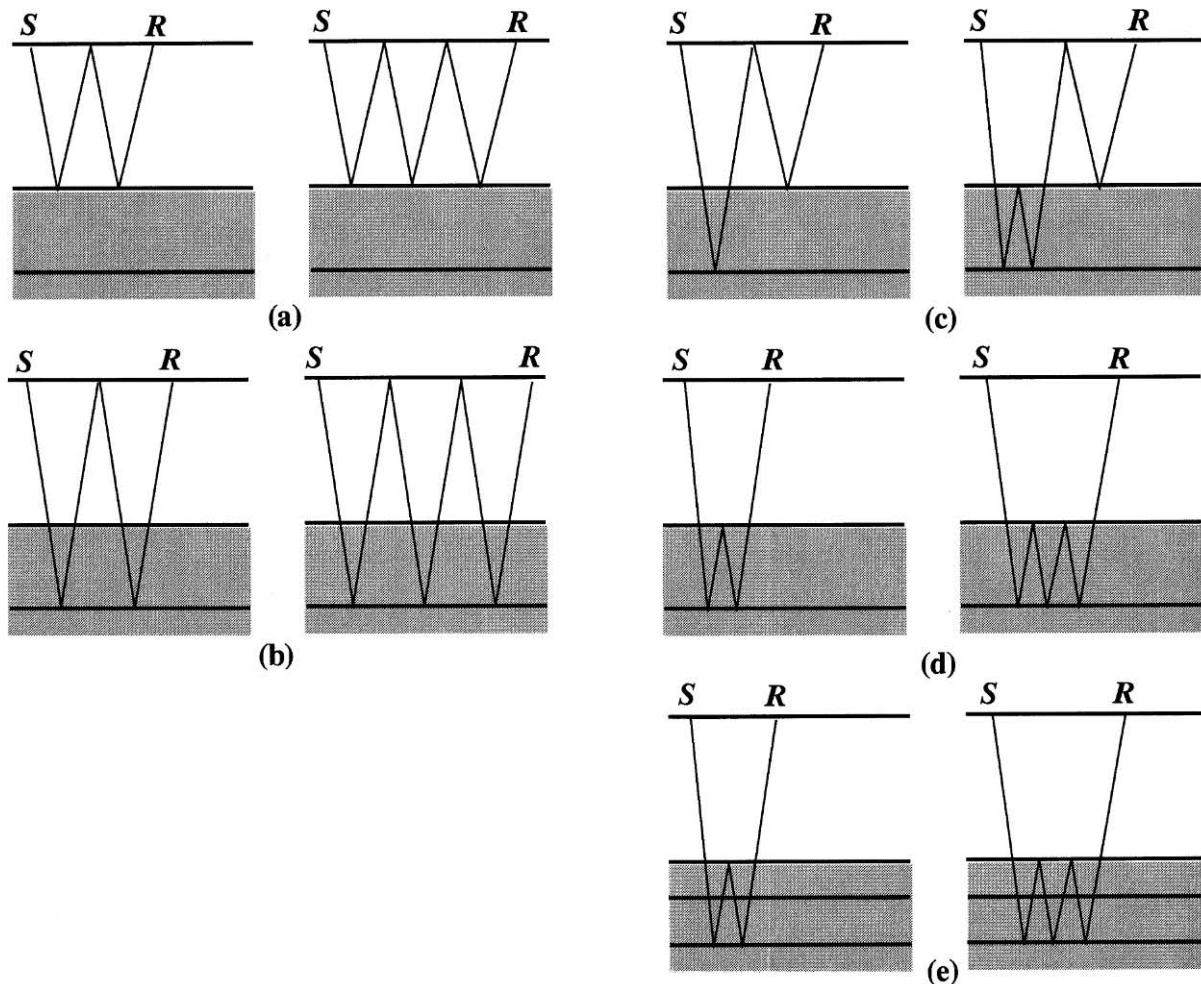


FIG. 6.0-16. DMO stack associated with the data as in Figure 6.0-14.



6.0-17. Migration of the DMO stack shown in Figure 6.0-16.



6.0-18. A sketch of raypaths associated with various types of multiples. The shallowest interface in each case represents the water bottom. See text for details.

to exploit the large moveout differences between primaries and multiples in the mute zone works against the methods based on velocity discrimination.

Periodicity of multiples is preserved for the ideal case of zero offset and horizontally layered earth. At nonzero offsets, periodicity often is destroyed even for the horizontally layered case. Nevertheless, periodicity is better preserved for the horizontally layered earth in the slant-stack domain. Multiple attenuation in this domain is discussed in Section 6.3.

There is also a problem caused by the application of geometric spreading correction (Section 1.4), when it is applied using the primary velocity function. This type of correction usually results in enhancement of the amplitudes of multiple reflections. The slant-stack approach (Section 6.3) is implemented before the geometric spreading correction, so there is no danger of amplifying the multiple energy.

In Sections F.4 and F.5, we shall review the theory of multiple attenuation using wave extrapolation techniques. These are targeted for a specific class of multiples — those which are either associated with the free surface or water bottom.

We now examine the various types of multiples in recorded marine data in different domains — shot records, common-offset sections and CMP gathers. Most multiple reflections arise from an interface with a strong impedance contrast such as the free surface and water bottom. Figure 6.0-18 shows raypath diagrams for:

- (a) water-bottom multiples of first- and second-order,
- (b) free-surface multiples of first- and second-order,
- (c) peg-leg multiples of first- and second-order,
- (d) intrabed multiples of first- and second-order, and
- (e) interbed multiples of first- and second-order.

These are but a few of the numerous configurations of raypaths associated with multiple reflections encountered in recorded data. Regardless of the type of multiples, they all have two common properties that can be exploited to attenuate them with varying degree of success — *periodicity* and *moveout* that is different from primaries.

Figure 6.0-19 shows selected marine shot records which exhibit a broad range of multiples. The shot records over the deep water contain long-period water-bottom multiples and peg-leg multiples associated with reflectors just below the water bottom. Whereas the shot records over the shallow water contain short-period multiples and reverberations. Note the guided waves in the shallow-water records that also contain multiples which have raypaths within the water layer.

Figure 6.0-20 and 6.0-21 show selected CMP gathers and segments of near-offset sections associated with the data as in Figure 6.0-19. The near-offset sections have been moveout-corrected to zero offset — thus the small differences in the arrival times between those on the near-offset trace in the CMP gathers and traces in these moveout-corrected near-offset sections. Observe the existence of a broad range of multiple types in these pairs of CMP gathers and near-offset sections. The velocity spectra computed from the CMP gathers in Figures 6.0-20 and 6.0-21 are displayed in Figure 6.0-22.

Treatment of Reverberations and Multiples by Conventional Processing

We shall apply a processing sequence to a marine 2-D data set that includes very basic steps without any special attempt to attenuate multiples. The objective is to examine the treatment of various types of multiples by prestack and poststack deconvolution, the stacking process itself, and by prestack and poststack migration.

Figures 6.0-23 through 6.0-34 show portions of the following processing products associated with the data as in Figure 6.0-20 and 6.0-21:

- (a) a moveout-corrected near-offset section,
- (b) CMP-stacked section with no prestack and poststack deconvolution,
- (c) CMP-stacked section with prestack deconvolution, only, and
- (d) CMP-stacked section with prestack and poststack deconvolution.

The velocity spectra computed at the central CMP locations from the data as in (b) and (c) for each panel are shown in Figures 6.0-35 and 6.0-36.

Note from the near-offset sections in Figures 6.0-23a through 6.0-34a the abundance of a wide variety of multiples. CMP stacking itself (Figures 6.0-23b through 6.0-34b) without the aid of any special multiple attenuation process suppresses a significant amount of energy associated with the multiples based on the moveout difference between the primaries and multiples.

Prestack deconvolution with the added power of conventional stacking (Figures 6.0-23c through 6.0-34c) greatly suppresses a larger portion of the energy associated with the multiples. The corresponding velocity spectra shown in Figures 6.0-35 and 6.0-36 illustrate the combined power of prestack deconvolution and conventional stacking in attenuating multiples. The cascaded effect of pre- and poststack deconvolution in attenuating multiples is demonstrated in Figures 6.0-23d through 6.0-34d.

Despite the theoretical limitation that periodicity of multiples strictly is preserved only for zero-offset recording over a horizontally layered earth, practical experience as exemplified by Figures 6.0-23 through 6.0-36 convincingly suggests that statistical deconvolution can be a powerful tool for multiple attenuation. Coupled with conventional stacking, which exploits the velocity discrimination property, these two processes constitute a powerful combination to attenuate a broad range of multiples.

How does migration treat multiples? Figure 6.0-37 shows shallow portion of a CMP stack before and after poststack migration. Note the diffracted first-order water-bottom multiple reflection at approximately 750 ms. Migration collapses the diffractions along the water bottom. However, the diffractions accompanying the first-order multiple reflection are overmigrated since the migration velocity is the primary velocity at 750 ms. The diffracted multiples would have been collapsed had the water velocity been used to migrate the data.

Figure 6.0-38a shows a portion of a CMP-stacked section that contains a strong primary reflection between 1 and 2 s and the associated first-order multiple with a steeper apparent dip between 1.8 and 3.2 s. The overmigration of multiple reflections by poststack migration (Figure 6.0-38b) is more pronounced in that the apparent dip of a multiple reflection is greater than the dip of the primary associated with that multiple. Poststack migration has treated the multiple reflection in Figure 6.0-38a as a dipping primary and moved it to a position based on the primary velocity that was used to migrate the stacked section.

Prestack migration can provide the bonus effect of attenuating multiples as a result of velocity discrimination between primaries and multiples. More specifically, by using a velocity field that is appropriate for migrating primaries, multiples are undermigrated. This

(text continues on p. 876)

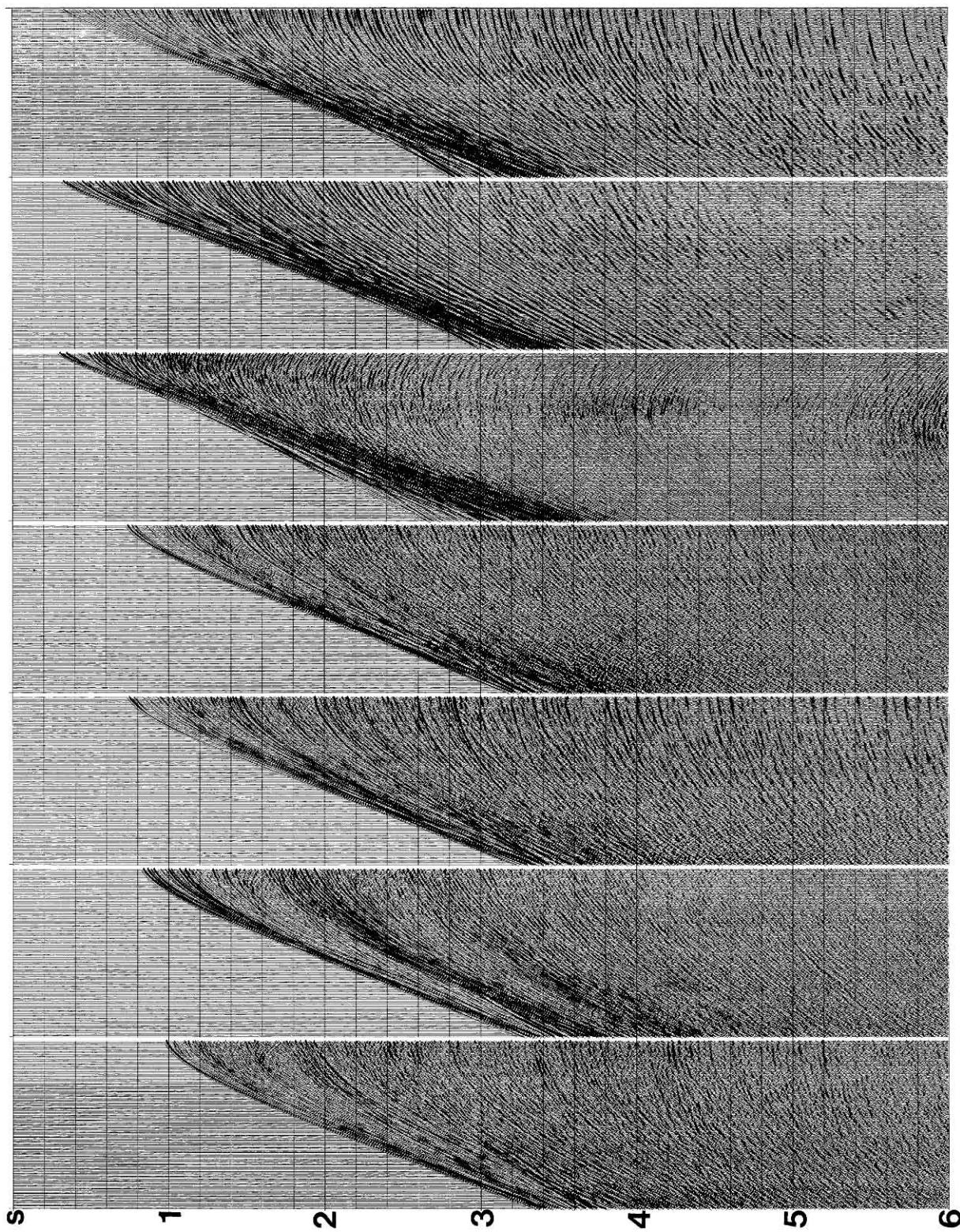


FIG. 6.0-19. Selected shot records from a marine 2-D line.

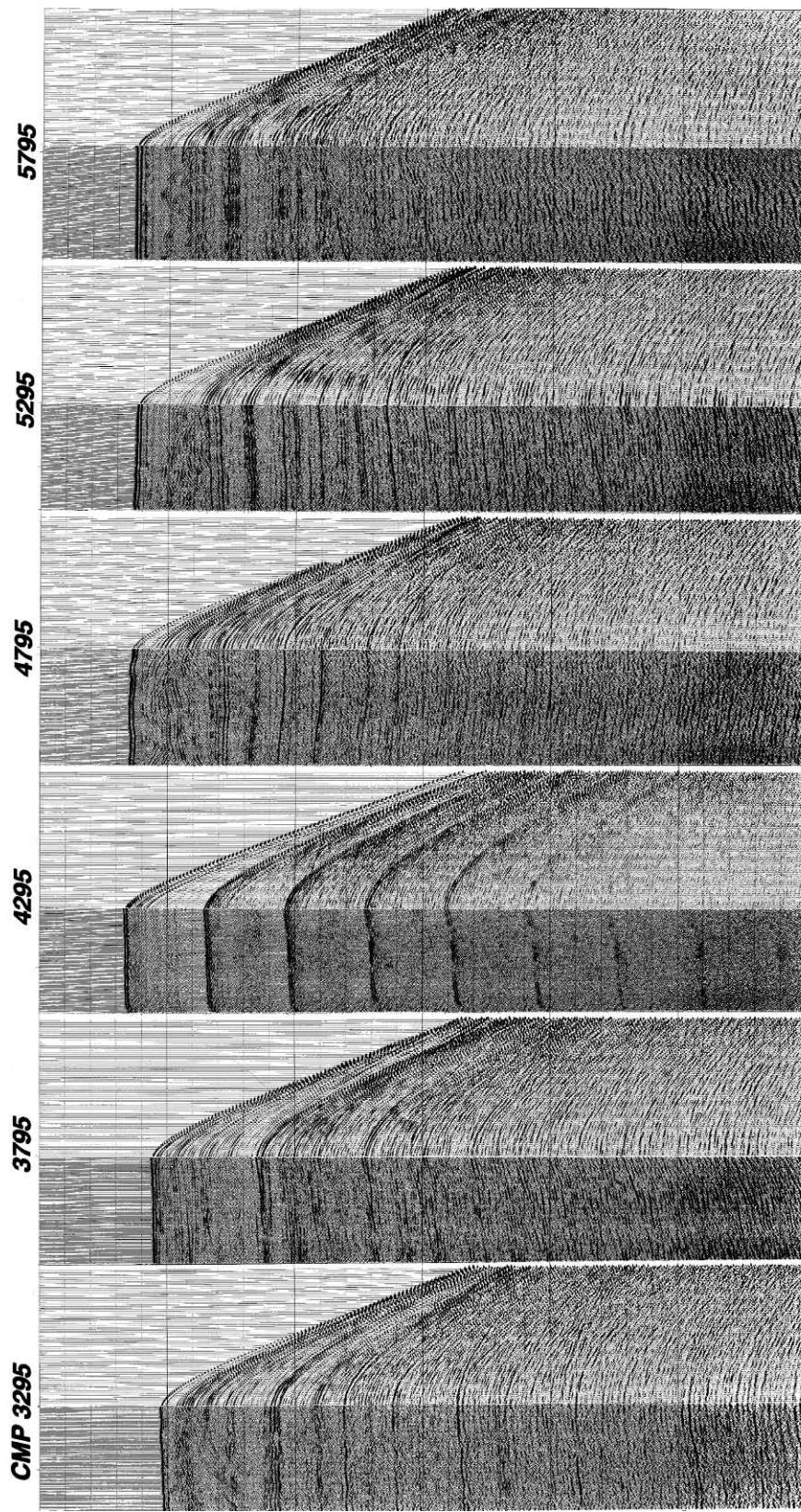


FIG. 6.0-20. Portions of the near-offset section at the vicinity of selected CMP locations along the line associated with the data as in Figure 6.0-19. Also shown are the CMP gathers augmented to the near-offset section at the selected locations.

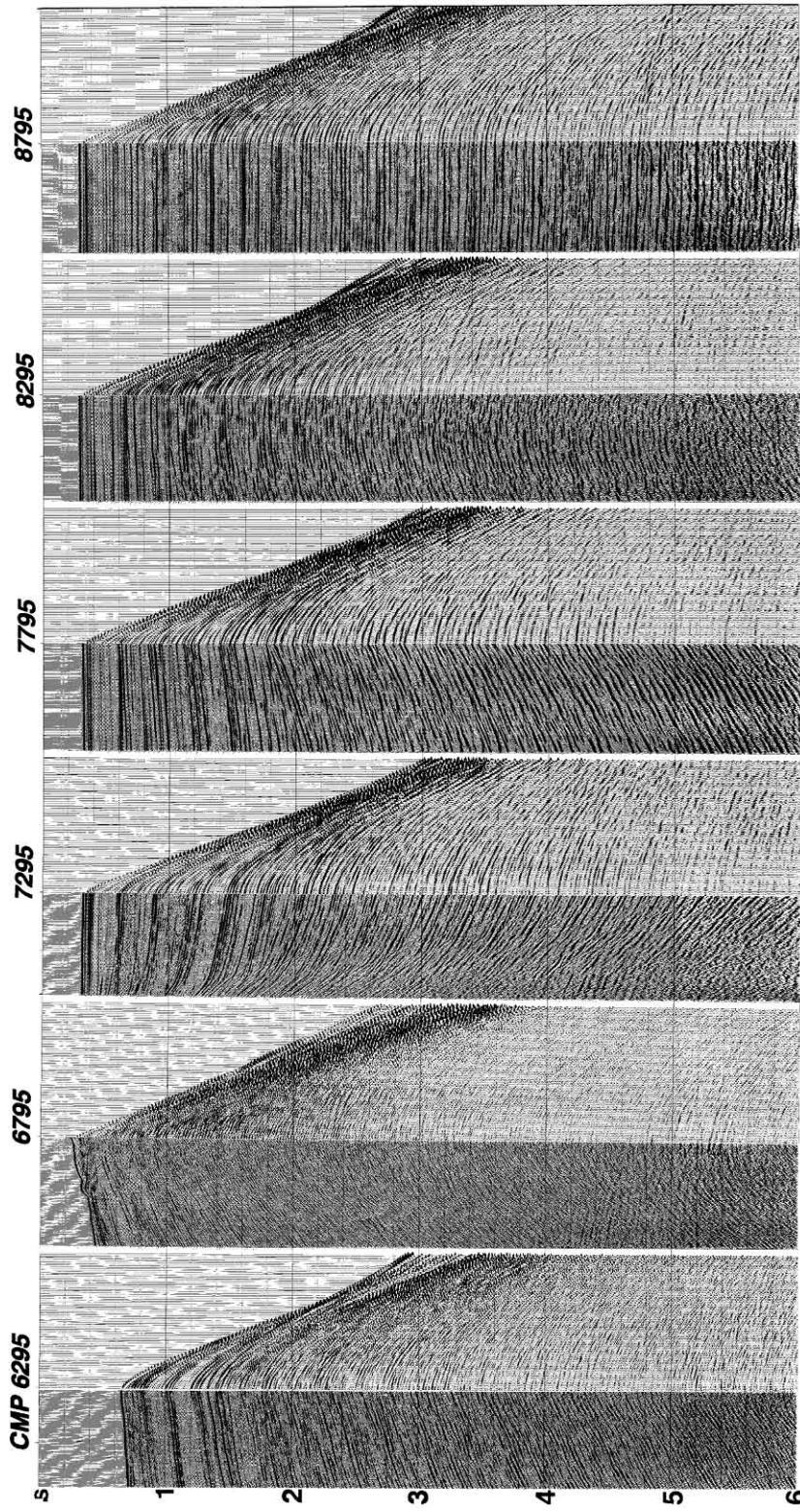


FIG. 6.0-21. Portions of the near-offset section at the vicinity of selected CMP locations along the line associated with the data as in Figure 6.0-19. Also shown are the CMP gathers augmented to the near-offset section at the selected locations.

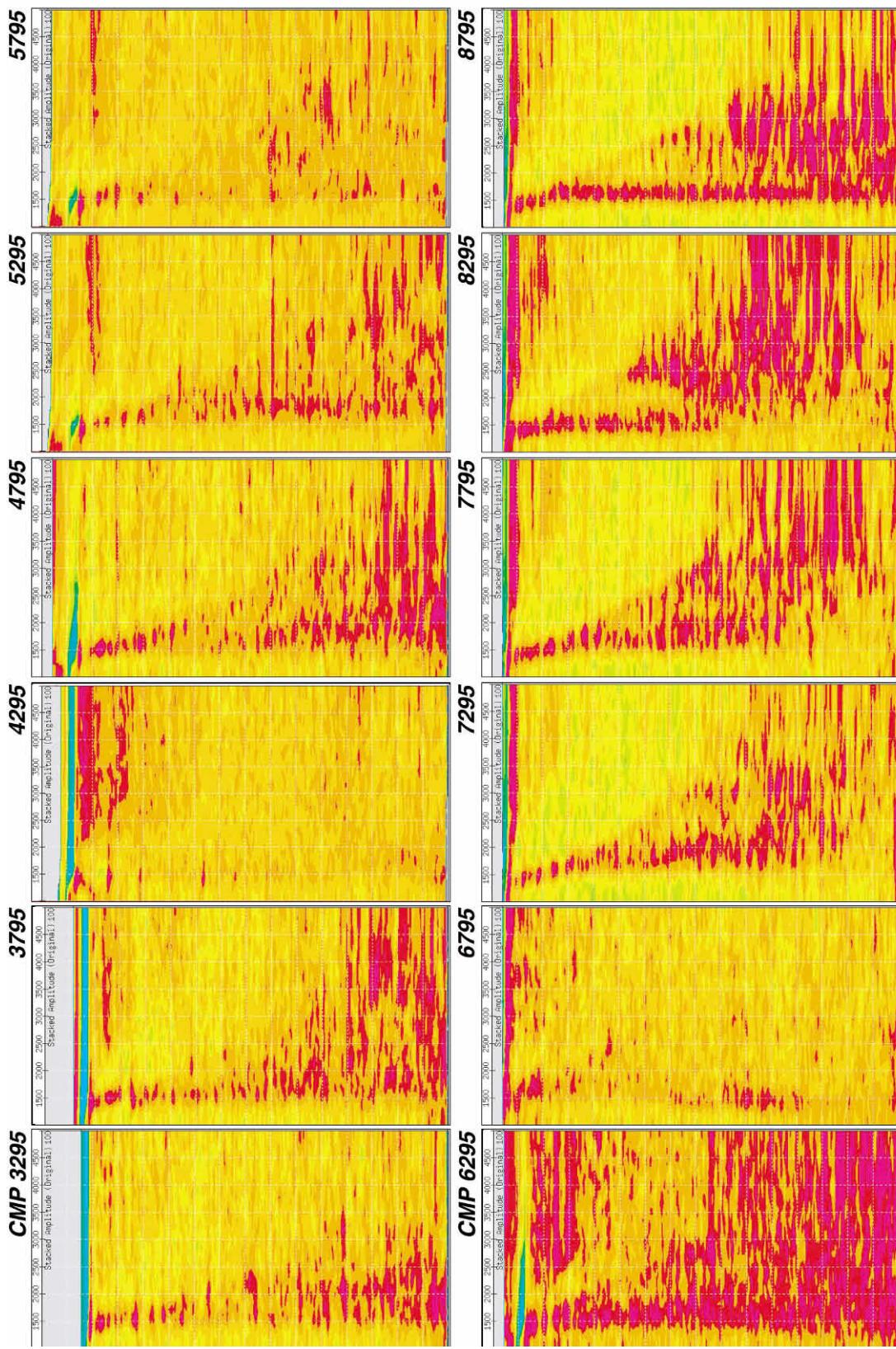


FIG. 6.0-22. Velocity spectra computed at the CMP locations as in Figures 6.0-20 and 6.0-21.

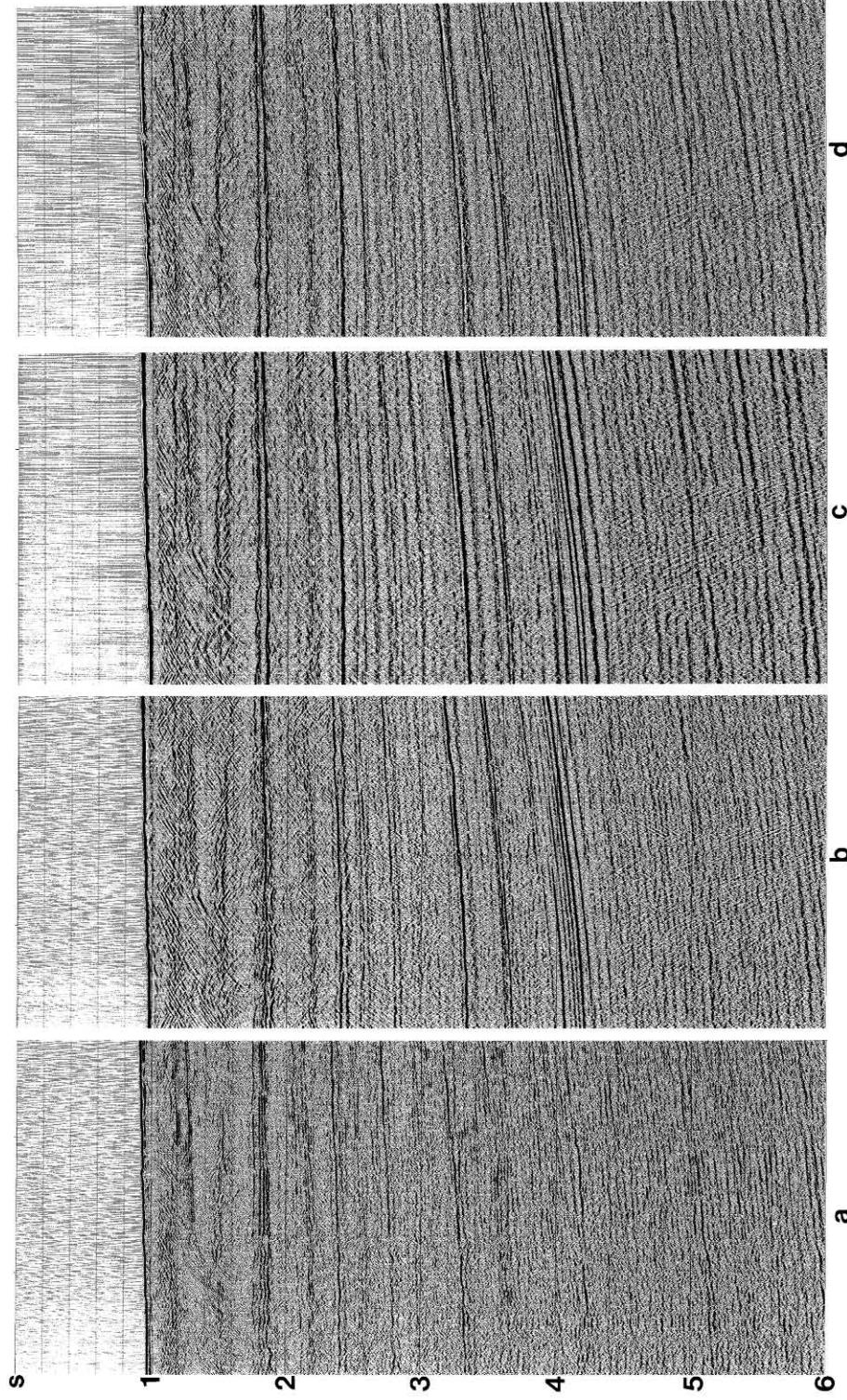


FIG. 6.0-23. Portions of sections associated with the data as in Figure 6.0-20a: (a) a near-offset section, (b) CMP stack with no prestack and poststack deconvolution, (c) CMP stack with prestack deconvolution, only, and (d) CMP stack with prestack and poststack deconvolution. The velocity spectra computed at the central CMP locations from the data as in (b) and (c) are shown in Figure 6.0-35.

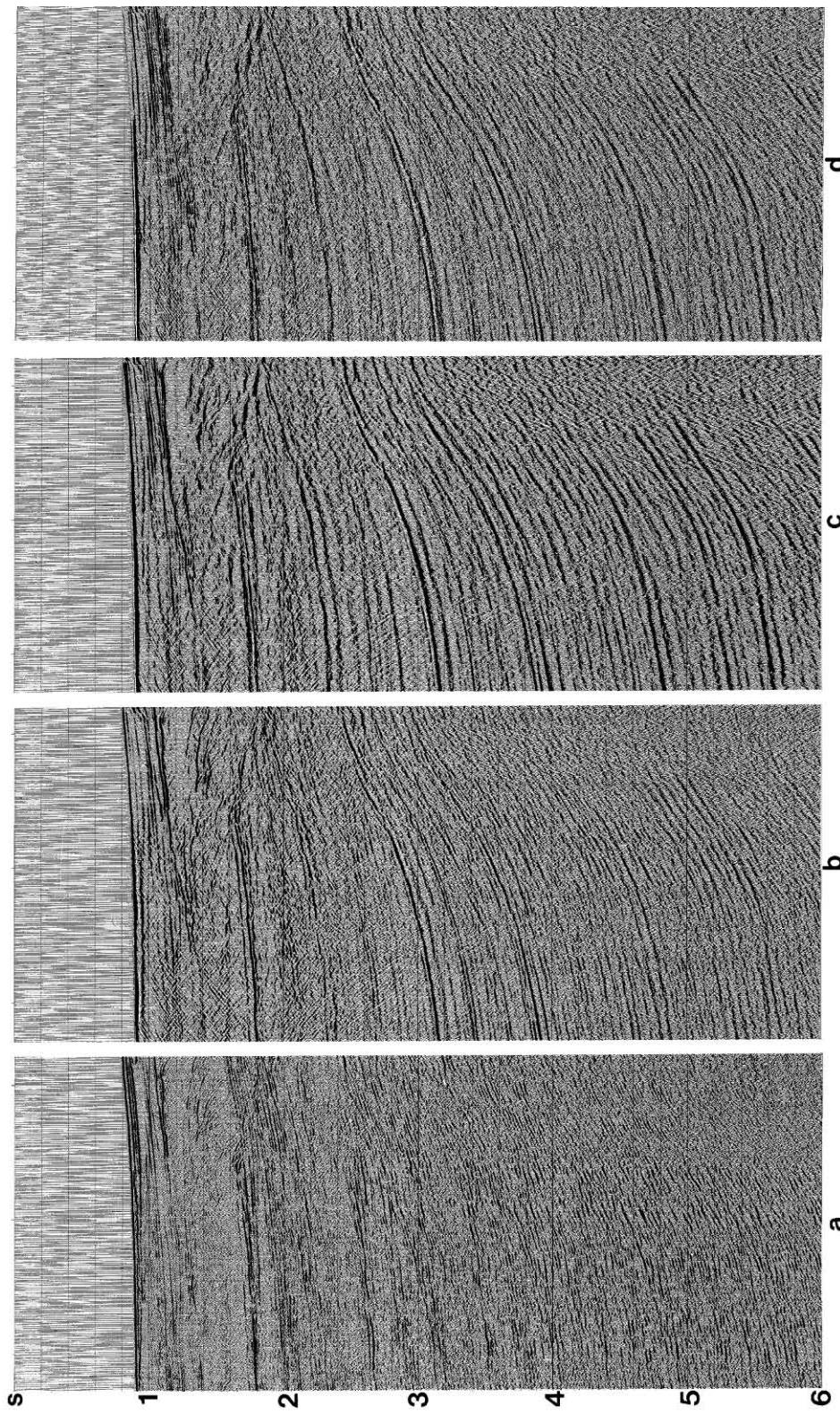


FIG. 6.0-24. Portions of sections associated with the data as in Figure 6.0-20b: (a) a near-offset section, (b) CMP stack with no prestack and poststack deconvolution, (c) CMP stack with prestack deconvolution, only, and (d) CMP stack with prestack and poststack deconvolution. The velocity spectra computed at the central CMP locations from the data as in (b) and (c) are shown in Figure 6.0-35.

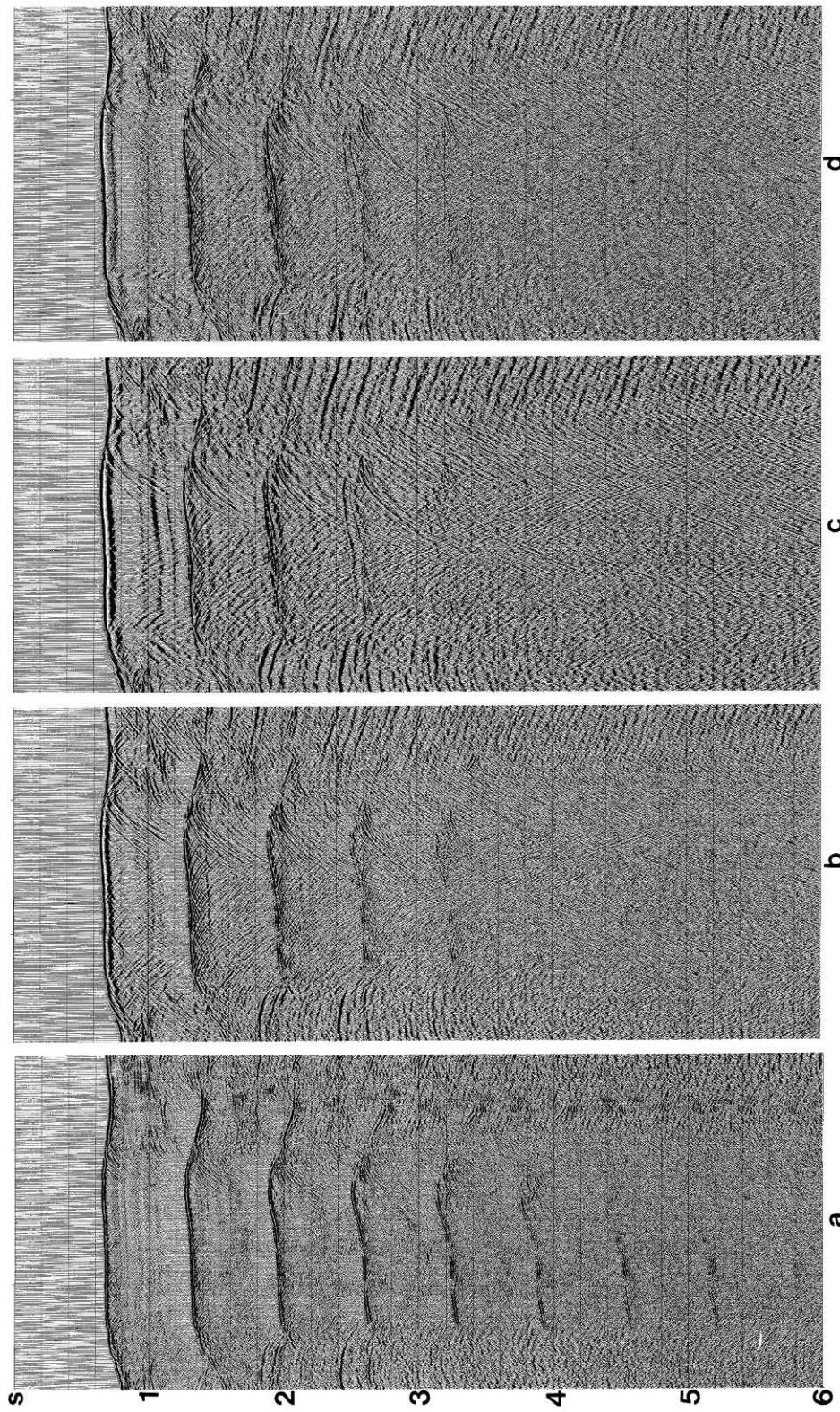


FIG. 6.0-25. Portions of sections associated with the data as in Figure 6.0-20c: (a) a near-offset section, (b) CMP stack with no prestack and poststack deconvolution, (c) CMP stack with prestack deconvolution, only, and (d) CMP stack with prestack and poststack deconvolution. The velocity spectra computed at the central CMP locations from the data as in (b) and (c) are shown in Figure 6.0-35.

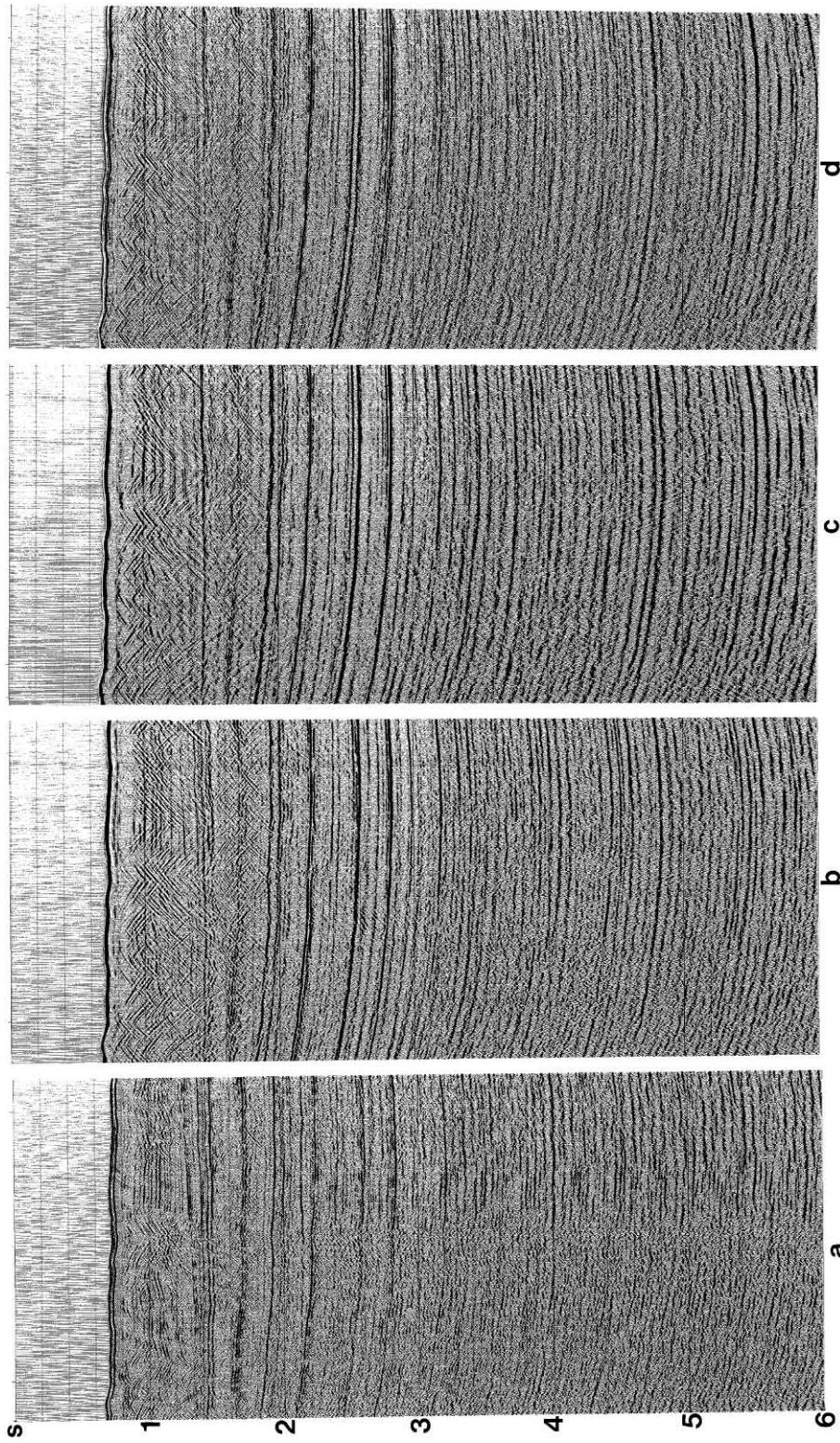


FIG. 6.0-26. Portions of sections associated with the data as in Figure 6.0-20d: (a) a near-offset section, (b) CMP stack with no prestack and poststack deconvolution, (c) CMP stack with prestack deconvolution, only, and (d) CMP stack with prestack and poststack deconvolution. The velocity spectra computed at the central CMP locations from the data as in (b) and (c) are shown in Figure 6.0-35.

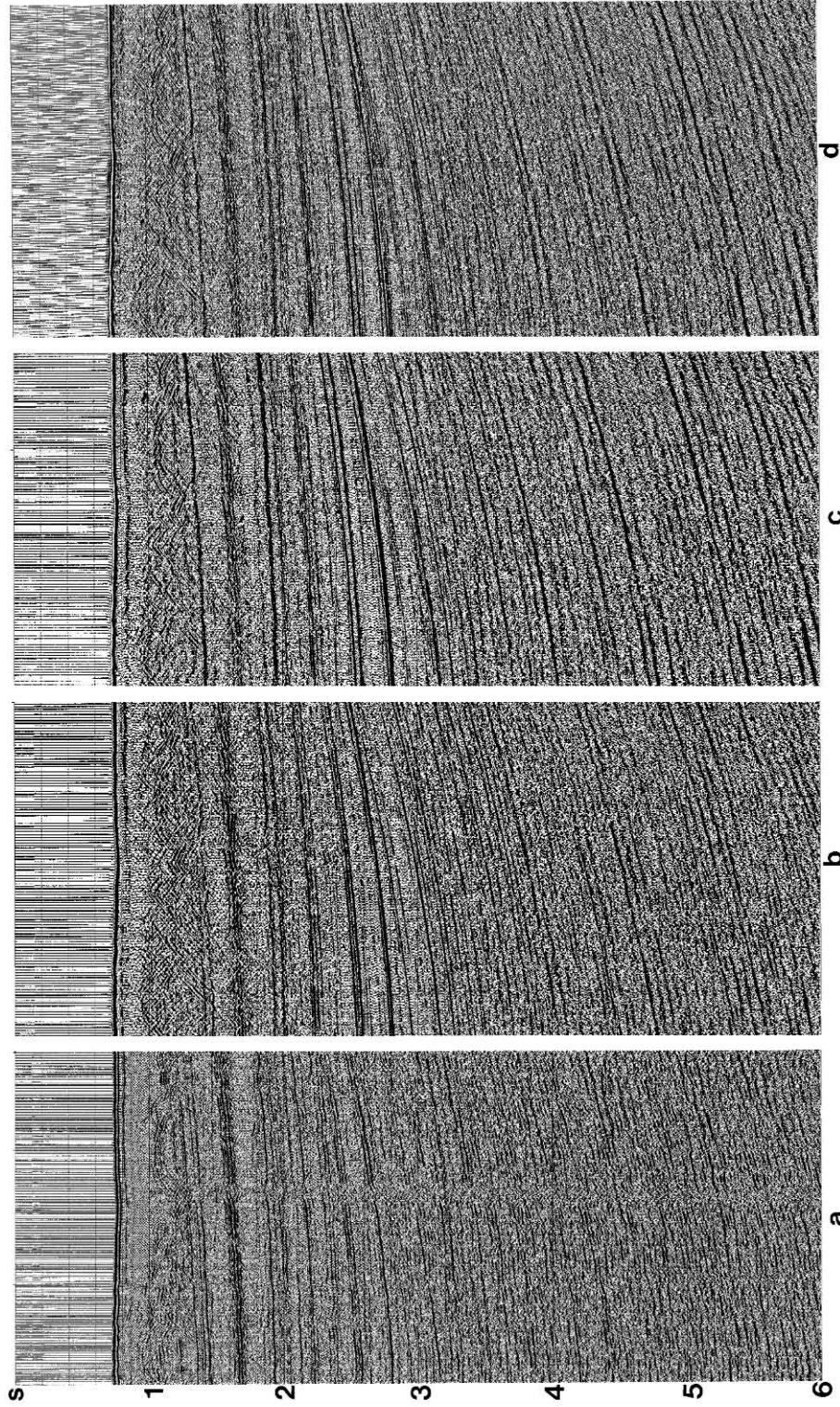


FIG. 6.0-27. Portions of sections associated with the data as in Figure 6.0-20e: (a) a near-offset section, (b) CMP stack with no prestack and poststack deconvolution, (c) CMP stack with prestack deconvolution, only, and (d) CMP stack with prestack and poststack deconvolution. The velocity spectra computed at the central CMP locations from the data as in (b) and (c) are shown in Figure 6.0-35.

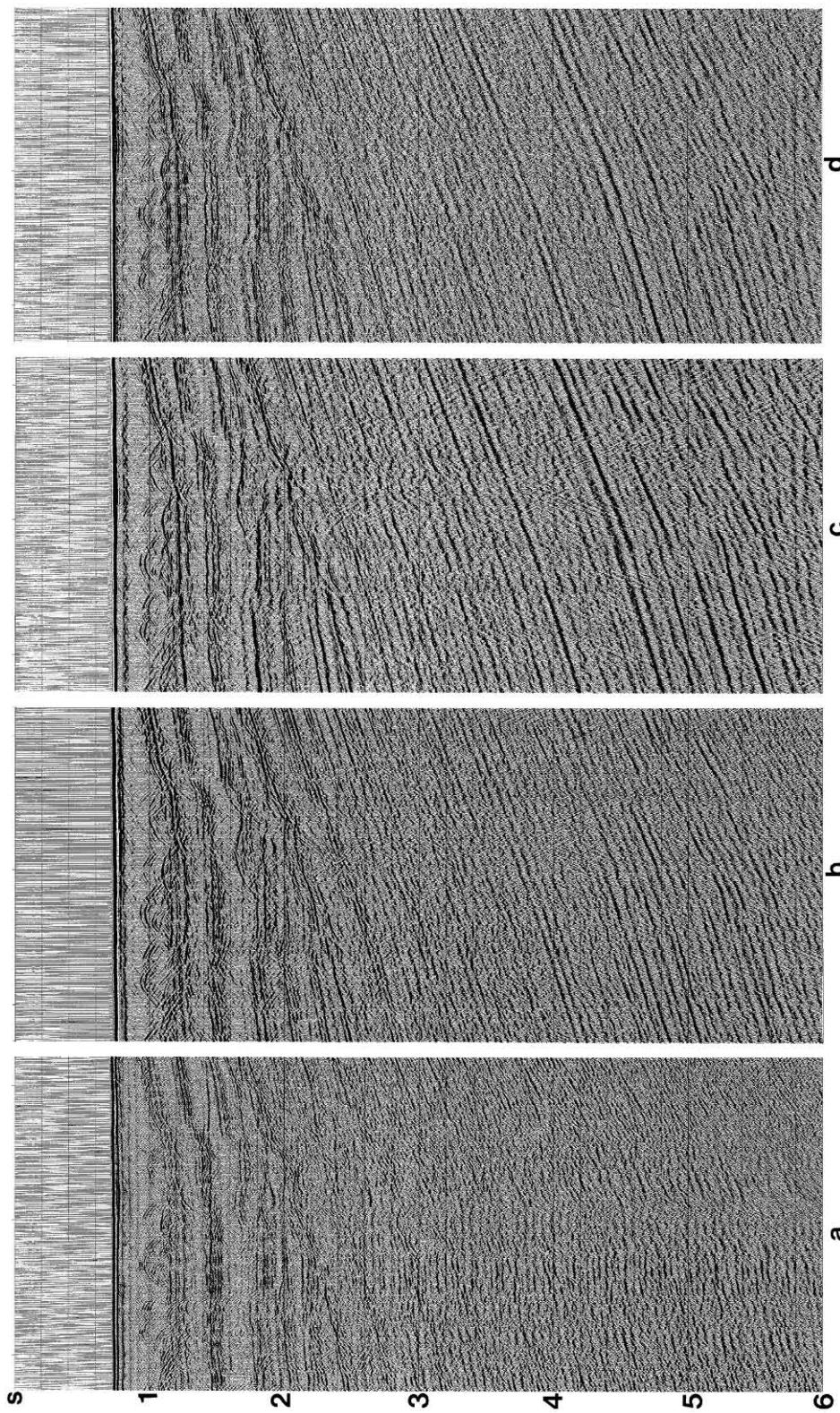


FIG. 6.0-28. Portions of sections associated with the data as in Figure 6.0-20f: (a) a near-offset section, (b) CMP stack with no prestack and poststack deconvolution, (c) CMP stack with prestack deconvolution, only, and (d) CMP stack with prestack and poststack deconvolution. The velocity spectra computed at the central CMP locations from the data, as in (b) and (c) are shown in Figure 6.0-35.

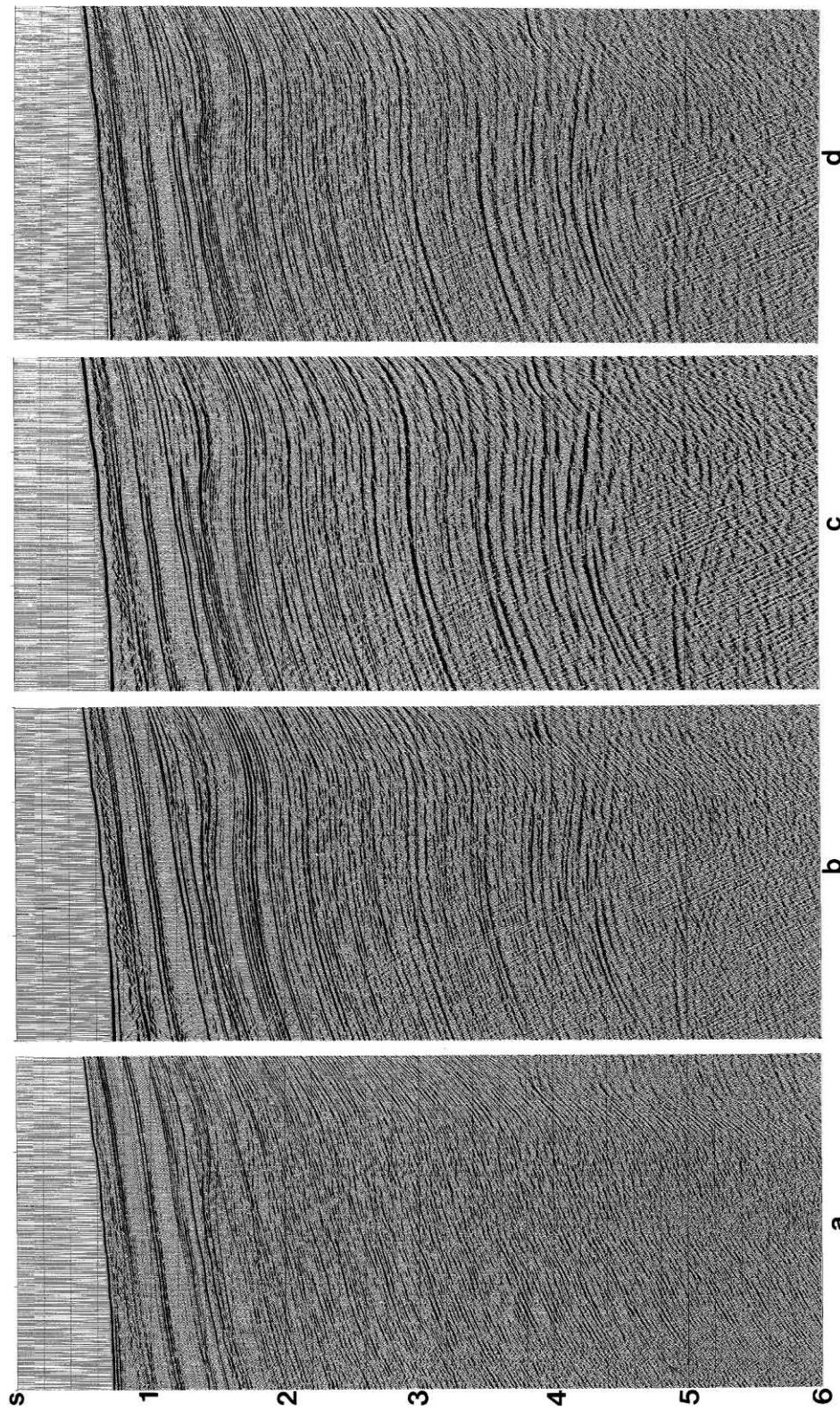


FIG. 6.0-29. Portions of sections associated with the data as in Figure 6.0-21a: (a) a near-offset section, (b) CMP stack with no prestack and poststack deconvolution, (c) CMP stack with prestack deconvolution, only, and (d) CMP stack with prestack and poststack deconvolution. The velocity spectra computed at the central CMP locations from the data as in (b) and (c) are shown in Figure 6.0-36.

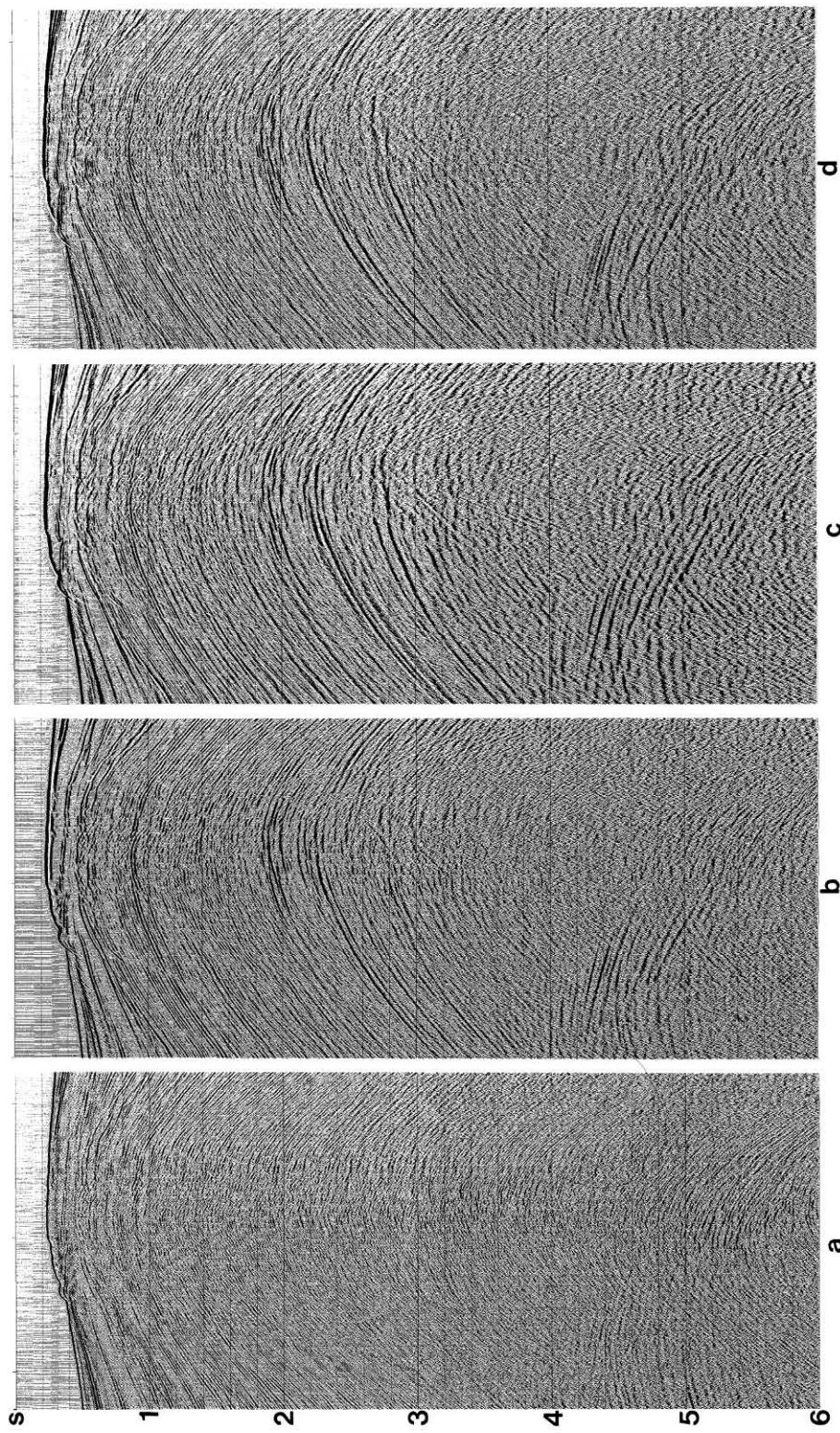


FIG. 6.0-30. Portions of sections associated with the data as in Figure 6.0-21b: (a) a near-offset section, (b) CMP stack with no prestack and poststack deconvolution, (c) CMP stack with prestack deconvolution, only, and (d) CMP stack with prestack and poststack deconvolution. The velocity spectra computed at the central CMP locations from the data as in (b) and (c) are shown in Figure 6.0-36.

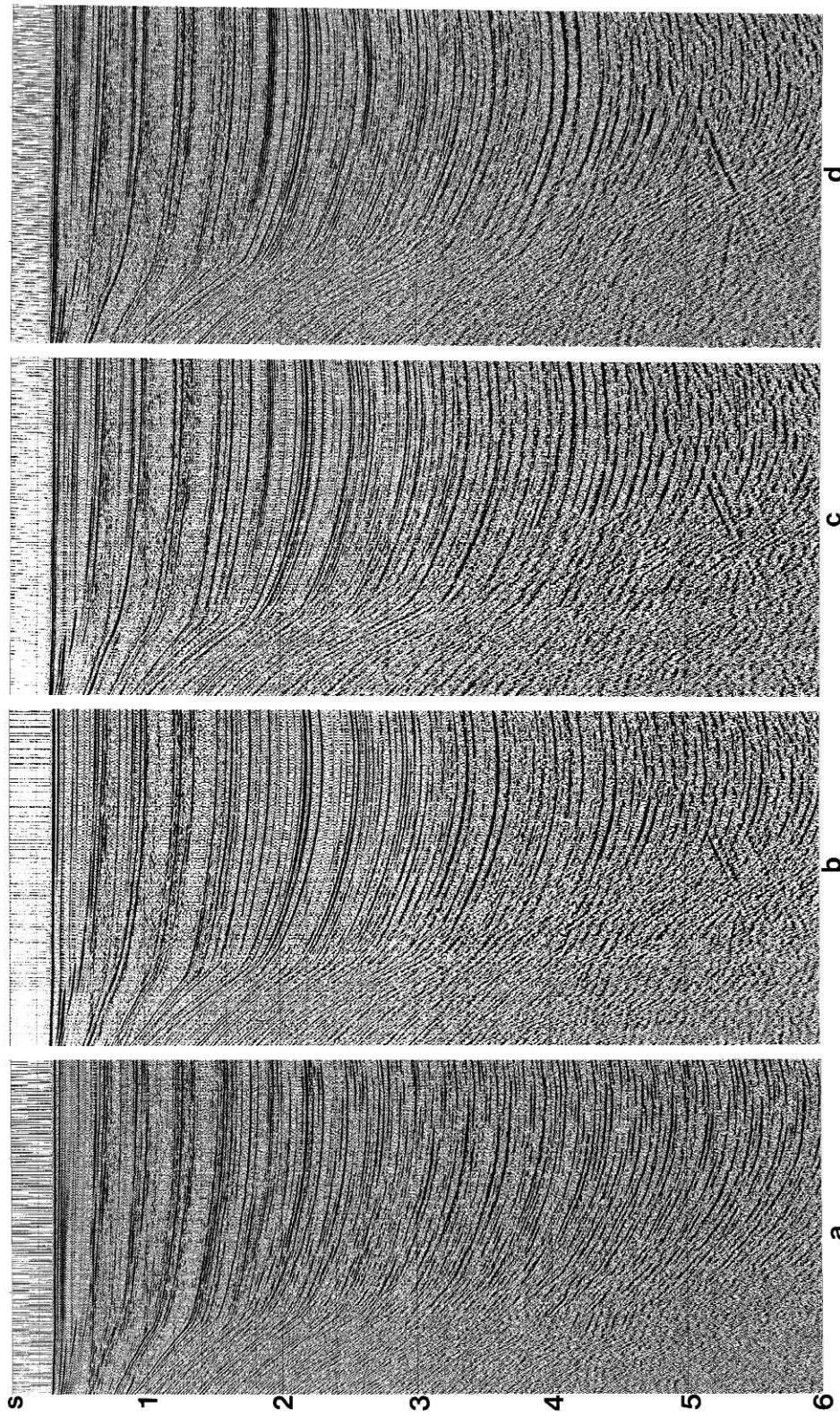


FIG. 6.0-31. Portions of sections associated with the data as in Figure 6.0-21c: (a) a near-offset section, (b) CMP stack with no prestack and poststack deconvolution, (c) CMP stack with prestack deconvolution, only, and (d) CMP stack with prestack and poststack deconvolution. The velocity spectra computed at the central CMP locations from the data as in (b) and (c) are shown in Figure 6.0-36.

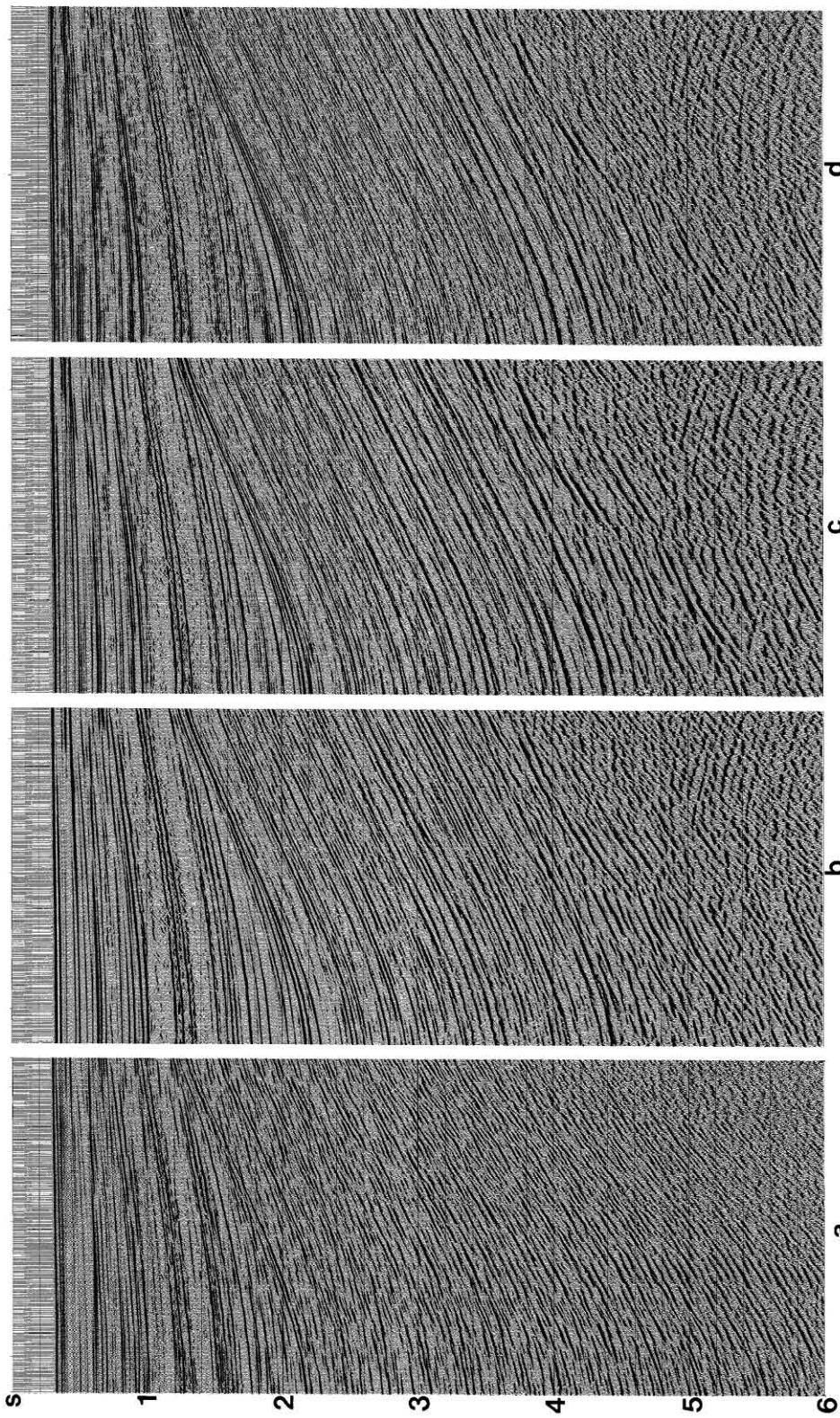


FIG. 6.0-32. Portions of sections associated with the data as in Figure 6.0-21d: (a) a near-offset section, (b) CMP stack with no prestack and poststack deconvolution, (c) CMP stack with prestack deconvolution, only, and (d) CMP stack with prestack and poststack deconvolution. The velocity spectra computed at the central CMP locations from the data as in (b) and (c) are shown in Figure 6.0-36.

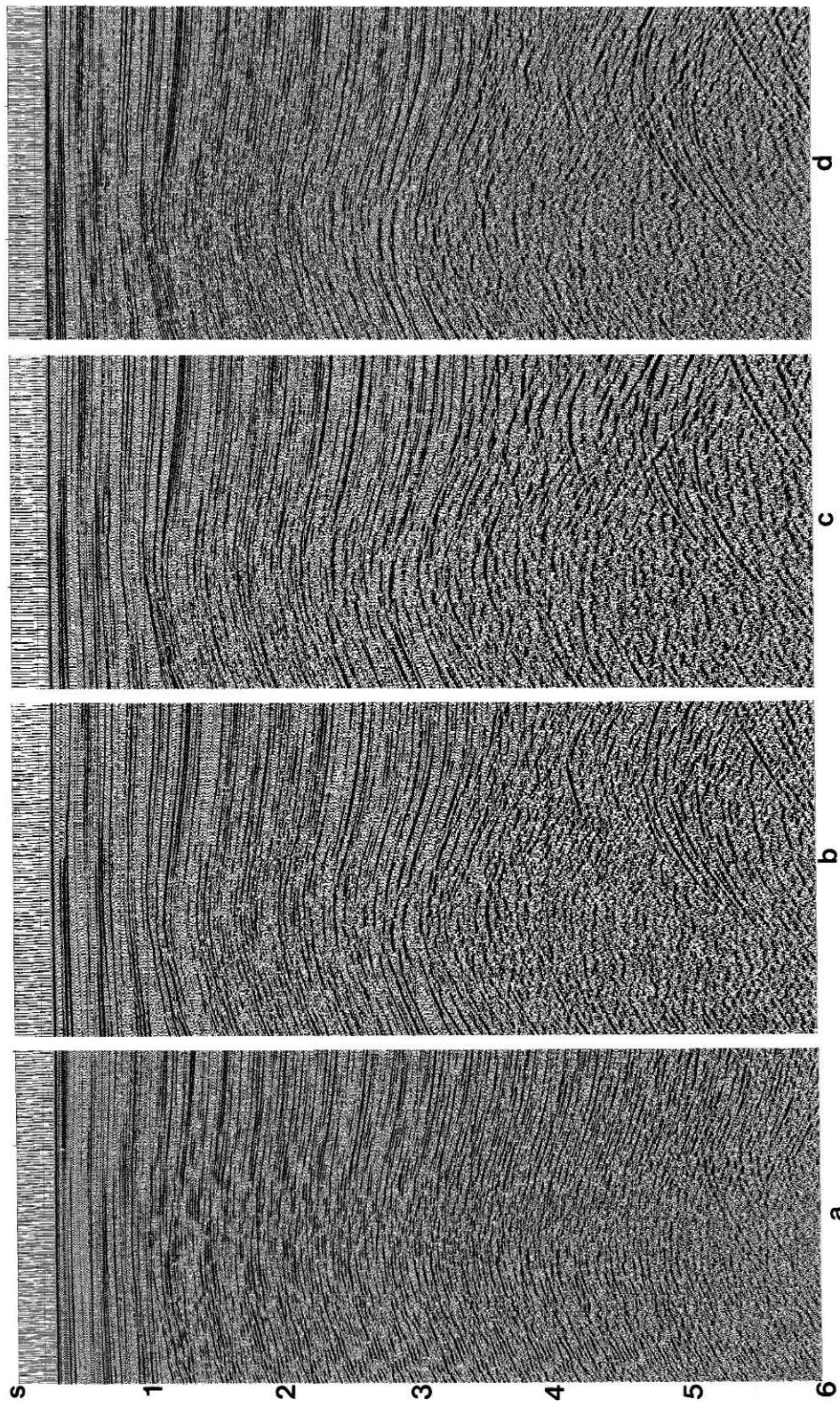


FIG. 6.0-33. Portions of sections associated with the data as in Figure 6.0-21e: (a) a near-offset section, (b) CMP stack with no prestack and poststack deconvolution, (c) CMP stack with prestack deconvolution, only, and (d) CMP stack with prestack and poststack deconvolution. The velocity spectra computed at the central CMP locations from the data as in (b) and (c) are shown in Figure 6.0-36.

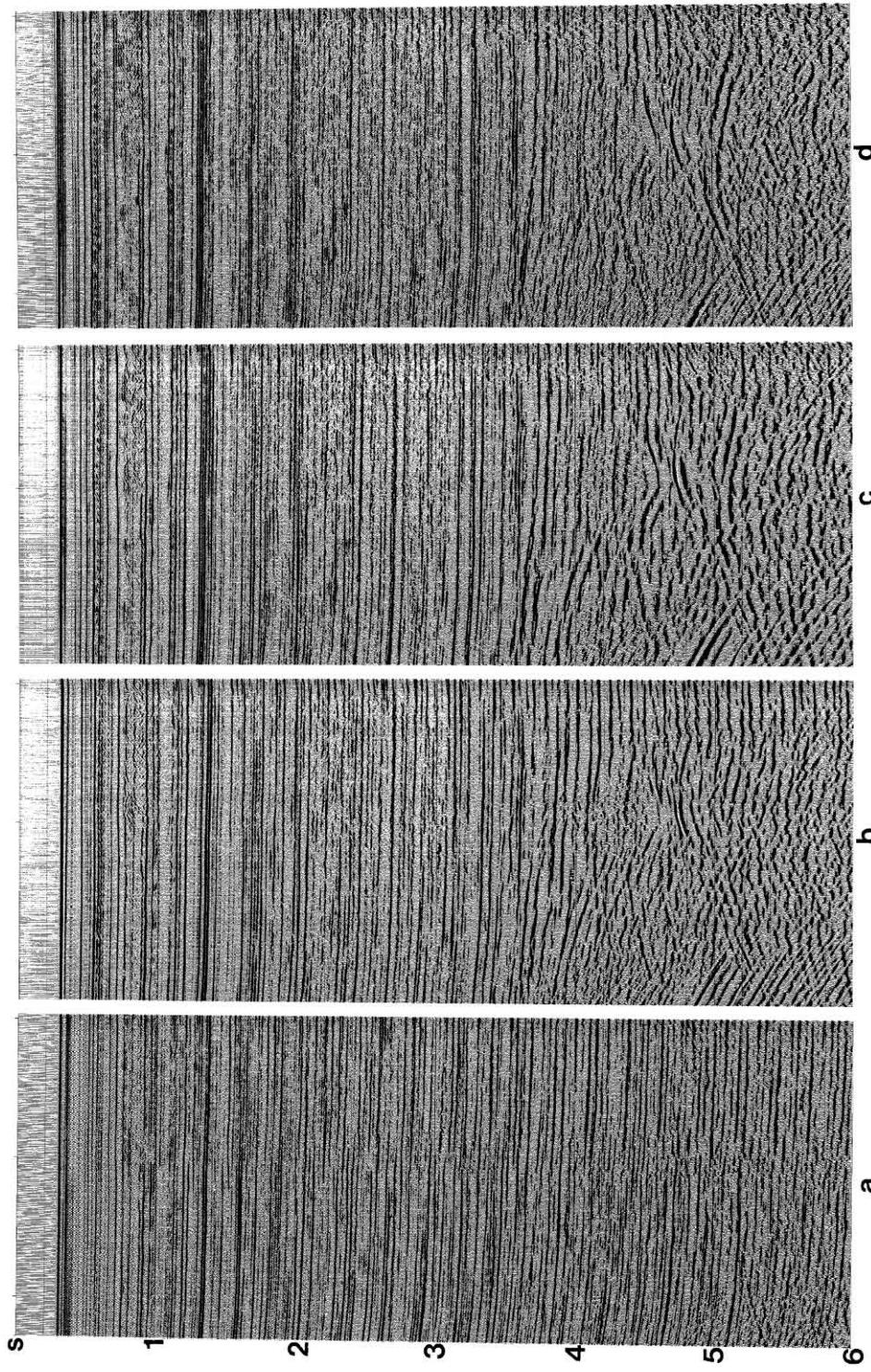


FIG. 6.0-34. Portions of sections associated with the data as in Figure 6.0-21f: (a) a near-offset section, (b) CMP stack with no prestack and poststack deconvolution, (c) CMP stack with prestack deconvolution, only, and (d) CMP stack with prestack and poststack deconvolution. The velocity spectra computed at the central CMP locations from the data as in (b) and (c) are shown in Figure 6.0-36.

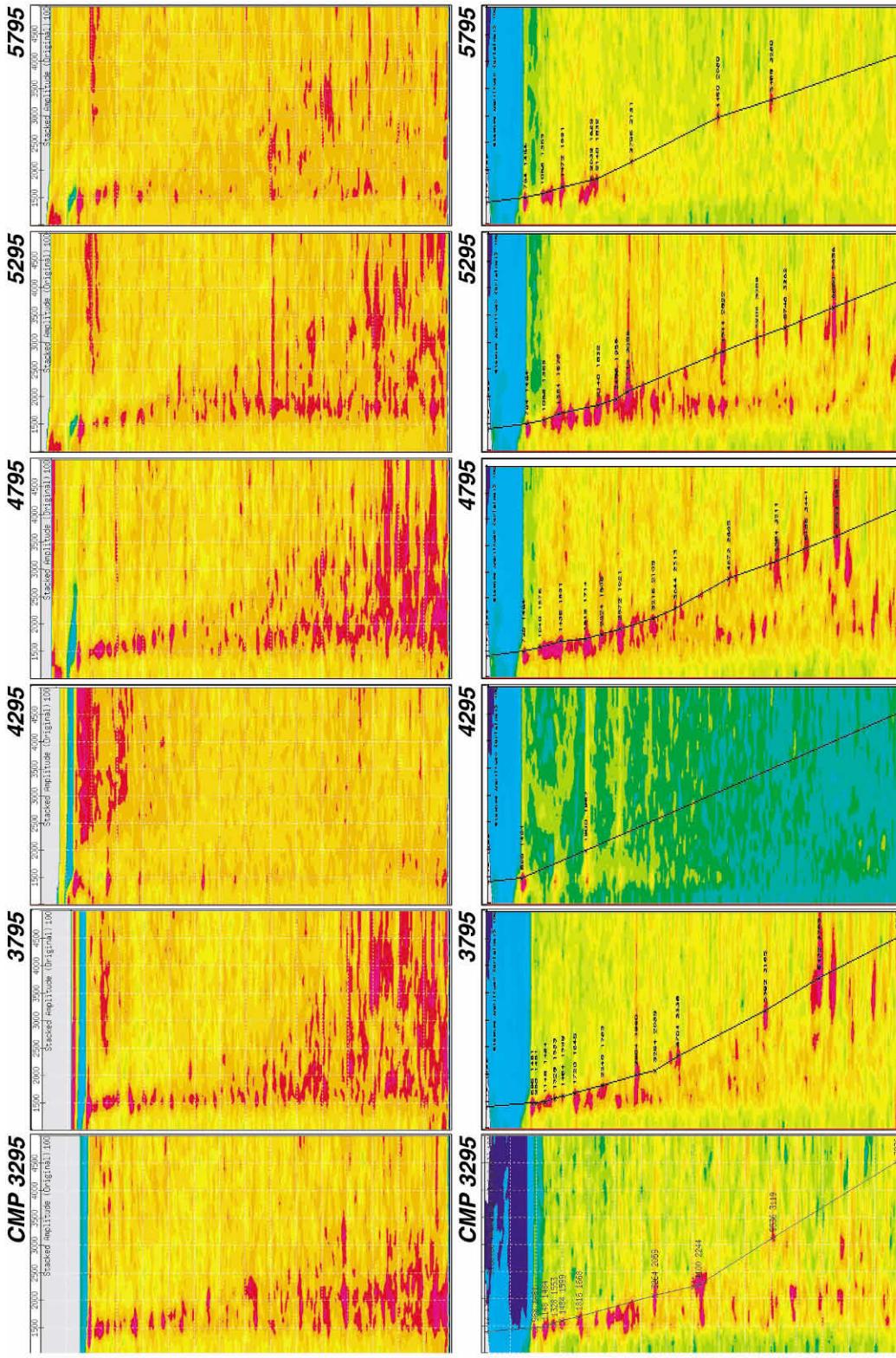


FIG. 6.0-35. The velocity spectra computed from the CMP gathers as in Figure 6.0-20 (top) with no deconvolution, and (bottom) with spiking deconvolution applied. Corresponding stacked sections are shown in Figures 6.0-23 through 6.0-28.

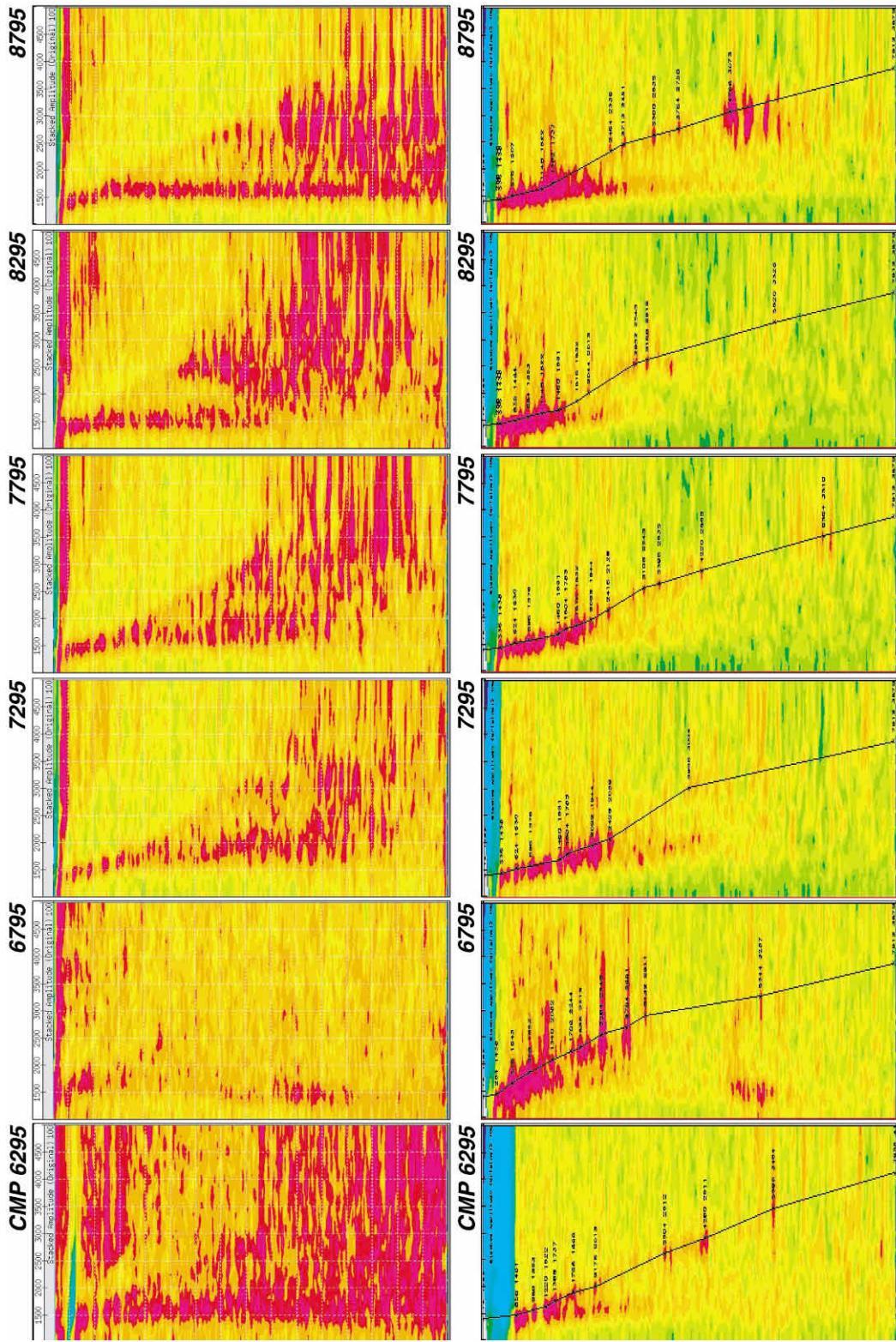


FIG. 6.0-36. The velocity spectra computed from the CMP gathers as in Figure 6.0-21 (top) with no deconvolution, and (bottom) with spiking deconvolution applied. Corresponding stacked sections are shown in Figures 6.0-29 through 6.0-34.

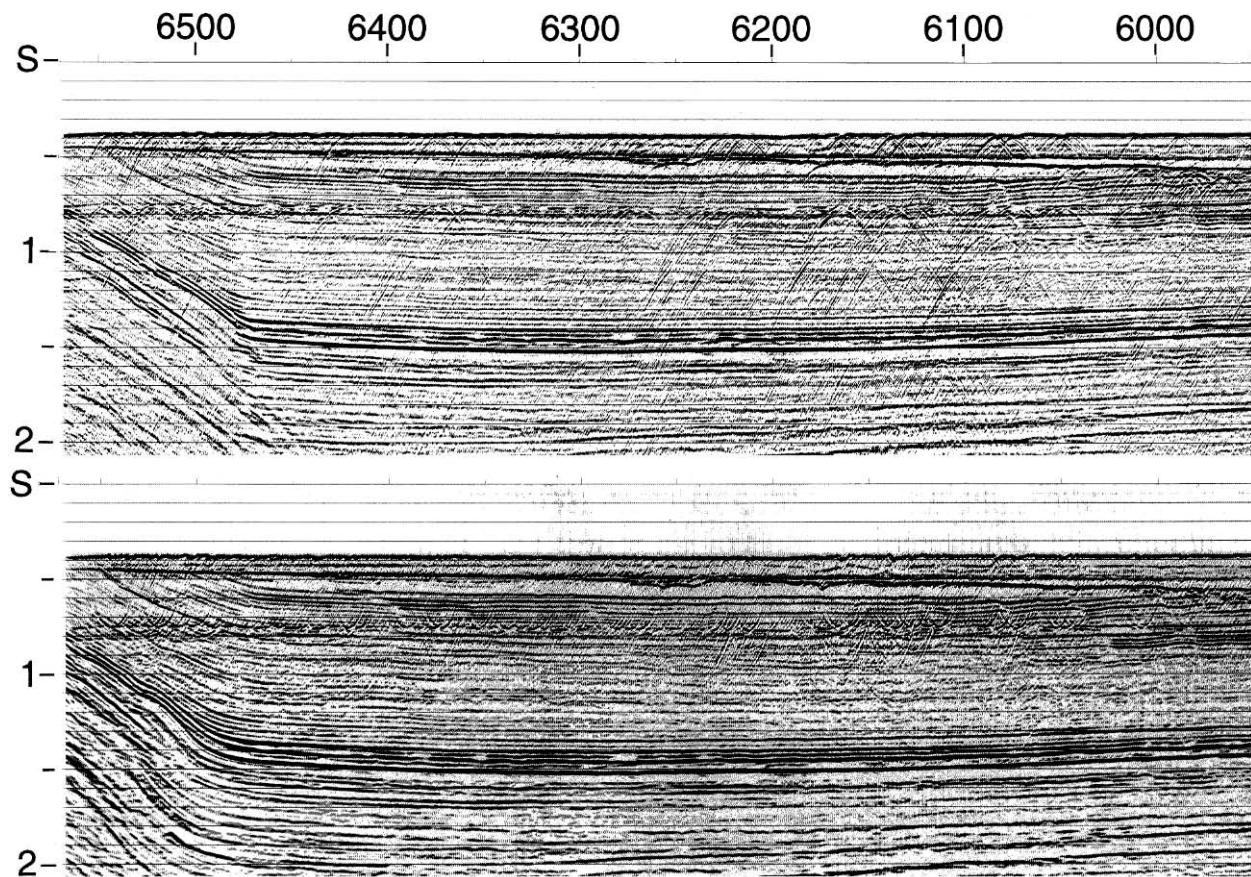


FIG. 6.0-37. Shallow portion of a CMP stack (top) and the same portion after time migration (bottom). Note the overmigrated diffracted water-bottom multiple at 0.75 s.

would result in residual moveout associated with multiples on common-reflection-point (CRP) gathers derived from prestack migration. Subsequent stacking of the CRP gathers would have an attenuation effect on multiples. Note the absence of the multiple in the prestack migrated section in Figure 6.0-38c.

Figure 6.0-39 shows selected CRP gathers from prestack time migration of data as in Figure 5.4-21 using the same velocity field as in Figure 5.4-20, but with no multiple attenuation. Note the large moveouts associated with the multiple reflections. As a result of the moveout difference between primaries and multiples, stacking of the CRP gathers can to a large extent attenuate multiples. Often, as in conventional CMP stacking, CRP stacking with (Figure 5.4-22) and without (Figure 6.0-40) multiple attenuation yields comparable image quality from prestack time migration. Nevertheless, the CRP gathers derived from data that have been subjected to multiple attenuation are preferred if a postmigration velocity update is required. Compare the CRP gathers from prestack time migration of data

with multiple attenuation (Figure 5.4-21) and without multiple attenuation (Figure 6.0-39), and note the interference of multiples when picking flat primaries.

Spatially Random Noise

The spatially random noise uncorrelated from trace to trace is largely attenuated by CMP stacking (Section 1.5). Any remaining noise on stacked data can be attenuated by spatial prediction filters. Figure 6.0-41 shows a stacked section before and after noise attenuation. The process of noise attenuation is meant to achieve attenuation of noise so as to enhance coherent events such as reflections on a stacked section. It is not meant to create any coherent events that do not exist in the data.

The spatial prediction filters also can be applied to common-offset data prior to stacking. They are conveniently designed and applied in the frequency-space domain. What is predictable by a prediction filter for a given frequency component is a signal in the lateral

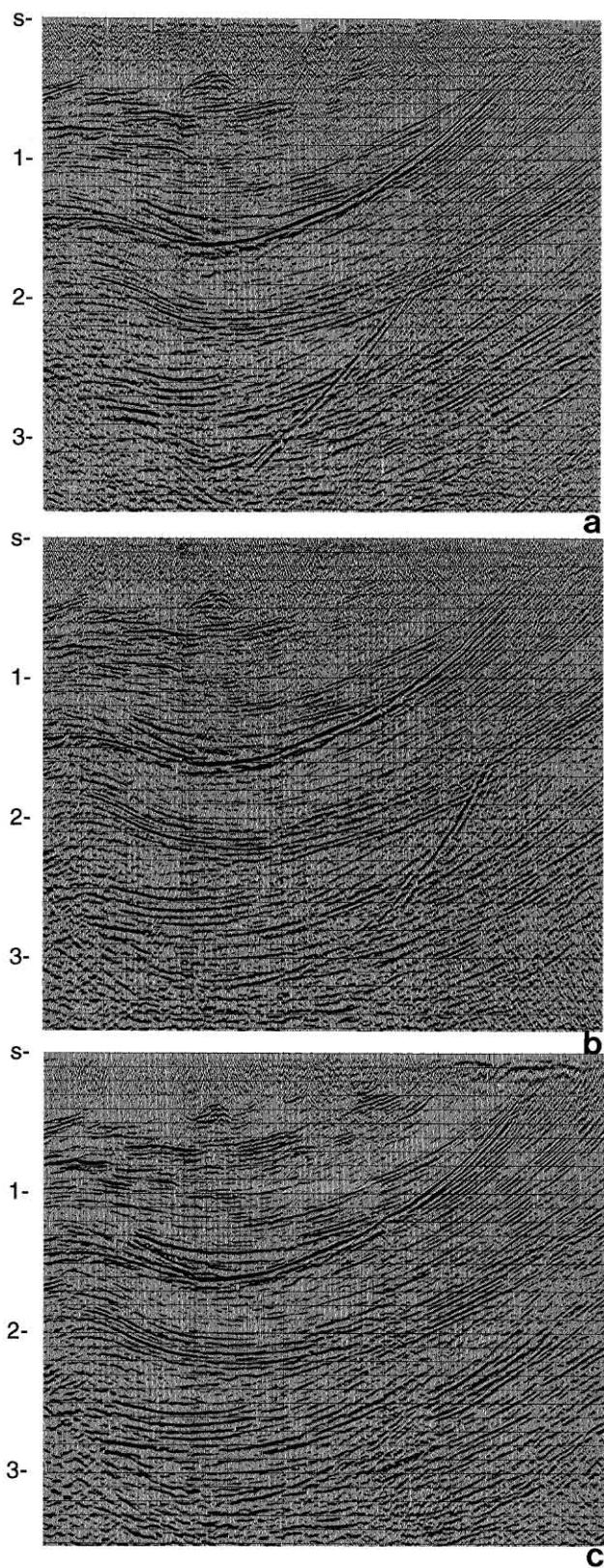


FIG. 6.0-38. (a) A portion of a CMP stack; (b) poststack time migration; (c) prestack time migration.

direction and what is not predictable is considered spatially random noise. This is just the opposite of what is intended by statistical deconvolution (Chapter 2). Specifically, the predictive deconvolution operator is a prediction error filter, and the output from predictive deconvolution is the unpredictable part of the input — the white reflectivity series. What is predictable by predictive deconvolution is multiples contained in a one-dimensional (1-D) seismogram associated with vertical incidence.

In Section 6.5, a frequency-space prediction filter for attenuation of spatially random noise is presented accompanied by a mathematical discussion in Section F.4.

6.1 MULTIPLE ATTENUATION IN THE CMP DOMAIN

We have observed many types of multiples on shot gathers in Section 1.3. Multiples are attenuated based on two principle criteria — periodicity and velocity discrimination. As in the case of coherent linear noise, these criteria are exploited in whichever domain they are applicable. For instance, periodicity is preserved to a great extent for short-period multiples and reverberations on CMP gathers, especially at near offsets. Periodicity also is preserved in the $\tau - p$ domain, provided multiples are associated with near-horizontal reflectors.

CMP stacking facilitates attenuation of multiples based on velocity discrimination between primaries and multiples. This criterion to attenuate multiples also can be exploited in the $f - k$, $\tau - p$, and Radon-transform domains. The degree of success depends on the moveout difference between primaries and multiples, and hence, on velocities and arrival times of primary reflections, and the cable length. Specifically, the moveout difference between primaries and multiples decreases at shallow times, low velocities, and at near offsets.

Periodicity of Multiples

When periodicity is preserved adequately, predictive deconvolution can be used to predict and attenuate multiples either in CMP or in the $\tau - p$ domain. For instance, short-period multiples and reverberations are largely attenuated by the application of predictive deconvolution to prestack data. Figure 6.1-1 shows selected CMP gathers along a marine line with the accompanying amplitude spectra and their autocorrelograms averaged over the traces of each gather. Note the abundance of guided

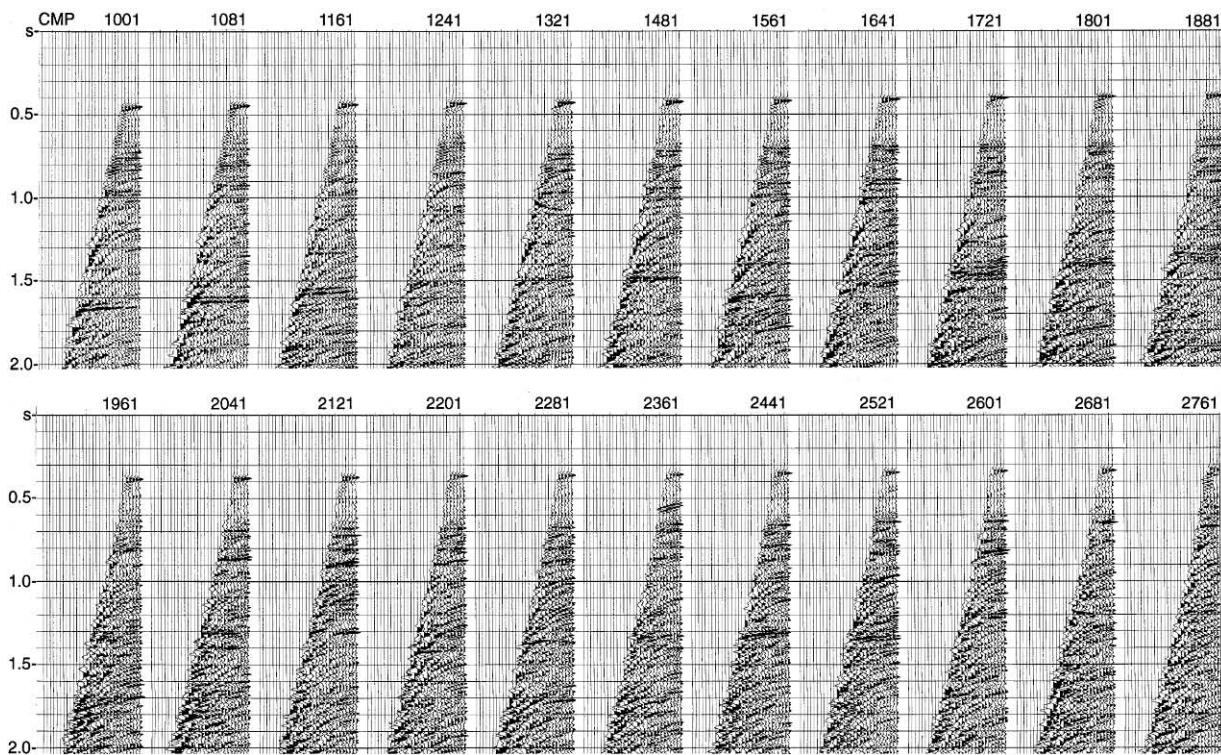


FIG. 6.0-39. Selected image gathers from prestack time migration using the velocity field shown in Figure 5.4-20. These gathers were obtained from data that were not subjected to multiple attenuation prior to prestack time migration. Compare with the gathers shown in Figure 5.4-21.

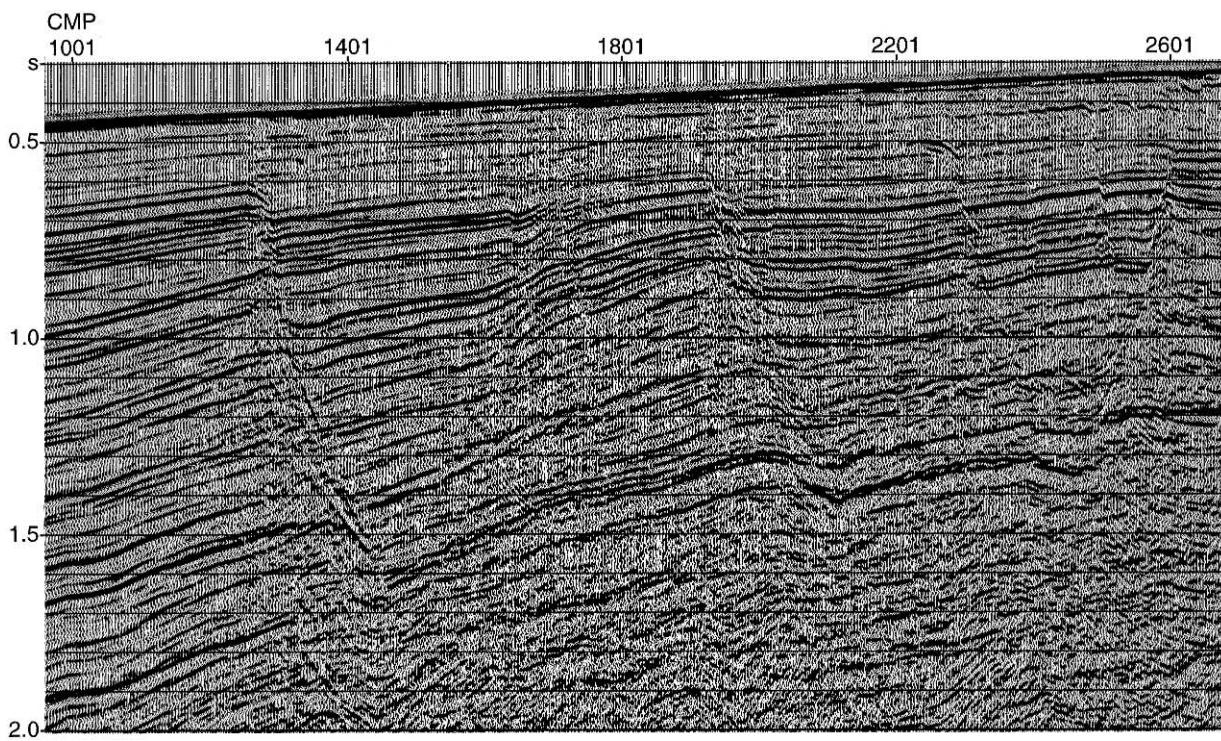


FIG. 6.0-40. The stack of image gathers as in Figure 6.0-39 derived from prestack time migration. Compare with the stack shown in Figure 5.4-22.

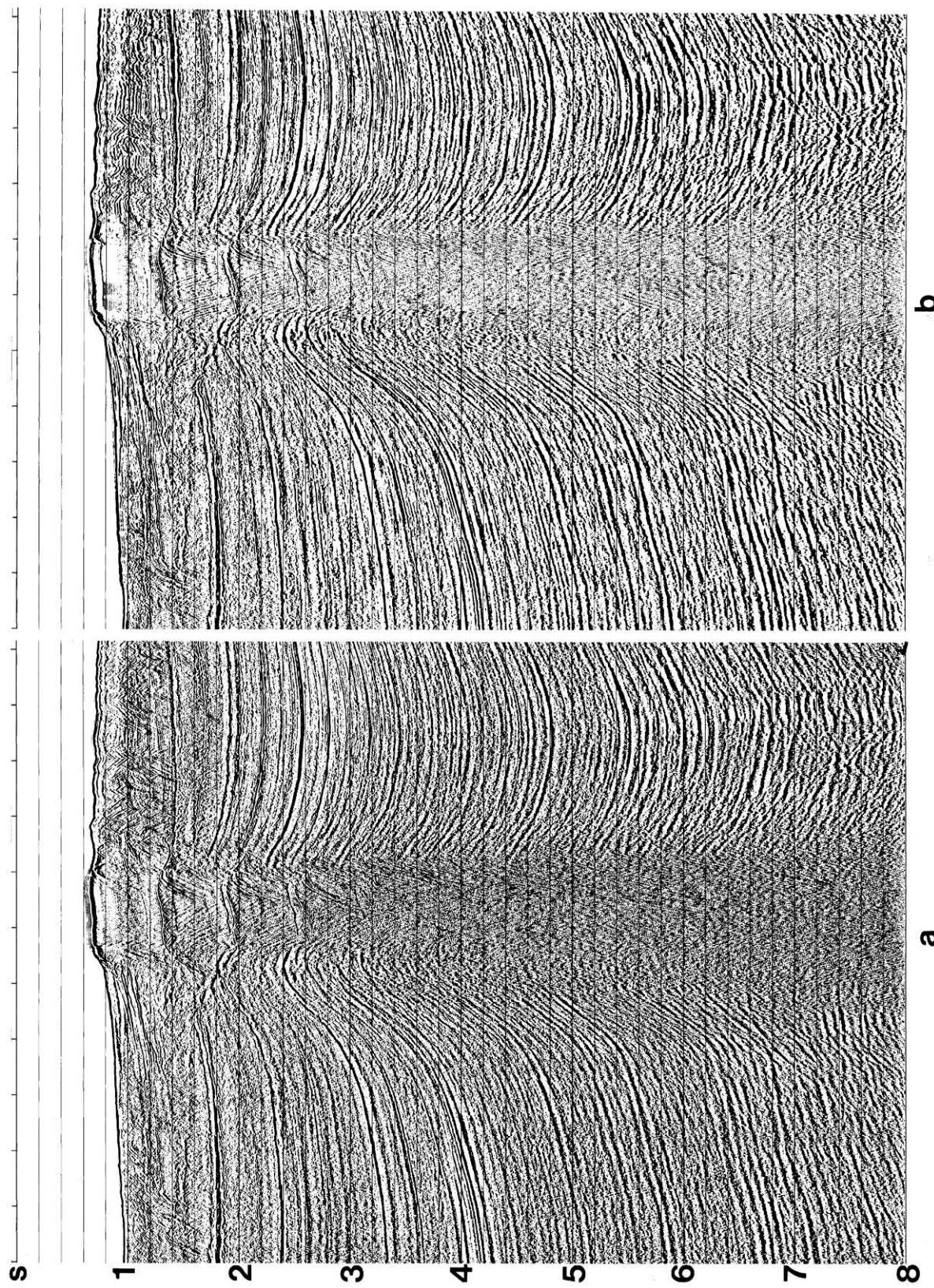


FIG. 6.0-41. A CMP stacked section (a) before, and (b) after random noise attenuation.

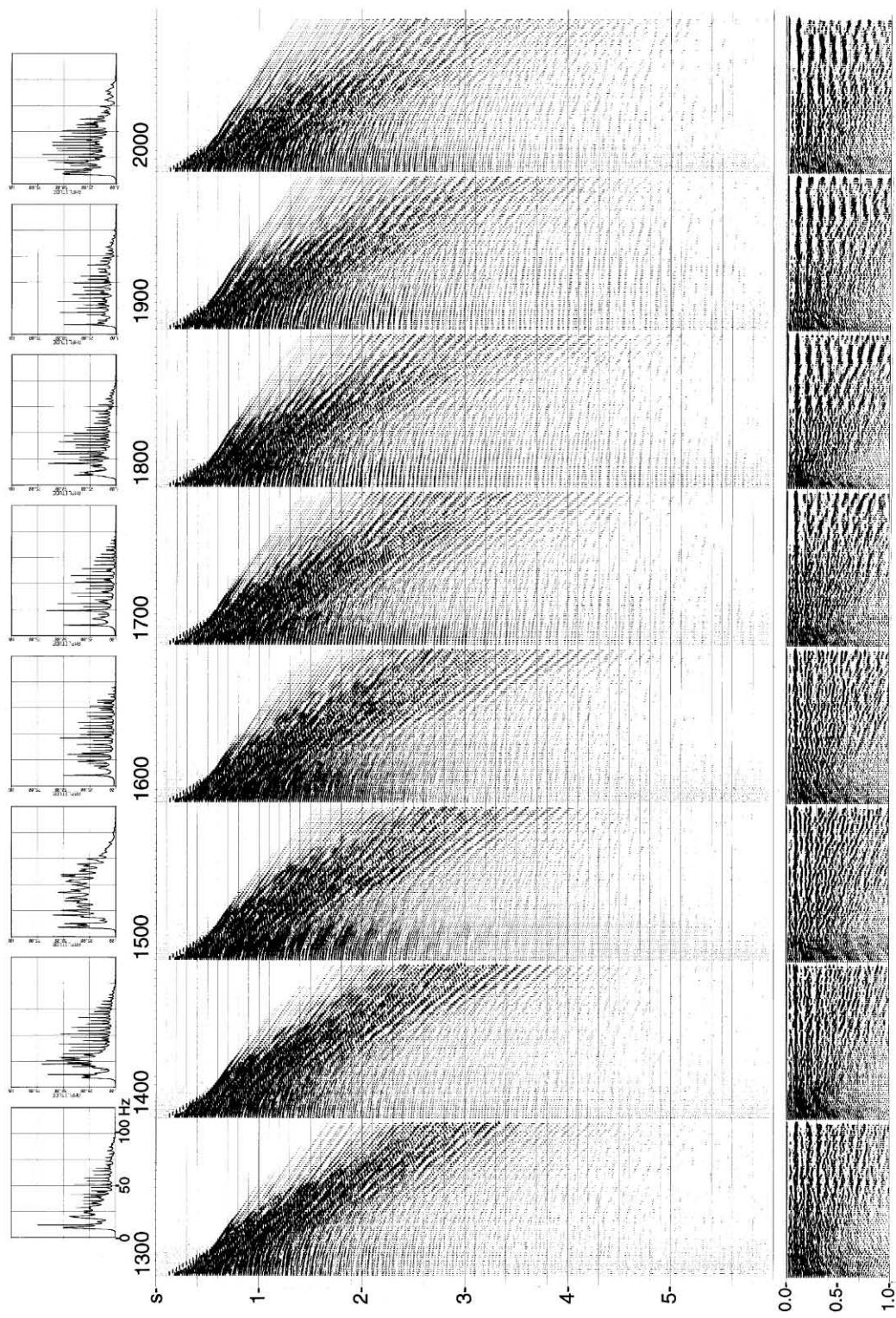


FIG. 6.1-1. Selected CMP gathers without geometric spreading correction. Average amplitude spectrum and autocorrelogram for each gather are shown on top and bottom, respectively.

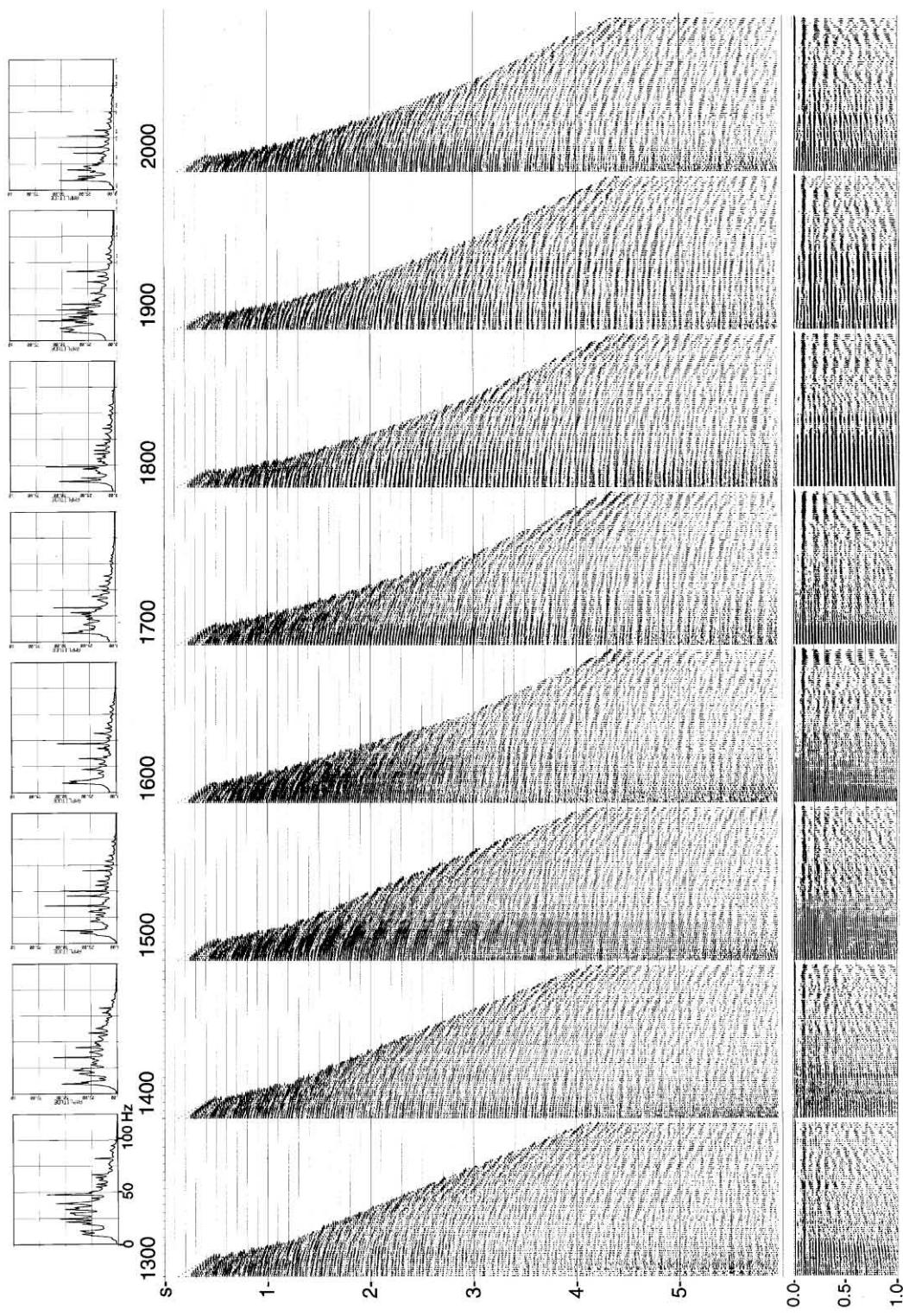


FIG. 6.1-2. Same gathers as in Figure 6.1-1 after t -squared scaling for geometric spreading correction and muting guided waves.

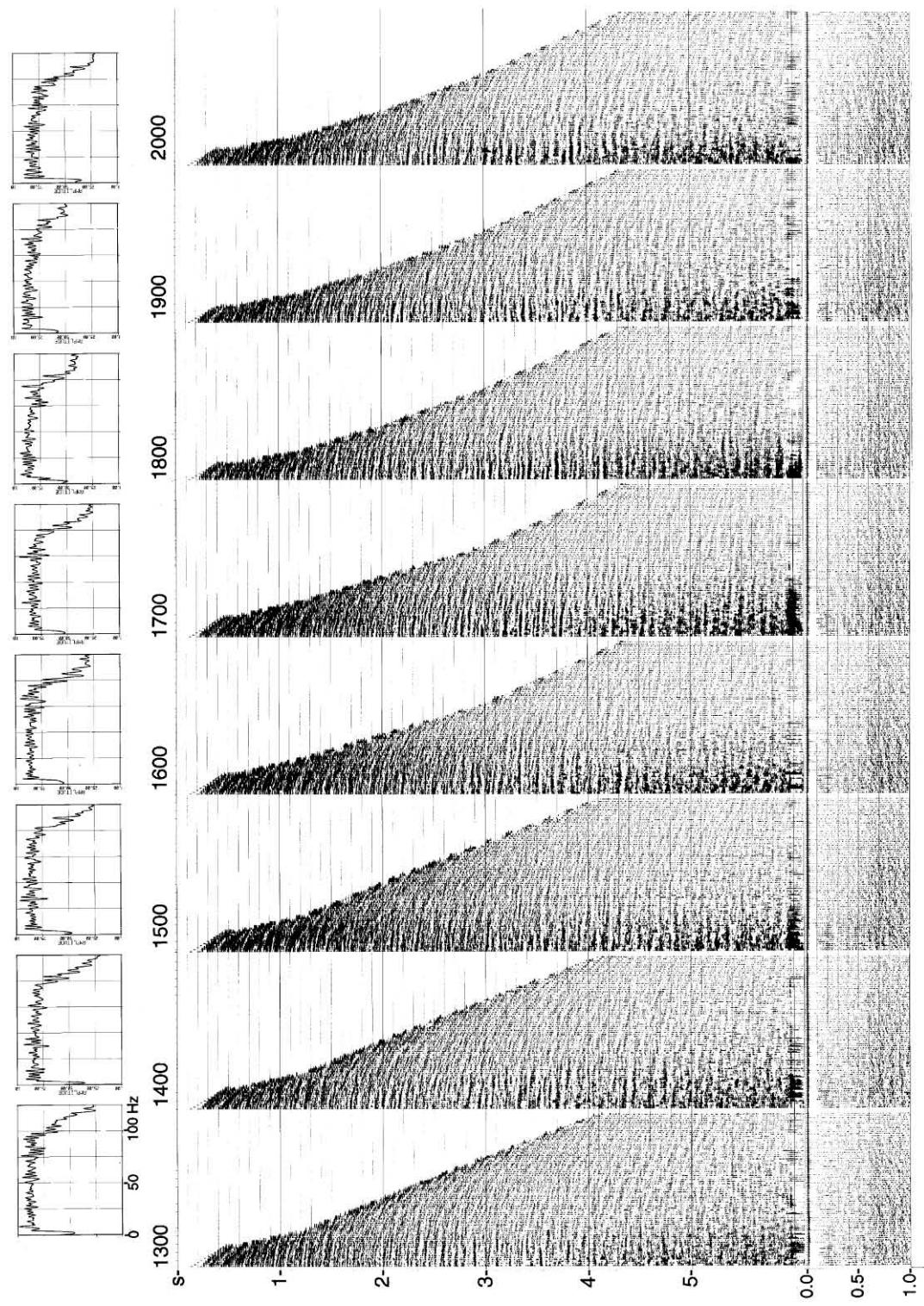


FIG. 6.1-3. Same gathers as in Figure 6.1-2 after predictive deconvolution.

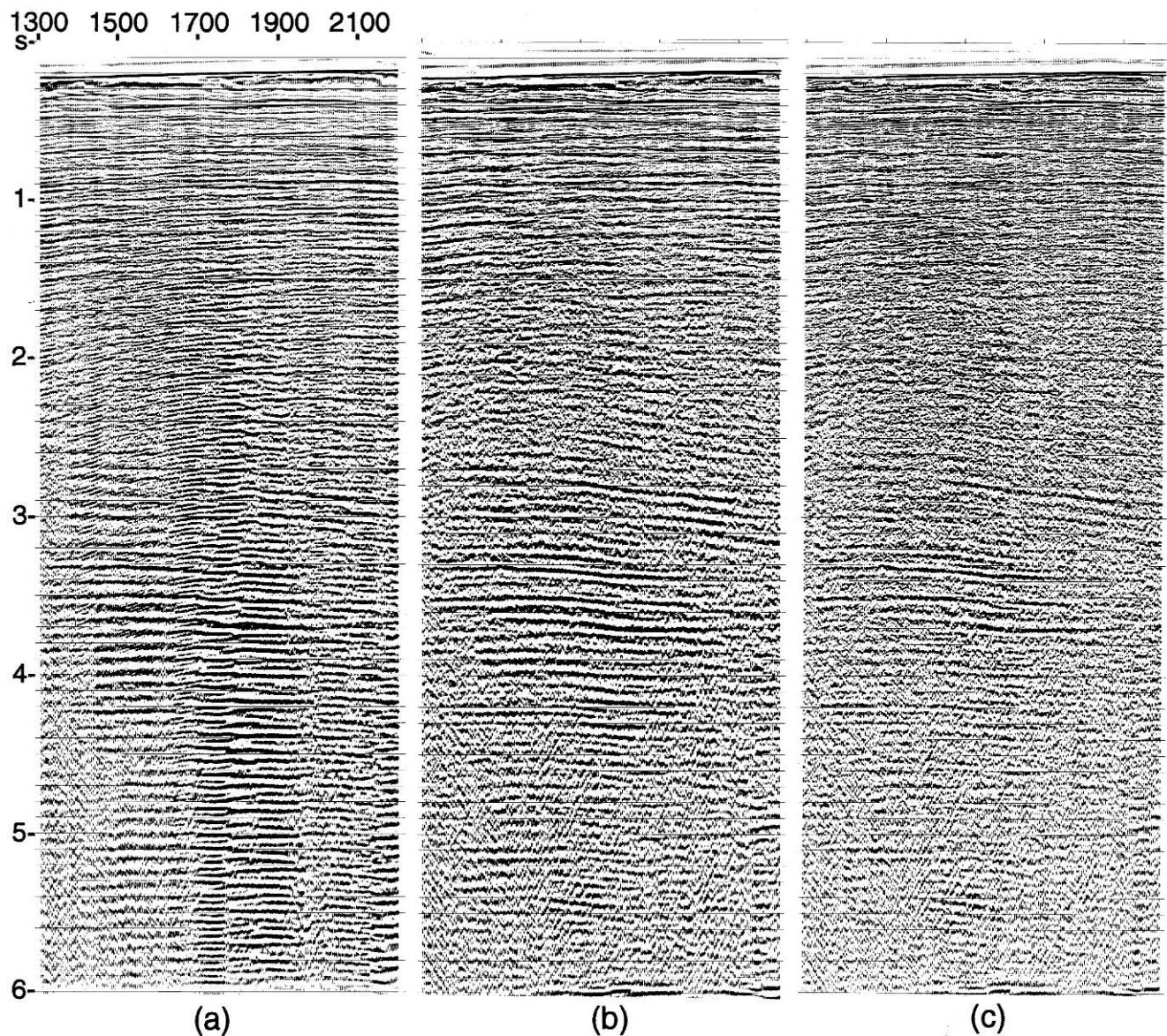


FIG. 6.1-4. (a) CMP stack associated with the gathers shown in Figure 6.1-2 without prestack deconvolution; (b) CMP stack associated with the gathers shown in Figure 6.1-3 with deconvolution before stack; (c) CMP stack as in (b) with the additional deconvolution after stack.

waves in the postcritical region (approximately between 0-0.5 s at near offset and 0-4 s at far offset), and short-period multiples and reverberations in the subcritical region (below 0.5 s at near offset and below 4 s at far offset). (See Section F.1 for modeling guided waves.) The peaks of the amplitude spectra are associated with the short-period multiples. The smaller the period of the multiples, the larger the separation of the peaks in the amplitude spectrum. The refracted arrival and its multiples as part of the guided wave energy indicate that the line has been recorded over a hard water-bottom area. Following t -squared scaling for geometric spreading correction and muting guided waves (Figure 6.1-2), the periodicity character of the multiples becomes more distinctive, particularly at near offsets. With the application of predictive deconvolution using unit-prediction lag (Figure 6.1-3), the amplitude spectrum is flattened within the passband, and multiples are greatly attenuated. The multiple attenuation also is indicated by the autocorrelograms of the deconvolved gathers in Figure 6.1-3.

Figure 6.1-4a shows the CMP stack associated with the gathers in Figure 6.1-2 without multiple attenuation, and Figure 6.1-4b shows the CMP stack associated with the gathers in Figure 6.1-3 with multiple attenuation using deconvolution. Compare these two stacked sections and note that deconvolution before stack has attenuated much of the short-period multiples. Additional deconvolution after stack further improves the vertical resolution by restoring the flatness of the spectrum within the passband (Figure 6.1-4c).

Figure 6.1-5 shows a CMP gather with and without deconvolution. Aside from water-bottom multiples, note the peg-leg multiples associated with the two primaries with arrival times of 1.5 and 2 s at near offset. The autocorrelogram clearly exhibits periodicity of the multiples especially at near offsets. Following predictive deconvolution (in this case with a unit-prediction lag), multiples are largely attenuated as seen in Figure 6.1-4b. The corresponding autocorrelogram is void of the energy associated with the reverberations and multiples. High-frequency random noise that has been boosted by the whitening effect of spiking deconvolution can be filtered out.

Figures 6.1-6 and 6.1-7 clearly demonstrate that conventional statistical deconvolution is a powerful method for attenuating not just short-period multiples and reverberations, but also moderately long-period multiples based on the periodicity criterion. The data shown in Figure 6.1-6 contain nearly flat primary reflections, while the data in Figure 6.1-7 contain some dipping primary reflections. The water-bottom multiples in both figures arrive at intervals of approximately

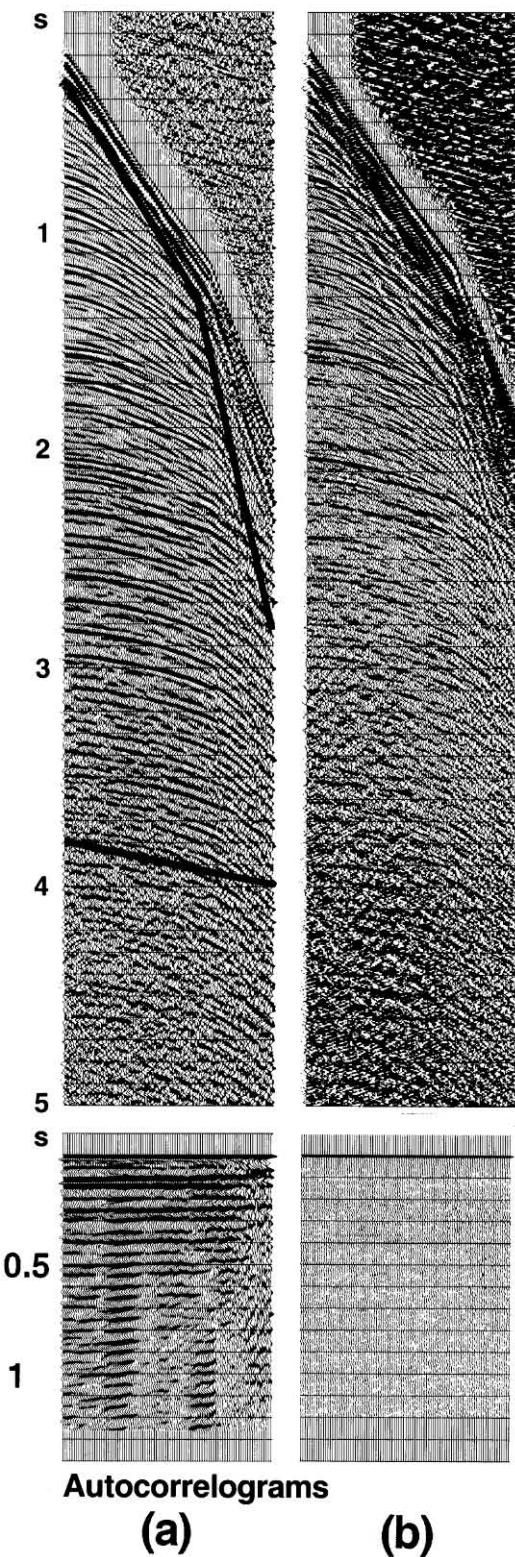


FIG. 6.1-5. A field record containing short-period reverberations before (a) and after deconvolution (b). The solid lines represent the start and end times for the autocorrelation estimation windows.

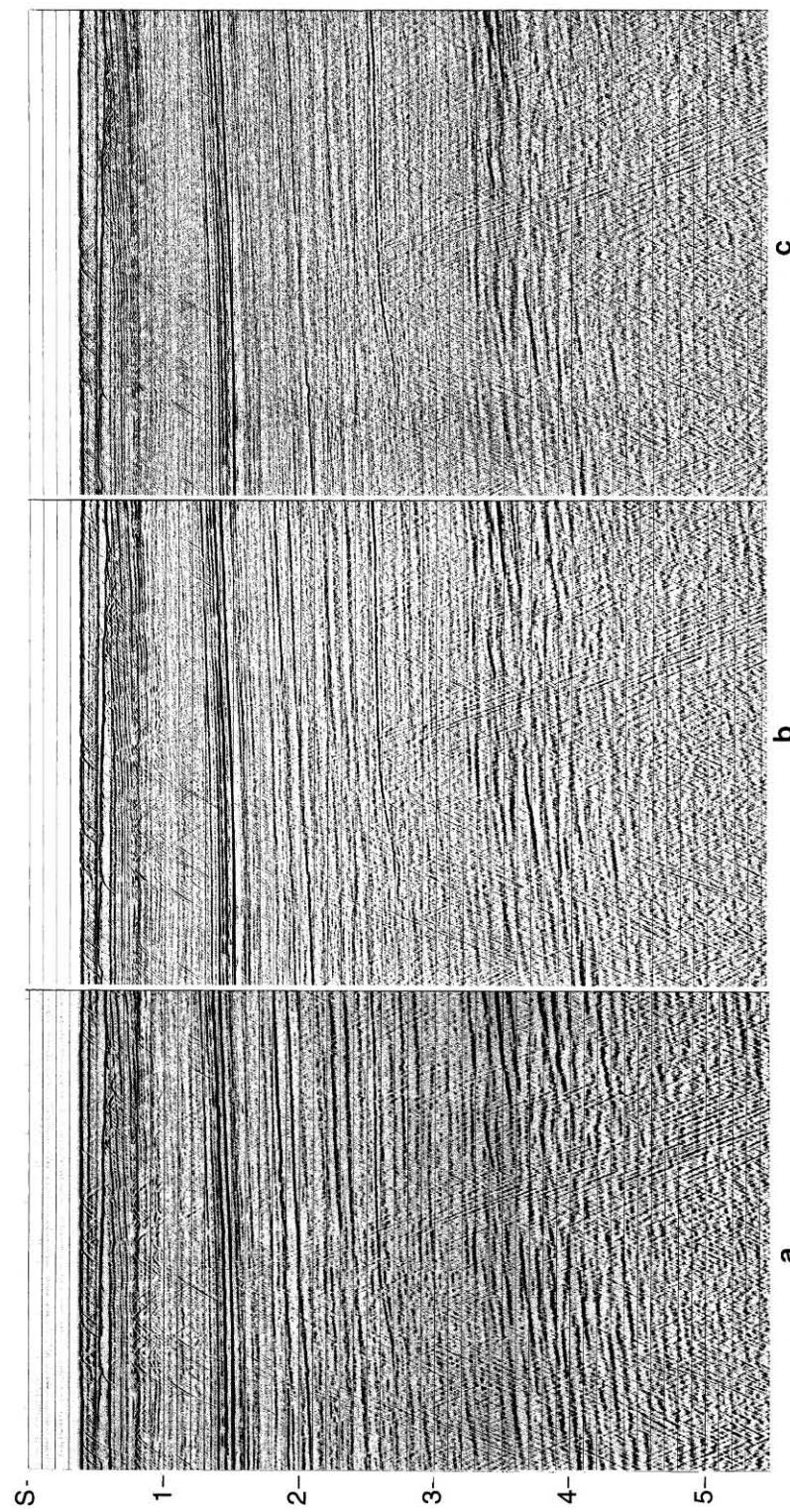


FIG. 6.1-6. A portion of a CMP stack (a) without deconvolution, (b) with prestack deconvolution, and (c) with pre- and poststack deconvolution. (Data courtesy Total Norway.)

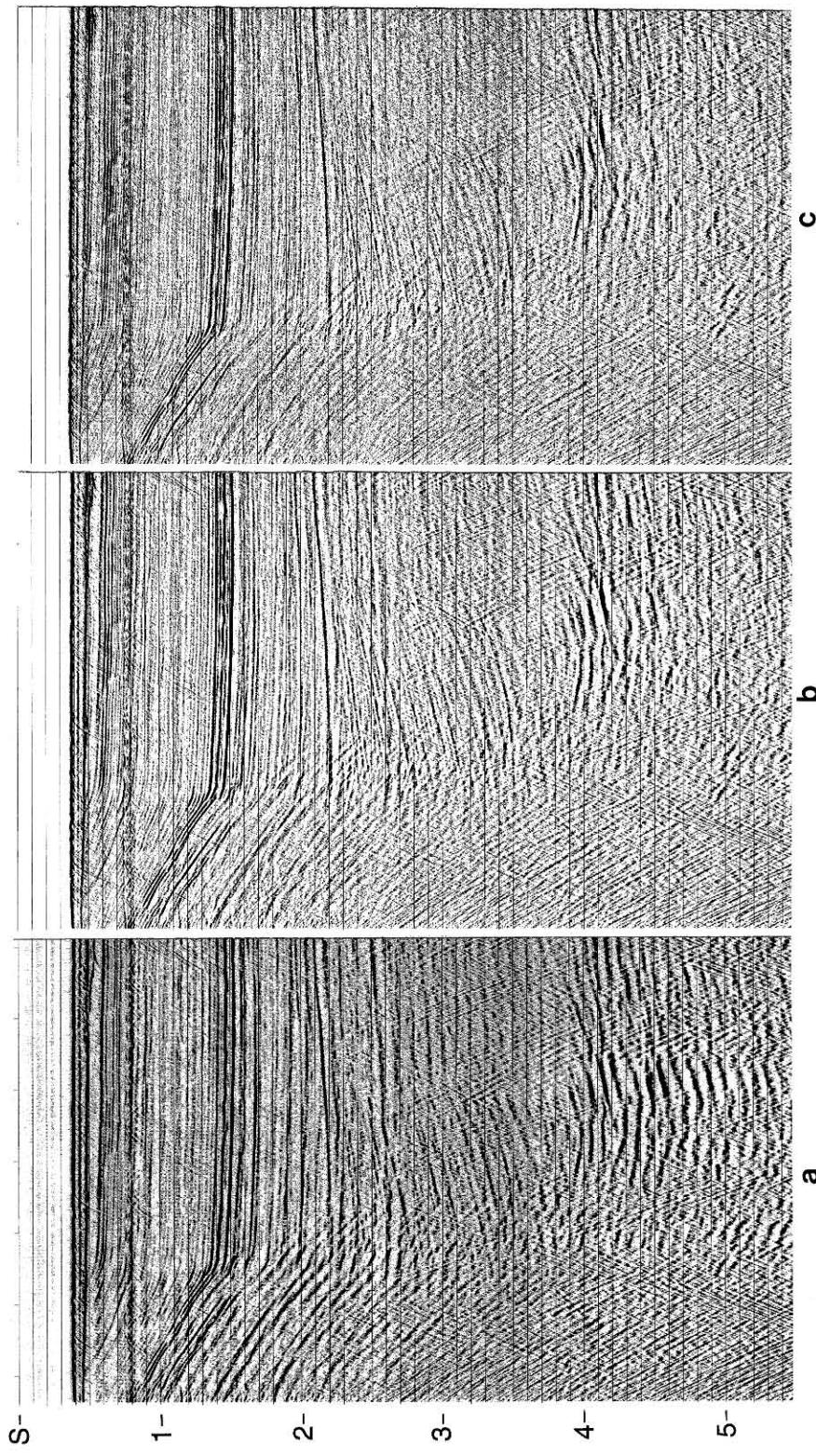


FIG. 6.1-7. A portion of a CMP stack (a) without deconvolution, (b) with prestack deconvolution, and (c) with pre- and poststack deconvolution. (Data courtesy Total Norway.)

350 ms. There also exist peg-leg multiples associated with the primaries at approximately 1.5 and 2.5 s in Figure 6.1-6, and the primaries at approximately 1.5 and 2.1 s in Figure 6.1-7. In a conventional processing sequence, prestack and poststack deconvolution combined with CMP stacking, which exploits velocity discrimination between primaries and long-period multiples, can significantly attenuate a large class of multiples.

Velocity Discrimination Between Primaries and Multiples

The CMP gathers in Figure 6.1-8a clearly illustrate the moveout difference between primaries and multiples. A primary p typically has less moveout than a multiple m . From the velocity spectrum in Figure 6.1-8b, note the difference between the velocity trends associated with primaries VP and multiples $VM1$ and $VM2$. The $VM1$ and $VM2$ velocity functions represent the water-bottom and peg-leg multiples, respectively. If NMO correction is applied using the primary velocities, as is normally done to generate final stacks, then the primaries are aligned while the multiples are undercorrected (Figure 6.1-8c). This suggests that CMP stacking itself is a viable method of multiple attenuation. The CMP stack derived from the gathers in Figure 6.1-8c is shown in Figure 6.1-8d.

The synthetic CMP gather in Figure 6.1-9c contains five primaries, including the water-bottom reflection W and the multiples associated with it. The velocity spectrum shows a significant separation between the velocity functions for multiples VM and primaries VP . Stacking with the primary velocity function should, to a large extent, discriminate against the multiples and result in a section that contains essentially the primary energy as shown in Figure 6.1-10. The stack trace in Figure 6.1-10c is repeated to better examine the relative amplitudes of the primaries and the multiples.

Stacking far offsets works to suppress multiples. However, stacking near offsets works against multiple attenuation, since the moveout difference between primaries and multiples is negligibly small on those offsets as in Figure 6.1-8c. The simplest way around this problem is to apply an inside mute to the CMP gathers before stacking. Another problem then emerges — the outside mute. The severity of this mute governs the amount of far-offset data left at early times for velocity discrimination (Figure 6.1-8c). If there is a severe multiple problem, an effort must be made to preserve the maximum amount of far-offset data associated with target events. The stacked section of Figure 6.1-8d with inside mute applied is shown in Figure 6.1-11a. When

compared with Figure 6.1-8d, note that the deeper peg-leg multiple below 4 s has been further attenuated by inside trace muting. The difference between the conventional CMP stack (Figure 6.1-8d) and the inside mute stack (Figure 6.1-11a) shown in Figure 6.1-11b indicates the amount of energy, mostly multiples, that was removed by the inside mute.

A variation of conventional muting, such as optimum-weighted stacking can produce better results. In such a scheme, weights between 0 and 1 are assigned to each offset during stacking. The smaller weights are normally assigned to the near offsets.

In summary, because there is relatively less moveout differential between the primaries and multiples in the near-offset range, the inside mute (or some kind of weighted stacking) helps suppress multiples. Hence, it may help to cascade any one of the multiple attenuation techniques described in this chapter with inside mute during stacking.

Karhunen-Loeve Transform

Actually, there is a much more powerful technique than inside-trace muting or optimum-weighted stacking to attenuate multiples. It is based on Karhunen-Loeve (K-L) transform (Jones and Levy, 1987; Ulrych et al., 1988; Al-Yahya, 1991). The basic underlying concept is that one can decompose a two-dimensional data set, such as a stacked section in space-time coordinates, into a number of components — the so-called eigenimages, starting with the first eigenimage that contains the highest correlatable events, moving onto the next eigenimage with events with less degree of correlation, all the way to the last eigenimage that comprises the least correlatable components. Each eigenimage comprises the same number of traces as the original data set. Singular-value decomposition (Section F.3) is one way of decomposing a data set into its eigenimages.

So, how is this transform applicable to stacking and multiple suppression? If you apply NMO correction to CMP gathers using the primary velocities, then the primaries will be flattened and thus will have the highest correlatability from trace to trace in the gathers. Hence, these primaries will map into the first eigenimage of the K-L transform. By retaining only the first eigenimage and discarding the others, and stacking the traces in the first eigenimage, one can obtain a stacked trace that is virtually free of random and coherent noise such as multiples. Of course, in reality, there is always some noise component that creeps into the first eigenimage. This happens, for example, when there is very little moveout

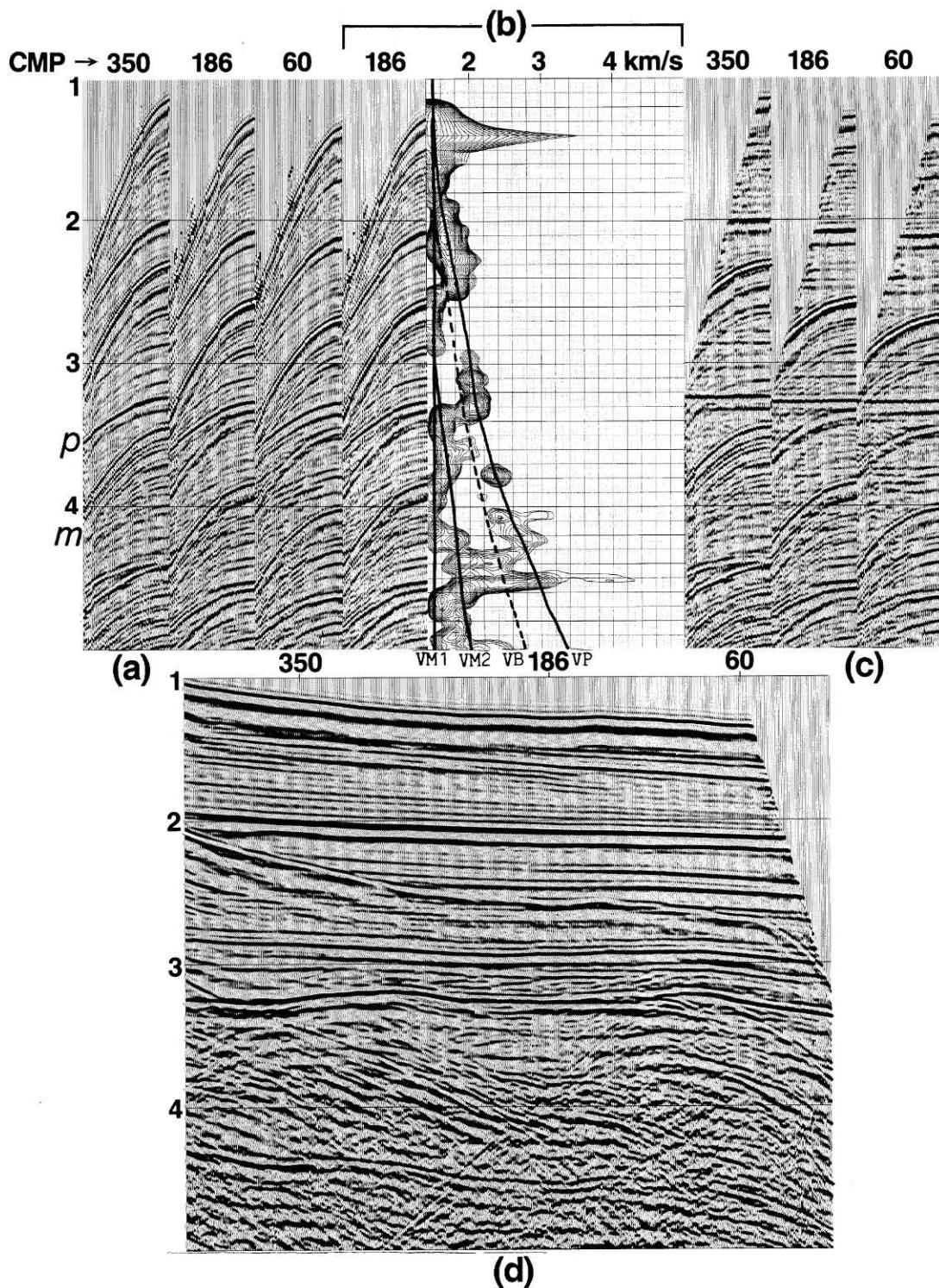


FIG. 6.1-8. (a) Three CMP gathers with strong multiples; (b) velocity analysis at CMP 186, where VP = primary velocity trend, $VM1$ = slow (water-bottom) multiples, and $VM2$ = fast (peg-leg) multiples. (VB is the velocity function used in generating Figure 6.2-15a.) For reference, the CMP gather is displayed next to the velocity spectrum. (c) The same CMP gathers as in (a) after NMO correction using the primary velocities. (d) CMP stack using the gathers as in (c). (Data courtesy Petro-Canada Resources.)

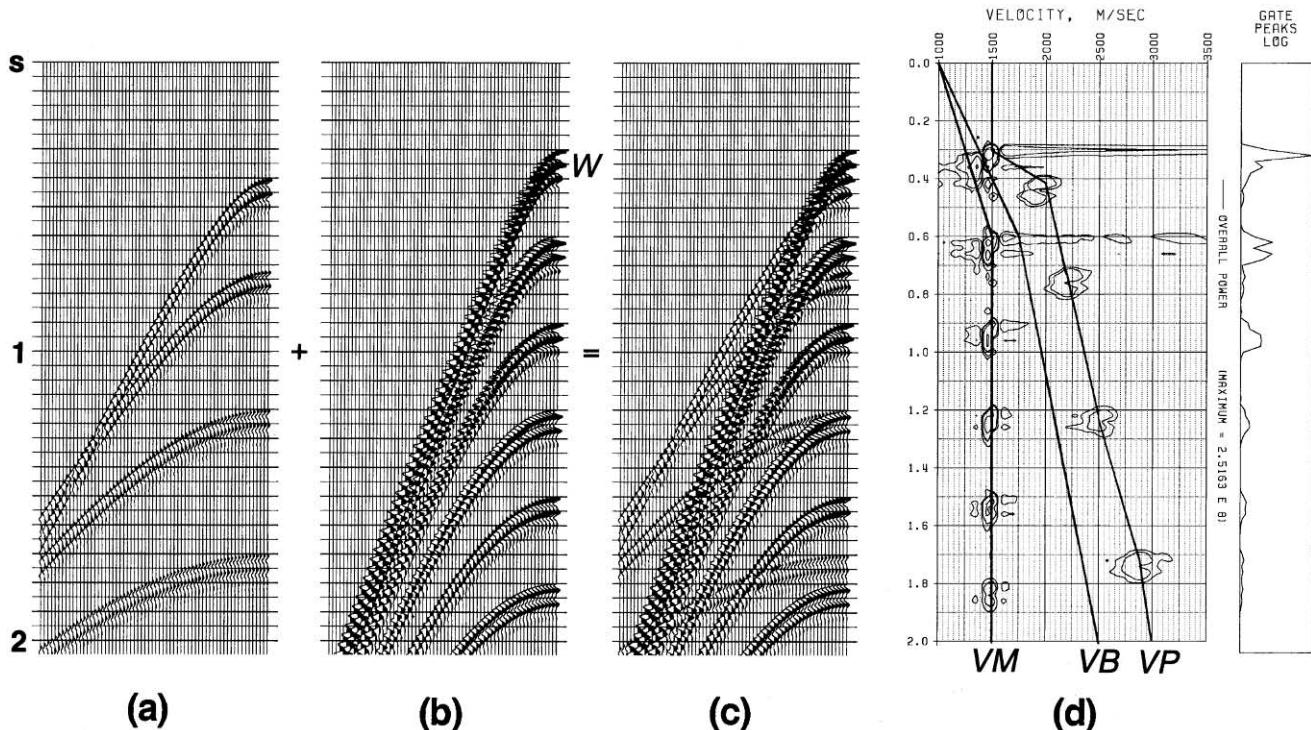


FIG. 6.1-9. Synthetic CMP gathers containing (a) primaries, (b) water-bottom multiples, (c) superposition of (a) and (b). (d) The velocity spectrum derived from (c). Here, W = water-bottom primary, VM = velocity function for multiples, VP = velocity function for primaries, VB = a velocity function between VM and VP used in generating Figure 6.2-12b.

difference between primaries and multiples. An alternative strategy that is aimed at multiple suppression involves moveout correction using multiple velocities, rather than primary velocities.

Start with a modeled CMP gather as shown in Figure 6.1-12a that contains a primary (arriving at 0.2 s at zero offset) and the associated multiples. This gather also contains three additional primaries (at 0.4, 0.8 and 1.2 zero-offset times) that are weaker in amplitude compared to the multiples. The moveout difference between the multiples and primaries is less than 100 ms at the far offset.

Apply NMO correction using the multiple velocity, in this case constant 3000 m/s. Multiples are flattened, and primaries are overcorrected (Figure 6.1-12b). Then perform singular-value decomposition, which is the basis for K-L transform, and examine the first eigenimage (Figure 6.1-12c). Note that the highest correlatable events in this gather are those events with the moveout velocity of 3000 m/s — the primary at 0.2-s zero-offset time and the associated multiples. Subtract this eigenimage from the original NMO-corrected gather (Figure 6.1-12b) to get the gather that is a composite of all the eigenimages except the first one (Figure 6.1-13a). Note that multiples have been attenuated and the weak primaries have been retained. Because we did not reject

the higher eigenimages associated with the least correlatable energy, including the random noise, this energy is present in the output gather in Figure 6.1-13a.

Finally, apply inverse NMO correction using the same multiple velocity function to obtain the gather after multiple attenuation (Figure 6.1-13b), which should

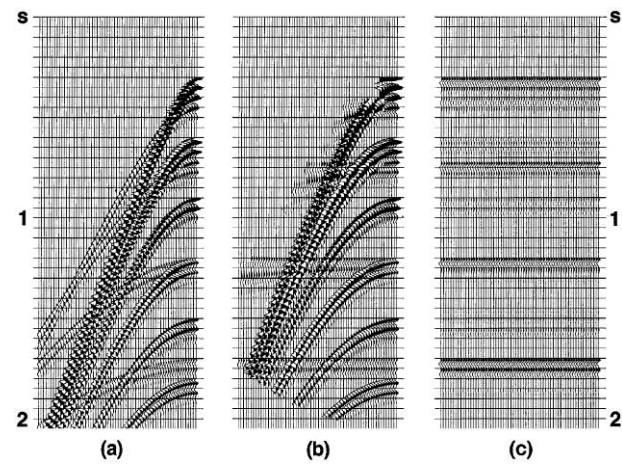
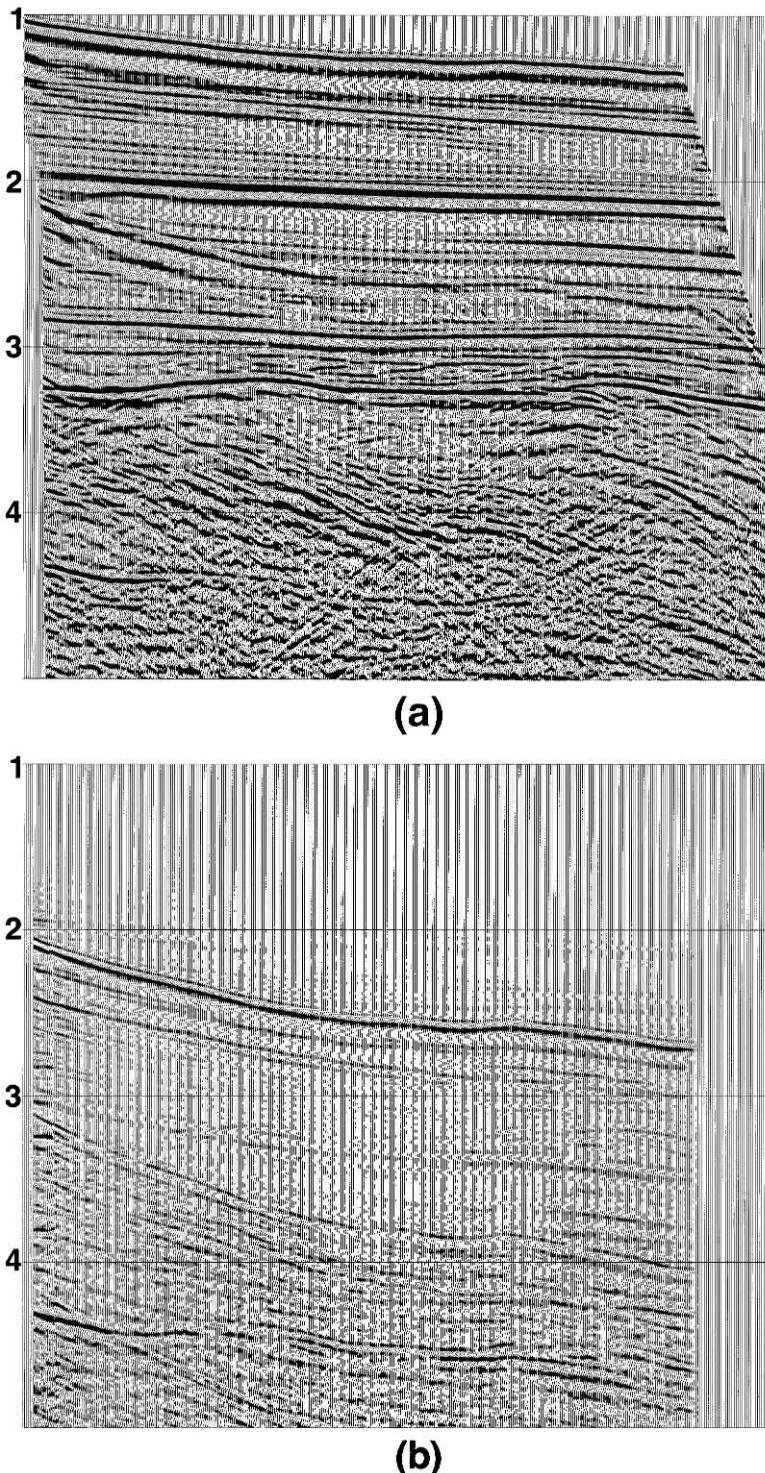
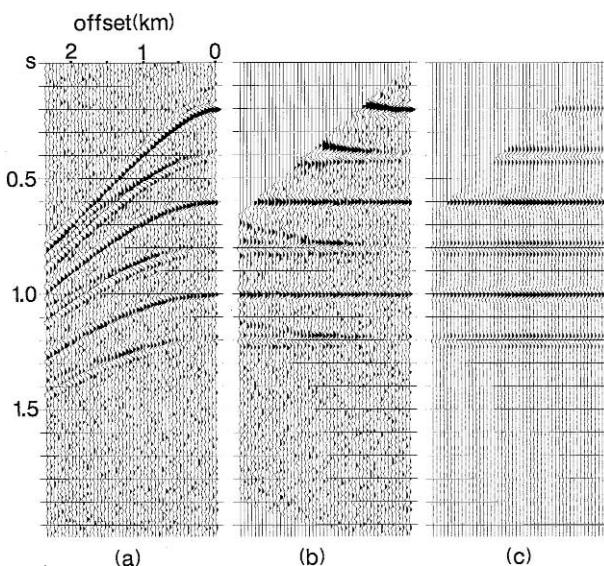


FIG. 6.1-10. (a) The CMP gather in Figure 6.1-9c and (b) after NMO correction using the primary velocity function (VP in Figure 6.1-9d). (c) The stack trace derived from (b) repeated to emphasize the strong events.



6.1-11. (a) The CMP stack derived from the CMP gathers in Figure 6.1-8c with inside mute applied. The inside mute pattern can be recognized on the left edge of the section. Compare this stack with that shown in Figure 6.1-8d. (b) The difference between the conventional CMP stack (Figure 6.1-8d) and the inside mute stack (a). (Data courtesy Petro-Canada Resources.)



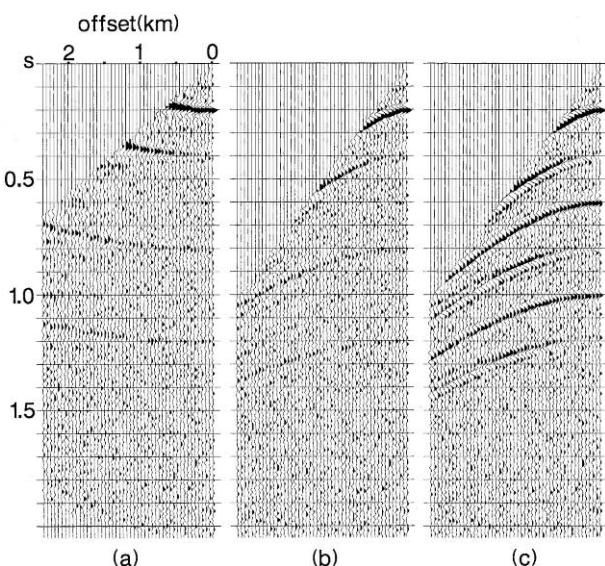
6.1-12. (a) A modeled CMP gather with a primary at 0.2-s zero-offset time and its multiples, and with three additional primaries at 0.4-, 0.8- and 1.2-s zero-offset times. The gather also contains band-limited random noise. (b) the same gather after NMO correction using the velocity of multiples (3000 m/s) and muting; (c) the eigenimage associated with the first eigenvalue derived from singular-value decomposition of the moveout-corrected gather. This eigenimage contains the primary at 0.2-s zero-offset time and its associated multiples.

be compared with the original gather without multiple attenuation (Figure 6.1-13c). Note that, the K-L transform, in principle, is a very powerful data decomposition technique that can be used to attenuate multiples.

In addition to multiple attenuation, the K-L transform also can be used to attenuate random noise by simply rejecting the corresponding eigenimages. For instance, a 60-trace CMP gather would be decomposed into 60 eigenimages. Those eigenimages with eigenvalues between, say 55 and 60, would contain the random noise to be rejected.

Figure 6.1-14a shows a CMP gather that contains strong water-bottom and peg-leg multiples. Following moveout correction using the water velocity, the water-bottom multiples are flattened, peg-legs are slightly overcorrected and primaries, which are visible at far offsets below 2 s, are significantly overcorrected (Figure 6.1-14b).

By the K-L transform, the gather is decomposed into its eigenimages. Figure 6.1-15 shows the reconstructed gather as in Figure 6.1-14b using only a subset of the eigenimages. The reconstructed gather using only the first eigenimage contains just a few of the strong moveout-corrected multiples. With the inclusion of additional eigenimages, the reconstructed gather is allowed to contain events with some moveout. By exam-



6.1-13. (a) The difference gather derived from subtracting the first eigenimage gather (Figure 6.1-12c) from the moveout-corrected gather (Figure 6.1-12b), (b) same difference gather after inverse moveout correction, and (c) original modeled gather as in Figure 6.1-12a with the stretch mute as in (b). The gathers in (c) and (b) are before and after multiple attenuation using the K-L transform.

ining the series of reconstructed gathers with a subset of eigenimages, a band of eigenimages that corresponds to multiples can be determined.

Figure 6.1-14c shows such a reconstructed gather using the eigenimages that correspond to the first 20 eigenvalues. Subtract the gather in Figure 6.1-14c from that in Figure 6.1-14b to obtain the gather that presumably contains the primary reflections (Figure 6.1-14d). Following the application of inverse moveout correction (Figure 6.1-14e) the data are ready for velocity analysis after multiple attenuation. Figure 6.1-16 shows a portion of the CMP stack associated with the data in Figure 6.1-14 with and without multiple attenuation using the K-L transform. While this example demonstrates that the method can be successful in attenuating multiples associated with near-horizontal reflections, it also can be a robust technique in handling multiples associated with moderately complex reflections. Figure 6.1-17 shows a portion of a CMP stack that contains a strong primary at 1.2 s at the left-hand edge of the section. The K-L transform method has largely attenuated the water-bottom and peg-leg multiples associated with the strong primary, and enhanced the primary events above it. Following the eigenimage decomposition, caution must be exercised in determining the number of eigenvalues included in the reconstruction of CMP gathers (Figure 6.1-15).

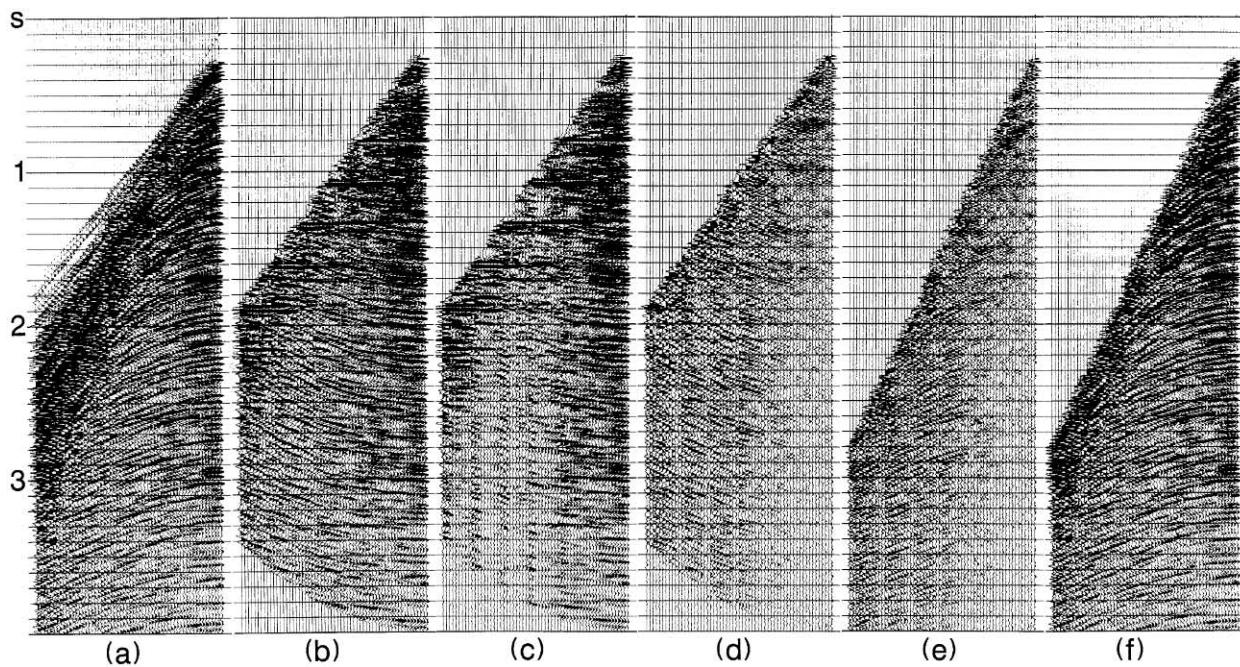


FIG. 6.1-14. (a) A CMP gather with an abundance of water-bottom and peg-leg multiples; (b) after moveout correction using the water velocity so as to flatten the water-bottom multiples; (c) the reconstructed gather using the eigenimages from the K-L transform that correspond to the first 20 eigenvalues; (d) the difference gather obtained by subtracting (c) from (b); (e) the gather in (d) after inverse moveout correction; (f) the original gather as in (a) after the same stretch mute as in (e). The gathers in (f) and (e) are before and after multiple attenuation using the K-L transform.

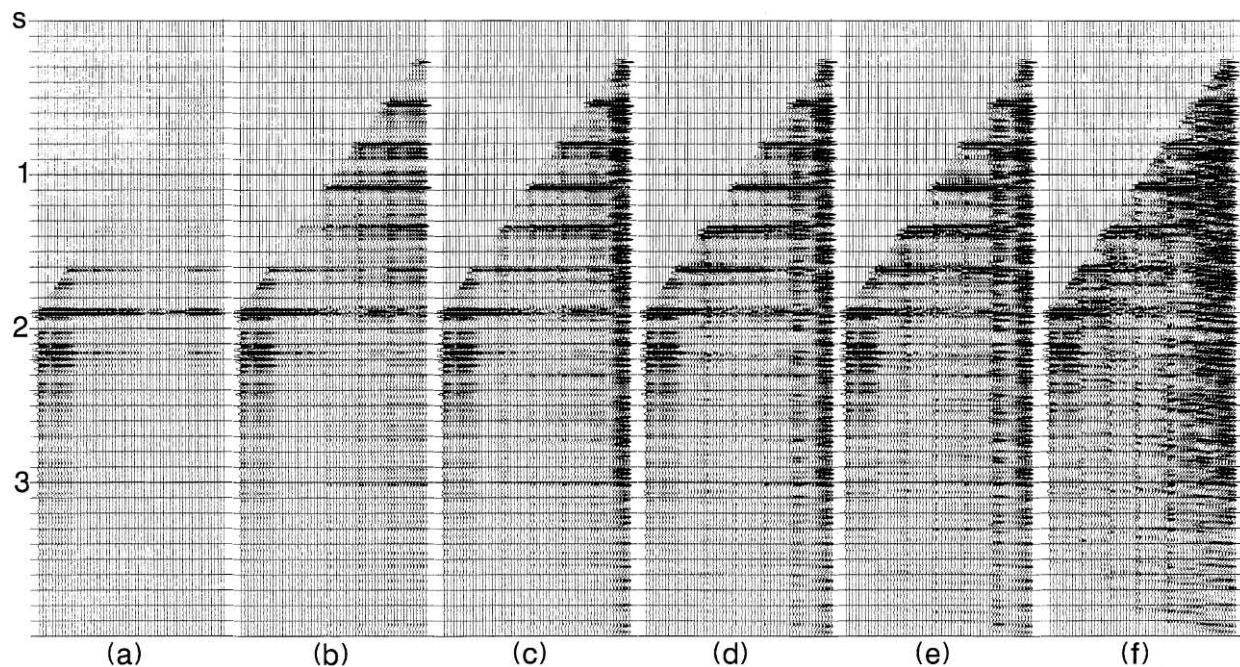


FIG. 6.1-15. Reconstruction of the CMP gather in Figure 6.1-14a using the eigenimages from the K-L transform that correspond, from (a) to (f), to the first 1, 2, 3, 4, 5, and 10 eigenvalues.

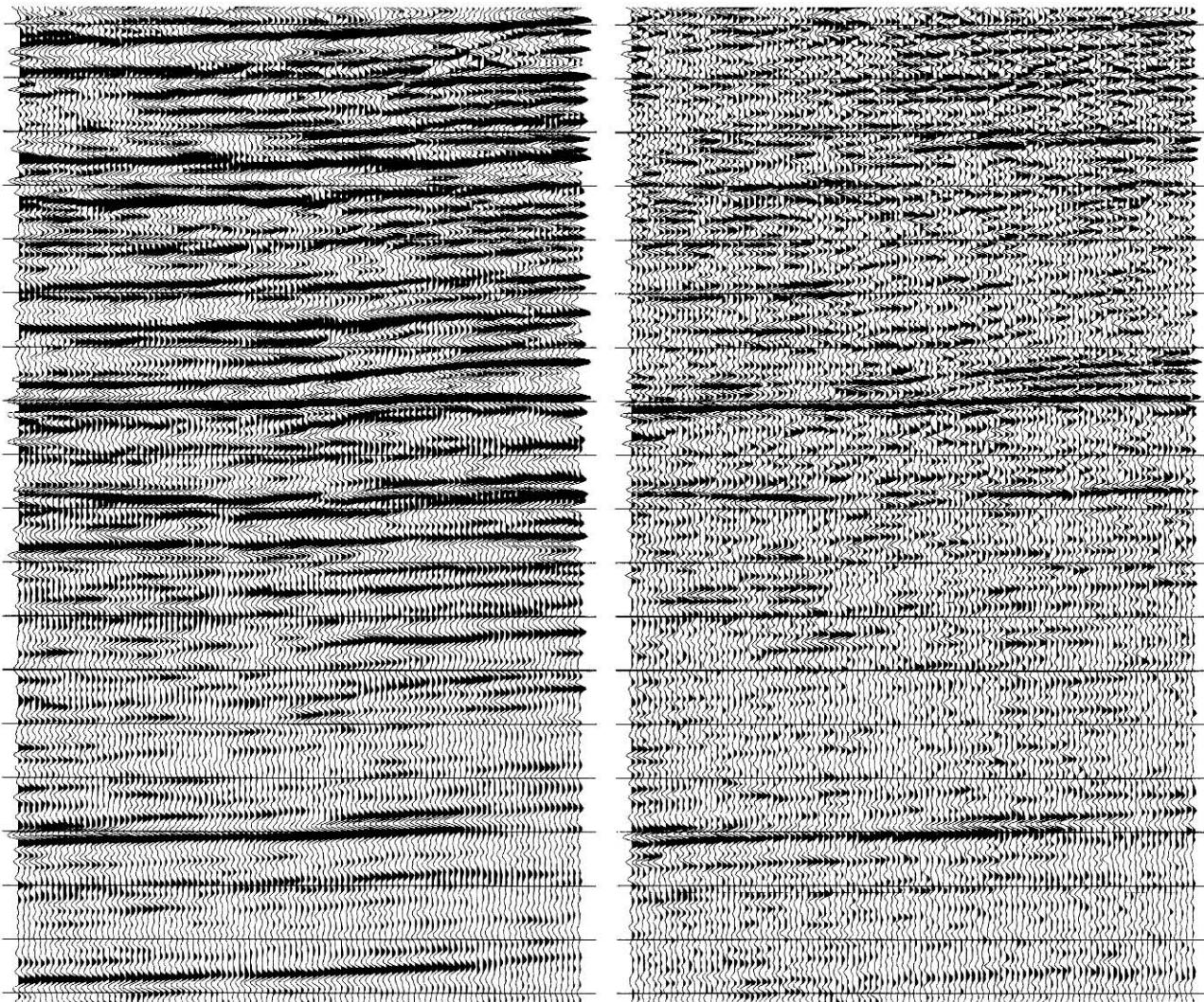


FIG. 6.1-16. A portion of the CMP stack associated with the data in Figure 6.1-14, without (left) and with (right) multiple attenuation using the K-L transform.

As mentioned earlier, a flat event within a data window in time and space has the highest degree of correlation from trace to trace, and thus, maps into the first eigenimage. Doicin and Spitz (1991) exploited this property in the frequency-space domain based on the earlier work by White (1984) to better separate primaries from peg-leg multiples into different eigenimages. Consider a portion of a common-offset section in Figure 6.1-18a associated with a marine data set. The water bottom is nearly flat at approximately 150 ms. The common-offset section exhibits a primary reflection (K) associated with an erosional unconformity in the neighborhood of 3 s. The flat water bottom gives rise to a series of peg-leg multiples (M_1 and M_2) of the primary reflection (K), arriving at an equal time interval.

If we perform horizon flattening on the primary reflection (K), then the multiple reflections (M_1 and M_2) would also be flattened. The eigenimage decomposition of the data window that excludes the flattened primary but includes the flattened multiples maps these into the first eigenimage. Reject the first few eigenimages and reconstruct the data window from the remaining eigenimages without the peg-leg multiples. The final step involves unflattening of the data. This process is applied to each of the common-offset sections and the data are stacked. Note the absence of the peg-leg multiples on the stacked section shown in Figure 6.1-18b. This section lends itself to an improved image of the dipping events below the unconformity (Figure 6.1-18c).

Peg-leg multiples associated with a reflector below a dipping water bottom exhibit a complex traveltime

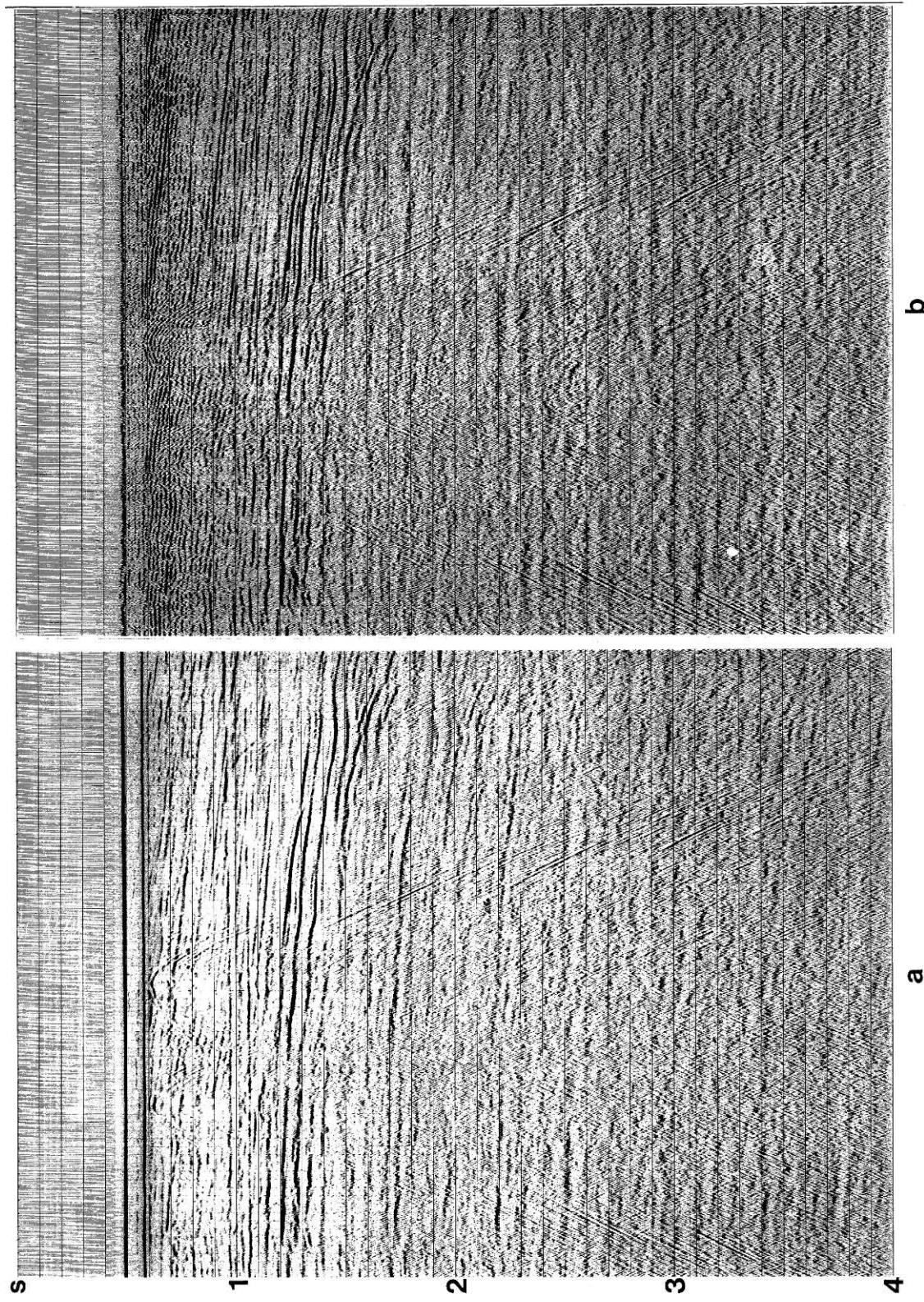


FIG. 6.1-17. A portion of a CMP stack without (left) and with (right) multiple attenuation using the K-L transform.

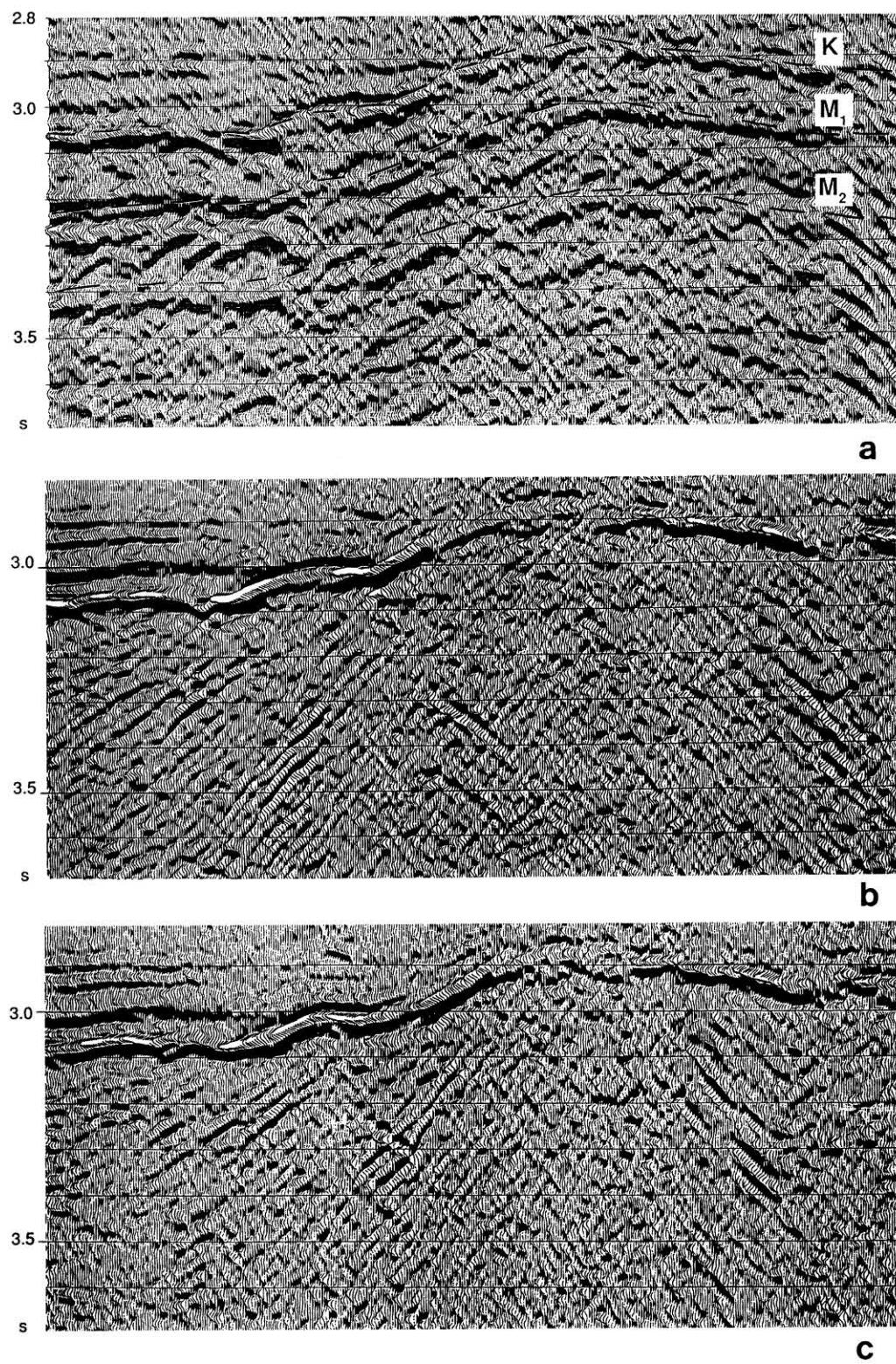


FIG. 6.1-18. (a) A portion of a common-offset section with a series of peg-leg multiples (M_1 and M_2) associated with a primary reflection (K), (b) the stacked section that corresponds to the data as in (a) after the application of peg-leg multiple attenuation using a frequency-space eigenimage decomposition, and (c) time migration of the stacked section as in (b) (Doicin and Spitz, 1991).

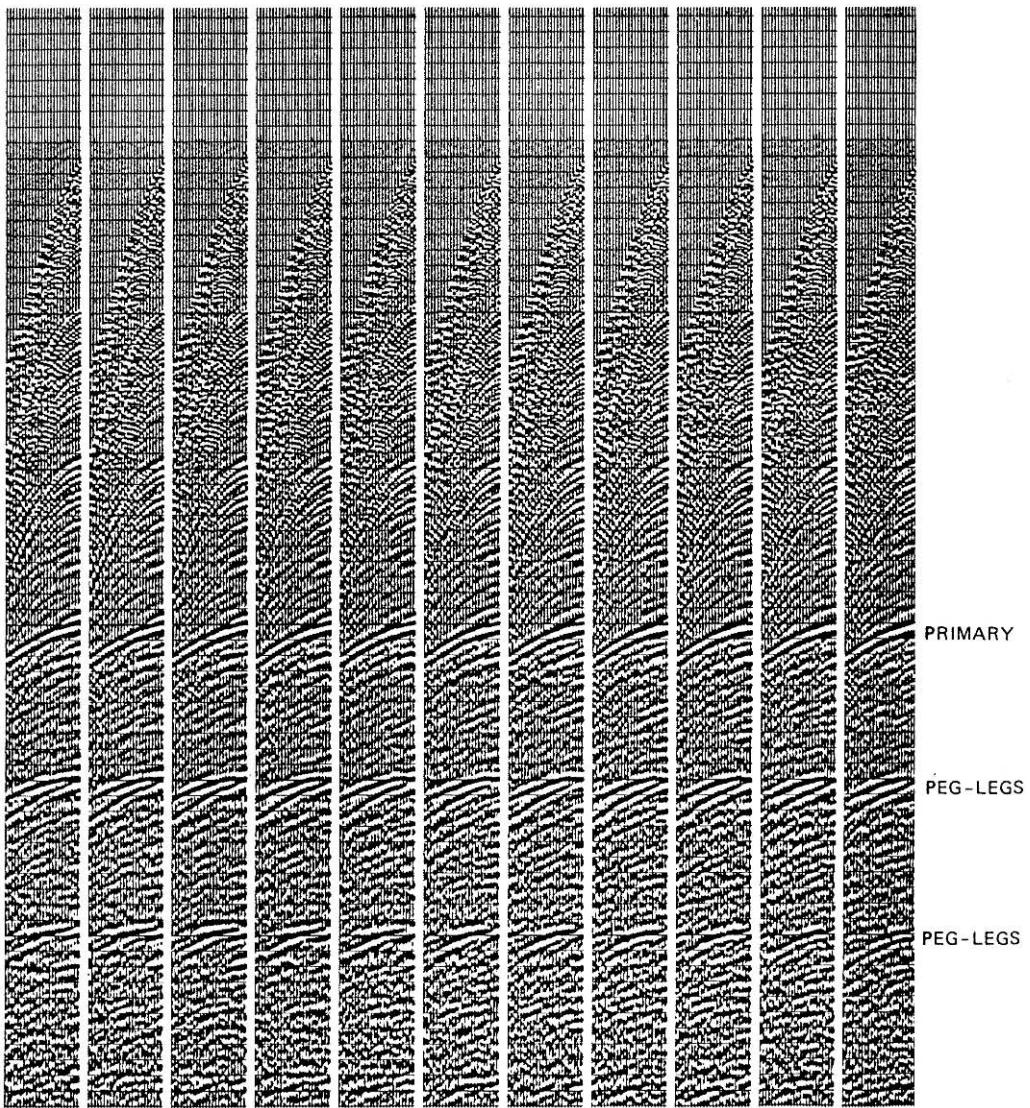


FIG. 6.1-19. Selected CMP gathers that exhibit split peg-leg multiples (Levin and Shah, 1977.)

behavior (Levin and Shah, 1977). Figure 6.1-19 shows selected CMP gathers that include peg-leg multiples of a complex nature. A sketch of raypaths associated with peg-leg multiples is shown in Figure 6.1-20. For a horizontally layered earth model, the peg-leg raypath segment on the source end (the solid path) of the CMP raypath and the peg-leg raypath segment on the receiver end (the dotted path) of the CMP raypath give rise to coincident arrival times on the CMP gather (Figure 6.1-20a). When there are dipping reflectors along the raypaths of the peg-leg multiples, the peg-leg raypath segment on the source end of the CMP raypath and the peg-leg raypath segment on the receiver end of the CMP raypath give rise to *split* peg-leg multiple arrivals (Figure 6.1-20b). Also note that, while the minimum

arrival time of the primary reflection is at near-offset trace, the minimum arrival time of the peg-leg multiple reflections is at some nonzero-offset trace. The split peg-leg multiples can be extremely troublesome when interpreting data recorded over a continental slope.

Modeling of Multiples

Another approach to multiple attenuation based on velocity discrimination operates on CMP gathers directly in the $t - x$ domain. Again, consider the synthetic CMP gather in Figure 6.1-21a, which is the same as that in Figure 6.1-9c. Apply NMO correction, this time using

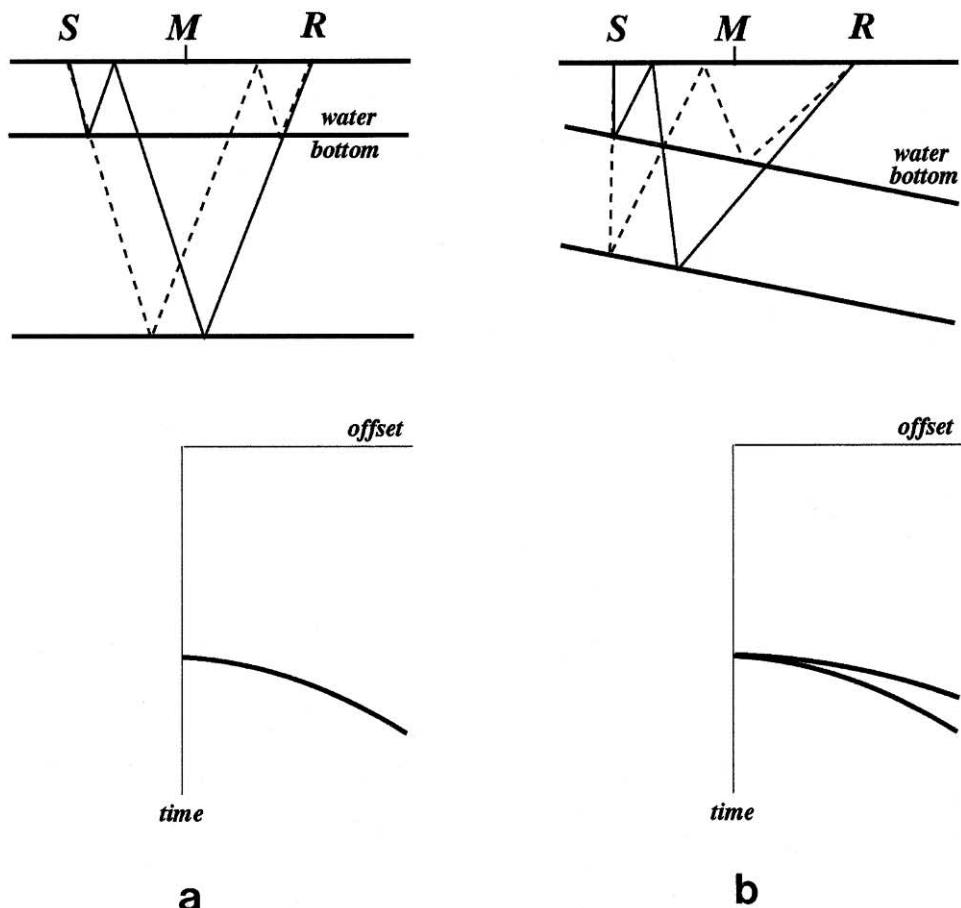


FIG. 6.1-20. Raypaths and traveltimes for peg-leg multiples associated with (a) horizontally layered earth model, and (b) an earth model with dipping reflectors.

the multiple velocity function labeled as VM in Figure 6.1-9d. The result is shown in Figure 6.1-21b, while the stack trace is shown in Figure 6.1-21c. This stack trace is called the model trace for multiples since it almost entirely contains the multiple energy. Subtract the model trace from the individual traces of the NMO-corrected gather (Figure 6.1-21b). The resulting traces essentially should contain only primary energy. Note that this model-based approach applies to one multiple velocity function at a time.

The main problem with this technique is constructing a model trace that contains only multiples. Because of slight waveform changes and the variation of the moveout differential between primaries and multiples with offset, the model trace for multiples will not represent multiples equally well for each offset. Better representations of multiple energy can be obtained by constructing individual model traces for each offset by stacking only a few traces on both sides of the trace associated with that offset.

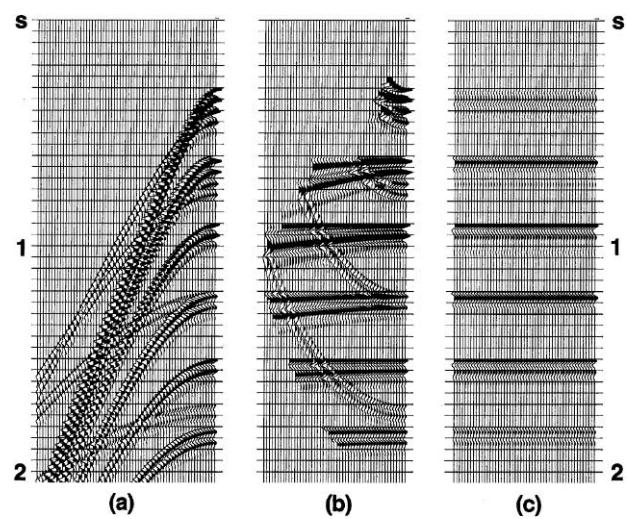


FIG. 6.1-21. (a) The modeled CMP gather in Figure 6.1-9c, (b) after NMO correction using the multiple velocity function (VM in Figure 6.1-9d). (c) The stack trace is repeated to emphasize the strong events.

Even if individual model traces were used, it is still difficult to generate model traces that do not contain some primary energy. Good attenuation of primary energy in the model trace ultimately depends on the moveout differential between primaries and multiples being a substantial fraction of the period of the seismic wavelet. At lower temporal frequencies, this usually is not the case and, hence, the model trace often includes some of the low-frequency components of the primaries. Consequently, subtraction of the model trace from the moveout-corrected traces often leads to attenuation of the multiples and the low-frequency components of the primaries. Exclusion of the low-frequency end of the spectrum in building the model traces is a way to deal with this latter problem.

To study the results of this subtraction technique on field data, consider the selected CMP gathers in Figure 6.1-8a. From the velocity spectrum in Figure 6.1-8b, note that the multiples can have more than one velocity trend (the velocity trends labeled as $VM1$ and $VM2$). The NMO-corrected CMP gathers in Figure 6.1-22a are obtained by using one of the velocity trends ($VM1$). The primaries are overcorrected, while the multiples associated with the velocity trend $VM1$ are flattened.

The velocity spectrum after multiple attenuation using the model-based subtraction technique (Figure 6.1-22b) shows an enhanced primary velocity trend. Also note the removal of the multiple trend ($VM1$) from the velocity spectrum. The selected CMP gathers following moveout correction using the primary velocities from Figure 6.1-22b are shown in Figure 6.1-22c. The stacked section after applying the multiple attenuation procedure is shown in Figure 6.1-22d.

The model-based approach can be cascaded to attenuate more than one class of multiples present in the data. Use of the multiple velocity trend labeled as $VM2$ in Figure 6.1-8b, yields the results shown in Figure 6.1-23. Input CMP gathers to the second pass (Figure 6.1-23a) are the output CMP gathers from the first pass (Figure 6.1-22c). Note the attenuation of the multiple trend $VM2$ from the velocity spectrum (Figure 6.1-23b). The deeper peg-leg multiple below 4 s has been attenuated further (compare Figures 6.1-22d and 6.1-23d).

The stacked sections resulting from the first pass (Figure 6.1-22d) and the second pass (Figure 6.1-23d) have a high-frequency character compared to the conventional CMP stack (Figure 6.1-8d). As indicated earlier, this effect can be suppressed by excluding the low frequencies from the model traces. Multiple attenuation using the filtered versions of the model traces yields the stacked sections in Figure 6.1-24.

6.2 FREQUENCY-WAVENUMBER FILTERING

Coherent linear events in the $t - x$ domain can be separated in the $f - k$ domain by their dips. This allows us to eliminate certain types of unwanted energy from the data. In particular, coherent linear noise in the form of ground roll, guided waves, and side-scattered energy commonly obscure primary reflections in recorded data. These types of noise usually are isolated from the reflection energy in the $f - k$ domain. From the field record in Figure 6.2-1a, note how ground-roll energy can dominate the data. Ground roll is a type of dispersive waveform that propagates along the surface and is low-frequency, large-amplitude in character. Typically, ground roll is suppressed in the field by using a suitable receiver array.

Figure 6.2-1b is the 2-D amplitude spectrum of the field record in Figure 6.2-1a. Here, various types of energy are well isolated from one another. Ground roll A , its backscattered component B , and guided waves C , are identifiable. Reflections D are situated around the frequency axis. As shown in Figure 6.2-1c, a fan is imposed on this spectrum within which the undesired energy is rejected. This is followed by inverse mapping back to the $t - x$ domain. The resulting filtered record in Figure 6.2-1d is largely free of ground-roll energy, except for the backscattered component. Defining a reject fan in the $f - k$ domain is one implementation of the process known as $f - k$ dip filtering.

Note that dip filtering is but one type of $f - k$ filtering. The reject zone in the $f - k$ domain may be specified not just as a fan but also as a shape suitable for the objective in mind. For instance, the reject zone may be defined as one entire quadrant of the $f - k$ plane in the case of multiple attenuation. It may only be one half of one quadrant in the case of a spatial antialiasing filter (Section 1.2). The following are the steps involved in $f - k$ filtering:

- (a) Starting with a common-shot or a CMP gather, or a CMP-stacked section, apply 2-D Fourier transform.
- (b) Define a 2-D reject zone in the $f - k$ domain by setting the 2-D amplitude spectrum of the $f - k$ filter to zero within that zone and set its phase spectrum to zero.
- (c) Apply the 2-D $f - k$ filter by multiplying its amplitude spectrum with that of the input data set.
- (d) Apply 2-D inverse Fourier transform of the filtered data.

(text continues on p. 904)

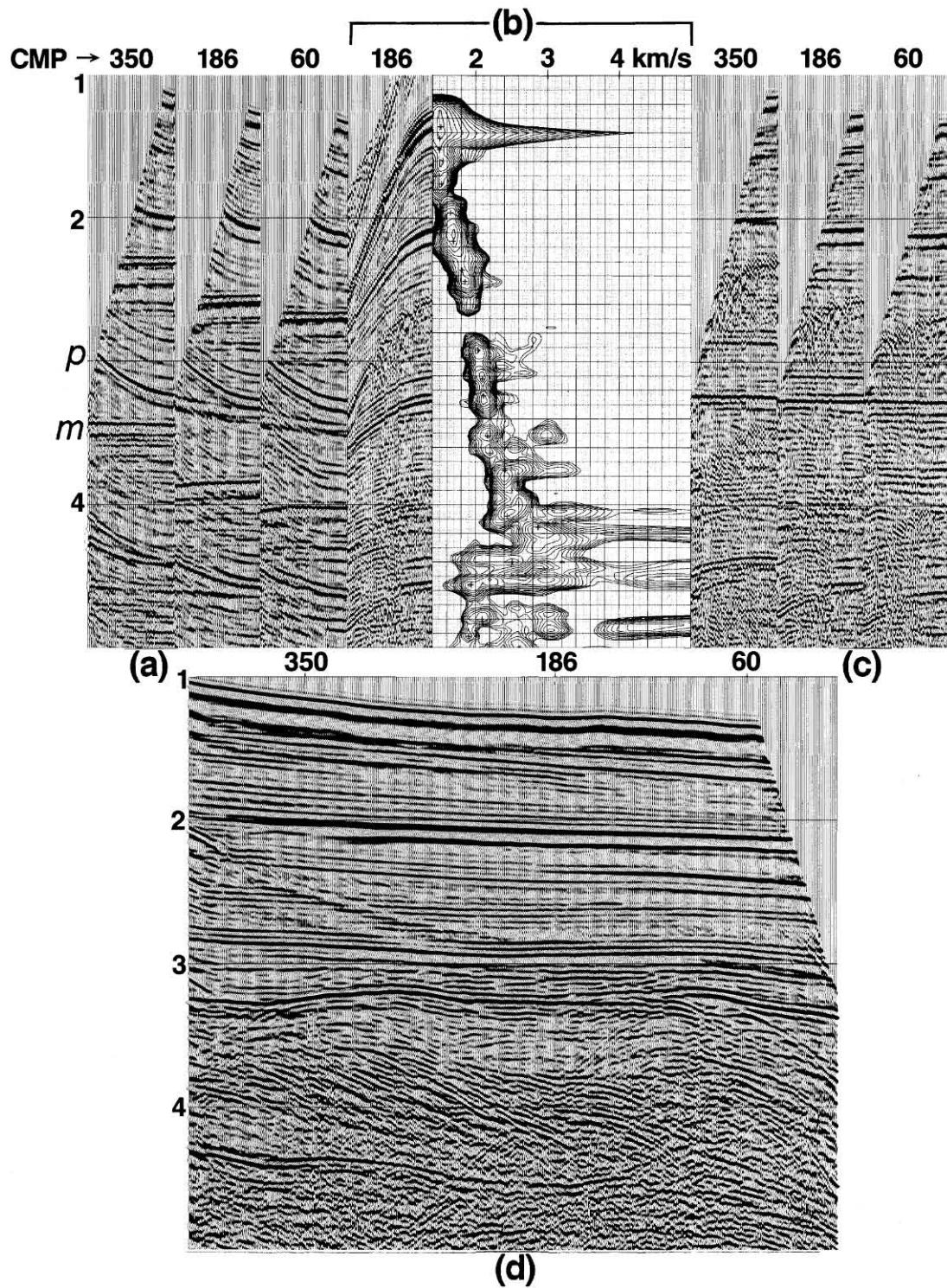


FIG. 6.1-22. (a) The CMP gathers in Figure 6.1-8a after NMO correction using slow multiple velocities (VM_1 in Figure 6.1-8b). (b) The velocity spectrum at CMP 186 after single-pass model-based subtraction for multiple attenuation. For reference, the CMP gather after multiple attenuation is shown to the left of the velocity spectrum. (Compare this with Figure 6.1-8b.) (c) The same CMP gathers as in (a) after the single-pass model-based subtraction for multiple attenuation, followed by NMO correction using primary velocities derived from velocity spectrum (b). (d) The CMP stack derived from the CMP gathers as in (c) after multiple suppression.

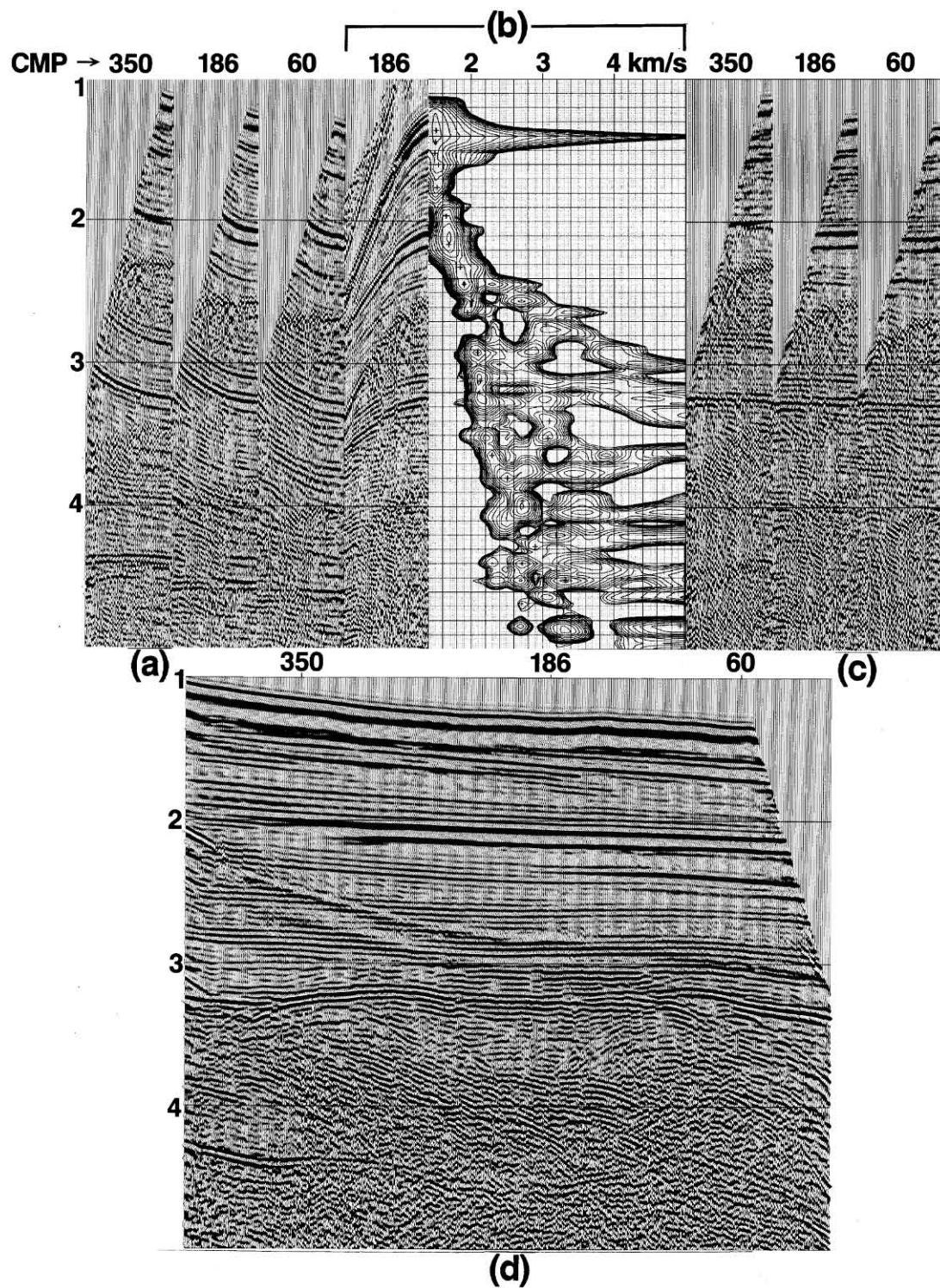


FIG. 6.1-23. (a) The CMP gathers from the first-pass model-based subtraction (Figure 6.1-22) after NMO correction using fast multiple velocities (VM_2 in Figure 6.1-8b). (b) The velocity spectrum at CMP 186 after the second-pass model-based subtraction for multiple attenuation. For reference, the CMP gather after multiple attenuation is shown to the left of the velocity spectrum. (c) The same CMP gathers as in (a) after the second-pass model-based subtraction for multiple attenuation, followed by NMO correction using primary velocities from (b). (d) The CMP stack derived from the CMP gathers as in (c) after the second-pass model-based subtraction for multiple attenuation.

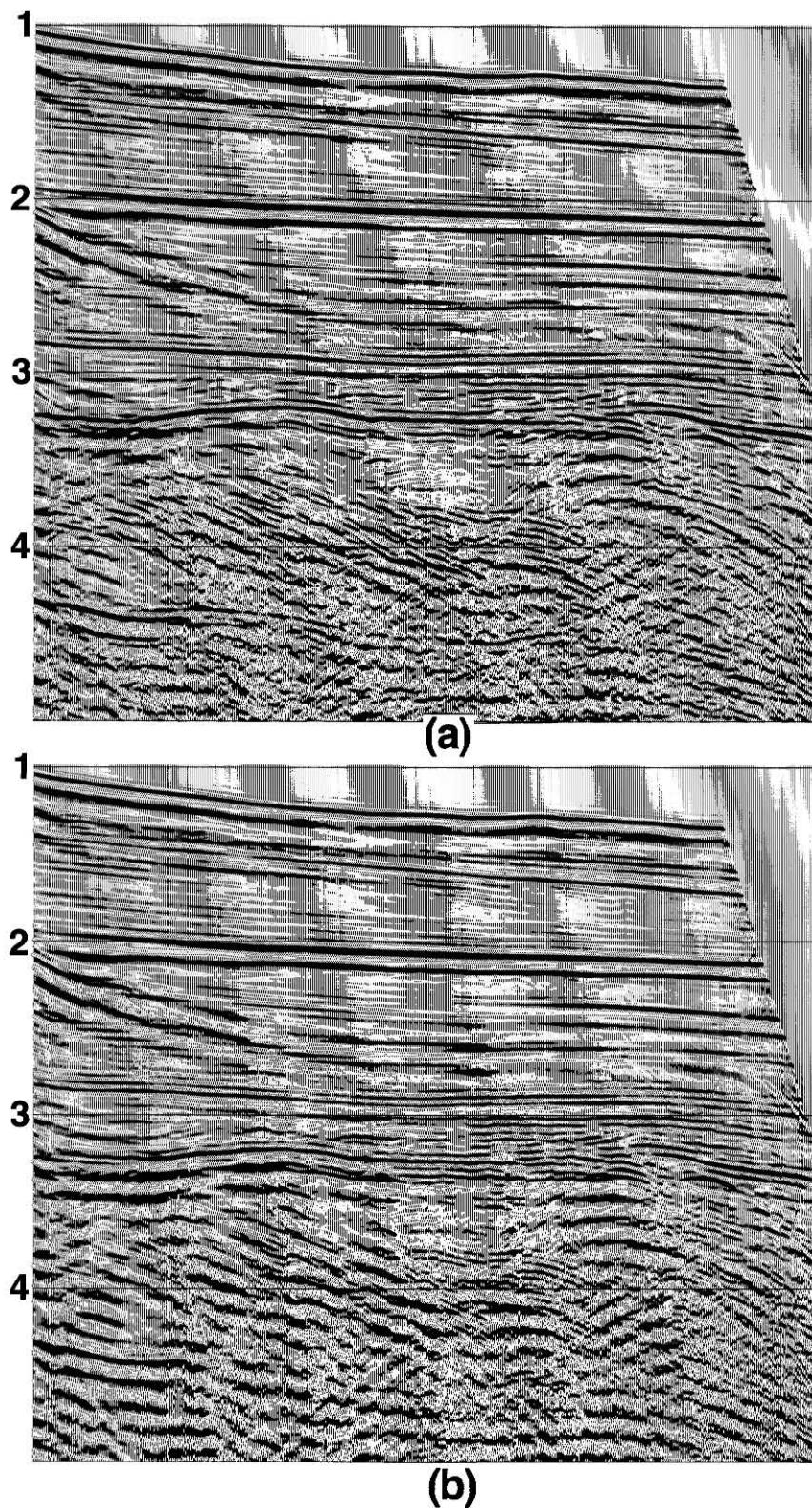


FIG. 6.1-24. The CMP stacks after the model-based subtraction for multiple attenuation, which was implemented using filtered model traces. (a) First pass using multiple velocities VM_1 and (b) second pass using multiple velocities VM_2 , as depicted in Figure 6.1-8b.

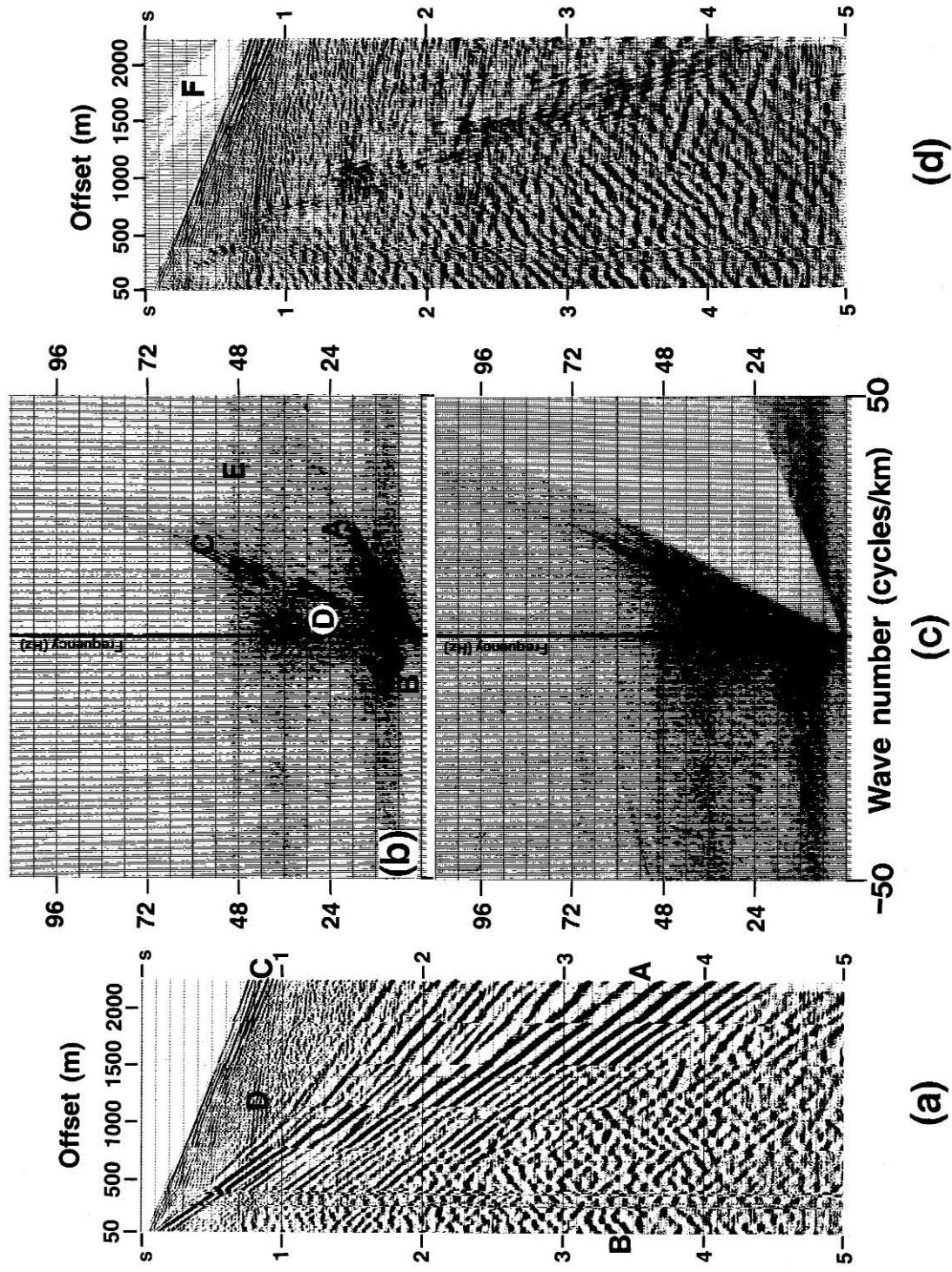


FIG. 6.2-1. (a) Composite field record obtained from a walk-away noise test. Trace spacing = 10 m, A = ground roll, B = a backscattered component of A, C = dispersive guided waves, D = primary reflection. Event E is referred to in Exercise 6-4. (b) The $f - k$ spectrum of this field record. (c) The $f - k$ spectrum of the field record after rejecting ground roll energy A. Compare this with the $f - k$ spectrum (b) of the original record. For display purposes, each spectrum is normalized with respect to its own maximum. (d) Dip-filtered field record whose $f - k$ spectrum is shown in (c). Compare this record with the original in (a). (Data courtesy Turkish Petroleum Corp.)

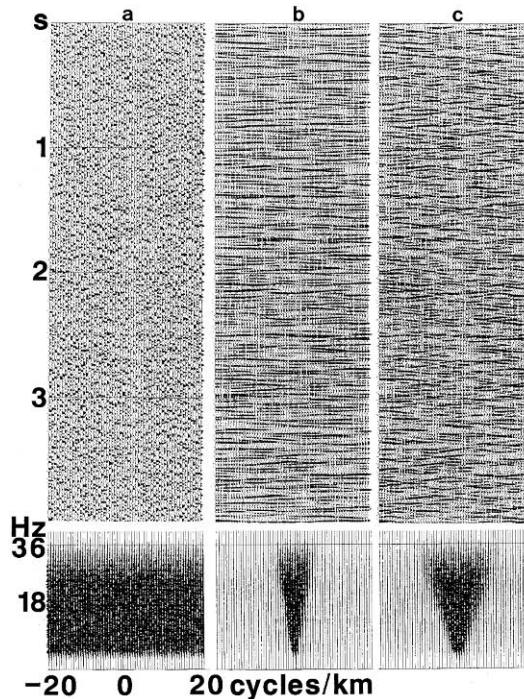


FIG. 6.2-2. (a) A synthetic CMP gather with band-limited random noise uncorrelated from trace to trace; the same gather after $f - k$ filtering with different pass-fans with dip bands: (b) $(+2, -2)$ ms/trace, and (c) $(+4, -4)$ ms/trace. The $f - k$ spectra are shown at the bottom of each panel. Note that random noise in $t - x$ domain maps onto a rectangular zone in the $f - k$ domain, with its top and base corresponding to the low- and high-frequency end of the passband.

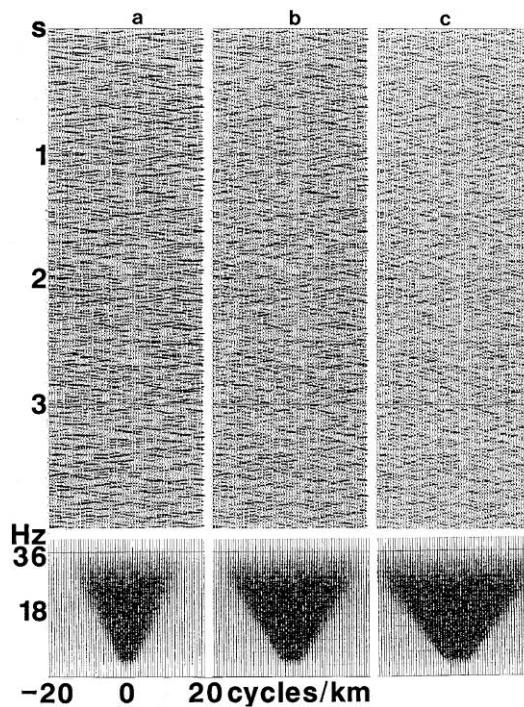


FIG. 6.2-3. A synthetic CMP gather as in Figure 6.2-2 with band-limited random noise uncorrelated from trace to trace after $f - k$ filtering with different pass-fans with dip bands: (a) $(+6, -6)$ ms/trace, (b) $(+8, -8)$ ms/trace, and (c) $(+10, -10)$ ms/trace. The $f - k$ spectra are shown at the bottom of each panel.

Practical issues associated with the 2-D Fourier transform and specifying a fan reject zone are outlined below:

- (a) Conventional implementations of the Fourier transform itself produce wraparound noise. This is apparent in Figure 6.2-1d, location *F*. To avoid this problem, the data must be extended beyond the ranges of the spatial and temporal axes by padding with zeroes. The size of the input gather typically is increased by a factor of 4, which is equivalent to doubling the length in *t* and *x*. This increases the cost but removes the wraparound effects.
- (b) The fan width must not be too narrow. This follows from previous observations of the 1-D Fourier analysis of frequency filters (Section 1.1). If the bandwidth of the reject zone were narrow, then the *t*–*x* response of the dip filter would have a large array of nonzero elements. Fortunately, coherent noise with large stepouts, such as ground roll, often is isolated in the *f*–*k* domain from the zone that includes the reflection signal. This is demonstrated by the example in Figure 6.2-1b. In such cases, ground-roll energy *A* is attenuated without damaging the reflection signal by using a large fan (Figure 6.2-1c).
- (c) As for the 1-D frequency filters (Section 1.1), the amplitude spectrum of the *f*–*k* filter must not have sharp boundaries. There must be a smooth transition from the reject zone to the pass zone. This is accomplished by tapering the fan edges, which is analogous to using slopes in frequency filtering. The amount of tapering must be large enough to be effective. On the other hand, it must not be so wide that it suppresses signal in the pass zone. Extra precaution is taken at low frequencies. As the fan thins to a zero width at the origin of the *f*–*k* domain, as in a wedge, the actual reject zone may invade the low-frequency components of the pass zone. This invasion occurs because the fan cannot get too narrow. It may be desirable to stop the reject zone just short of the low frequencies. This effectively excludes the low frequencies from the *f*–*k* dip filtering action.
- (d) Spatial aliasing often causes poor *f*–*k* filter performance. The fan reject zone must be extended to the spatially aliased frequency components. A practical approach to this problem is to apply linear moveout correction to the data before *f*–*k* filtering so that the unwanted signal appears at lower dips, thus eliminating the spatial aliasing effects. The linear moveout then is removed after *f*–*k* filtering. Unfortunately, this may not always work, since events that are not spatially aliased before may be spatially aliased after linear moveout.

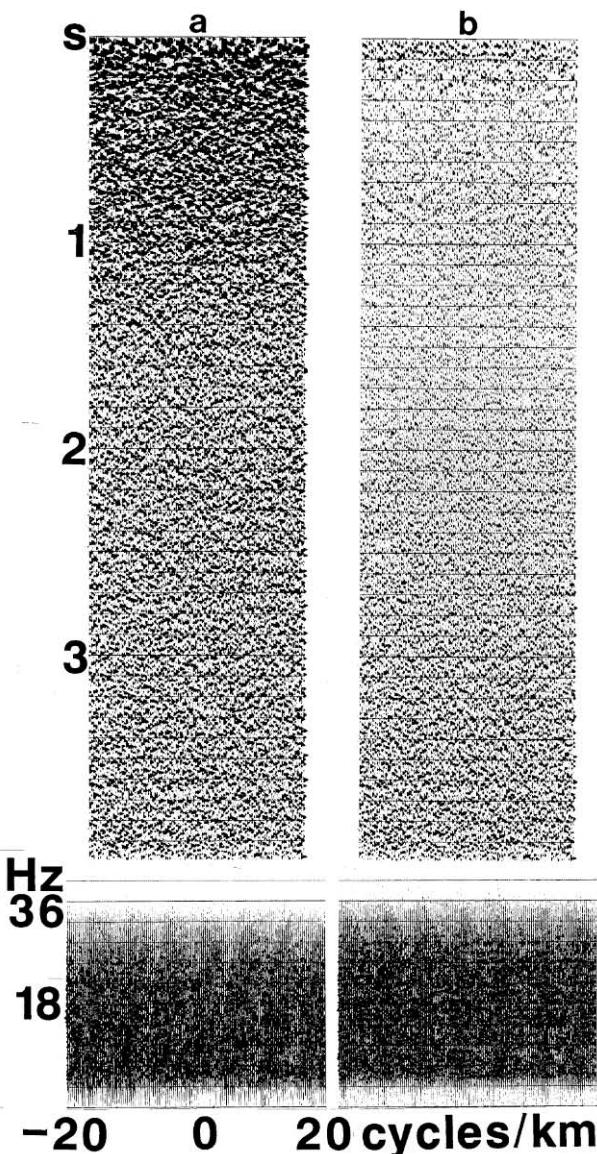


FIG. 6.2-4. (a) Stack of synthetic CMP gathers as in Figure 6.2-2a without *f*–*k* filtering, and (b) stack of synthetic CMP gathers as in Figure 6.2-2b with *f*–*k* filtering using a dip band of (+2, -2) ms/trace.

Random Noise and Frequency-Wavenumber Filtering

Treatment of random noise uncorrelated from trace to trace by *f*–*k* filtering is an important aspect of the process. Figure 6.2-2 shows a synthetic CMP gather which contains only band-limited random noise. Note that the *f*–*k* spectrum exhibits the random character of the data — there is energy at all wavenumbers up to the Nyquist and at all frequencies within the passband.

After the application of a narrow-fan $f - k$ dip filter, note that the CMP gather contains coherent events with dips that correspond to the pass-fan in the $f - k$ domain. By widening the pass-fan of the $f - k$ dip filter, dip range of the coherent events in the gather is broadened as demonstrated in Figure 6.2-3. As the pass-fan is widened, the coherence of events in the gather becomes increasingly less apparent, while the randomness character becomes more predominant and eventually similar to that of the input gather.

Figure 6.2-4a shows a stack of several CMP gathers as in Figure 6.2-2a with band-limited random noise. Note that stacking of CMP gathers which contain just random noise yields a stack which contains, again, random noise. The $f - k$ spectrum exhibits the random character of the stacked data — there is energy at all wavenumbers up to the Nyquist and at all frequencies within the passband. Figure 6.2-4b shows a stack of $f - k$ filtered CMP gathers as in Figure 6.2-2b. Note that stacking of $f - k$ filtered CMP gathers with random noise yields, once again, a section which largely contains just random noise, despite the nonrandom character of the input gathers (Figure 6.2-2b).

The stacked section in Figure 6.2-4a was displayed at a very high gain to differentiate the noise levels at shallow and late times. The reason why the noise level is stronger at the shallow portion is because the muting after NMO correction has caused lower fold in stacking, and hence less attenuation of the random noise during stacking. The stack of the CMP gathers with $f - k$ dip filtering (Figure 6.2-4b) does not exhibit the organized character seen in the CMP gathers themselves (Figure 6.2-2b), because the stacked amplitudes are uncorrelated from one gather to another. The relatively higher amplitudes at late times in Figure 6.2-4b result from less attenuation of the organized noise on CMP gathers at late times during stacking — less attenuation, because the stepout of the organized noise at late times happens to be very similar to the moveout implied by the velocity function used in NMO correction.

Statics Corrections and Frequency-Wavenumber Filtering

It should be noted that coherent linear noise on shot gathers can be influenced kinematically by surface topography and a near-surface refractor geometry. Specifically, linearity of the coherent noise may be distorted across a shot record. Distortions along a linear event in the $t - x$ domain cause smearing of energy over a broad range of wavenumbers in the $f - k$ domain. This, in turn, would make it difficult to specify a pass-fan for

reflection energy. It can be concluded that statics corrections, at least in the form of field statics, should be applied to shot records prior to $f - k$ filtering.

Dip Filtering of Coherent Linear Noise

Figure 6.2-5 shows four common-shot gathers, while Figure 6.2-6 shows their $f - k$ spectra before and after $f - k$ dip filtering. The pass or reject zones in the $f - k$ spectra do not need to be constrained to fan shape. The left half of the spectra mostly contain spatially aliased data. By keeping the fan shape in the right quadrant, while zeroing out most of the left quadrant, the coherent noise trains, including the aliased energy, are eliminated.

Because aliasing is a serious concern in $f - k$ filtering, it is advisable to apply it to shot gathers rather than to CMP gathers, since CMP gathers can have twice the trace spacing of shot gathers. Nevertheless, two neighboring CMP gathers can be interleaved before applying $f - k$ dip filtering, then split afterward, thus alleviating aliasing. Such implementation is permissible provided the composite gather does not exhibit any traveltime shifts caused by changes in reflector geometries or lateral variations in velocities. Coherent noise as seen on the shot gathers in Figure 6.2-5 is best attenuated in the shot-gather domain. When sorted into CMP gathers, no significant remnant of this noise is left in the data (Figure 6.2-7). Figure 6.2-8a shows the stacked section derived from the CMP gathers in Figure 6.2-7a with no $f - k$ filtering. Note the linear noise left in the stacked section. The CMP gathers with $f - k$ filtering (Figure 6.2-7b) yield a stack that is virtually free of linear noise (Figure 6.2-8b).

Coherent linear noise on stacked data also can be suppressed by poststack migration that incorporates dip filtering. If coherent linear noise is associated with side scatterers, then much of it can be attenuated by a constant-velocity DMO correction (Section 5.2). If $f - k$ filtering were not applied to common-shot gathers containing side-scattered energy, then a stacked section with coherent linear noise could result (Figure 6.2-9a). Figure 6.2-9b shows that this noise can be attenuated by $f - k$ dip filtering the stacked section. Could this noise attenuation be done better? If an $f - k$ filter were applied to shot records, then the stack in Figure 6.2-9c results. When compared to the result in Figure 6.2-9b, the result in Figure 6.2-9c seems to offer better resolution. The prestack $f - k$ filtered data also yield an improved velocity analysis (Figure 6.2-10).

Practical experience with $f - k$ filtering proves that an even better stack may result when both common-shot and common-receiver gathers are $f - k$ filtered.

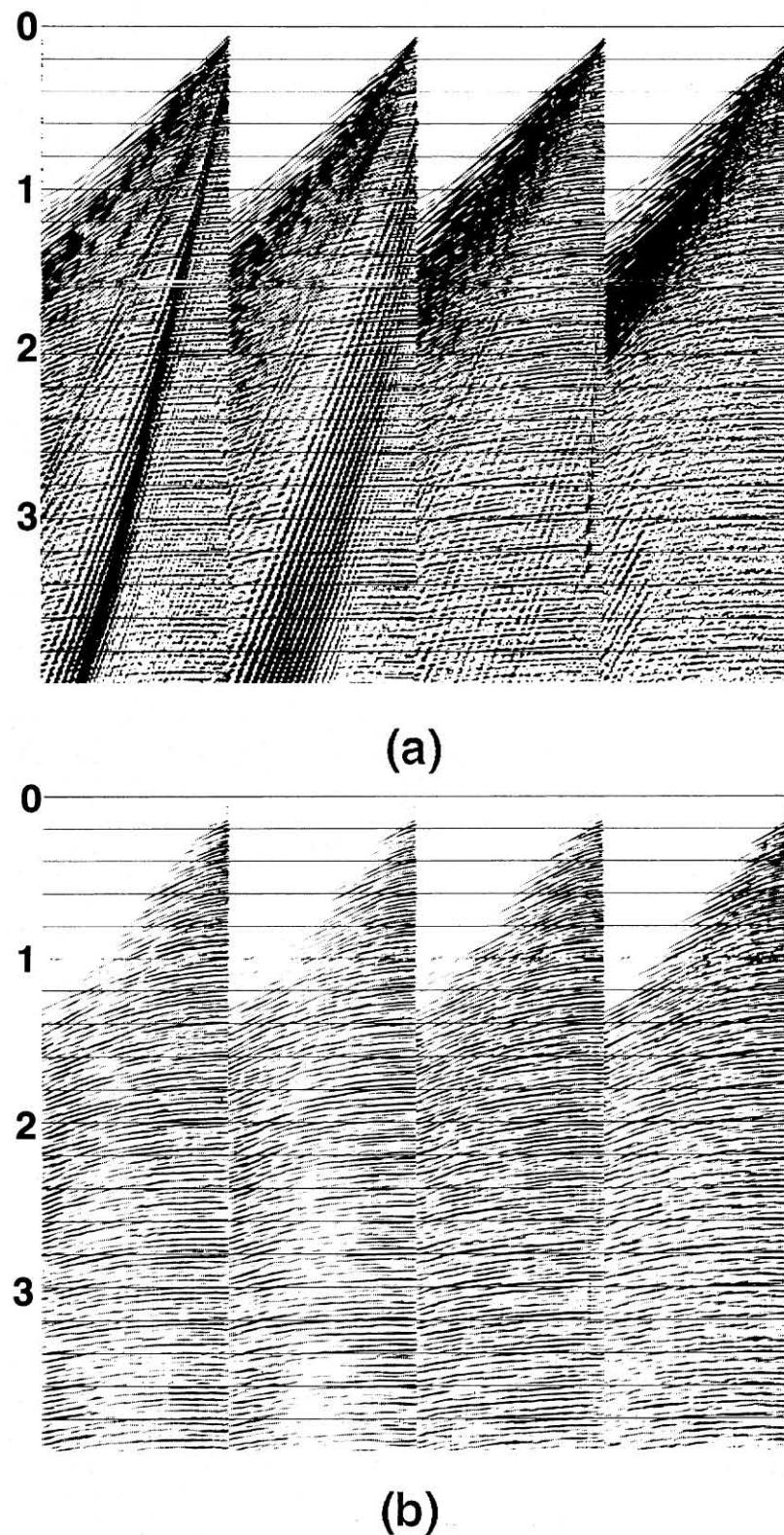


FIG. 6.2-5. Four shallow marine records (a) before and (b) after $f - k$ dip filtering to remove coherent linear noise. The coherent noise seen in these records is primarily of the guided wave type. (Data courtesy Deminex Petroleum.)

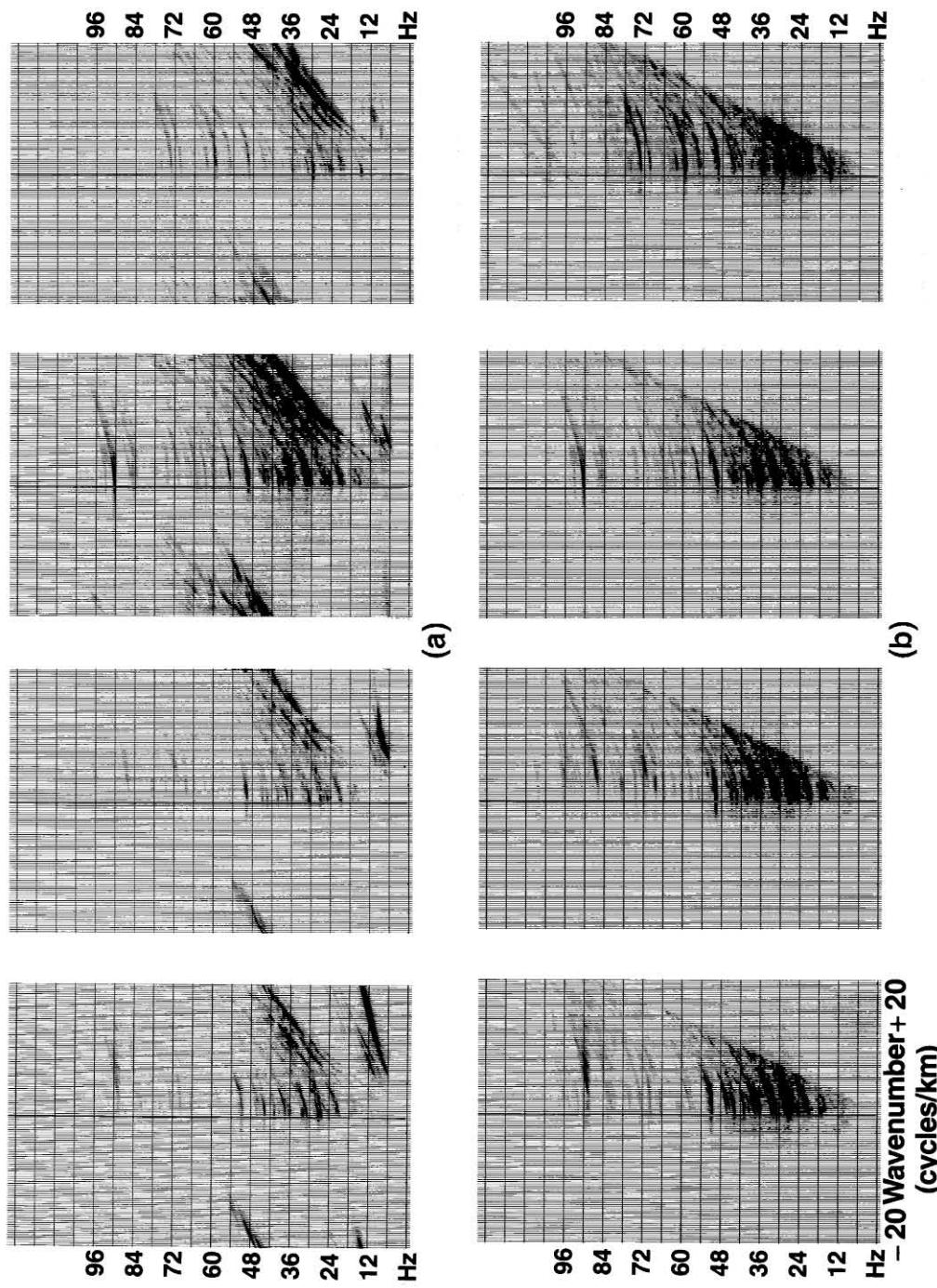


FIG. 6.2-6. The $f - k$ spectra of the shot gathers in Figure 6.2-5 (a) before and (b) after $f - k$ dip filtering.

The resulting stack is shown in Figure 6.2-9d. Compare this with stacked sections in Figures 6.2-9b,c. If $f - k$ filtering were done on only the shot gathers, then a good portion of coherent noise may remain in the data. Although this remaining noise may be attenuated by a second pass of $f - k$ filtering on receiver gathers, enhanced smearing of the data can degrade reflector definition.

Frequency-Wavenumber Multiple Attenuation

Figure 6.2-11a shows the synthetic CMP gather from Figure 6.1-9c and its 2-D amplitude spectrum. The primary and multiple energy can be separated into two different quadrants in the $f - k$ plane. This is achieved by NMO correcting the gather using a velocity function (labeled as VB in Figure 6.1-9d) that is between the

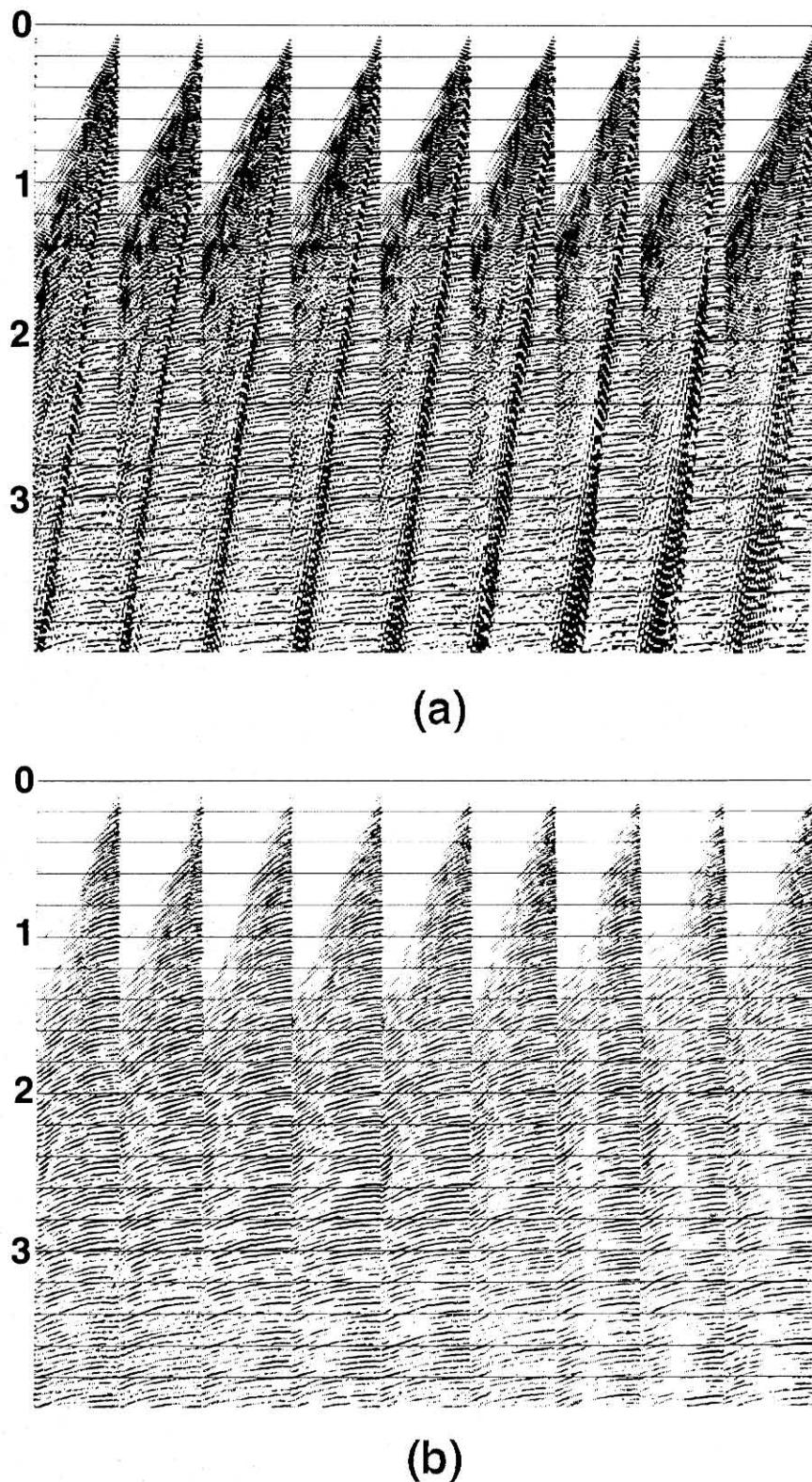


FIG. 6.2-7. The CMP gathers from a shallow marine survey (a) before and (b) after $f - k$ dip filtering implemented in the shot-gather domain to remove coherent linear noise. (These are the same data as in Figure 6.2-5.) (Data courtesy Deminex Petroleum.)

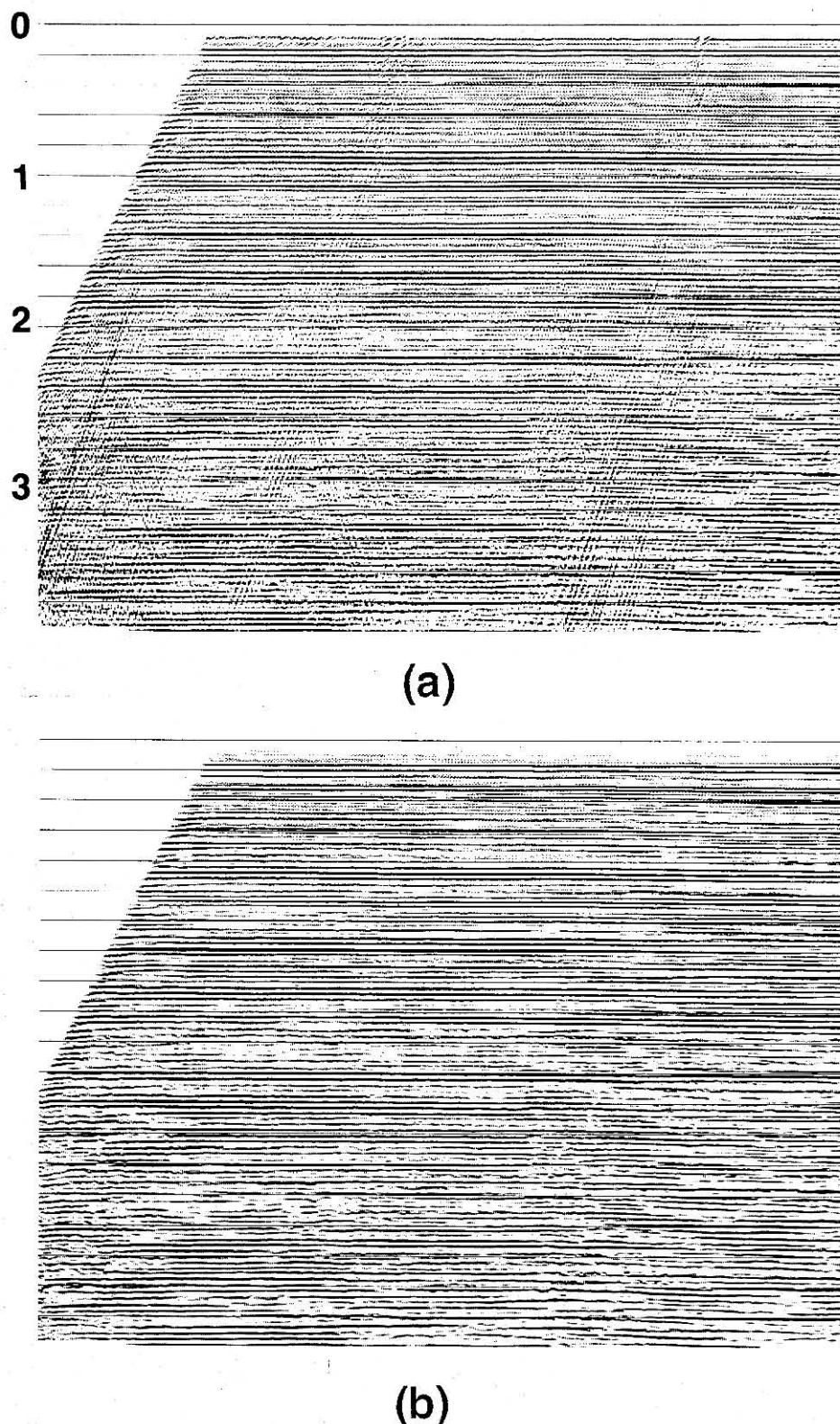


FIG. 6.2-8. (a) CMP stack with some coherent linear noise; and (b) $f - k$ dip filtering before stack. Selected CMP gathers are shown in Figure 6.2-7. (Data courtesy Deminex Petroleum.)

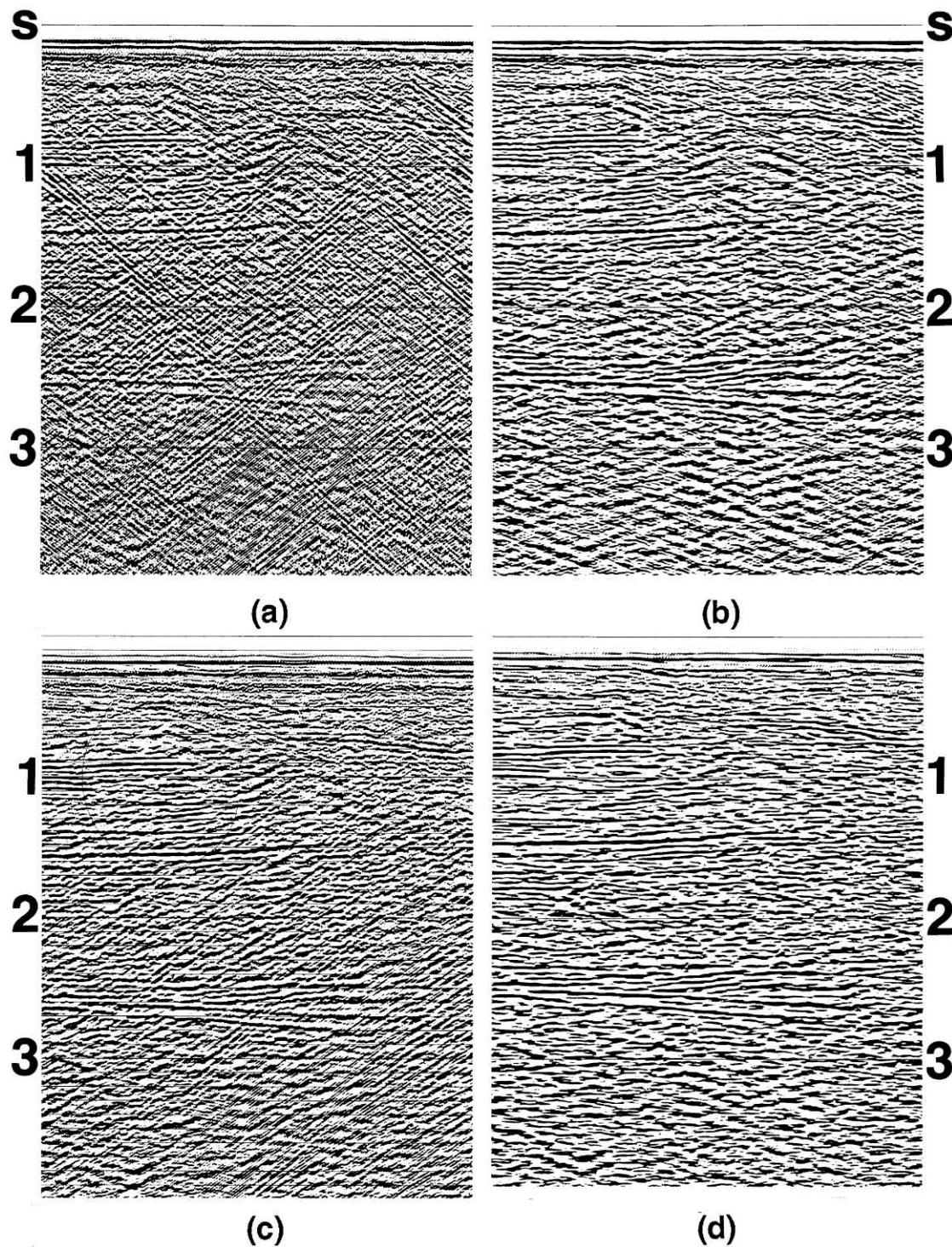


FIG. 6.2-9. (a) CMP stack contaminated by coherent noise. Associated common-shot and CMP gathers are shown in Figure 6.0-1. (b) The same CMP stack $f - k$ filtered after stack. (c) CMP stack $f - k$ filtered before stack. (d) CMP stack $f - k$ filtered twice before stack — first, in common-shot domain, second, in common-receiver domain. (Data courtesy Taylor Woodrow Energy Ltd.)

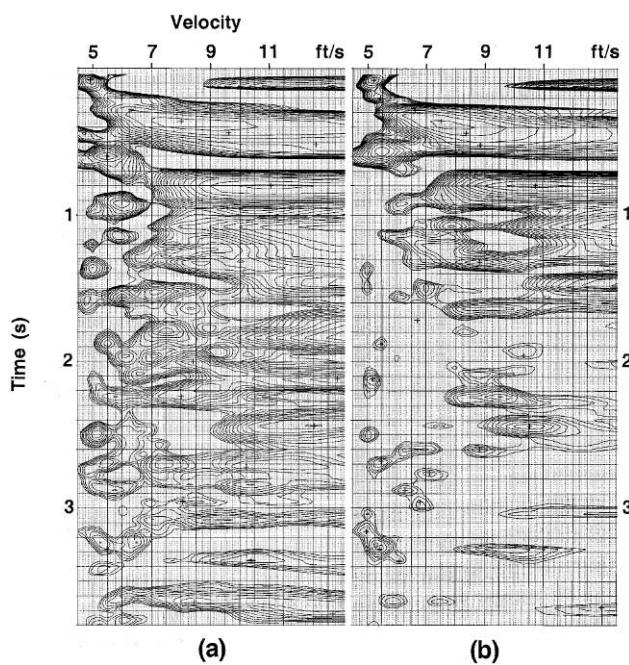


FIG. 6.2-10. Velocity spectrum associated with the data in Figure 6.0-1b (a) without and (b) with $f - k$ dip filtering.

primary and multiple velocities. The resulting NMO-corrected gather and its 2-D amplitude spectrum are shown in Figure 6.2-11b. The multiples are undercorrected, while the primaries are overcorrected. In the $f - k$ domain, the multiples and primaries for the most part map onto two different quadrants (labeled as P for primaries and M for multiples). The exception to this separation is the near-offset energy (both primary and multiple), which almost entirely maps along the frequency axis. This occurs because multiples and primaries have no significant moveout difference at near offsets. Aliased energy (such as A) is wrapped around and mapped to the wrong quadrant. (Spatial aliasing is discussed in detail in Section 1.2.)

Multiples can be attenuated by zeroing the quadrant corresponding to multiple energy in the $f - k$ domain (Figure 6.2-11c) (Ryu, 1980; Sengbush, 1983). However, note that spatially aliased multiple energy remains in the gather (labeled as A in Figure 6.12-11c). As shown in Figure 6.2-11d, besides zeroing out the multiple quadrant, a reject zone labeled as R can be imposed on the primary quadrant. The $f - k$ filtered CMP gather (Figure 6.2-11d) now also is free of the aliased energy (compare with Figure 6.2-11c). Inverse NMO correction (Figure 6.2-11e) using the same intermediate velocity function VB (Figure 6.1-9d) restores the original moveout of the primaries. Following this procedure, apply NMO correction using the primary velocity function VP (Figure 6.1-9d) as shown in Figure 6.2-11f.

The stacked trace of this gather displayed repeatedly exhibits very little multiple energy (Figure 6.2-11g).

The sequence for $f - k$ filtering of multiple attenuation is as follows:

- (a) Apply moveout correction to CMP gathers using a velocity function v_b such that $v_m < v_b < v_p$, where v_m and v_p are velocity functions associated with multiples and primaries, respectively.
- (b) Apply 2-F Fourier transform.
- (c) Zero the quadrant associated with the multiples and, if required, the zone that contains the energy associated with the aliased multiples within the primaries quadrant.
- (d) Apply inverse 2-D Fourier transform.
- (e) Apply inverse moveout correction using the velocity function v_b as in step (a).
- (f) Perform velocity analysis to update the picks for primary velocity functions.

Now consider the field data example shown in Figure 6.2-12. The moveout difference between the primaries and multiples is apparent in the CMP gathers (Figure 6.1-8a). To the left of the primary velocity function labeled as VP in Figure 6.1-8b, all peaks are associated with water-bottom and peg-leg multiples. Apply moveout correction using a velocity function VB that lies between the primary and multiple velocities. As a result, the multiples are undercorrected and the primaries are overcorrected as shown in Figure 6.2-12a. Now consider the moveout of primaries and multiples in the $f - k$ domain. The primary and multiple indicated in Figure 6.1-8a map to the same quadrant (say positive quadrant) in the $f - k$ domain before moveout correction. The same events after moveout correction using an intermediate velocity map into two different quadrants; in particular, the multiple maps into the positive quadrant and the primary maps into the negative quadrant. Thus, by zeroing one quadrant in which the multiples are clustered, the primaries can be enhanced.

A CMP gather and the associated velocity spectrum following $f - k$ multiple attenuation are shown in Figure 6.2-12b. When compared with Figure 6.1-8b, Figure 6.2-12b shows that the energy in the multiples region in the velocity spectrum was attenuated, while the primary velocity trend was enhanced. Finally, Figure 6.2-12c shows selected CMP gathers after moveout correction using the primary velocities picked from the velocity spectrum in Figure 6.2-12b. Stacking of these gathers yields the section in Figure 6.2-12d. This section should be compared with Figures 6.1-8d.

(text continues on p. 920)

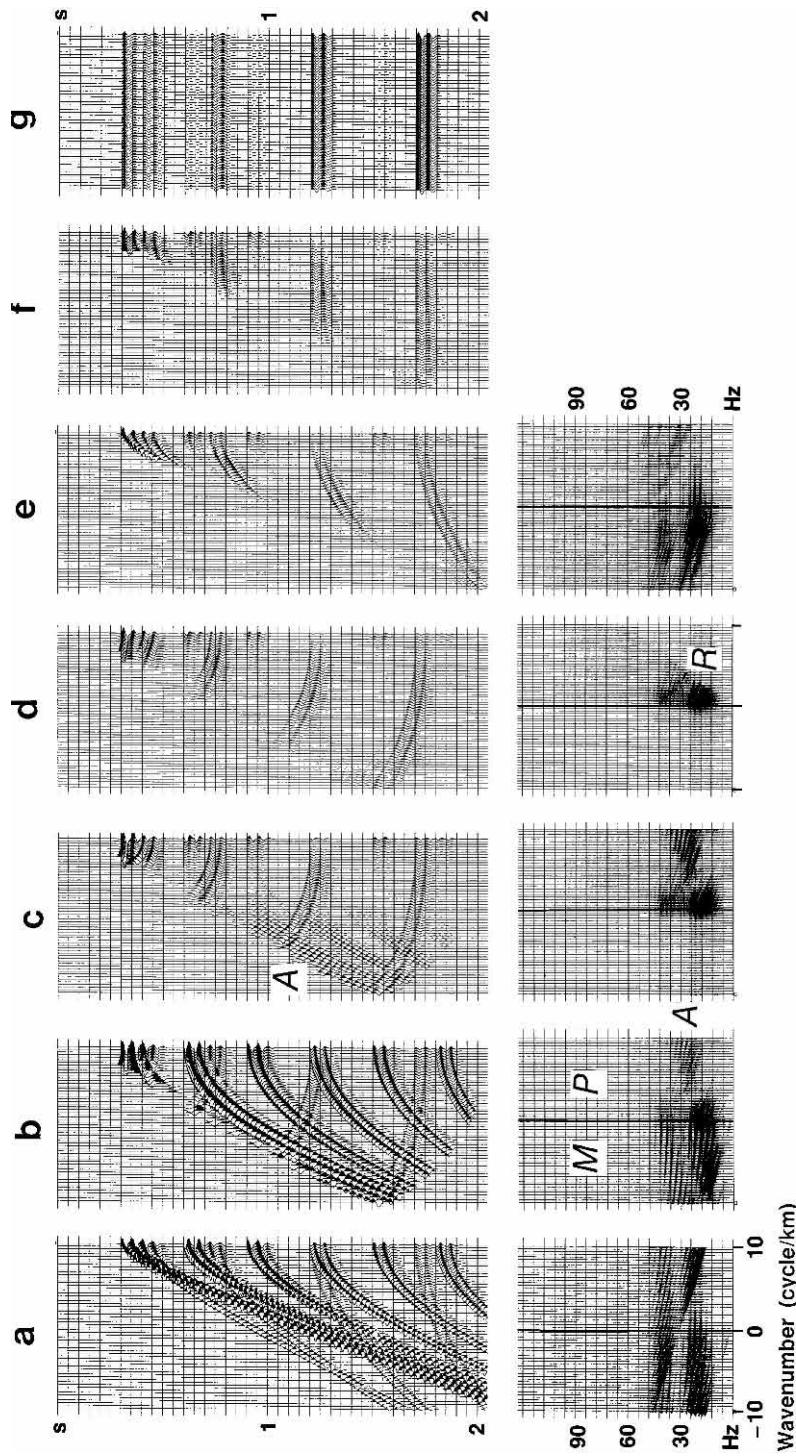


FIG. 6.2-11. (a) The synthetic CMP gather same as in Figure 6.1-9c; (b) after NMO correction using a velocity function (labeled as VB in Figure 6.1-9d) between the multiple and primary trend; (c) the result of zeroing the $f - k$ quadrant associated with multiples; (d) the same as (c), except that in addition to zeroing the left quadrant, a portion of the right quadrant in the $f - k$ spectrum (denoted by R) also is zeroed to suppress aliased energy; (e) the result of applying inverse NMO correction to (a) using the velocity function labeled as VB in Figure 6.1-9d; (f) the result of applying NMO correction to (e) using the primary velocity function labeled as VP in Figure 6.1-9d; (g) stack of (c) repeated to emphasize the strong events. The bottom panels show the corresponding $f - k$ spectra.

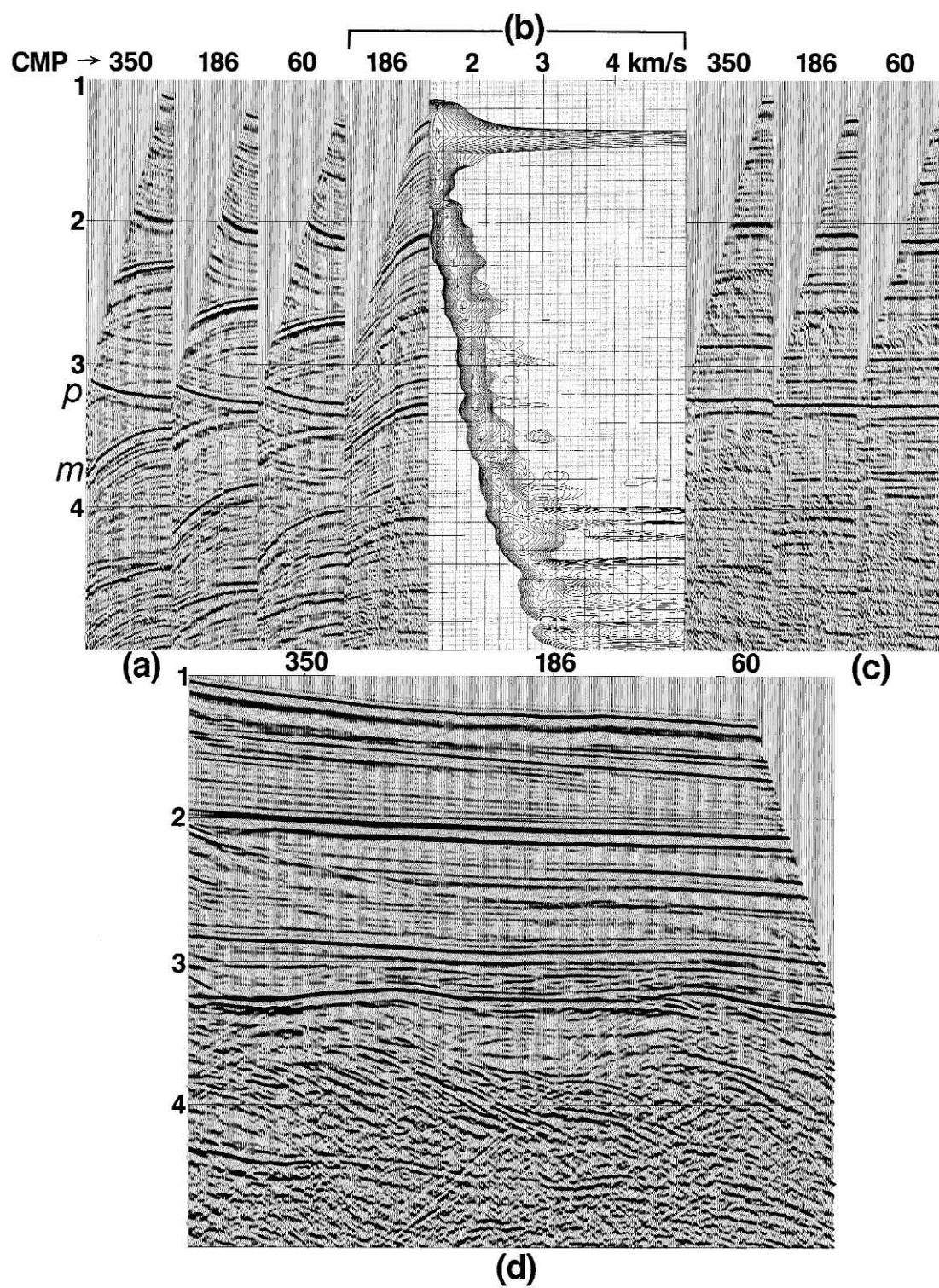


FIG. 6.2-12. (a) The CMP gathers in Figure 6.1-8a after NMO correction using a velocity function (labeled as VB in Figure 6.1-8b) between the primary and multiple velocities; (b) velocity spectrum at CMP 186 estimated from the $f - k$ dip-filtered gather shown to the left of the spectrum. Compare this with Figure 6.1-8b. (c) The same CMP gathers as in (a) after $f - k$ multiple attenuation followed by NMO correction using the primary velocities derived from velocity spectrum (b). (d) The CMP stack derived from the CMP gathers as in (c) after $f - k$ multiple attenuation.

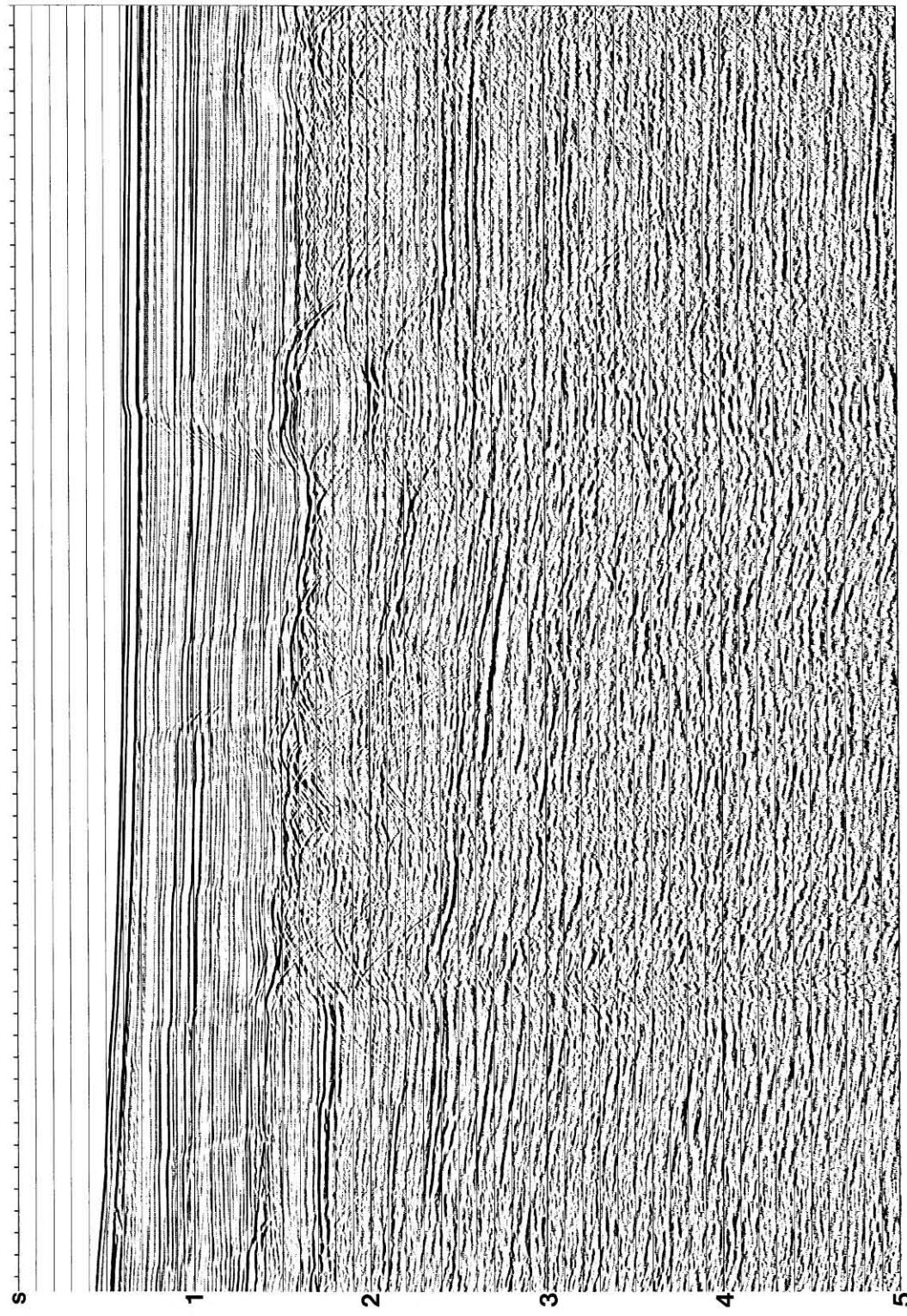


FIG. 6.2-13. A CMP stack with no multiple attenuation, including pre- and poststack deconvolution.

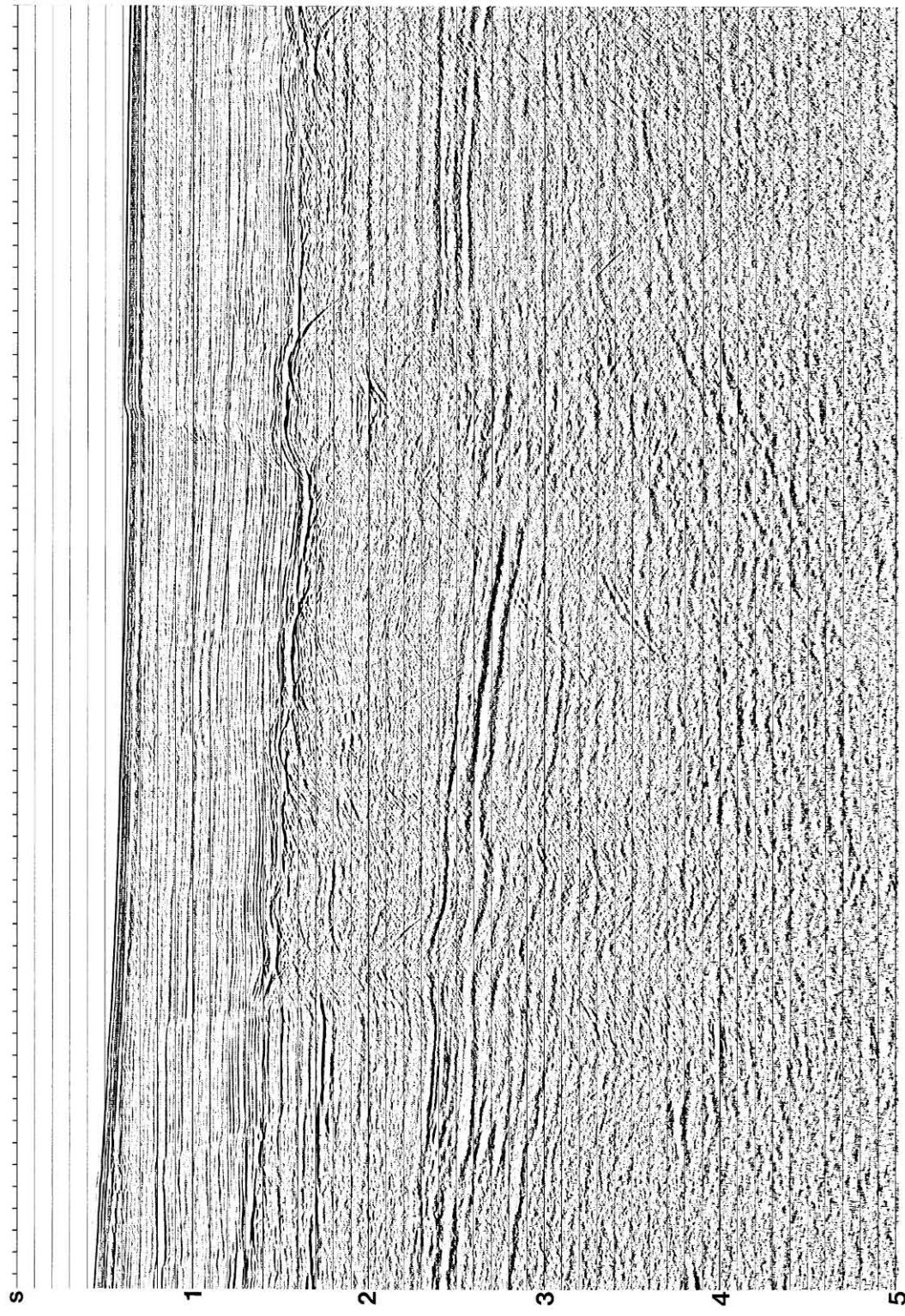


FIG. 6.2-14. The CMP stack as in Figure 6.2-13 with prestack deconvolution, $f - k$ filtering for multiple attenuation, and poststack deconvolution.

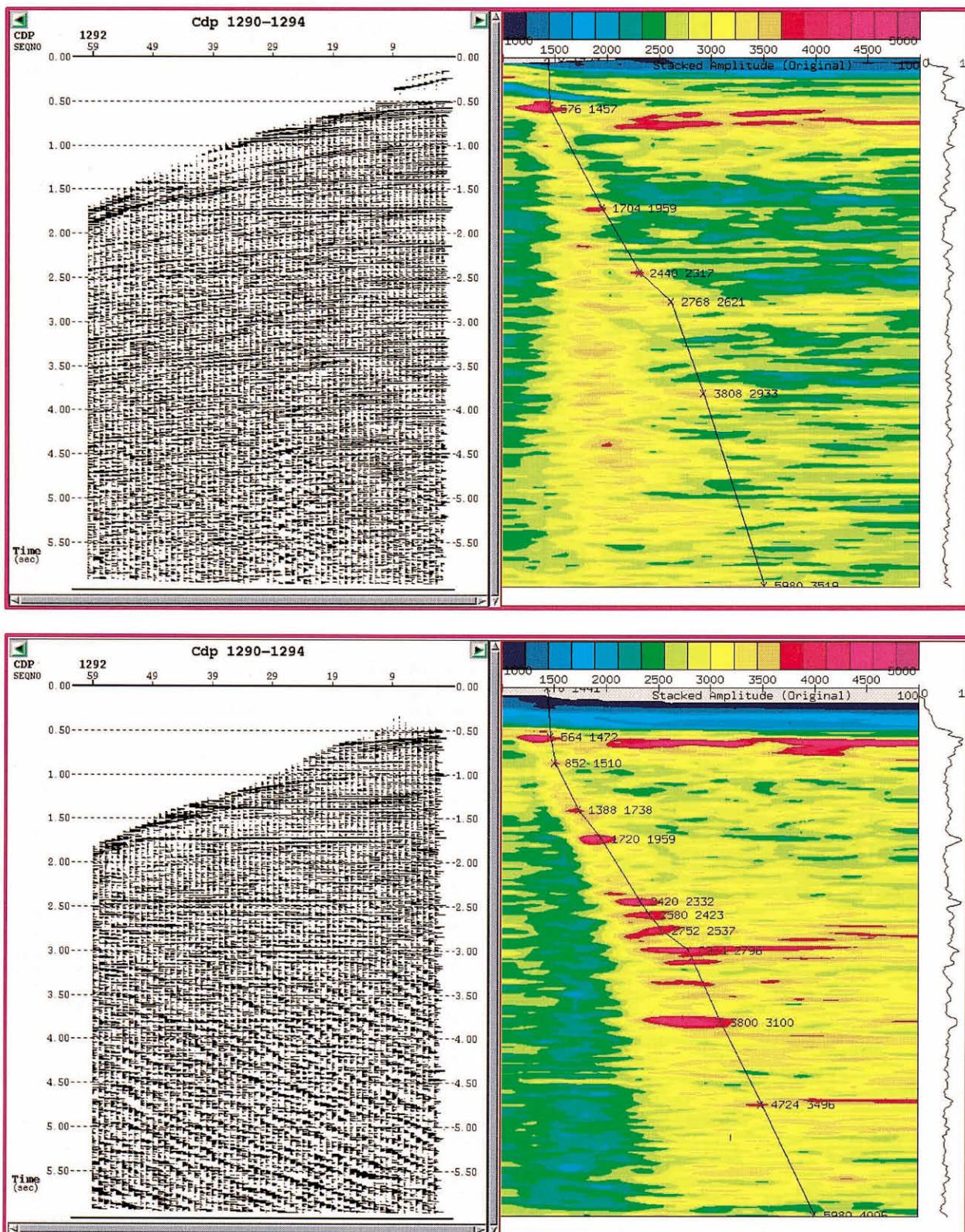


FIG. 6.2-15. An NMO-corrected CMP gather (left column) and the corresponding velocity spectrum (right column) associated with: (top row) the stacked data shown in Figure 6.2-13, and (bottom row) the stacked data shown in Figure 6.2-14.

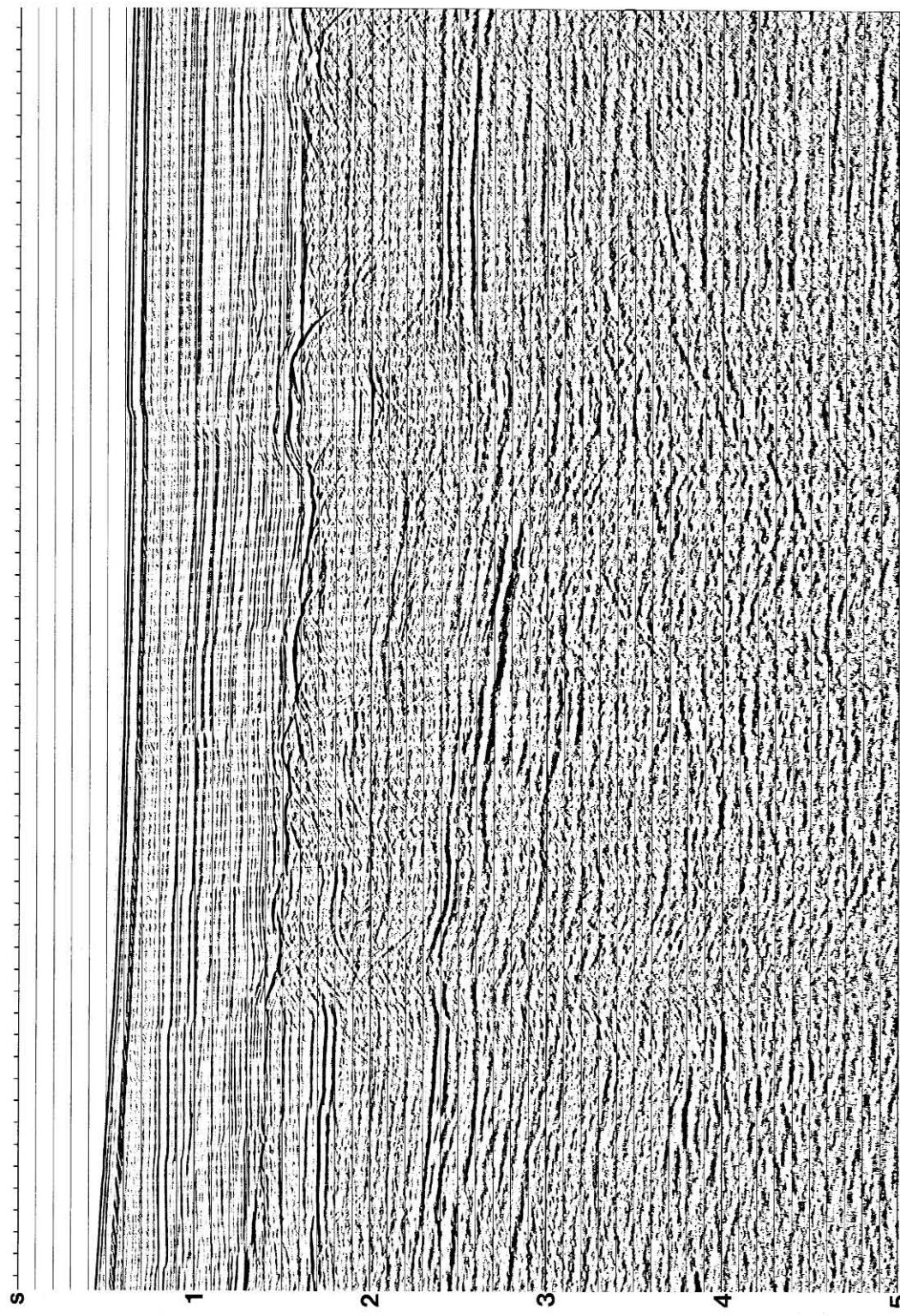


FIG. 6.2-16. The CMP stack as in Figure 6.2-13 with prestack deconvolution.

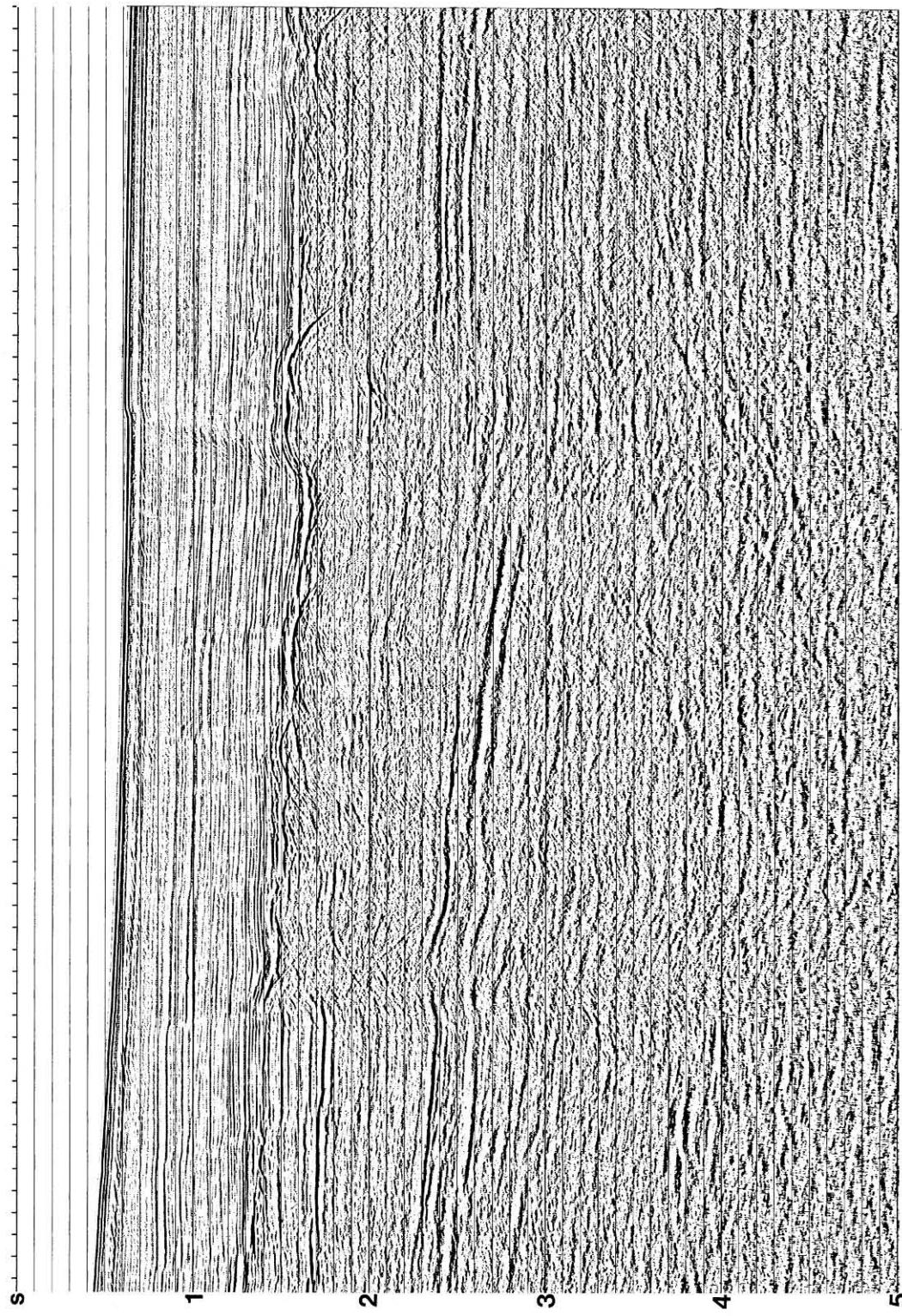


FIG. 6.2-17. The CMP stack as in Figure 6.2-13 with pre- and poststack deconvolution.

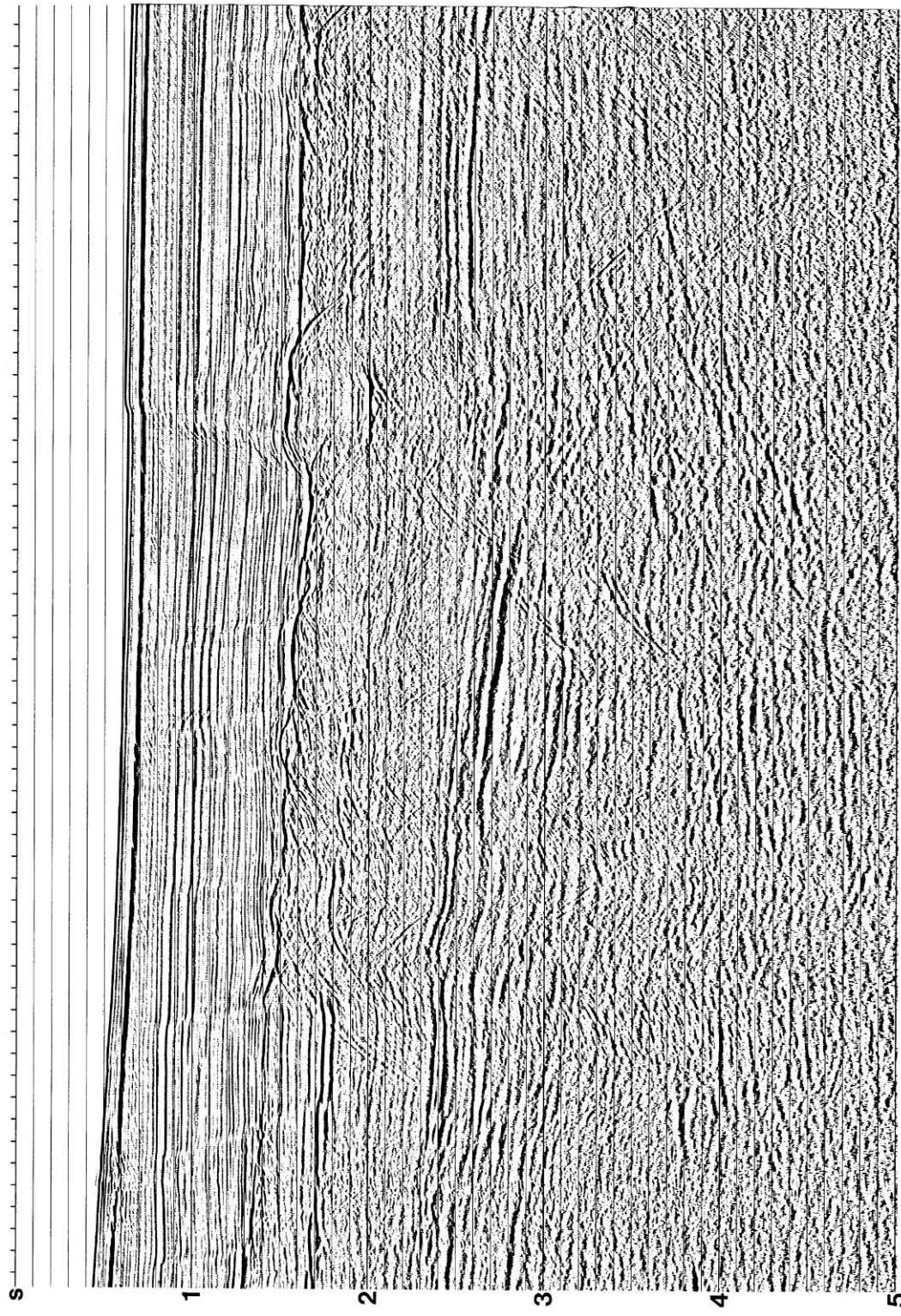


FIG. 6.2-18. The CMP stack as in Figure 6.2-13 with prestack deconvolution and $f - k$ filtering for multiple attenuation.

In practice, there are variations in selecting the velocity function used to apply moveout correction prior to $f - k$ filtering. An alternative strategy is to apply NMO correction using the multiple velocity, then zero the energy along the frequency axis in addition to that in the multiple quadrant of the $f - k$ spectrum. Another strategy is to apply NMO correction using primary velocities and place a tight pass-zone around the frequency axis. Finally, note that the $f - k$ method of velocity discrimination is one type of $f - k$ filtering. Thus, we must deal with the same practical issues discussed in Section 1.2 — in particular, wraparound, spatial aliasing, and tapering over the boundary between the pass and reject zones.

Multiples are best attenuated when a combination of two methods based on periodicity of multiples and velocity discrimination between primaries and multiples are used. Figure 6.2-13 shows a CMP-stacked section with no attempt made to attenuate the multiples. Specifically, the processing sequence did not include deconvolution nor $f - k$ filtering. Note the abundance of peg-leg multiples associated with the strong reflections; these multiples dominate the section below 2 s.

By combining prestack deconvolution with $f - k$ filtering followed by poststack deconvolution, as demonstrated in Figure 6.2-14, multiples in Figure 6.2-13 are largely attenuated despite the complicated nature of the reflectors that originate the peg-legs. The class of multiples present in the stacked section of Figure 6.2-13 is clearly identified in the corresponding velocity spectrum shown in Figure 6.2-15. Note that much of the energy associated with the multiples is absent in the velocity spectrum shown in Figure 6.2-15 corresponding to the stacked section in Figure 6.2-14. Compare the velocity spectra in Figure 6.2-15 computed from the CMP gather without and with multiple attenuation and note that, following multiple attenuation, the energy of the primaries has been enhanced relative to that of the multiples.

Prestack deconvolution alone has limited effect in attenuating multiples (Figure 6.2-16). When combined with poststack deconvolution, however, it often is successful in attenuating a large class of multiples (Figure 6.2-17). The key to effective multiple attenuation by predictive deconvolution is to be generous with the operator length. As for the example shown in Figure 6.2-17, an operator length as long as 480 ms may need to be considered.

A combination of prestack deconvolution and $f - k$ filtering for multiple attenuation yields the section shown in Figure 6.2-18. Compare with Figure 6.2-17 and note the more effective multiple attenuation by combining deconvolution with $f - k$ filtering. The addition of poststack deconvolution to the sequence that includes

prestack deconvolution and $f - k$ filtering yields the most favorable result within the context of multiple attenuation (Figure 6.2-14).

6.3 THE SLANT-STACK TRANSFORM

In Section 1.2, we learned that the 2-D Fourier transform is one way to decompose a wavefield into its plane-wave components, each with a unique frequency and each traveling at a unique angle from the vertical direction. In this section, we shall discuss the domain of ray parameter and present another way to decompose the wavefield into its plane-wave components.

Plane-wave decomposition of a wavefield, such as a common-shot gather, can be achieved by applying linear moveout and summing amplitudes over the offset axis. This procedure is called *slant stacking*. An underlying assumption of slant stacking is that of a horizontally layered earth model. Conventional processing is done primarily in midpoint-offset coordinates. Slant stacking replaces the offset axis with the ray parameter p axis. The ray parameter is the inverse of the horizontal phase velocity. A group of traces with a range of p values is called a slant-stack gather.

Several processing techniques have been devised, with varying degrees of success, in midpoint-ray-parameter coordinates. Examples include trace interpolation, multiple attenuation, time-variant dip filtering, refraction inversion, velocity analysis, migration before stack, and deconvolution. Taner (1977) was the first to introduce the midpoint-ray-parameter coordinates. He discussed the interpretive use of plane-wave stacks, where several constant p sections are superimposed over a restricted range of p values to enhance dipping events. Other processing methods were investigated later, such as migration (Ottolini, 1982) and velocity analysis (Schultz and Claerbout, 1978; Diebold and Stoffa, 1981; and Gonzalez-Serrano, 1982). Alam and Lasocki (1981) and Alam and Austin (1981) discussed possible applications in trace interpolation and multiple attenuation, respectively. McMechan and Yedlin (1981) devised a method to obtain phase velocity curves for dispersive waves using slant-stack transformation (Section F.1). Clayton and McMechan (1981) devised a method to invert a refracted wavefield, which involves downward continuation in the slant-stack domain (Section F.2). Based on downward continuation of a slant-stack gather, Schultz (1982) developed a technique to estimate interval velocities.

Physical Aspects of Slant Stacking

We now examine the physical aspects of constructing a slant-stack gather. Each trace in this gather represents

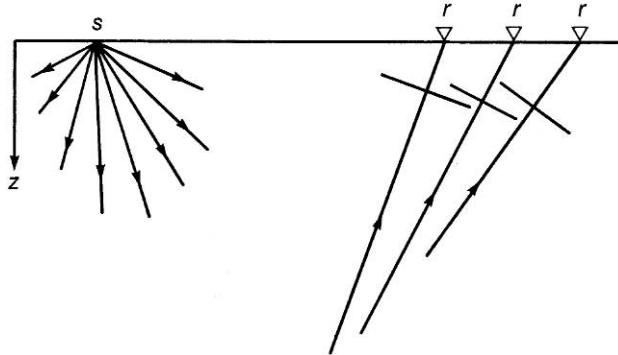


FIG. 6.3-1. A seismic source generates waves that propagate in all directions; waves traveling in different directions are recorded at different receiver locations.

a plane wave that propagates at a certain angle from vertical. In reality, when a dynamite source explodes, the energy propagates at all angles (Figure 6.3-1). The reflected energy arrives at different receiver groups at different angles because of the offset between source and receiver locations. The farther the offset or the shallower the reflecting interface, the more oblique the angle of the upcoming wavefront.

As an aid in defining a scheme for constructing slant-stack gathers, first consider how plane waves can be generated. Imagine a line of point sources as shown in Figure 6.3-2. Assume that this line of sources is activated so that all points on the line are excited simultaneously, and each point generates a spherical wavefield. Some distance from the surface, the spherical wavefronts superimpose and result in a plane wave that travels vertically downward. This plane wave reflects from an interface and is recorded by a receiver at the surface. (Actually, there are source types, such as Geoflex and Primacord, which approximate short line sources.)

Instead of a vertically traveling plane wave, a plane wave that travels at a desired angle from vertical can be generated using the same line of point sources as illustrated in Figure 6.3-3. To do this, the point sources must be activated in succession starting at one end of

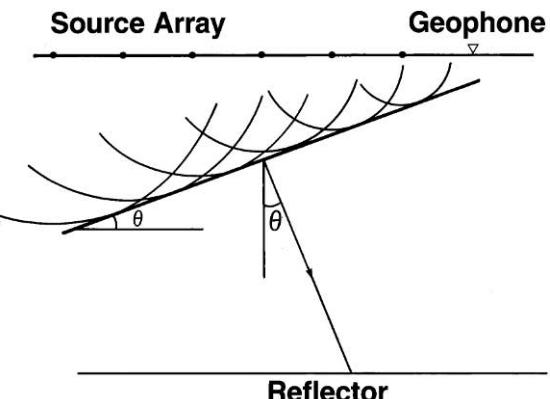


FIG. 6.3-3. A plane wave that travels at angle θ from vertical is generated by setting off many shots (starting from left) at appropriate time intervals.

the line with an equal time delay between them. When a particular point source is activated, the wavefront generated from the previous source location already will have traveled a certain distance into the earth. When all the spherical wavefronts generated by the various sources superimpose, the result is a tilted plane wavefront. This plane wave then propagates, reflects from an interface, and is recorded by a receiver at the surface.

The amount of tilt of the wavefront, defined by the angle of propagation of the plane wave, can be controlled. Consider the raypath-wavefront geometry in Figure 6.3-4. By the time the wavefront generated at source location S_1 reaches point A in the subsurface, the point source at location S_2 should be excited so that the desired angle is attained. Define the distance between S_1 and S_2 as Δx , and the medium velocity with which the waves travel as v . If it takes Δt time for the wavefront to go from S_1 to A , using the triangle S_1AS_2 , then the dip angle θ of the plane wave is given by

$$\sin \theta = \frac{v\Delta t}{\Delta x}. \quad (6-1)$$

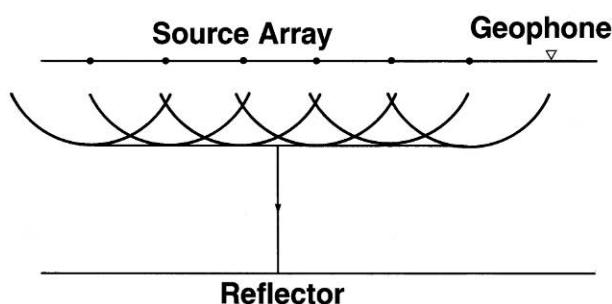


FIG. 6.3-2. A vertically incident plane wave is generated by setting off many shots in unison.

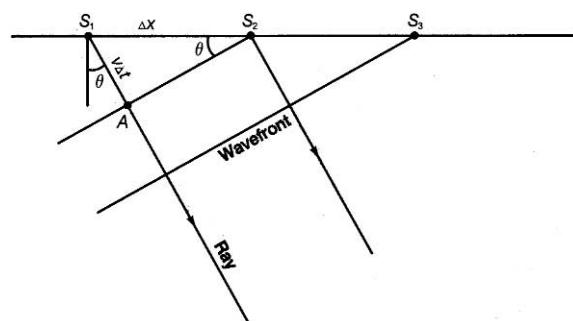


FIG. 6.3-4. Computation of time interval between shots (S) to generate the oblique plane wave in Figure 6.3-3.

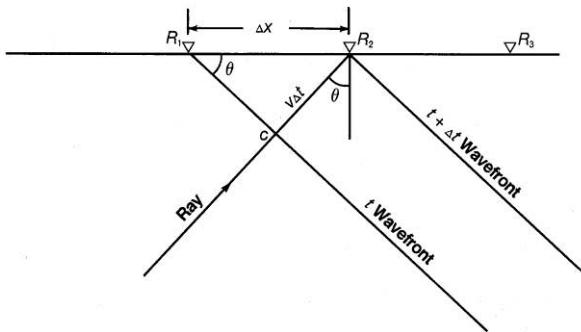


FIG. 6.3-5. The reciprocity principle applied to the geometry of Figure 6.3-4 to replace shots (S) with receivers (R).

The active source location must therefore travel with speed given by

$$\frac{\Delta x}{\Delta t} = \frac{v}{\sin \theta} \quad (6-2)$$

along the horizontal direction, and the point source at location S_2 must be excited so that we can catch the wavefront at S_1 as it reaches point A on the wavefront in the subsurface. The velocity $(v/\sin \theta)$ with which the source location must move is called the *horizontal phase velocity*.

From the experiments illustrated by Figures 6.3-2 and 6.3-3, note that a plane wave propagating at an angle from the vertical can be generated by:

- (1) Placing a line of point sources at the earth's surface.
- (2) Exciting the point sources in succession with a time delay.
- (3) Superimposing the responses that are in the form of spherical wavefronts.

The superimposed response is recorded on a single receiver (Figure 6.3-3). This response is in the form of a plane wave that is reflected from an interface. Superposition means summing over the shot axis for a given receiver location. Using the reciprocity principle, summation also can be performed over the receiver axis for a given shot location.

We just discussed how a common-shot gather as a single wavefield can be decomposed into its plane-wave components. By replacing the shot axis in Figure 6.3-4 with the receiver axis, the raypath geometry in Figure 6.3-5 results. The time delay associated with the plane wave that travels at angle θ from the vertical is given by

$$\Delta t = \frac{\sin \theta}{v} \Delta x. \quad (6-3a)$$

Snell's law says that the quantity $\sin \theta/v$, which is the inverse of the horizontal phase velocity, is constant

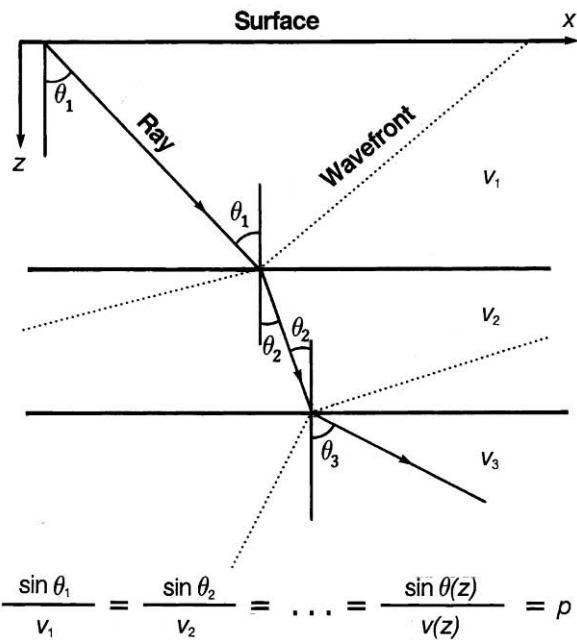


FIG. 6.3-6. If the ray parameter p is specified, then the ray can be traced in a horizontally layered earth model with a known velocity function $v(z)$.

along a raypath in a layered medium (Figure 6.3-6). This constant is called the ray parameter p . Equation (6-3a) then is rewritten as

$$\Delta t = p \Delta x. \quad (6-3b)$$

The angle of propagation of the plane wave is controlled by adjusting the p value. If the ray parameter p is specified, then the ray can be traced in a horizontally layered earth model with a known velocity function $v(z)$. Setting $p = 0$ corresponds to a plane wave that travels vertically.

Given the ray parameter p and the velocity function $v(z)$ for the layered earth, the family of raypaths associated with a particular p value can be traced as shown in Figure 6.3-7. A plane wave that travels in a layered earth is called a *Snell wave* (Claerbout, 1978). This type of plane wave changes its direction of propagation at each layer boundary according to Snell's law (Figure 6.3-6). For a single p value, note that the signal is recorded at many offsets (Figure 6.3-7).

In general, receivers at all offsets record plane waves of many p values. To decompose a shot gather into its plane-wave components, all the trace amplitudes in the gather must be summed along several slanted paths, each with a unique time delay defined by equation (6-3b).

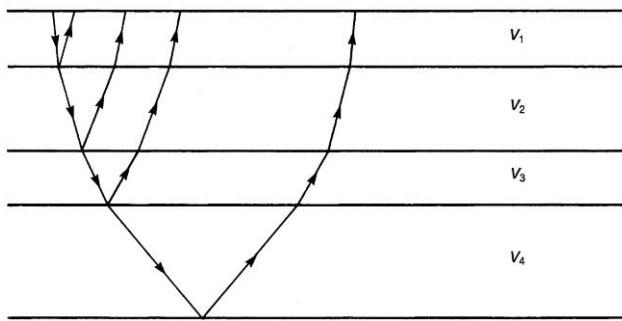


FIG. 6.3-7. Some raypaths for a given p value, corresponding to a single trace in the $\tau - p$ domain.

As long as there is no dip, the traveltimes in a common-shot and a common-midpoint gather are indistinguishable. Since a CMP gather is not a single wavefield, plane-wave decomposition would not seem to apply to CMP gathers. However, the equivalence of CMP gathers and common shot gathers in a horizontally layered earth provides a rationale for applying plane-wave decomposition to both types of gathers.

Slant-Stack Transformation

Two steps typically are used in synthesizing plane waves by summing amplitudes in the offset domain along slanted paths (Figure 6.3-8). First, a linear moveout (LMO) correction is applied to the data through a coordinate transformation defined by (Claerbout, 1978)

$$\tau = t - px, \quad (6-4a)$$

where p is the ray parameter, x is the offset, t is the two-way traveltime, and τ is the intercept time at $p = 0$. Next, the data are summed over the offset axis by

$$S(p, \tau) = \sum_x P(x, \tau + px), \quad (6-4b)$$

where, $S(p, \tau)$ represents a plane wave with ray parameter $p = \sin \theta/v$. By repeating the LMO correction for a range of p values and performing the summation in equation (6-4b), a complete slant-stack gather is constructed. A slant-stack gather, in practice, alternatively is referred to as a $\tau - p$ gather; it consists of all the dip components within the specified range of p values in the original offset data.

The mapping from the $t - x$ domain to the $\tau - p$ domain is reversible (Thorson, 1978). First, apply inverse linear moveout (LMO) correction to the data in the $\tau - p$ domain by

$$t = \tau + px. \quad (6-5a)$$

$P(x, t) : \text{input data}$



$\tau = t - px : \text{Linear Moveout}$

p

$$S(p, \tau) = \sum_x P(x, t = \tau + px)$$



slant-stack gather

FIG. 6.3-8. Construction of slant-stack gathers.

Then, sum the data in the $\tau - p$ domain over the ray parameter p axis to obtain

$$P(x, t) = \sum_p S(p, t - px). \quad (6-5b)$$

To restore amplitudes properly, *rho filtering* is applied before inverse mapping. This is accomplished by multiplying the amplitude spectrum of each slant-stack trace by the absolute value of the frequency. Rho filtering is equivalent to differentiating the wavefield before the summation that is involved in the integral formulation of migration (Section 4.1).

There is a distinction between slant stack and the exact plane-wave decomposition of a wavefield. Treitel et al. (1982) mathematically analyzed the plane-wave decomposition process and distinguished between conventional slant stack described here and what may be called the proper slant stack. A conventional slant stack yields an exact plane-wave decomposition when we deal with line sources; a proper slant stack yields an exact plane-wave decomposition when we deal with point sources. A proper slant stack is generated using the same steps that we just described for a conventional slant stack except that a convolution of the LMO-applied wavefield by a filter operator is performed before summation. This operator corrects for 3-D effects by converting a wavefield that was obtained from a point source into a wavefield that was obtained from a line source. As far as kinematics is concerned, the two types of slant stacking are equivalent. They differ only in treatment of amplitudes (Treitel, personal communication).

A schematic description of the plane-wave mapping given by equations (6-4a,b) is shown in Figure 6.3-9. We

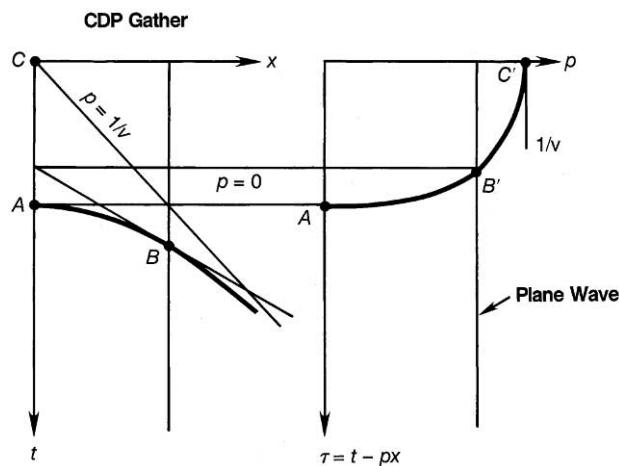


FIG. 6.3-9. A hyperbola in a CMP gather maps onto an ellipse in the $\tau - p$ domain.

start by summing amplitudes in the offset domain along the horizontal path $p = 0$. This line intersects the reflection hyperbola in the vicinity of apex A . Thus, point A maps onto point A' on the $\tau - p$ plane, corresponding to the trace with $p = 0$. By tilting the line of summation, the hyperbola is intersected at location B , which maps onto B' . Note that a major contribution to summation along the slanted path comes in the area of the tangential point B . This zone of tangency is called the Fresnel zone.

The Fresnel zone gets broader for higher velocities and deeper events. In fact, the summation over the offset axis after linear moveout correction can be confined to the Fresnel zone. The steepest necessary path of summation is along $p = 1/v$, which is the asymptote to the hyperbola. This path corresponds to rays that are 90 degrees to the vertical. The energy along the asymptote maps to C' on the p -axis. By using the mapping described previously — linear moveout correction followed by summation over the offset axis for a range of p -values (equations 6-4a,b), the hyperbolic trajectories in the $t - x$ domain are mapped to elliptical trajectories in the $\tau - p$ domain. In reality, we never record a hyperbola with infinite extent nor a zero-offset trace. Therefore, the elliptical path in the $\tau - p$ domain never is complete from A' to C' .

Figure 6.3-10 illustrates the $\tau - p$ transform of more than one hyperbolic event in the $t - x$ domain. Subcritical reflections A and D (those with an angle of incidence smaller than the critical angle) map into the region of lower p -values, while supercritical reflections C (wide-angle reflections) map into the region of higher p values. Ideally, a linear event in the offset domain, such as a refraction arrival B , maps to a point in the slant-stack domain. Conversely, a linear event in the slant-stack domain maps to a point in the offset domain.

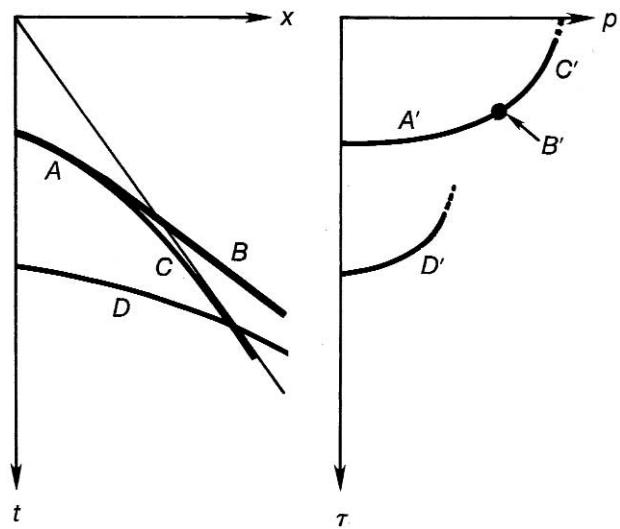


FIG. 6.3-10. Various arrivals on a CMP gather mapped onto the corresponding $\tau - p$ gather. Events A , B , C and D map onto A' , B' , C' and D' .

Figure 6.3-11 shows a shot gather that contains predominantly water-bottom and peg-leg multiples. The horizontal axis in the $\tau - p$ domain, in this example, is horizontal phase velocity $1/p$. Besides the water-bottom reflection W , there are two distinct primaries, P_1 and P_2 . Multiple reflections map along the elliptical trajectories that converge at $p = (1/1500)$ s/m, the inverse of the water velocity.

A shot gather containing linear events is shown in Figure 6.3-12. Note the strong amplitudes on the $\tau - p$ gather that correspond to the guided waves observed in the offset data. Again, the horizontal axis in the $\tau - p$ domain is horizontal phase velocity $1/p$. In both field data examples shown in Figures 6.3-11 and 6.3-12, the $\tau - p$ gathers were constructed using only positive p -values. Thus, the backscattered energy, for instance in the shot gather shown in Figure 6.3-12, is not represented in the $\tau - p$ gather.

Practical Aspects of Slant Stacking

First, we examine the interrelations between various domains used in seismic data processing. Consider a band-limited dipping event in the $t - x$ domain as shown in Figure 6.3-13. The offset range is from 250 to 5000 m with a trace spacing of 50 m. This event is mapped along a radial line AA' in the $f - k$ domain.

The slope of the radial line, ω/k_x is related to the horizontal phase velocity $v/\sin\theta$ by the relationship

$$\frac{\omega}{k_x} = \frac{v}{\sin\theta}. \quad (6-6)$$

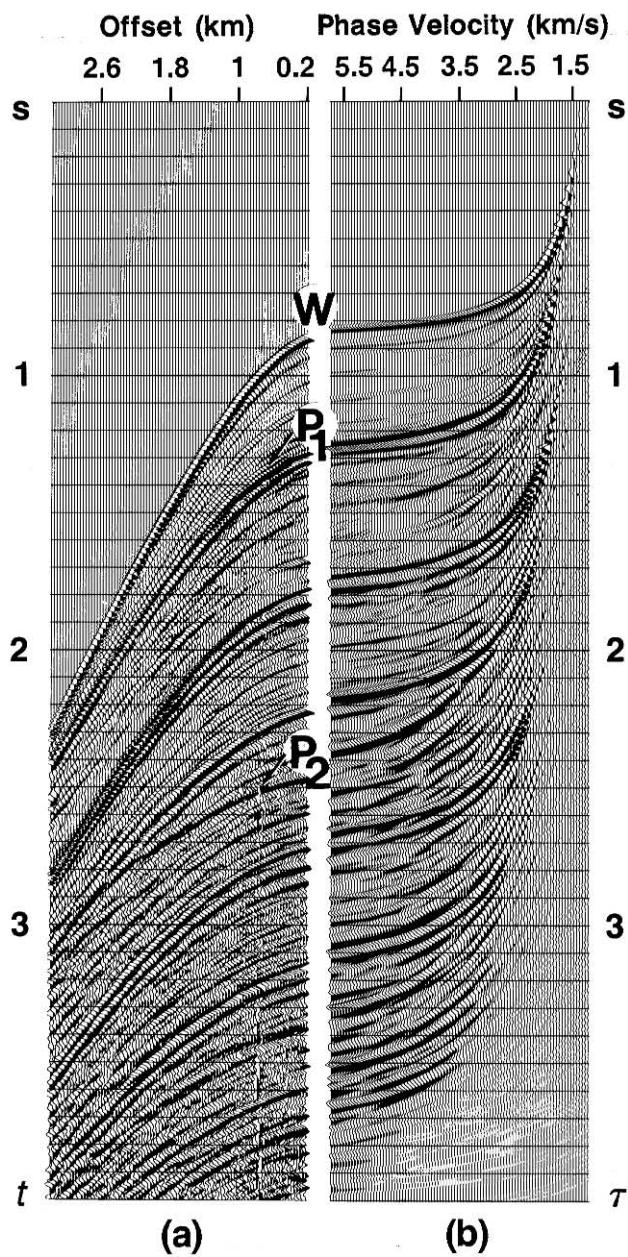


FIG. 6.3-11. (a) A shot gather containing primary and multiple reflections, (b) the corresponding $\tau-p$ gather. The horizontal axis in (b) is horizontal phase velocity $1/p$. (Data courtesy Shell and Esso.)

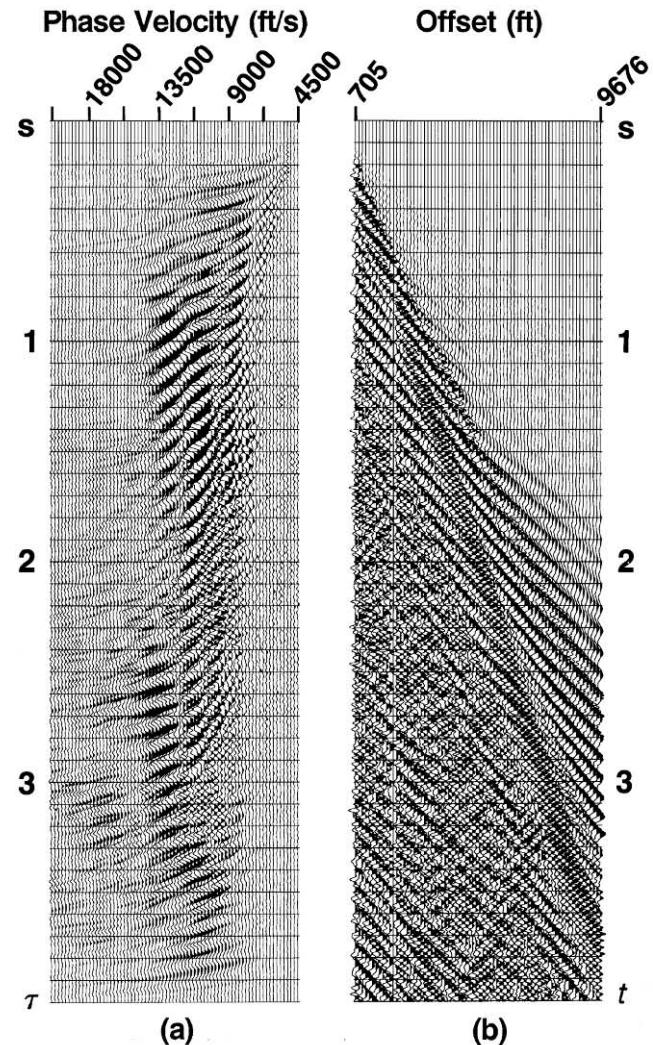


FIG. 6.3-12. (a) A $\tau-p$ gather and (b) the corresponding shot gather. The horizontal axis in (b) is horizontal phase velocity $1/p$.

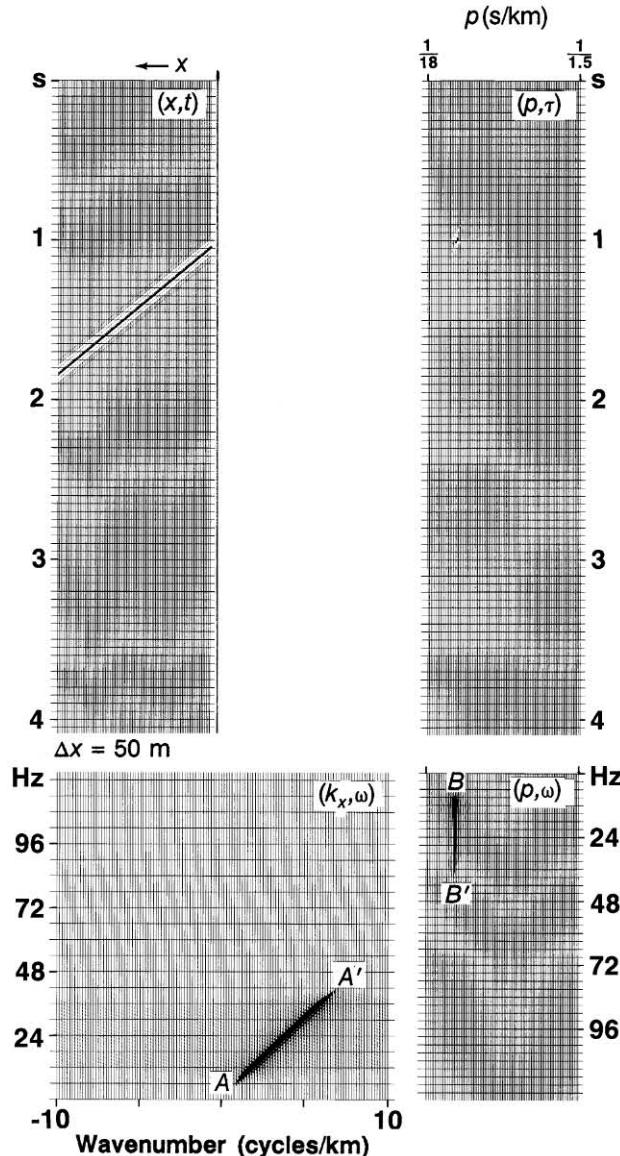


FIG. 6.3-13. A single dipping event in various domains.

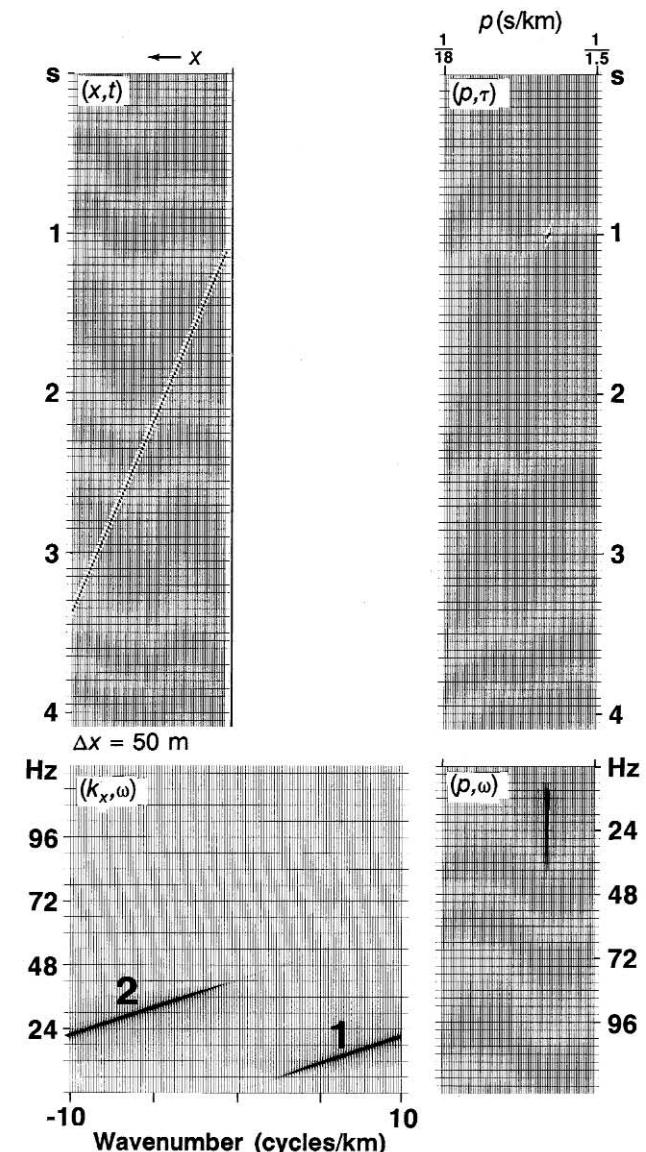


FIG. 6.3-14. A spatially aliased single dipping event in various domains.

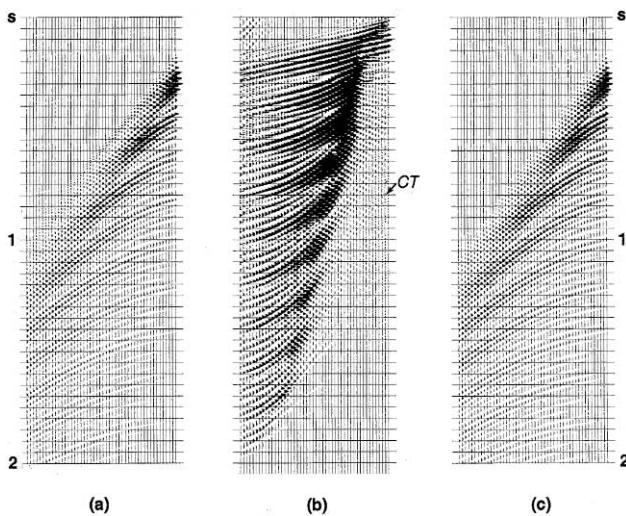


FIG. 6.3-15. Slant stacking is invertible: (a) A CMP gather is mapped from $t - x$ domain onto $\tau - p$ domain (b), from which the original gather can be reconstructed (c). The linear streaks labeled as CT in (b) are caused by the finite cable length.

Substitute for $p = \sin \theta/v$ to find the relationship between the variables in the transform domain given by

$$k_x = p\omega. \quad (6-7)$$

Figure 6.3-13 also shows the mapping of the dipping event to the $\tau - p$ domain. Note that a linear event in the $t - x$ domain maps onto a point in the $\tau - p$ domain. Converse also is true — a linear event in the $\tau - p$ domain maps onto a point in the $t - x$ domain.

A 1-D Fourier transform of the slant-stack traces in the time direction gives the amplitude spectrum in the $\omega - p$ plane, which also is shown in Figure 6.3-13. Actually, the $\omega - p$ plane describes the frequency dependency of horizontal phase velocity and is used in analyzing guided waves (Section F.1). The energy along the radial direction AA' in the $\omega - k_x$ domain is equivalent to that along the vertical direction BB' in the $\omega - p$ domain.

Figure 6.3-14 shows a spatially aliased dipping event. Again, as in Figure 6.3-13, the offset range is from 250 to 5000 m with a trace spacing of 50 m. The wraparound observed in the $\omega - k_x$ plane results from the inadequate spatial sampling of the event. Note that both the unaliased component, segment 1, and the aliased component, segment 2, map onto a single p trace. We expect the spatially aliased part to map onto a number of negative p traces. However, if this were the case, then the aliased frequency range (21 to 42 Hz) would be absent from the $\omega - p$ plane in which only the positive p values were included.

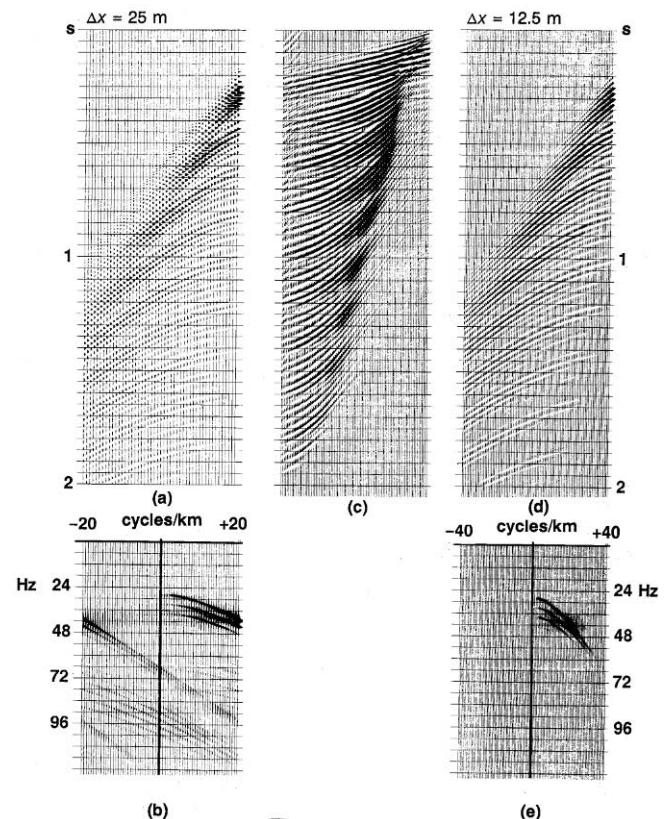


FIG. 6.3-16. Slant stack can be used for trace interpolation: (a) a $t - x$ gather is transformed to a $\tau - p$ gather (c), and is reconstructed using a finer trace spacing (d). The corresponding $f - k$ spectra show spatial aliasing in the original gather (b), which was eliminated after reconstruction (e).

We now outline the steps involved in slant-stack processing that includes forward and inverse $\tau - p$ transforms.

- Start with the offset data, apply linear moveout correction for a specified value of p , and sum over offset (equations 6-4a,b). Repeat for a range of p values, the output is the slant-stack gather (Figure 6.3-8).
- Apply a particular process in the slant-stack domain, such as dip filtering or deconvolution.
- Apply *rho filtering* to the processed slant-stack gather.
- Then, apply inverse linear moveout correction for a specified offset value, and sum over the p -range (equations 6-5a,b). Repeat for all offsets; the output is the slant-stack processed offset data.

We illustrate the forward and inverse $\tau - p$ transforms using the synthetic CMP gather shown in Figure 6.3-15. This figure also shows the slant-stack and reconstructed CMP gather without any process applied, except the rho filter. The linear streaks labeled as CT

on the slant-stack gather in Figure 6.3-15 are caused by the finite cable length. To minimize the streaks, for each trace in the $t - x$ domain, Kelamis and Mitchell (1989) limit the mapping from the $t - x$ domain to the $\tau - p$ domain to a time-variant zone in the $\tau - p$ domain. Specifically, only one trace at a time from the $t - x$ domain is mapped onto all p traces. The resulting $\tau - p$ gather is muted on both the low and high end of the p -axis in a time-varying manner. The mute functions are based on a representative primary velocity function.

During reconstruction of the $t - x$ gather, we do not have to use the same trace spacing that was used for the original $t - x$ gather. Consider the synthetic CMP gather in Figure 6.3-16a. The 2-D amplitude spectrum shows that frequencies above 48 Hz are spatially aliased (Figure 6.3-16b). This gather can be mapped to the slant-stack domain (Figure 6.3-16c) and reconstructed using a finer trace spacing (Figure 6.3-16d). The original trace spacing is 25 m; the reconstructed gather has a trace spacing of 12.5 m. The 2-D amplitude spectrum of the trace-interpolated gather shows that no frequencies are spatially aliased (Figure 6.3-16e). Nevertheless, note the missing high-frequency energy beyond 60 Hz. This energy mainly is along the steep direct arrival path in the input gather (Figure 6.3-16a) and is absent in the output gather (Figure 6.3-16d). We see that reconstruction can be successful even for spatially aliased data, provided dips do not have a wide range of variation.

Slant-Stack Parameters

A single dipping event in the $t - x$ domain ideally maps onto a single trace in the $\tau - p$ domain that represents the dip of that event (Figure 6.3-13). However, because of the discrete sampling along the p -axis and because only a finite number of p traces are spanned from a finite number of offset traces, an imperfect mapping results. When plotted with a higher gain, the slant-stack gather in Figure 6.3-13 seems surprisingly different (Figure 6.3-17b). The linear streaks are contributions from end points E and F of the dipping event in the $t - x$ domain. More specifically, point E maps onto A and B when p is set to its minimum and maximum values, respectively. For any intermediate value of p , point E maps along AB . Similarly, the other end point F maps along CD .

Linear streaks that result from end effects associated with cable truncation are only one type of artifact encountered when constructing slant stacks. Another type of artifact is the high-frequency wavetrain that is especially apparent on traces with large p values as in

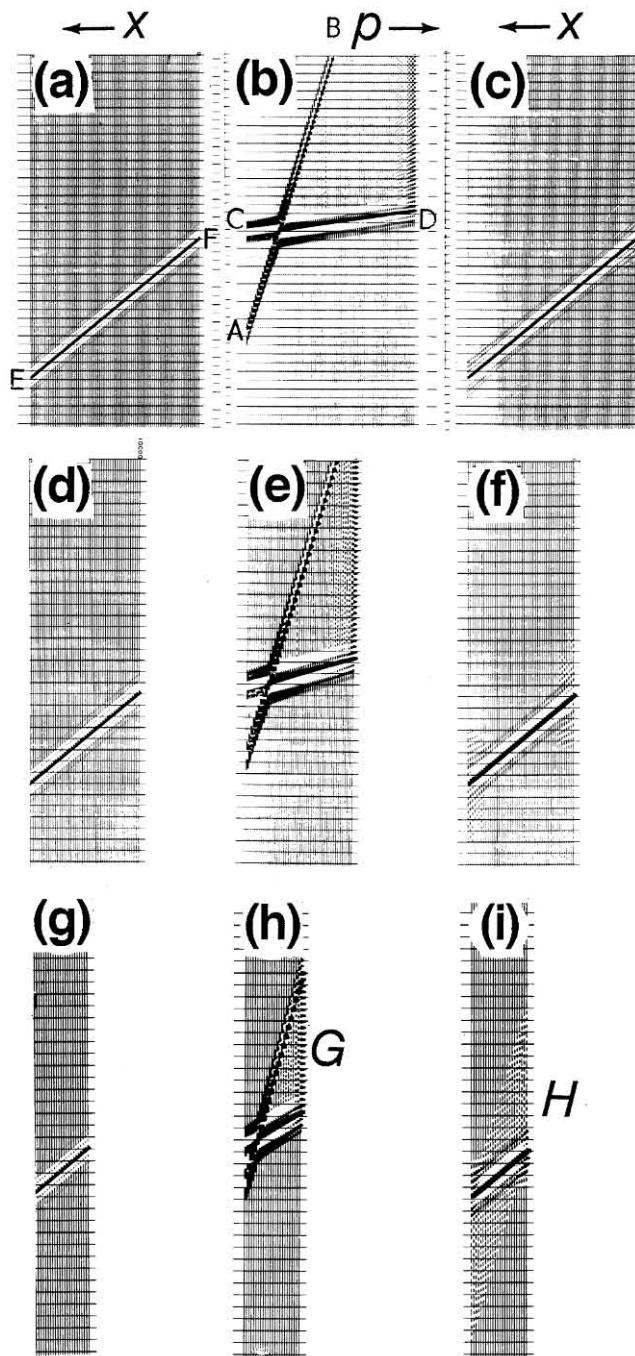


FIG. 6.3-17. Panels (a), (d), and (g) are the input CMP gathers, which contain a single dipping event EF . Panels (b), (e), and (h) are the corresponding slant-stack gathers. Panels (c), (f), and (i) are the reconstructed offset gathers. The slant-stack and reconstructed gathers are displayed at a higher gain than the input gathers.

Figure 6.3-17a. It occurs because the dipping event is sampled along steep slanted paths.

Several practical considerations affect the artifact level in slant stacks. A short cable length in the $t - x$

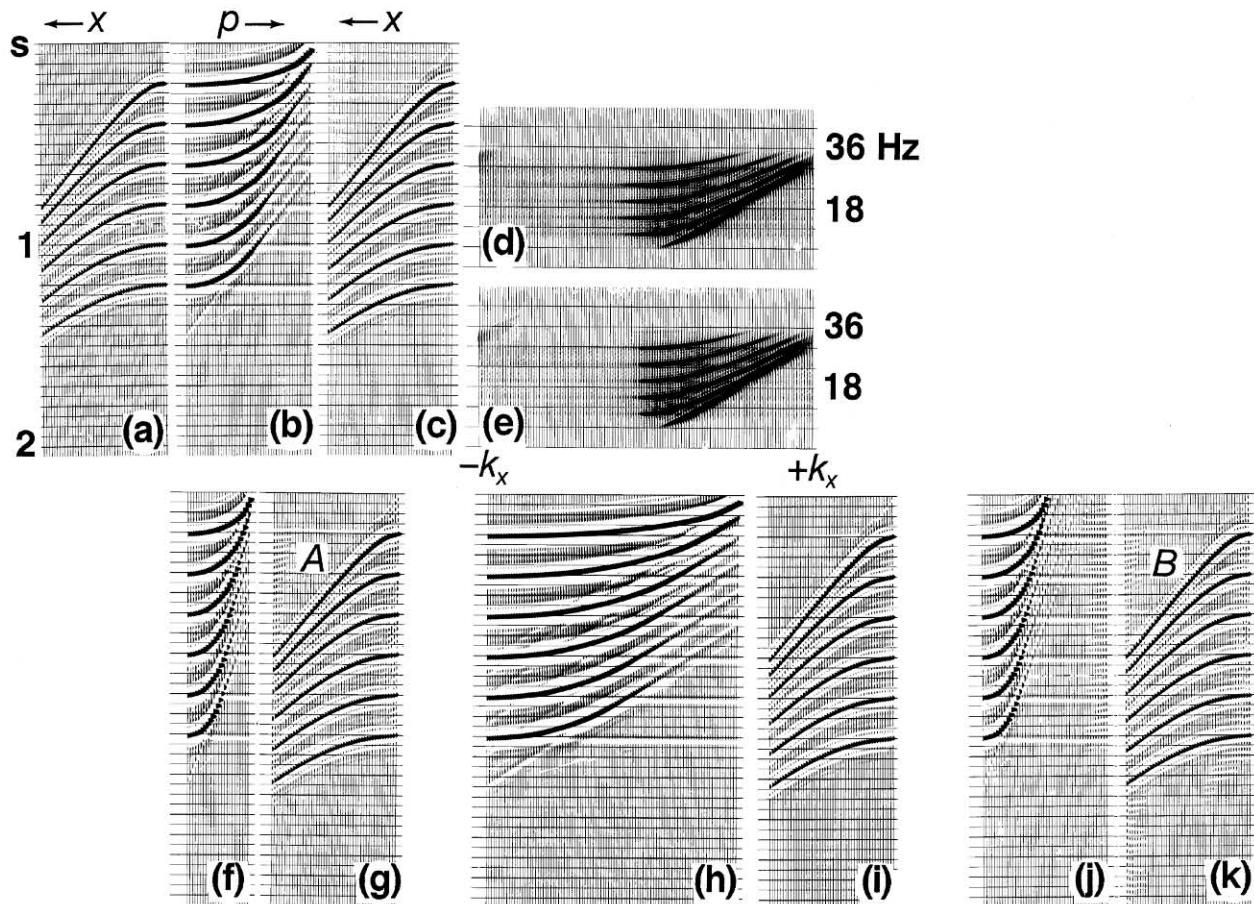


FIG. 6.3-18. (a) Input gather, (b) slant-stack gather, (c) reconstructed offset gather, (d) $f - k$ spectrum of panel (a), (e) $f - k$ spectrum of panel (c). Panels (f), (h), and (j) are the slant-stack gathers derived from the input gather (a) using different numbers of p -values and ranges, while panels (g), (i), and (k) are reconstructions from them. Input (a) is the same for all cases. See text for details.

domain enhances the end effects and, thus causing poor reconstruction as demonstrated in Figure 6.3-17. Start with an offset gather that contains a single dipping event EF in panel (a). Panel (b) is the $\tau - p$ gather and panel (c) is the reconstructed $t - x$ gather from it. To emphasize the artifacts, the last two panels of the sets of three are displayed at a higher gain compared to the original. Using two-thirds of the offset gather, panel (d), the $\tau - p$ gather and the reconstruction from it were obtained as shown in panels (e) and (f). Finally, using only one-third of the original gather, panel (g), panels (h) and (i) are obtained. Note that short cables produce artifacts G and H on the slant-stack and reconstructed gathers. Accurate construction of slant-stack gathers usually requires sufficiently long cable length and adequately small offset interval.

To study the sampling along the p -axis and the range of p values used in constructing a slant-stack

gather, consider the synthetic gather shown in Figure 6.3-18a, which consists of hyperbolic events. These events are mapped along the ellipses in the slant-stack gather (Figure 6.3-18b). The following values were chosen: the number of p traces n_p equal to the number of x traces n_x ; the minimum p value, $p_{min} = 0$; and the maximum p value, p_{max} set to the largest dip present in the data. Reconstruction using these parameters produced an accurate result (Figure 6.3-18c). There is some difference in the 2-D amplitude spectra of the original, panel (d), and the reconstructed gathers panel (e), because p_{min} was set to zero.

What happens when the p -axis is undersampled? Figure 6.3-18f shows the slant-stack gather and Figure 6.3-18g shows the reconstructed gather that is obtained by setting $n_p = n_x/2$ and keeping (p_{min}, p_{max}) the same as in panel (b); thus, the p -increment is twice as large as in panel (b). The input gather is the same as it was

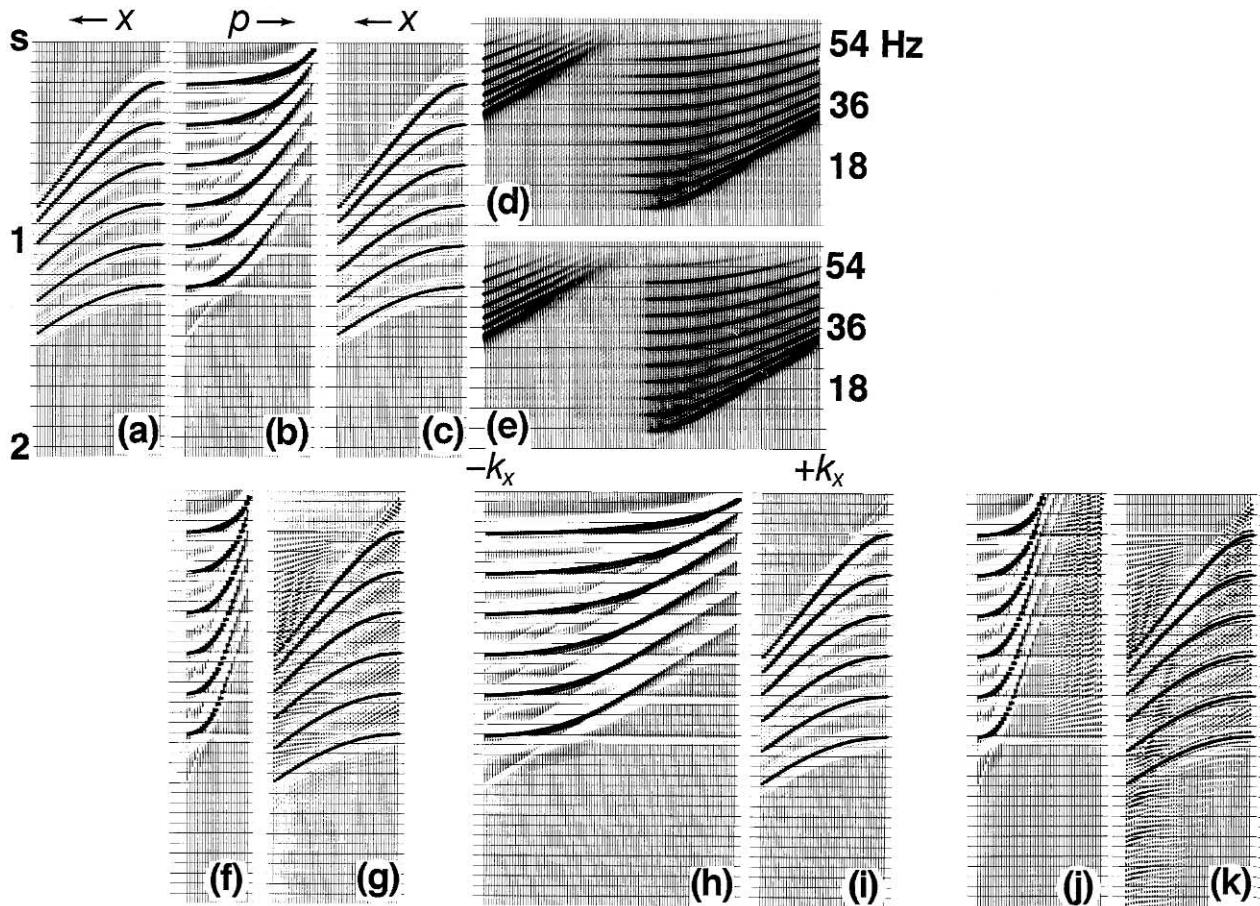


FIG. 6.3-19. The same sequence of panels as in Figure 6.3-18, except that the input gather contains spatially aliased frequency components. Note wraparound in the $f - k$ spectrum (d).

in panel (a). Note that undersampling along the p -axis introduces some noise, labeled as A in Figure 6.3-18g, into the reconstructed gather.

Consider the opposite situation of oversampling along the p -axis as in Figure 6.3-18h. Here, $n_p = 2n_x$ and the (p_{min}, p_{max}) range is the same as in Figure 6.3-18b. Note that oversampling in the p -axis does no harm, but gains nothing either (Figure 6.3-18i). Although not shown here, further experiments show that regardless of spread length, oversampling in the p -domain does not improve the quality of the reconstructed gather.

In practice, we may encounter an inappropriate choice of the (p_{min}, p_{max}) range, meaning that p_{max} corresponds to a larger dip than is present in the input gather (Figure 6.3-18j). Here, $n_p = n_x$, $p_{min} = 0$, p_{max} is twice as large as the value chosen in Figure 6.3-18b, and the p -increment is the same as in Figure 6.3-18f. Thus, the right half of the p -gather (Figure 6.3-18j) does not contain dip components that are present in the input data (Figure 6.3-18a). Instead, the right half

contains noise resulting from cable truncation and sampling along steep slanted paths with p -values associated with dips not contained in the offset data. This results in some noise in the reconstructed gather, labeled as B in Figure 6.3-18k. In practice, suitable muting in the p -domain can eliminate the artifacts caused by spurious p traces — as in the right half of Figure 6.3-18j.

Now consider a synthetic gather that contains spatially aliased events. Figure 6.3-19 shows panels that are equivalent to those in Figure 6.3-18, except that the input gather (Figure 6.3-19a) has spatially aliased frequency components. It is clear that the artifacts observed in Figure 6.3-19 are more pronounced. However, note that if the (p_{min}, p_{max}) range, n_p and the p -increment are chosen properly (Figure 6.3-19b), then reconstruction is quite accurate, even with spatially aliased data. The amplitude spectrum of the original gather (Figure 6.3-19d) and that of the reconstructed gather (Figure 6.3-19e) are almost identical, except that the latter does not contain unaliased energy for $p < 0$, which was not included in constructing Figure 6.3-19b.

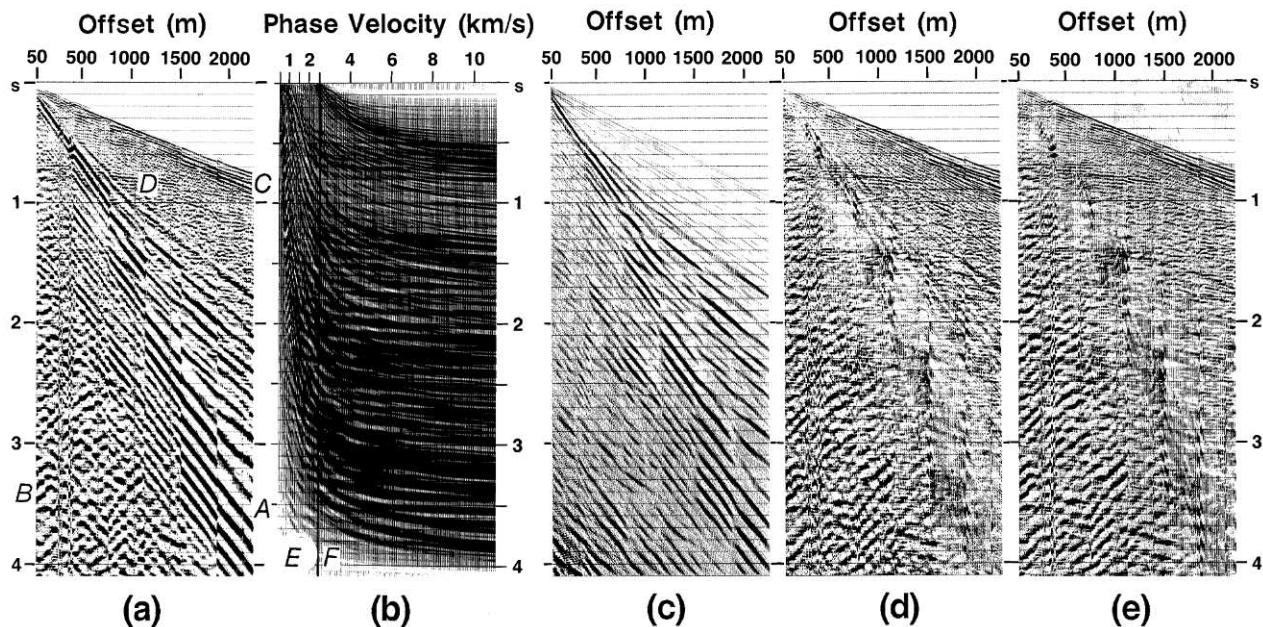


FIG. 6.3-20. (a) A field data set with strong ground-roll energy A , its backscattered component B , guided waves C , and a strong reflection D ; (b) $\tau - p$ gather obtained from this field data set; (c) reconstruction of the field record using the portion to the left of the solid vertical line in (b) (zone E); (d) dip-filtered data obtained by subtracting the gather in (c) from the original data in (a); (e) the original data set (a) after $f - k$ dip filtering. (Data courtesy Turkish Petroleum Corporation.)

Again, we see the case of an undersampled p -axis causing some noise in the reconstructed gather, the case of oversampled p -axis causing no harm, and finally, inappropriate inclusion of the p -values corresponding to dips absent from the input gather causing noise in the reconstructed gather.

This experimental study and other similar studies of the parameters involved in slant-stack processing lead to the following empirical statements:

- $n_p = n_x$ is a good, general rule.
- The (p_{min}, p_{max}) range should only span the dip components of interest in the data. For example, for marine CMP data, $p_{min} = 0$, $p_{max} = (1/1500)$ s/m.
- The p -increment then is $(p_{max} - p_{min})/n_x$. Sampling along the p -axis also can be done with equal increment in horizontal phase velocity $1/p$.

Time-Variant Dip Filtering

The slant-stack domain is convenient for implementing dip filtering. To illustrate this, consider the problem of attenuating the strong ground roll in the field record in Figure 6.3-20a, which was obtained from a walk-away noise test. For simplicity, ignore the backscattered

Rayleigh waves, since removing them would mean computing negative p traces. Figure 6.3-20b shows the $\tau - p$ gather obtained from this field data set. Phase velocity is varied from 500 m/s to over 10 000 m/s. The ground roll generally has very low phase velocity and is mapped to the left of the solid line at 2500 m/s, labeled as E in Figure 6.3-20b.

Suppose that the $\tau - p$ gather traces that contain the ground roll are used to reconstruct the $t - x$ gather with the original offsets. The reconstructed gather shown in Figure 6.3-20c contains only the dips that we want to remove from the original wavefield. If this reconstructed gather is subtracted from the original gather (Figure 6.3-20a), the result is the dip-filtered shot record shown in Figure 6.3-20d. An alternate way to compute the dip-filtered shot record is to use, for reconstruction, the slant-stack traces that are only within zone F to the right of the solid line in Figure 6.3-20b. With either approach, the amplitudes at the boundary between the pass and reject zones, the solid line at 2500 m/s in Figure 6.3-20b, must be tapered to reduce artifacts in the reconstructed $t - x$ gather.

Dip filtering in the slant-stack domain should be nearly equivalent to the $f - k$ dip filtering process described in Section 6.2. Figure 6.2-1b shows the 2-D amplitude spectrum of the original field record of Figure 6.2-1a, which is the same data set as in Figure 6.3-20a.

The reject zone is defined by the fan in Figure 6.2-1c, which is equivalent to zone E to the left of the vertical line in Figure 6.3-20b.

When compared with the slant-stack output (Figure 6.3-20d), the result of $f - k$ dip filtering of the field data set in Figure 6.3-20e suggests basically no difference in performance. However, with the slant-stack approach, dip filtering can be applied in a time-variant manner. This means that the boundary between the pass and reject zones need not be vertical as in Figure 6.3-20b. Also, with the slant-stack technique, we can work with data that are irregularly spaced along the offset axis. This is not the case for the $f - k$ method of dip filtering, since the fast Fourier transform requires data with equal trace spacing. On occasion, dip filtering also is incorporated into multiple attenuation in the slant-stack domain to further eliminate multiples.

An application of time-variant dip filtering to reduce the cable truncation effects on slant-stack gathers (Figure 6.3-17) is provided by Kelamis and Mitchell (1989). Their procedure is outlined below:

- Map a single trace in the offset domain to the slant-stack domain over a specified range of p -values (equations 6-4a,b).
- Apply a time-varying filter by muting inner and outer portions of the slant-stack gather. The mute functions are prescribed using a velocity filter that depends on time and offset.
- Repeat steps (a) and (b) for all offset traces in the input gather and sum the resulting slant-stack gathers.
- Apply *rho filtering* to the summed slant-stack gather.
- Following a specific process in the slant-stack domain, such as deconvolution, apply inverse linear moveout correction for a specified offset value, and sum over the p -range (equations 6-5a,b). Repeat for all offsets; the output is the slant-stack processed offset data.

Slant-Stack Multiple Attenuation

The slant-stack multiple attenuation technique is based on prediction of multiples. Alam and Austin (1981) and Treitel et al. (1982) investigated the application of predictive deconvolution in the slant-stack domain for multiple attenuation. The application of predictive deconvolution to multiple attenuation is valid strictly for vertical incidence and the zero-offset case. Multiples are not periodic at nonzero offsets. Figure 6.3-21 shows a sketch of a shot gather with primary P (water-bottom reflection) and its multiples M_1 , M_2 with the corresponding slant-stack gather.

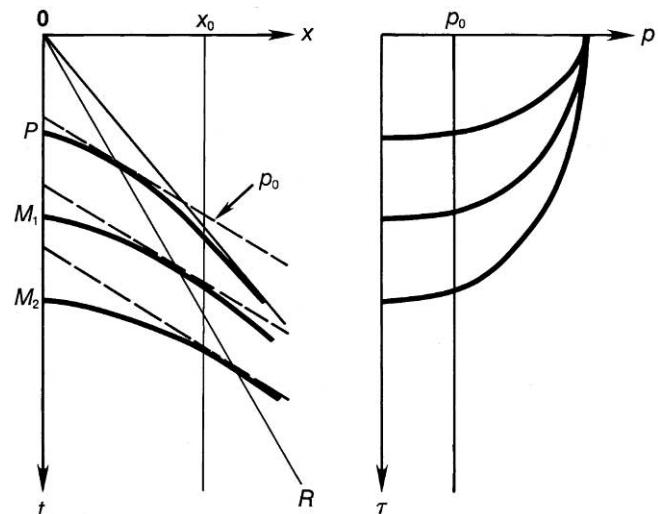


FIG. 6.3-21. The periodicity of multiples along radial trace OR and down the p traces.

between the multiple arrivals at a particular offset x_0 are equal only if $x = 0$.

Taner (1980) first recognized that the time separations between the arrivals are equal along a radial direction OR . A trace can be constructed by extracting the samples along one of these radial directions. The angle of propagation is constant along this *radial trace* (Ottolini, 1982). A radial trace in a layered medium is called a *Snell trace* (Claerbout, 1985). In a layered medium, the Snell trace would not follow a straight path as in Figure 6.3-21, since its angle of propagation changes at layer boundaries according to Snell's law (Figure 6.3-6).

Taner (1980) applied predictive deconvolution along radial traces to successfully eliminate long-period multiples. Note that the magnitude of the time separations between multiples is different from one radial trace to another (Figure 6.3-21). However, the time separations are equal along each of the slanted paths of summation. Therefore, a predictive deconvolution operator can be designed from the autocorrelogram of each p trace (such as that denoted by p_0 in Figure 6.3-21) and applied to suppress multiples. This is demonstrated in Figure 6.3-22. The synthetic shot gather contains a water-bottom reflection and its multiples (Figure 6.3-22a). Note that the periodic nature of the multiples is not apparent on the autocorrelogram. Therefore, predictive deconvolution should not be expected to do well in attenuating these multiples when applied to the shot gather.

The shot gather in Figure 6.3-22a now is transformed to the slant-stack domain. Figures 6.3-22c and 6.3-22e show the slant-stack gather before and after predictive deconvolution was applied. Figure 6.3-22g shows

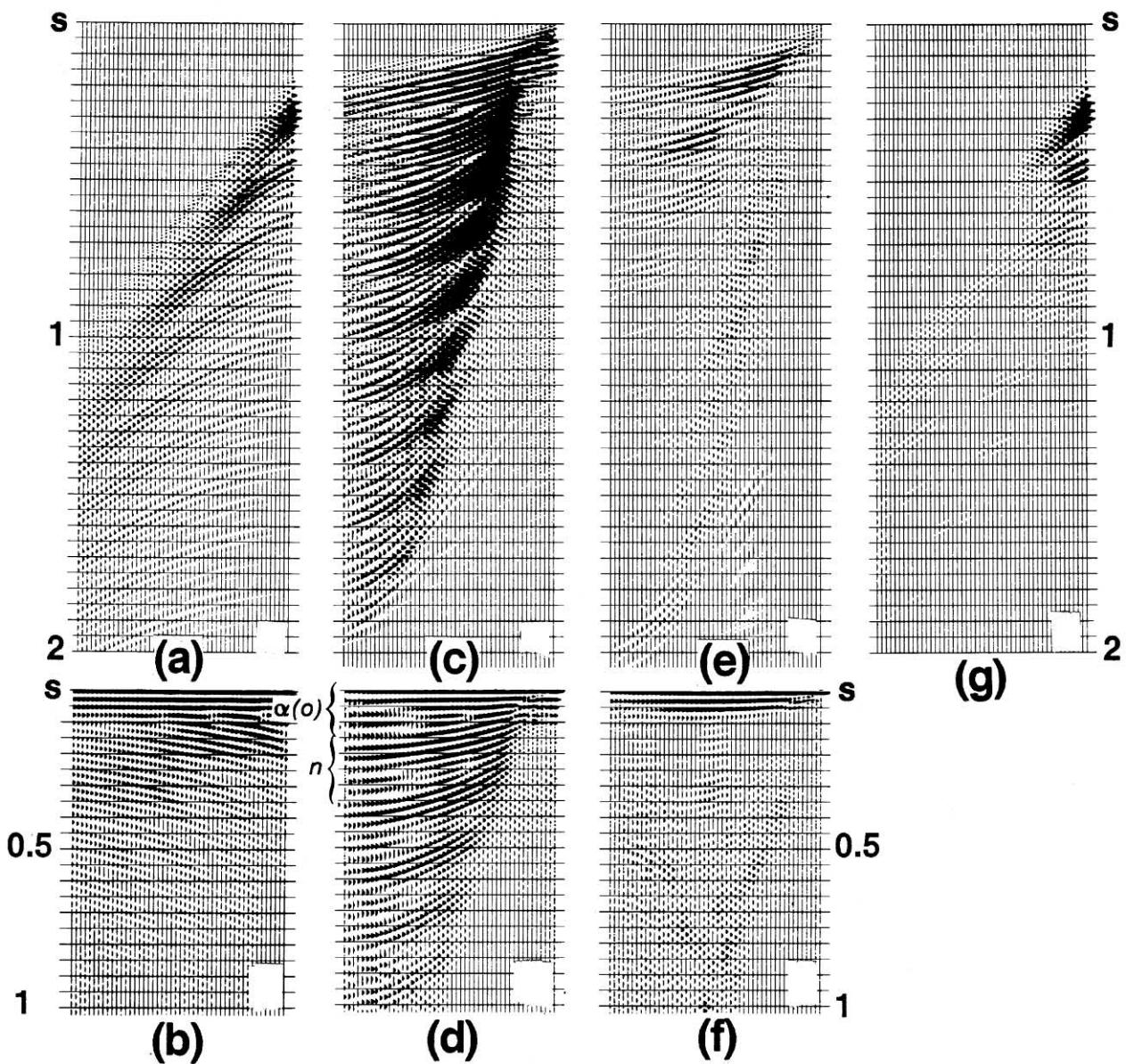


FIG. 6.3-22. Multiple attenuation in the slant-stack domain. (a) A shot gather; (b) its autocorrelogram; (c) the slant-stack gather; (d) the autocorrelogram of (c); (e) the slant-stack gather after predictive deconvolution, where operator length = 240 ms and prediction lag at $p = 120$ ms; (f) the autocorrelogram of (e); (g) reconstruction of the shot gather from (e).

reconstruction of the shot gather from the slant-stack gather in Figure 6.3-22e. Autocorrelograms before and after deconvolution in the slant-stack domain are shown beneath the respective panels. Unlike in the autocorrelogram of the shot gather in Figure 6.3-22b, the periodic nature of the multiples in the data is pronounced in the autocorrelogram of the slant-stack gather (Figure 6.3-22d). Note that the periodicity of multiples changes from one p trace to the next. The largest period occurs along the trace that corresponds to the minimum

p value. The autocorrelogram after predictive deconvolution shows that the energy in the lags less than the specified prediction lag is retained, while the multiple energy is attenuated (Figure 6.3-22f).

Prediction lag α and operator length n must be specified by examining the autocorrelogram of the slant-stack gather (Figure 6.3-22d). These two parameters are specified for the trace corresponding to the lowest p value, as indicated in Figure 6.3-22d. Operator length is kept constant, while prediction lag is adjusted based

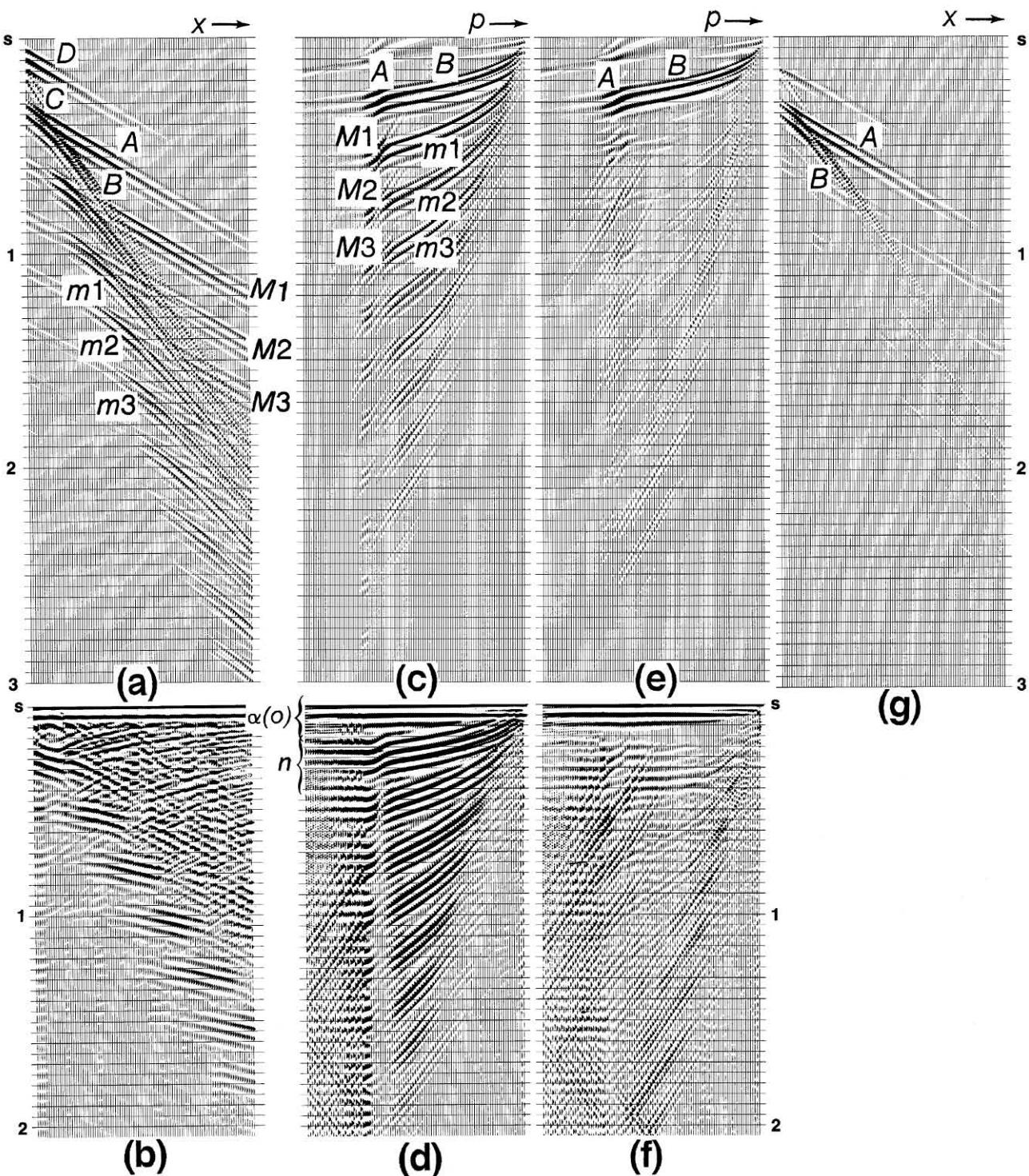


FIG. 6.3-23. (a) Simulation of the shot gather shown in Figure F-1a by normal-mode modeling; (b) autocorrelogram of this synthetic gather; (c) slant stack of the synthetic gather; (d) autocorrelogram of the slant-stack gather; (e) the slant-stack gather in (c) after predictive deconvolution; (f) the autocorrelogram of (e); (g) reconstruction of the synthetic gather from the slant-stack gather in (e). (Refer to the text for a description of the labeled events.)

on the p value across the gather (Alam and Austin, 1981):

$$\alpha(p) = \alpha(0)\sqrt{1 - p^2 v_w^2}, \quad (6-8)$$

where $\alpha(0)$ = prediction lag at $p = 0$ and v_w is the velocity of the primary reflection, the multiples of which are targeted for attenuation. At higher p values, the prediction lag decreases. Compare the reconstructed offset gather (Figure 6.3-22g) with the input gather (Figure 6.3-22a), and note that the output contains the water-bottom primary (the only one present in the input data) and a residual of the first multiple.

Multiple attenuation in the slant-stack domain is demonstrated further by the synthetic data in Figure 6.3-23a. The synthetic shot record in Figure 6.3-23a is a simulation of the shot gather in Figure F-1a using normal-mode modeling (Section F.1). Several arrivals are identified: C is the direct arrival; A is the refracted arrival associated with the hard water bottom; B is the water-bottom reflection; $M1$, $M2$, and $M3$ are the refracted multiples; and $m1$, $m2$ and $m3$ are the reflected multiples. D is an artifact of the normal-mode modeling technique (Section F.1).

Figure 6.3-23c is the slant-stack gather of the synthetic shot record in Figure 6.3-23a. This gather should be compared with the slant-stack gather of the field data in Figure F-1b. Refraction A and its multiples $M1$, $M2$, and $M3$ map onto points in the slant-stack domain. Figure 6.3-23d is the autocorrelogram of the $\tau - p$ gather. Unlike the autocorrelogram of the offset data (Figure 6.3-23b), note that it exhibits the periodic nature of the multiples in the data. After applying predictive deconvolution, the slant-stack gather in Figure 6.3-23e results. Only the refracted arrival A and the water-bottom reflection B remain. The nearly linear streaks, which also are present in the unprocessed slant-stack gather (Figure 6.3-23c), are artifacts caused by the finite cable length. The autocorrelogram after deconvolution is free from the multiple energy (Figure 6.3-23f). The prediction lag and operator length for the minimum p -value are as labeled in Figure 6.3-23d. Adjustment for the prediction lag was made across the gather using equation (6-8). Finally, reconstruction of the shot gather is shown in Figure 6.3-23g. When compared with Figure 6.3-23a, note that both the refracted and reflected primaries are retained, while their associated multiples are largely attenuated.

The performance of slant-stack multiple attenuation on field data now is examined. Figure 6.3-24a shows a shot gather that contains a strong water-bottom reflection A , two distinct primaries B and C , the water-bottom multiples D and E , and the peg-leg F , which is associated with the primary event B . The slant-stack gathers before and after predictive deconvolution are

shown in Figures 6.3-24b and 6.3-24d with their respective autocorrelograms (Figures 6.3-24c and 6.3-24e). Note that multiples are significantly attenuated in the reconstructed gather (Figure 6.3-24f).

Choice of the prediction lag and operator length is tricky for this particular data set. From the autocorrelogram in Figure 6.3-24c, note the energy G , which is caused by the correlation of two primaries — A and B in Figure 6.3-24a. Energy H is caused by the correlation of the water-bottom multiples. Prediction lag is chosen to retain primary energy G , and the operator length is chosen to include the multiple energy H . Note that in Figure 6.3-24e multiple energy H is significantly attenuated and primary energy G is preserved.

Since slant stacking is a plane-wave decomposition, and since plane waves do not have spherical divergence, input to slant stacking must not be compensated for by geometric spreading. Preserving correct amplitude relationships is essential for the effectiveness of slant-stack multiple attenuation. The geometric spreading correction is applied to offset data by using a primary velocity function. This enhances the multiples in the data and destroys the amplitude relationship between them. Predictive deconvolution in the offset domain then may not suppress these multiples effectively.

After multiple attenuation in the slant-stack domain, reconstruction of the offset data is performed, the geometric spreading correction is applied, and processing is continued. Figures 6.3-25a and 6.3-25b show the shot gathers in Figures 6.3-24f and 6.3-24a after the geometric spreading correction. Note that strong multiples are attenuated significantly after deconvolution in the slant-stack domain. While the autocorrelogram of the shot gather with slant-stack processing (Figure 6.3-24c) exhibits the presence of strong multiples, the autocorrelogram of the shot gather without slant-stack processing does not exhibit the periodicity of multiples (Figure 6.3-25c).

Figures 6.1-2, 6.1-3, and 6.1-5 show that when multiples are in the form of short-period reverberations, the autocorrelogram of the offset data seems to adequately represent the periodic nature of multiples. Hence, predictive deconvolution of the offset data often can remove reverberations. On the other hand, long-period multiples are poorly represented by the autocorrelogram of the offset data (Figure 6.3-25c) and are better defined in the slant-stack domain (Figure 6.3-24c).

Figure 6.3-26 shows the stacked section that corresponds to the field data in Figure 6.3-25b. The slant-stack processed section, which corresponds to the data in Figure 6.3-25a, is shown in Figure 6.3-27. Major primary reflections stand out more distinctively in the slant-stack processed section.

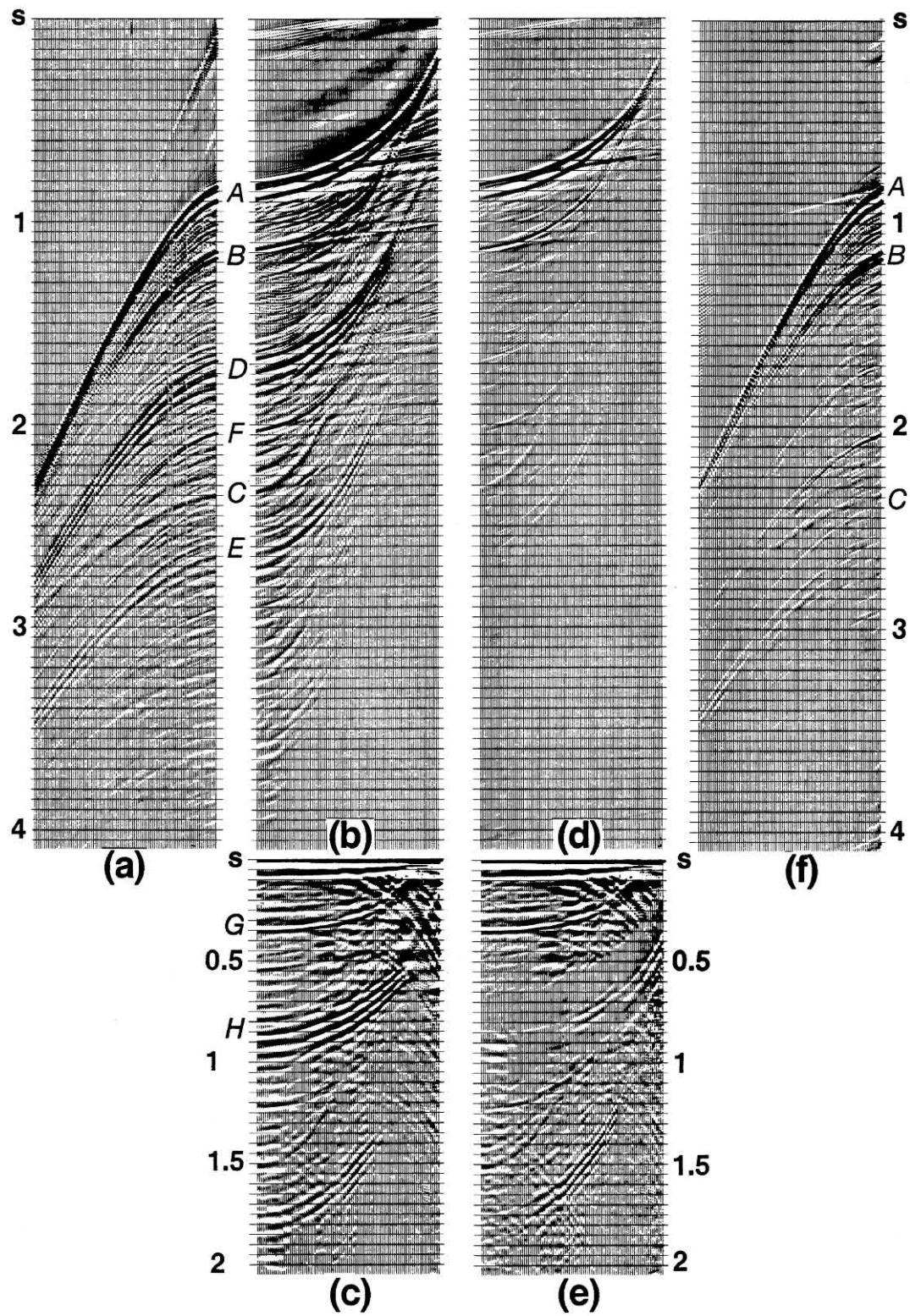


FIG. 6.3-24. Multiple attenuation in the slant-stack domain. (a) A field record without geometric spreading correction; (b) the slant-stack gather obtained from it; (c) the autocorrelogram of (b); (d) the slant-stack gather after predictive deconvolution, where operator length = 400 ms and prediction lag (at $p = 0$) = 700 ms; (e) the autocorrelogram of (d); (f) reconstruction of the shot gather from (d).

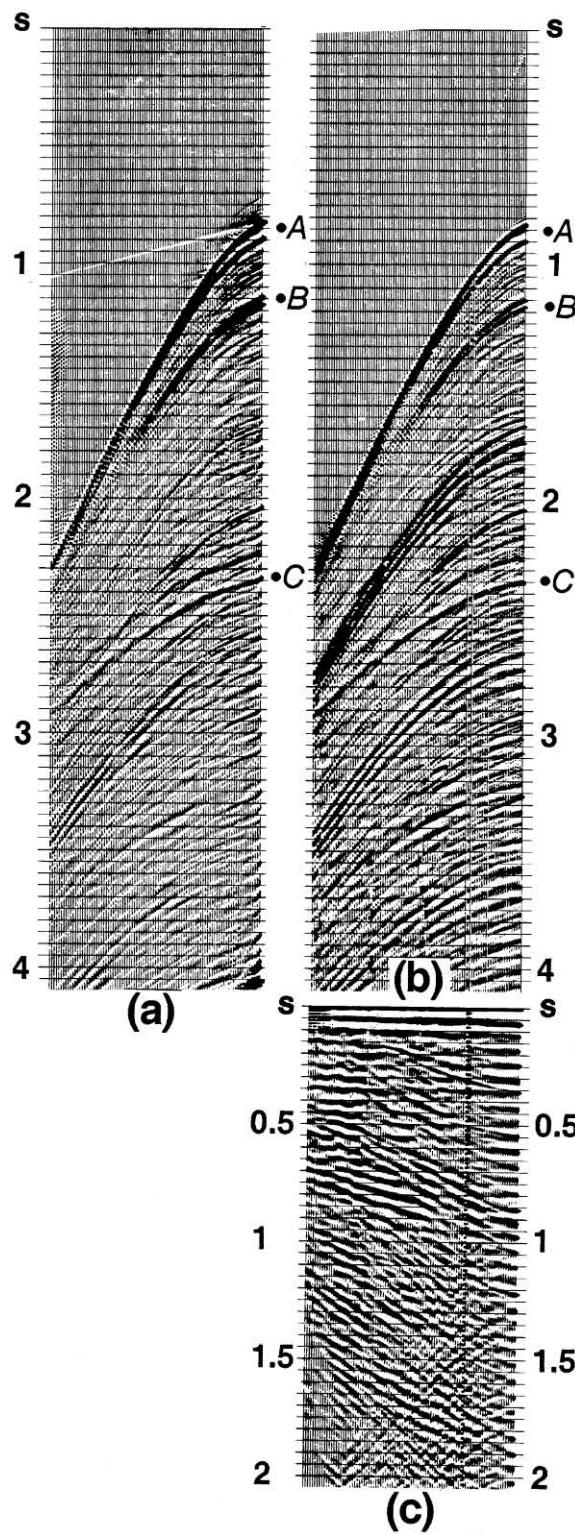


FIG. 6.3-25. (a) Shot gather in Figure 6.3-24f after geometric spreading correction; (b) shot gather in Figure 6.3-24a after geometric spreading correction; (c) autocorrelogram of (b). Events A, B and C are the primaries labeled as in Figure 6.3-24a.

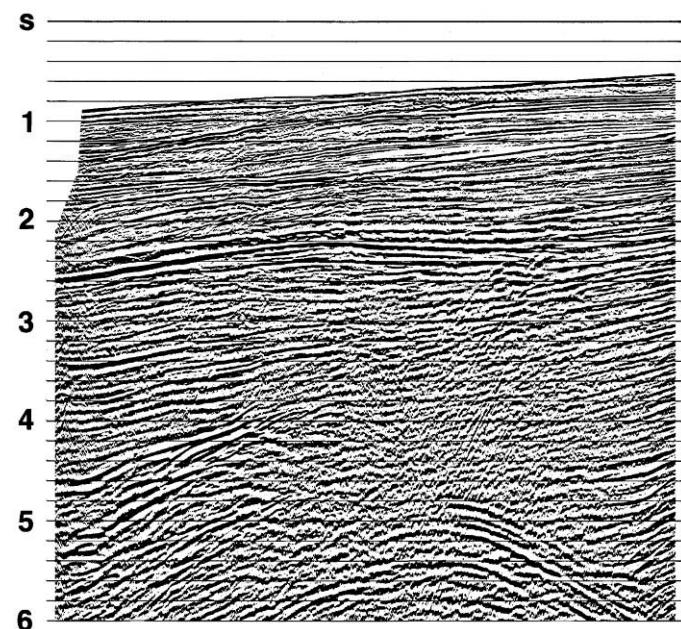


FIG. 6.3-26. A CMP stack associated with the gather shown in Figure 6.3-25b.

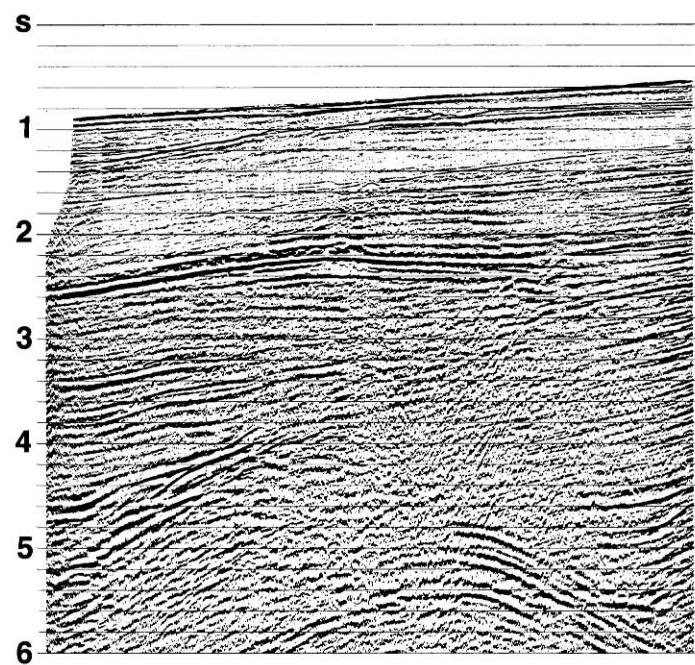


FIG. 6.3-27. A CMP stack associated with the gather shown in Figure 6.3-25a after slant-stack multiple attenuation. Compare with Figure 6.3-26.

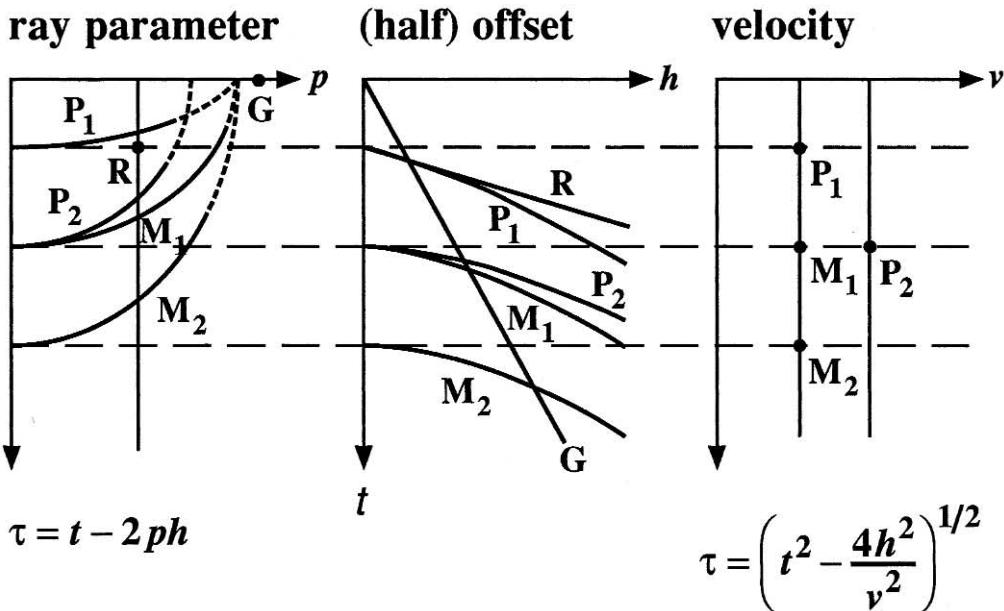


FIG. 6.4-1. Slant-stack (left) and velocity-stack (right) mapping of a CMP gather (center). (See text for details.)

6.4 THE RADON TRANSFORM

In the previous section, we discussed slant-stack transformation and its application to multiple attenuation. *Slant-stack* transformation involves the application of *linear moveout* correction and summation over the offset axis. As a result of this mapping, the offset axis is replaced with the ray-parameter axis. The relationship between the input coordinates (h, t) and the transform coordinates (p, τ) is given by the linear moveout equation

$$t = \tau + 2ph, \quad (6-9a)$$

where p is the ray parameter (Section 6.3), t is the two-way traveltime, τ is the two-way intercept time at $p = 0$, and h is the half-offset.

A companion mapping is called *velocity-stack* transformation which involves application of *hyperbolic moveout* correction and summation over the offset axis. As a result of this mapping, the offset axis is replaced with the velocity axis. The relationship between the input coordinates (h, t) and the transform coordinates (v, τ) is given by the hyperbolic moveout equation

$$t^2 = \tau^2 + \frac{4h^2}{v^2}, \quad (6-9b)$$

where t is the two-way traveltime, τ is the two-way zero-offset time, h is the half-offset and v is the stacking velocity.

Refer to Figure 6.4-1 to review the nature of these two transformations. A linear event in the offset do-

main, such as a refracted arrival R or linear noise G , *ideally* maps onto a point in the ray-parameter domain. A hyperbolic event such as a primary (P_1, P_2) or a multiple (M_1, M_2, M_3) is mapped onto an ellipse in the ray-parameter domain. Since we always have a truncated hyperbola, we inevitably would have a truncated ellipse. A fast-velocity hyperbola maps onto a tighter ellipse than a slow-velocity hyperbola.

Multiples are not periodic in the offset domain, even for a horizontally layered earth model; but they are periodic in the ray-parameter domain. Thus we can use the periodicity for predicting and attenuating multiples in the slant-stack domain as was demonstrated in Section 6.3.

Again, we refer to Figure 6.4-1 and now turn our attention to velocity-stack transformation. Since the mapping function is hyperbolic, in this case, a hyperbola in the offset domain, such as a primary or a multiple, *ideally* maps onto a point in the velocity domain. Hence, we are able to distinguish between multiples and primaries in the velocity domain based on velocity discrimination and use this criterion to attenuate multiples.

The ideal circumstances described by Figure 6.4-1 that a linear event in the offset domain maps onto a point in the ray-parameter domain using equation (6-9a), and a hyperbolic event in the offset domain maps onto a point in the velocity domain using equation (6-9b) do not hold in reality. Specifically, a *conventional* velocity-stack gather consists of constant-velocity

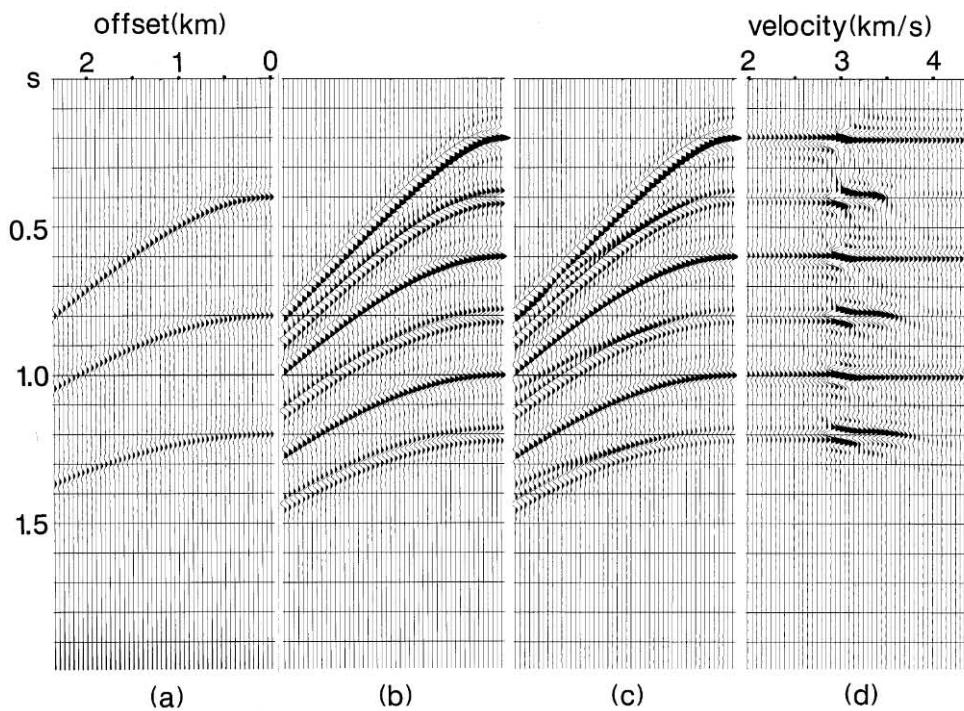


FIG. 6.4-2. (a) A synthetic CMP gather with three primary reflections; (b) a synthetic CMP gather with one primary reflection (arrival time at 0.2 s at zero-offset time) and its multiples; (c) composite CMP gather containing the primaries and multiples in (a) and (b); (d) the conventional velocity-stack gather derived from the composite CMP gather using equation (6-10a). Note the amplitude smearing along the velocity axis.

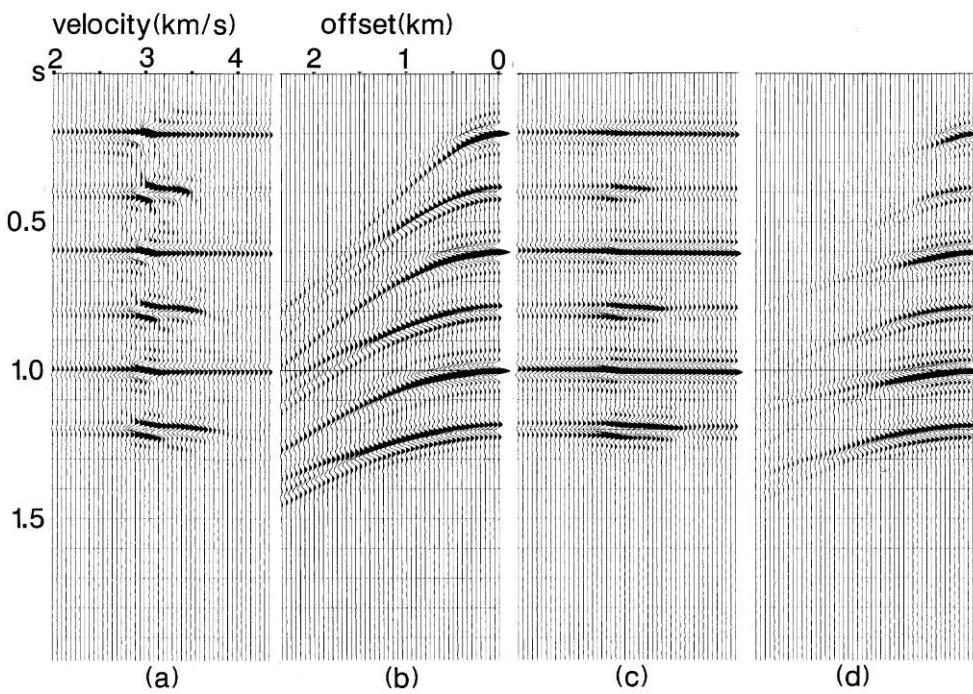


FIG. 6.4-3. (a) The same velocity-stack gather as in Figure 6.4-2d; (b) the CMP gather reconstructed from the velocity-stack gather in (a) using equation (6-10b); (c) velocity-stack gather derived from (b) using equation (6-10a); (d) CMP gather reconstructed from (c) using equation (6-10b). Note the degradation of velocity resolution on the velocity-stack gather (c) due to reduction of far-offset amplitudes (b).

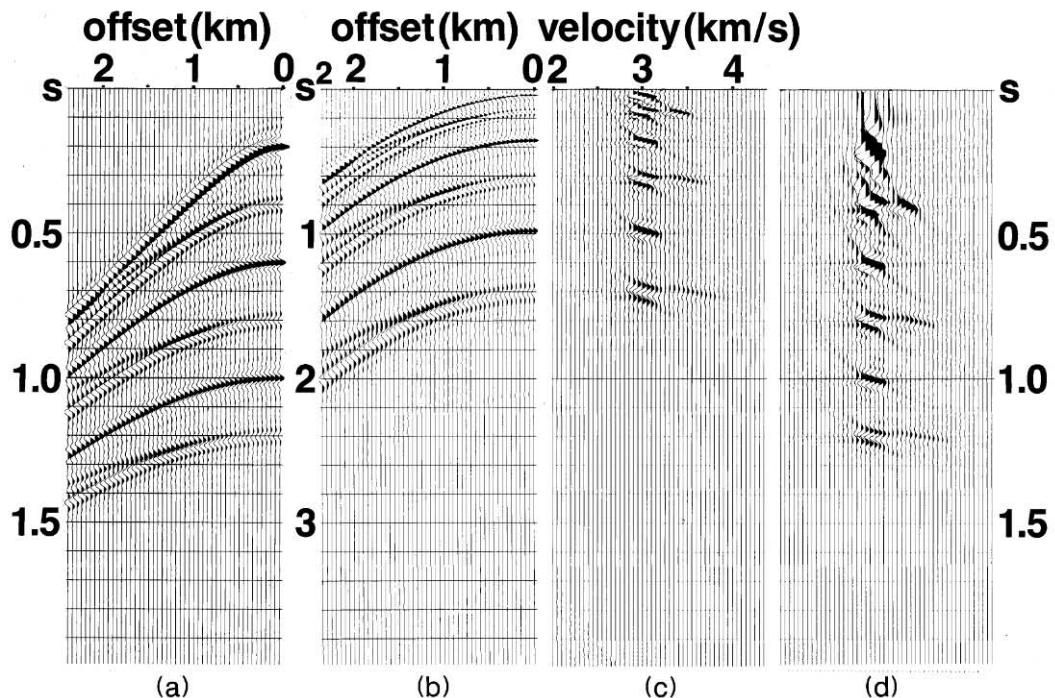


FIG. 6.4-4. (a) The CMP gather of Figure 6.4-2c before, and (b) after t^2 -stretching — note the vertical axis is in units of t^2 ; (c) the velocity-stack gather that represents the Radon transform of (b) using the singular-value decomposition procedure described in Section F.3; (d) the same velocity-stack gather as in (c) after undoing the t^2 -stretching.

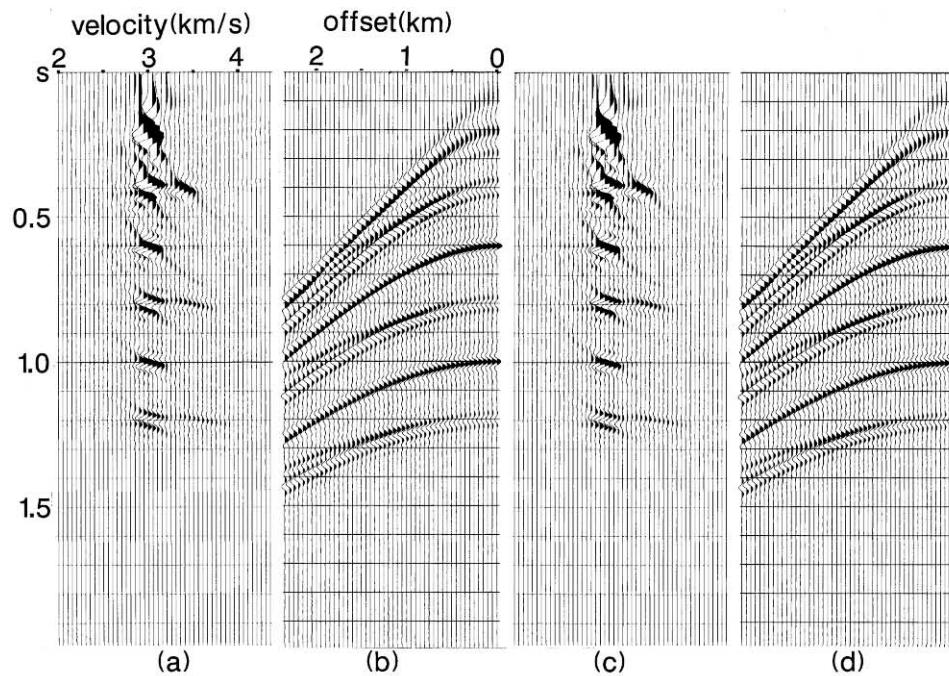


FIG. 6.4-5. (a) The same velocity-stack gather as in Figure 6.4-4d; (b) the CMP gather reconstructed from the velocity-stack gather in (a) using equation (6-10b); (c) velocity-stack gather that represents the Radon transform of (b) using the singular-value decomposition procedure described in Section F.3; (d) CMP gather reconstructed from (c) using equation (6-10b). Note the accurate reconstruction of the CMP gather (b) from the proper velocity-stack gather (a) compared to the reduction of far-offset amplitudes on the CMP gather in Figure 6.4-3b reconstructed from the conventional velocity-stack gather in Figure 6.4-3a.

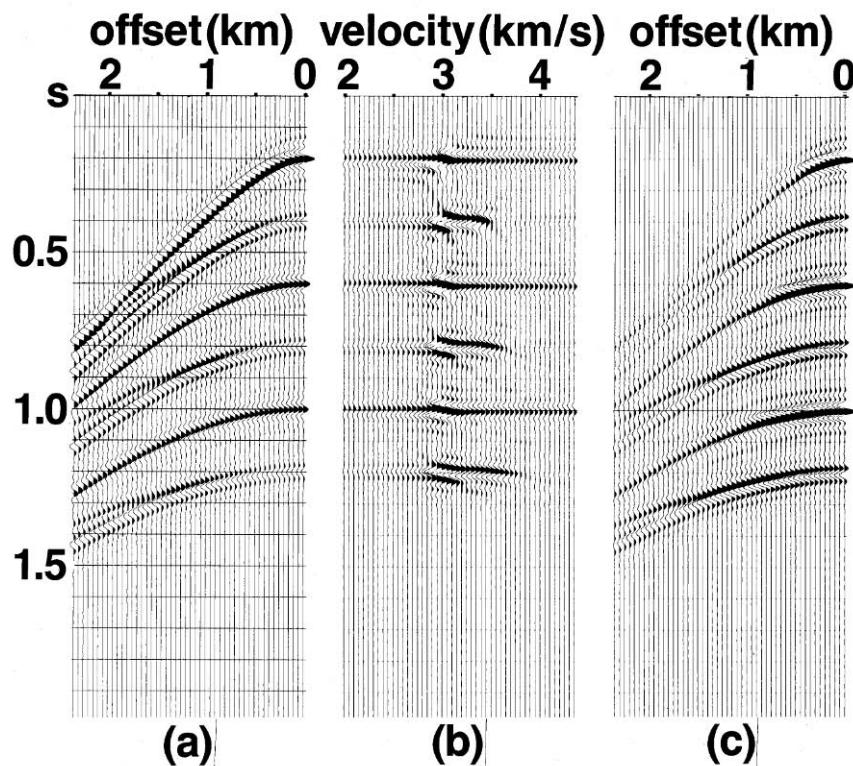


FIG. 6.4-6. (a) Synthetic CMP gather; (b) conventional velocity-stack gather; (c) reconstructed CMP gather.

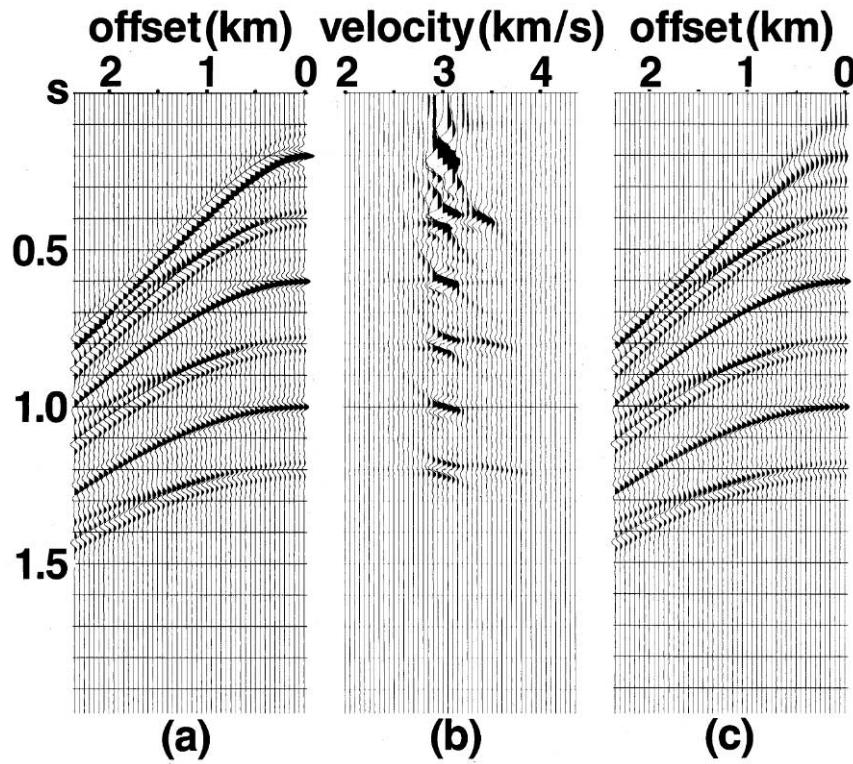


FIG. 6.4-7. (a) Synthetic CMP gather; (b) velocity-stack gather based on the discrete Radon transform; (c) reconstructed CMP gather.

CMP-stacked traces. It emphasizes the energy associated with the events that follow hyperbolic traveltime trajectories in the CMP gather. A fundamental problem with velocity-stack transformation is that a CMP gather only includes a cable-length portion of a hyperbolic traveltime trajectory. The finite cable length, discrete sampling along the offset axis and the closeness of hyperbolic summation paths at near offsets cause smearing of the stacked amplitudes along the velocity axis. Unless this smearing is removed, inverse mapping from the velocity domain back to the offset domain does not reproduce the amplitudes in the original CMP gather.

The gather resulting from the inverse mapping can be considered as the modeled CMP gather that contains only the hyperbolic events present in the actual CMP gather. A least-squares minimization of the energy contained in the difference between the actual CMP gather and the modeled CMP gather removes smearing of amplitudes on the velocity-stack gather and increases velocity resolution. A practical application of this procedure is in the separation of multiples from primaries.

Velocity-Stack Transformation

Consider the synthetic CMP gather in Figure 6.4-2c. This gather is a composite of the CMP gather with three primary reflections shown in Figure 6.4-2a and the CMP gather with one primary and its multiples shown in Figure 6.4-2b. Note that the three primaries of the CMP gather in Figure 6.4-2a arrive at the same zero-offset times as the multiples, and the moveout between the primaries and multiples is less than 100 ms at the far offset (2350 m).

Traces in the composite CMP gather (Figure 6.4-2c) are stacked with a range of constant velocities, and the resulting stacked traces are displayed side by side, forming the conventional velocity-stack gather shown in Figure 6.4-2d. Note that the maximum stacked amplitudes correspond to the primary and multiple velocities. The lower-amplitude horizontal streaks in the velocity-stack gather (Figure 6.4-2d) are a result of the contribution of small offsets, while the large-amplitude regions are a result of the contribution of the full range of offsets (Sherwood and Poe, 1972).

The mapping from the offset domain to the velocity domain is achieved by applying hyperbolic moveout correction and summing over offset given by

$$u(v, \tau) = \sum_h d(h, t = \sqrt{\tau^2 + 4h^2/v^2}), \quad (6-10a)$$

where t is the two-way traveltimes, τ is the two-way zero-offset time, h is the half-offset, and v is the stacking velocity. The input $d(h, t)$ represents the CMP gather, and

the output $u(v, \tau)$ represents the velocity-stack gather. The inverse mapping from the velocity space back to the offset space is achieved by applying inverse hyperbolic moveout correction and summing over velocity given by

$$d'(h, t) = \sum_v u(v, \tau = \sqrt{t^2 - 4h^2/v^2}), \quad (6-10b)$$

where $d'(h, t)$ represents the modeled CMP gather.

Figure 6.4-2d was obtained by using equation (6-10a) in which the summation is performed over a finite range of offsets. At first, it appears that by using equation (6-10b), in which the summation is performed over a range of velocities, the original data $d(h, t)$ in Figure 6.4-2c can be reconstructed from the data in Figure 6.4-2d. The modeled CMP gather $d'(h, t)$ using equation (6-10b) is shown in Figure 6.4-3b. Observe the relative weakening of amplitudes at far offsets, especially along events with large moveout. Repeated transformations using equations (6-10a) and (6-10b) from the velocity domain to the offset domain (Figure 6.4-3) further reduce the amplitudes at far offsets.

Results shown in Figure 6.4-3 demonstrate clearly that the discrete transforms given by equations (6-10a) and (6-10b) are not exact inverses of each other. The discrete summation in equation (6-10a) over a *finite* range of offsets causes mapping of amplitudes along a hyperbolic event in the offset domain (Figure 6.4-2c) to depart from the ideal point in the velocity domain and results in the smearing of amplitudes along the velocity axis (Figure 6.4-2d). Amplitude smearing means the loss of velocity resolution between two events with little moveout difference.

To understand the inverse problem of restoring the data in the offset domain from the data in the velocity domain, consider the integral forms of equations (6-10a) and (6-10b). Reflection times on a CMP gather associated with a horizontally layered earth model can be represented by a Taylor series of the form $t = \tau + c_1 h^2 + c_2 h^4 + \dots$, where c_1, c_2, \dots are scalar coefficients (Hubral and Krey, 1980). By including as many terms as desired in the Taylor expansion, the traveltime curve can be expressed by $t = \tau + \phi(v, h)$. This makes the integral form of equation (6-10a) a special form of the generalized Radon transform (Beylkin, 1987) given by

$$u(v, \tau) = \int_{-\infty}^{\infty} d[h, t = \tau + \phi(v, h)] dh. \quad (6-11a)$$

Here, the integration is along curves expressed as linear functions of traveltimes, t and τ . Accordingly, $d(h, t)$ and its Radon transform $u(v, \tau)$ are defined as continuous functions in the offset and velocity domains, respectively.

The integral form of equation (6-10b), however, is not the exact inverse of equation (6-11a). Instead, Radon's inversion formula given by (Beylkin, 1987)

$$d(h, t) = \int_{-\infty}^{\infty} \rho(\tau) * u[v, \tau = t - \phi(v, h)] dv \quad (6-11b)$$

incorporates convolution of $u(v, \tau)$ with the rho filter $\rho(\tau)$ prior to integration over velocity. In equation (6-11b), the asterisk denotes convolution. For 2-D data, as for any process that involves summation over a finite spatial aperture (Section 4.1), the rho filter $\rho(\tau)$ has a Fourier transform of the form $\sqrt{\omega} \exp(i\pi/4)$, where ω is the temporal frequency.

The Discrete Radon Transform

In practice, a discrete form of the rho filter $\rho(\tau)$ can be convolved with the discrete form of $u(v, \tau)$ prior to summing over a finite range of velocities to reconstruct the original data $d(h, t)$. Note that the rho filter is a 1-D filter that operates on each trace of $u(v, \tau)$, individually. It can account for the suppression of high frequencies during summation along discretely sampled traveltime curves, $t = \tau + \phi(v, h)$. However, one can intuitively contend that the rho filtering alone cannot remove the amplitude smearing along the velocity axis in Figure 6.4-2d. Based on a rigorous mathematical analysis, Beylkin (1987) showed that a discrete form of Radon's inversion formula (equation 6-11b) can be expressed as a least-squares solution to a set of linear system of equations. We shall review the discrete Radon transform for the special case of velocity-stack transformation.

To reduce the amplitude smearing on conventional velocity-stack gathers Thorson and Claerbout (1985) proposed a least-squares formulation. There is one issue, however, we must take into consideration before we seek a practical scheme to compute the inverse Radon transform defined by equation (6-11b). To comply with the linear form the Radon transform defined by equation (6-11a), apply stretching in the time direction by setting $t' = t^2$ and $\tau' = \tau^2$ (Yilmaz, 1989). Equation (6-9b) then takes the form

$$t' = \tau' + \frac{4h^2}{v^2}. \quad (6-12)$$

In the stretched coordinates, equations (6-10a,b) become:

$$u(v, \tau') = \sum_h d(h, t' = \tau' + 4h^2/v^2) \quad (6-13a)$$

and

$$d'(h, t') = \sum_v u(v, \tau' = t' - 4h^2/v^2). \quad (6-13b)$$

As a result of the t^2 -stretching, hyperbolic events in the offset domain are transformed to parabolic events described by the travelttime equation (6-12). Note that, unlike the hyperbolic events, the moveout $4h^2/v^2$ associated with the parabolic events is time-independent.

The objective is to estimate the transform $u(v, \tau')$ such that the difference between the actual CMP gather $d(h, t')$ and the modeled CMP gather $d'(h, t')$ is minimum in the least-squares sense. A direct solution for $u(v, \tau')$ requires computing the inverse of a large matrix which may have dimensions of $60\,000 \times 60\,000$ for a typical field data set (Section F.3).

To circumvent solving a problem that involves a very large matrix, Fourier transform the CMP gather $d(h, t')$ in the direction of the stretch variable t' . Correspondingly, apply Fourier transform to equation (6-13b) with respect to t' :

$$d'(h, \omega') = \sum_v u(v, \omega') \exp(-i\omega' 4h^2/v^2), \quad (6-14)$$

where ω' is the Fourier dual of t' .

For each ω' , define $\mathbf{d}' : d'(h, \omega')$ and $\mathbf{u} : u(v, \omega')$ as complex vectors in h and v , respectively. Now, consider equation (6-14) in matrix notation:

$$\mathbf{d}' = \mathbf{L}\mathbf{u}. \quad (6-15)$$

The complex matrix \mathbf{L} is given by equation (F-19) of Section F.3. The complex vectors \mathbf{d}' and \mathbf{u} have lengths n_h , the number of offsets, and n_v , the number of constant velocities used in the transform defined by equation (6-14), respectively. The complex matrix \mathbf{L} then has dimensions $n_h \times n_v$. For a typical field data set, $n_h = 60$ and $n_v = 60$; hence, the complex matrix \mathbf{L} may have dimensions of 60×60 . As such, instead of solving one single problem using equation (6-13b) in the stretched time t' domain that involves a very large matrix, we solve n_ω problems, where n_ω is the number of frequencies ω' , in the Fourier transform domain using equation (6-14) involving a small matrix \mathbf{L} of equation (F-19).

We now restate our objective within the context of the matrix equation (6-15): For each ω' , estimate the complex vector $\mathbf{u} : u(v, \omega')$ such that the difference $\mathbf{e} : e(v, \omega')$ between the complex vector of the actual CMP gather $\mathbf{d} : d(h, \omega')$ and that of the modeled CMP gather $\mathbf{d}' : d'(h, \omega')$ is minimum in the least-squares sense.

Following Lines and Treitel (1984), the solution for equation (6-15) that minimizes the error vector \mathbf{e} in the least-squares sense is derived in Section F.3 and is given by

$$\mathbf{u} = (\mathbf{L}^T \mathbf{L})^{-1} \mathbf{L}^T \mathbf{d}, \quad (6-16)$$

where \mathbf{T} denotes transpose of the matrix \mathbf{L} , the asterisk denotes complex conjugate and $(\mathbf{L}^T \mathbf{L})^{-1} \mathbf{L}^T$ is the least-squares (also called generalized) inverse of \mathbf{L} .

Equation (6-16) gives the unconstrained least-squares solution for \mathbf{u} , which may be unstable if the matrix $\mathbf{L}^T \mathbf{L}$ does not have a stable inverse. Stability is attained by constraining the solution, which requires replacing $\mathbf{L}^T \mathbf{L}$ in equation (6-16) with $\mathbf{L}^T \mathbf{L} + \beta \mathbf{I}$, where β is called the damping factor (also called the Lagrange multiplier) and \mathbf{I} is the identity matrix (Lines and Treitel, 1984). Also, there can be singularities or near singularities in the matrix \mathbf{L} . This is primarily because of the nonuniqueness of hyperbolic summation paths at and near zero offset, and discrete sampling over a finite range of offsets. The method of singular-value decomposition (SVD) is used to obtain the least-squares solution for \mathbf{u} of equation (6-16) when the matrix \mathbf{L} is singular or near singular (Section F.3).

We now outline the velocity-stack processing with reduced amplitude smearing based on the discrete hyperbolic Radon transform.

- (a) Start with a CMP gather, $d(h, t)$ and apply t^2 -stretching, $d(h, t' = t^2)$.
- (b) Fourier transform in the t' direction, $d(h, \omega')$.
- (c) For each ω' , set up the \mathbf{L} matrix (equation F-16) based on the geometry of the CMP gather and solve for \mathbf{u} of equation (6-16) using the singular-value decomposition (Section F.3).
- (d) Inverse Fourier transform to get $u(v, \tau')$.
- (e) Undo the t^2 -stretching to get $u(v, \tau)$, the velocity-stack gather with reduced amplitude smearing.
- (f) Perform a desired operation, such as muting the zone of multiples, in the velocity-stack domain.
- (g) Finally, perform inverse mapping back to the offset domain to get the modeled CMP gather $d'(h, t)$ using equation (6-10b). During this inverse mapping, multiples, primaries, or all of the hyperbolic events can be modeled.

The velocity-stack gather estimated by equation (6-16) as described by the above sequence is one form of the generalized discrete forward Radon transform (Beylkin, 1987).

Recall that the minimum error associated with the least-squares solution is the difference between the actual CMP gather and the modeled CMP gather obtained from inverse mapping from the Radon transform domain back to the offset domain using equation (6-10b). Since the forward mapping defined by equation (6-10a) involves hyperbolic events, only, from the offset domain to the velocity domain, this difference gather should contain only the nonhyperbolic events, such as

random or linear noise, that may be present in the original CMP gather.

The Parabolic Radon Transform

An alternative to stretching in the time direction to attain the linear form of the Radon transform (equations 6-13a,b) is given by Hampson (1986). First, the input CMP gather is NMO corrected using the hyperbolic moveout equation

$$t_n = \sqrt{t^2 - \frac{4h^2}{v_n^2}}, \quad (6-17a)$$

where t_n is the time after NMO corection, and v_n is the hyperbolic moveout correction velocity function. Resulting moveouts of the events, which were originally hyperbolic, are now *approximately* parabolic:

$$t_n = \tau + qh^2, \quad (6-17b)$$

where τ is the two-way zero-offset time, and q is the parameter that defines the curvature of the parabola.

In the coordinates of the NMO-corrected gather $d(h, t_n)$, equations (6-10a,b) take the forms

$$u(q, \tau) = \sum_h d(h, t_n = \tau + qh^2) \quad (6-18a)$$

and

$$d'(h, t_n) = \sum_q u(q, \tau = t_n - qh^2). \quad (6-18b)$$

The strategy for computing the hyperbolic Radon transform by performing least-squares minimization for each frequency component of the input data in the stretched coordinates also applies to the moveout-corrected data to compute the parabolic Radon transform. Fourier transform the moveout-corrected CMP gather $d(h, t_n)$ in the direction of the moveout correction time variable t_n . Correspondingly, apply Fourier transform to equation (6-18b) with respect to t_n to obtain

$$d'(h, \omega_n) = \sum_q u(q, \omega_n) \exp(-i\omega_n qh^2), \quad (6-19)$$

where ω_n is the Fourier dual of t_n .

For each ω_n , define $\mathbf{d}' : d'(h, \omega_n)$ and $\mathbf{u} : u(q, \omega_n)$ as complex vectors in h and q , respectively. With the new definitions of \mathbf{d}' and \mathbf{u} , equation (6-19) can then be written in the matrix form of equation (6-15), where \mathbf{L} now is a complex matrix given by equation (F-29) of Section F.3. The solution that minimizes the least-squares error vector $\mathbf{e} : e(h, \omega_n)$, now defined in the ω_n domain, accordingly, is given by equation (6-16).

The complex vectors \mathbf{d}' and \mathbf{u} have lengths n_h , the number of offsets, and n_q , the number of constant q values used in the transform defined by equation (6-19), respectively. The complex matrix \mathbf{L} then has dimensions $n_h \times n_q$. For a typical field data set, $n_h = 60$ and $n_q = 60$; hence, the complex matrix \mathbf{L} may have dimensions of 60×60 . As for equation (6-13b), instead of solving one single problem using equation (6-18b) in the moveout correction time t' domain that involves a very large matrix, we solve n_ω problems, where n_ω is the number of frequencies ω_n , in the Fourier transform domain using equation (6-19) involving a small matrix \mathbf{L} of equation (F-29).

We now outline the velocity-stack processing based on the discrete parabolic Radon transform (Hampson, 1986).

- (a) Start with a CMP gather, $d(h, t)$ and apply NMO correction, $d(h, t_n)$.
- (b) Fourier transform in the t_n direction, $d(h, \omega_n)$.
- (c) For each ω_n , set up the \mathbf{L} matrix (equation F-29) based on the geometry of the CMP gather and solve for \mathbf{u} of equation (6-16) using the singular-value decomposition (Section F.3).
- (d) Inverse Fourier transform to get $u(q, \tau)$, the parabolic Radon transform.
- (e) Perform a desired operation, such as muting the zone of multiples, in the parabolic Radon transform domain.
- (f) Perform inverse mapping back to the offset domain to get the modeled NMO-corrected CMP gather $d'(h, t_n)$. During this inverse mapping, multiples, primaries, or all of the hyperbolic events can be modeled.
- (g) Undo the moveout correction to get the modeled CMP gather $d'(h, t)$.

As events on the NMO-corrected CMP gather deviate from the ideal parabolic form, there can be degradation in the ability to map those events into the Radon-transform domain (q, τ) (Hampson, 1986). Moreover, stretch muting that is normally required after NMO correction can remove the far-offset data significantly. The t^2 -stretching circumvents these shortcomings and replaces the moveout correction of the CMP gather. In practice, both hyperbolic and parabolic schemes in various forms are used to attenuate multiples.

Practical Considerations

Figure 6.4-4 shows the modeled CMP gather before and after t^2 -stretching. Note that the hyperbolas in Figure

6.4-4a are replaced with parabolas in Figure 6.4-4b. The t^2 -transformation causes compression on data before 1 s and stretching on data after 1 s. As mentioned earlier, a nice property of the parabolic moveout is that it is invariant along the axis $t' = t^2$ for a specific value of velocity (equation 6-12). The sampling rate along the t^2 -axis was set equal to t'/n_t , where n_t is the number of samples along the t -axis. There can be a potential problem of aliasing near $t = 0$, causing frequency distortion for shallow events. This problem can be avoided by finer sampling along the t' -axis.

By using the singular-value decomposition procedure described in Section F.3, we obtain the Radon transform represented by the velocity-stack gather in the stretched coordinates as shown in Figure 6.4-4c. Finally, we undo the stretching to get the Radon transform represented by the velocity-stack gather in Figure 6.4-4c. Compare this with the conventional velocity-stack gather in Figure 6.4-2d. Note the significant reduction of amplitude smearing and enhancement of velocity resolution in the velocity-stack gather based on the Radon transform. In particular, multiples and primaries now are clearly distinguishable. Nevertheless, there is some frequency distortion of the wavelet associated with the shallowest event in the Radon transform (Figure 6.4-4d), primarily because of stretching and un-stretching.

By using the Radon transform (Figure 6.4-5a), the CMP gather can be faithfully reconstructed (Figure 6.4-5b). Compare the panels in Figure 6.4-5 with those in Figure 6.4-3. Note that, unlike the conventional velocity-stack gather, repeated application of the Radon transformation always reproduces the CMP gather with minimal amplitude distortion (Figures 6.4-5b and 6.4-5d), with the exception of frequency distortion at the very early times.

To summarize the construction of velocity-stack gathers using the conventional procedure defined by equation (6-10a) and the Radon transform based on equation (6-16), we refer to Figures 6.4-6 and 6.4-7. Starting with the synthetic CMP gather (Figure 6.4-6a), we use equation (6-10a) to get the conventional velocity-stack gather (Figure 6.4-6b), and the reconstructed gather from it (Figure 6.5-6c) using equation (6-10b). Again, starting with the same synthetic CMP gather (Figure 6.4-7a), we obtain the velocity-stack gather based on the Radon transform (Figure 6.4-7b) defined by equation (6-16), and the reconstructed gather from it (Figure 6.4-7c) using equation (6-10b). It is important to note that the reconstruction procedure using equation (6-10b) to obtain the modeled CMP gather is the same in both Figures 6.4-6 and 6.4-7. The difference lies in the way the velocity-stack gather is created — the conventional approach causes amplitude

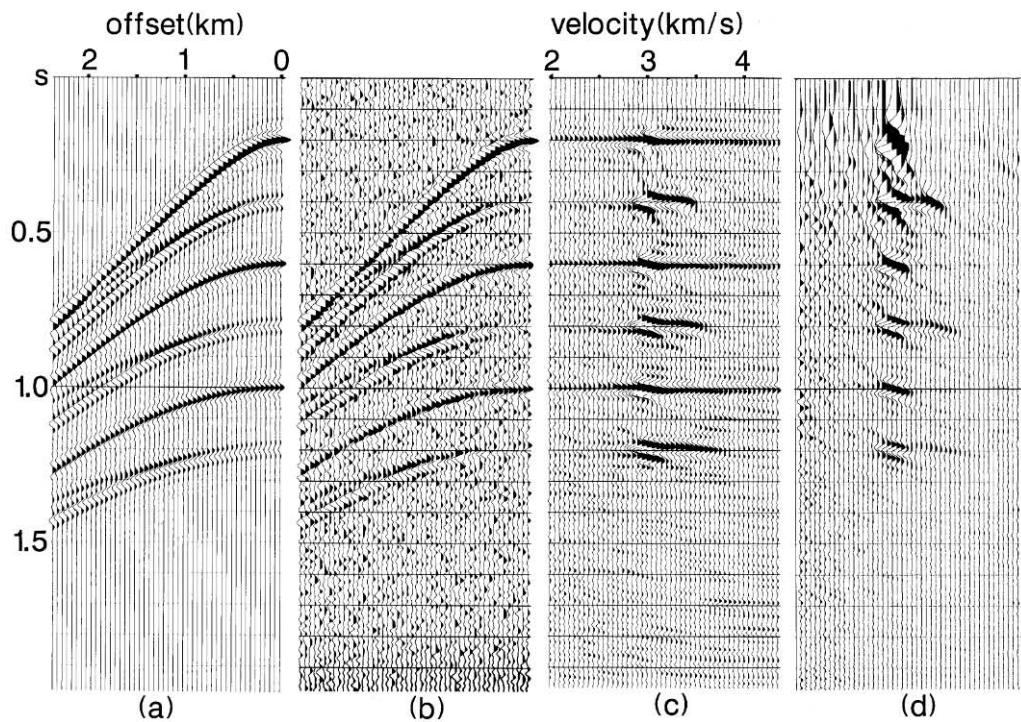


FIG. 6.4-8. (a) The synthetic CMP gather as in Figure 6.4-2c; (b) the same gather with added band-limited random noise; (c) the conventional velocity-stack gather (b); (d) the discrete Radon transform of (b). Note the improved velocity resolution in (d) as compared to the amplitude smearing in (c).

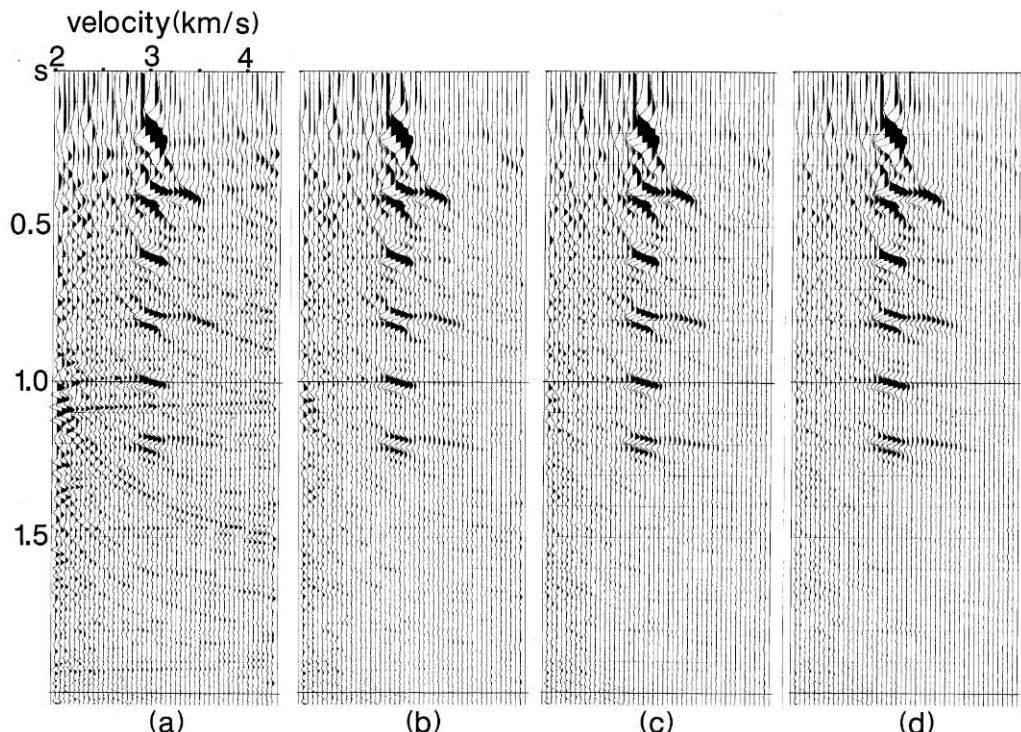


FIG. 6.4-9. (a) Velocity-stack gathers associated with the noise-contaminated CMP gather shown in Figure 6.4-8b estimated using β factors incorporated into the computation of the discrete Radon transform based on equation (6-16): (a) 0.01 percent, (b) 0.5 percent, (c) 1 percent, and (d) 5 percent.

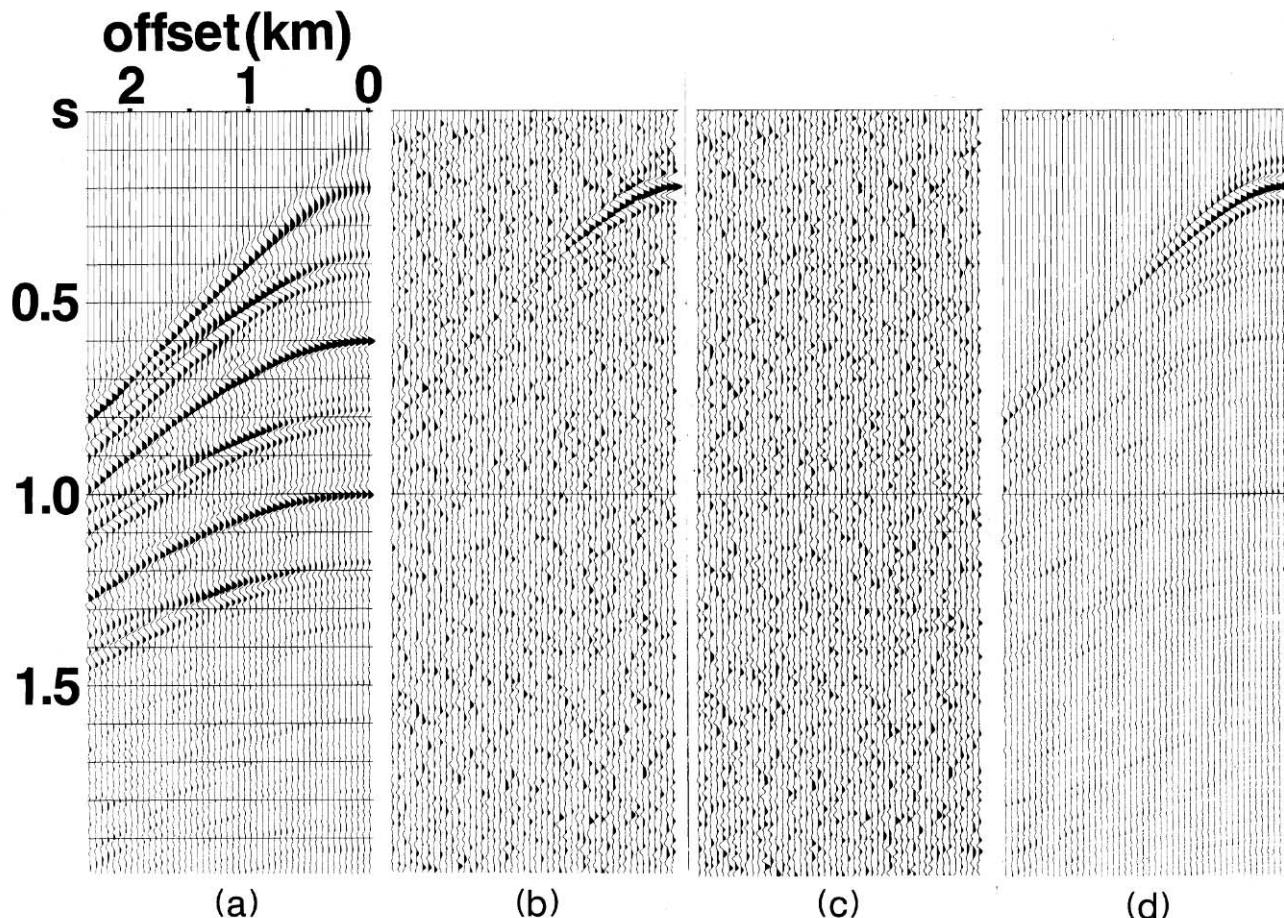


FIG. 6.4-10. (a) The modeled CMP gather reconstructed from the velocity-stack gather shown in Figure 6.4-8d; (b) the difference between the modeled CMP gather in (a) and the actual CMP gather in Figure 6.4-8b; (c) the noise component present in the actual CMP gather in (a); (d) difference between (b) and (c). Ideally, (d) should contain zero amplitudes.

smearing along the velocity axis (Figure 6.4-6c), and the procedure based on the Radon transform reduces this smearing and thus increases the resolution along the velocity axis (Figure 6.4-7c).

Now we examine the performance of the Radon transform in the presence of random noise. Consider the CMP gather in Figure 6.4-8a after the addition of band-limited random noise that is uncorrelated from trace to trace (Figure 6.4-8b). Figure 6.4-8c shows the conventional velocity-stack gather constructed by using equation (6-10a), and Figure 6.4-8d shows the velocity-stack gather constructed by using the Radon transform based on equation (6-16). When the data are contaminated by noise, choice of the damping factor β to stabilize the solution represented by equation (6-16) has a significant impact on the quality of the velocity-stack gather. It is important to emphasize that for the velocity-stack construction using the hyperbolic discrete Radon transform, noise is anything but hyperbolic events.

The β factor is equivalent to the prewhitening factor in Wiener-Levinson deconvolution. In this regard, the optimum β factor depends significantly upon the noise level in the data. Figure 6.4-9 shows estimates of the velocity-stack gathers using four different values of the β factor. For the noise-free case (Figure 6.4-7), theoretically, the best choice of β should be zero; however, to avoid exaggeration of numerical roundoff errors, β should be chosen to be a very small number. A practical rule of thumb is that stability in the SVD procedure does not improve further for β factors beyond a certain value (compare Figures 6.4-9c and d). For field data, a value of 1% of the largest eigenvalue of the matrix $\mathbf{L}^T \mathbf{L}$ of equation (6-16) often yields adequate results (Section F.3).

Since the elements of the matrix \mathbf{L} in equation (6-16) depends on the geometry of the CMP gather under consideration, estimation of the Radon trans-

form \mathbf{u} would normally require singular-value decomposition (equation F-22) for each individual gather. To circumvent the repeated application of the singular-value decomposition — a numerically intensive scheme, the Radon transform estimation procedure can be made efficient by implementing a two-staged computation. First, the part of the Radon transform associated with the operator \mathbf{L}^T in equation (6-16) can be computed using the actual offset distribution of the input CMP gather. Second, the part of the Radon transform associated with the operator $(\mathbf{L}^T \mathbf{L})^{-1}$ is computed by the singular-value decomposition only once for the entire data set using an offset distribution that may be considered an acceptable average of the actual offset distributions of the CMP gathers along the line traverse.

Finally, we examine the ability of the Radon transform in separating hyperbolic events from band-limited random noise. Consider the same noisy gather as in Figure 6.4-8b. Reconstruct this CMP gather as shown in Figure 6.4-10a using the velocity-stack gather shown in Figure 6.4-8d, and subtract the result from the original noisy CMP gather (Figure 6.4-8b). This difference gather is shown in Figure 6.4-10b, and it represents the least-squares error e defined as the difference between the actual CMP gather \mathbf{d} and the modeled CMP gather \mathbf{d}' defined by equation (6-15). Ideally, it should contain anything but hyperbolic events. Nevertheless, the missing high-frequency components in the shallowest part of the reconstructed CMP gather have leaked into the difference gather (Figure 6.4-10d). The actual random noise added to the original CMP gather (Figure 6.4-8a) is shown in Figure 6.4-10c. Compare the extracted noise (Figure 6.4-10b) with the actual noise (Figure 6.4-10c) and note that the difference between the two (Figure 6.4-10d) contains negligibly small residual amplitudes aside from some remnants of the hyperbolic events.

Impulse Response of the Velocity-Stack Operator

An isolated spike in the offset domain (Figure 6.4-11a) maps to the velocity domain using equation (6-10a) along a curved trajectory (Figure 6.4-12a). Solve equation (6-9b) for v to obtain the equation for this trajectory in the velocity domain:

$$v = \frac{2h}{\sqrt{t^2 - \tau^2}}. \quad (6-20)$$

The curvature is greater for a spike situated at far offset than a spike situated at near offset (Figures 6.4-11b and 6.4-12b). Also, the curvature is greater for a spike situated at an early time on a given offset than a spike situated at a late time on the same offset (Figures 6.4-11c and 6.4-12c).

Inverse transformation of the conventional velocity-stack gathers (Figures 6.4-12a,b,c) back to the offset domain does not reproduce the isolated spikes (Figures 6.4-13a,b,c). Instead, the amplitudes are smeared across each of the CMP gathers. The amplitude smearing is worse for spikes situated at near offsets (Figure 6.4-13b) and late times (Figure 6.4-13c).

Figures 6.4-14a,b,c show the velocity-stack gathers based on the Radon transform of equation (6-16) associated with the isolated spikes in Figures 6.4-11a,b,c. Inverse mapping these velocity-stack gathers, in contrast with the results obtained from inverse mapping of the conventional velocity-stack gathers (Figures 6.4-13a,b,c), yields a fairly good focusing of energy to the isolated spike locations (Figures 6.4-15a,b,c).

How is the velocity-stack processing affected by irregularities in the data? Refer to the CMP gather in Figure 6.4-11d. It contains a trace with a monofrequency signal, another trace with polarity reversed, a dead trace, and another trace with a dead zone. The conventional velocity-stack gather is shown in Figure 6.4-12d, and the CMP gather reconstructed from it is shown in Figure 6.4-13d. Compare this figure with Figure 6.4-11d and note the differences along the reflection hyperbolas in amplitude and curvature where the anomalous traces are located. Also, note the smearing of the monofrequency signal over a large range of traces away from the original trace location. The velocity-stack gather based on the Radon transform associated with the CMP gather in Figure 6.4-11d is shown in Figure 6.4-14d. The CMP gather reconstructed from it (Figure 6.4-15d) shows less smearing of the monofrequency signal. As with the conventional velocity-stack gather, however, the dead trace and the trace with a dead zone in the original CMP gather (Figure 6.4-11d) again have been replaced with nonzero amplitudes, and traveltimes have been distorted along the reflection hyperbolas where the anomalous traces are located.

The transform parameters of practical importance are the velocity range and the velocity increment used in constructing velocity-stack gathers. The velocity range should span the velocities associated with primary and multiple reflections. A good practice for the choice of velocity increment is such that the number of traces in velocity space is set equal to the traces in the offset space.

Field Data Examples

We shall now consider field data examples of the Radon transform. Figure 6.4-16a shows a deep-water CMP

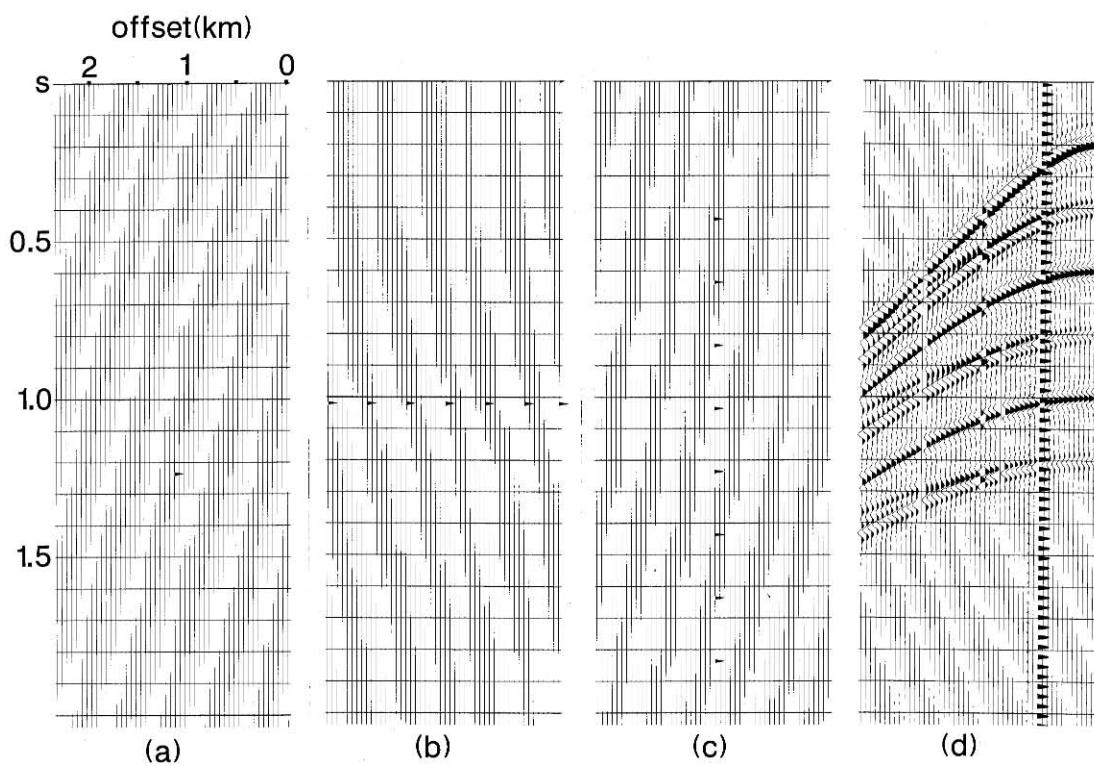


FIG. 6.4-11. Synthetic CMP gathers that contain (a) a single spike; (b) a series of spikes at equal time but at different offsets; (c) a series of spikes at equal offset but at different times; (d) anomalous traces.

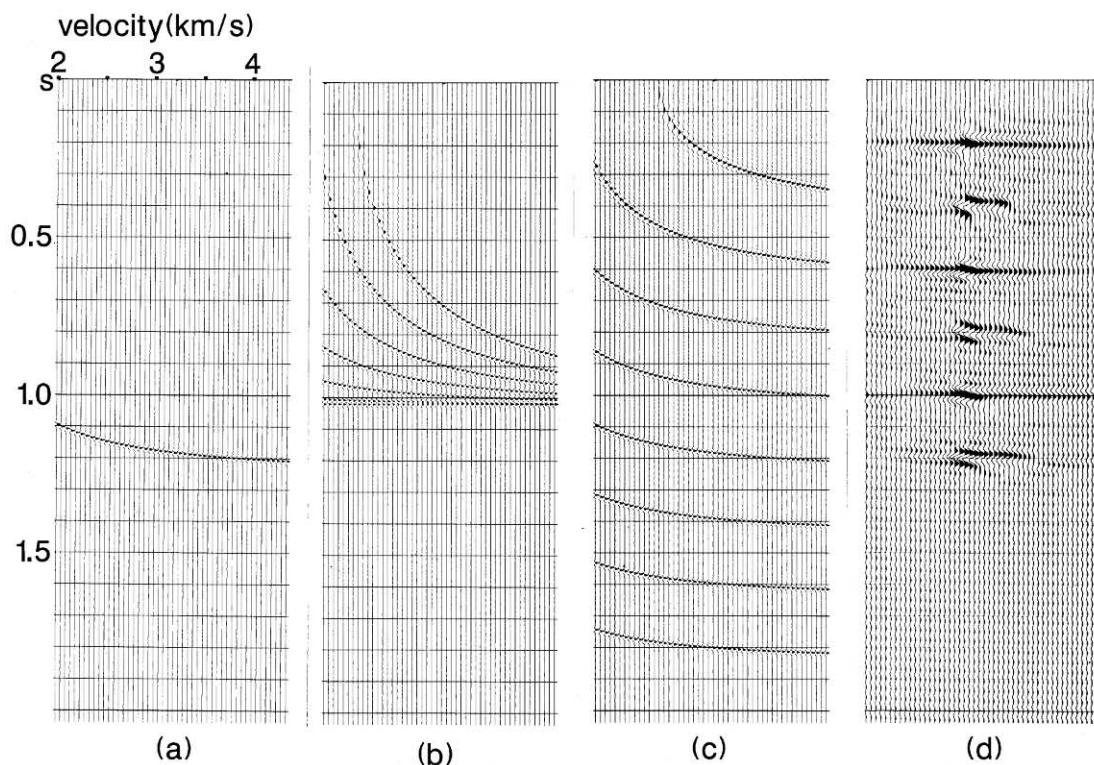


FIG. 6.4-12. Conventional velocity-stack gathers associated with the CMP gathers in Figure 6.4-11.

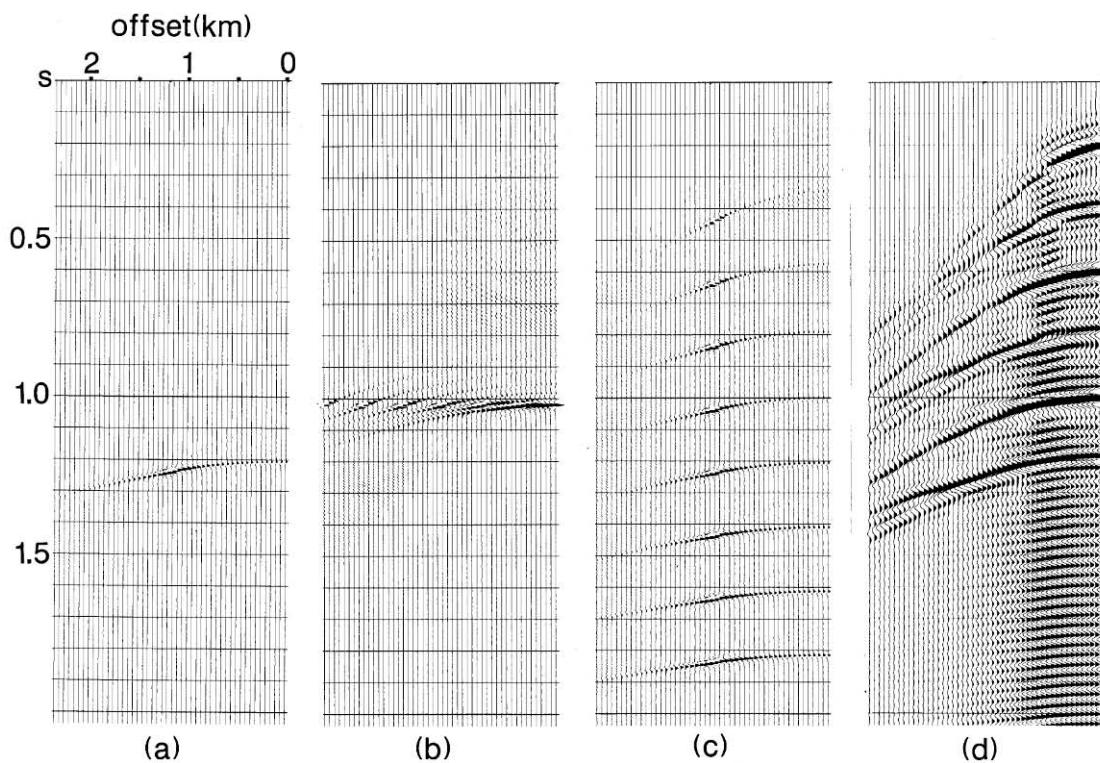


FIG. 6.4-13. Reconstructed CMP gathers from the conventional velocity-stack gathers in Figure 6.4-12. Compare with Figure 6.4-11.

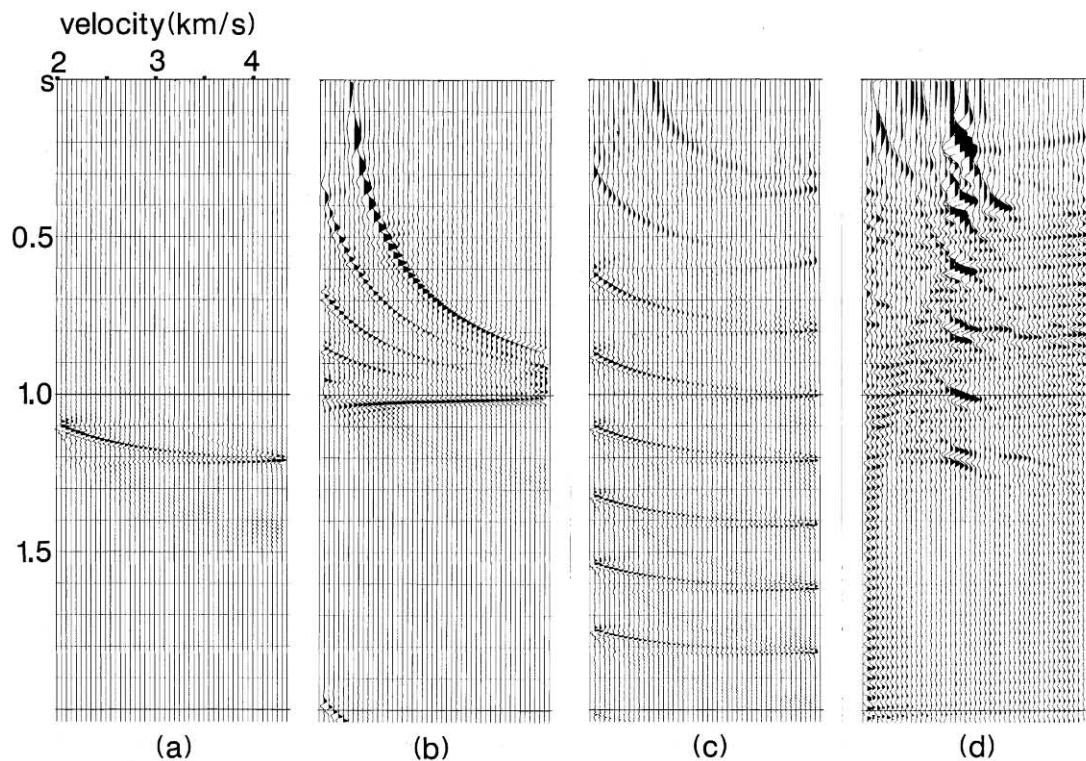


FIG. 6.4-14. Velocity-stack gathers that represent the Radon transforms of the CMP gathers in Figure 6.4-11. Compare with Figure 6.4-12.

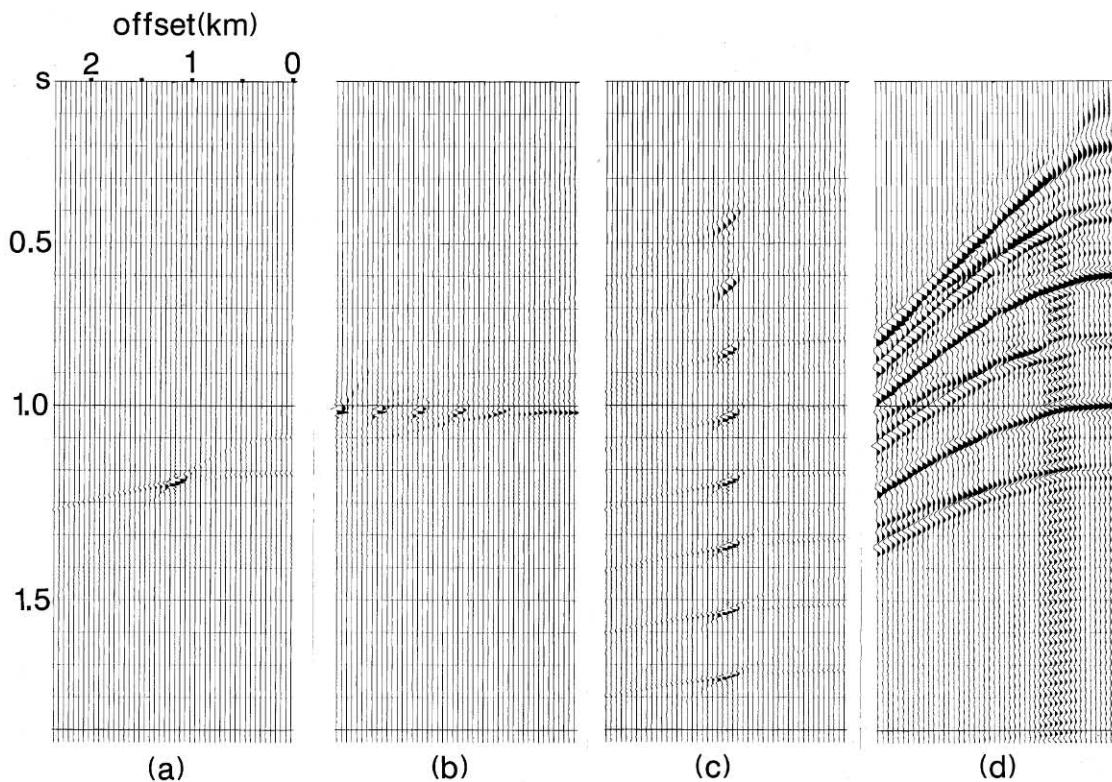


FIG. 6.4-15. Reconstructed CMP gathers from the proper velocity-stack gathers in Figure 6.4-14. Compare with Figures 6.4-11 and 6.4-13.

gather that contains strong multiples below 3.5 s. The conventional velocity-stack gather (Figure 6.4-16b) shows the familiar amplitude smearing, whereas the velocity-stack gather based on the Radon transform (Figure 6.4-16c) shows better focusing of hyperbolic events. The reconstructed CMP gather (Figure 6.4-16d) contains all the hyperbolic events present in the original CMP gather (Figure 6.4-16a) and excludes noise. The amplitudes on the reconstructed CMP gather appear to be faithfully restored to their original values.

A noisier CMP gather from a shallow-water survey is shown in Figure 6.4-17a. Note the strong-amplitude, low-frequency bursts of energy similar to ground roll. A spike in the offset domain maps along a curved trajectory in the velocity domain; the larger the offset and the shallower the time at which this spike is located, the more the curvature of the trajectory (Figures 6.4-11 through 6.4-15). Note the presence of curved trajectories in the conventional velocity-stack gather in Figure 6.4-17b. Although the velocity-stack gather based on the Radon transform (Figure 6.4-17c) also contains these features, it does not have the amplitude smearing that dominates the conventional velocity-stack gather. The CMP gather reconstructed from the velocity-stack

gather shown in Figure 6.4-17c contains all the hyperbolic events and excludes the random noise and coherent noise with linear moveout present in the original CMP gather (compare Figures 6.4-17a and d).

The result shown in Figure 6.4-17d suggests that velocity-stack transformation, when implemented as a special form of the discrete Radon transform, can be used to attenuate random and coherent linear noise on CMP data (Hampson, 1987).

Another potential application of velocity-stack processing is in the construction of high-resolution constant-velocity stacks. Figure 6.4-18 shows constant-velocity-stack panels constructed from about 100 CMP gathers. These panels were generated twice — by computing conventional velocity-stack gathers and sorting them to CVS panels, and by computing velocity-stack gathers using the Radon transform and sorting the results into CVS panels. The multiples contaminate the primaries on the panels based on conventional velocity-stack gathers even though the constant-velocity range used is associated with the primaries. This is because of the lateral smearing of amplitudes associated with multiples and primaries in the velocity space as illustrated in Figure 6.4-2d. The multiples appear to be significantly attenuated on the panels based on the velocity-

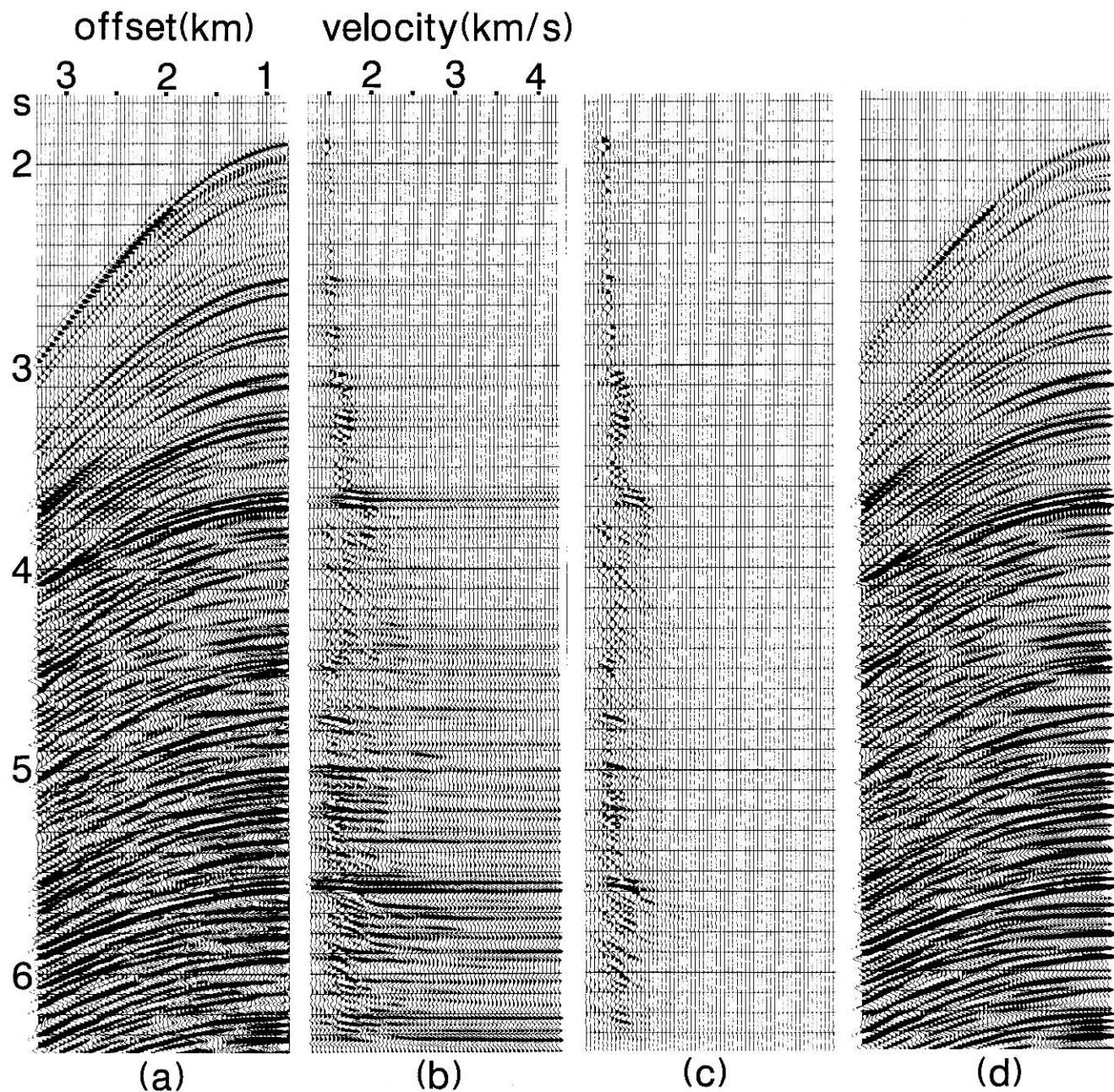


FIG. 6.4-16. (a) A deep-water CMP gather with strong multiples; (b) the conventional velocity-stack gather; (c) the proper velocity-stack gather; (d) the CMP gather reconstructed from (c). Compare with (a) and note the preservation of amplitudes along hyperbolic events. (Data courtesy Norwegian Petroleum Directorate.)

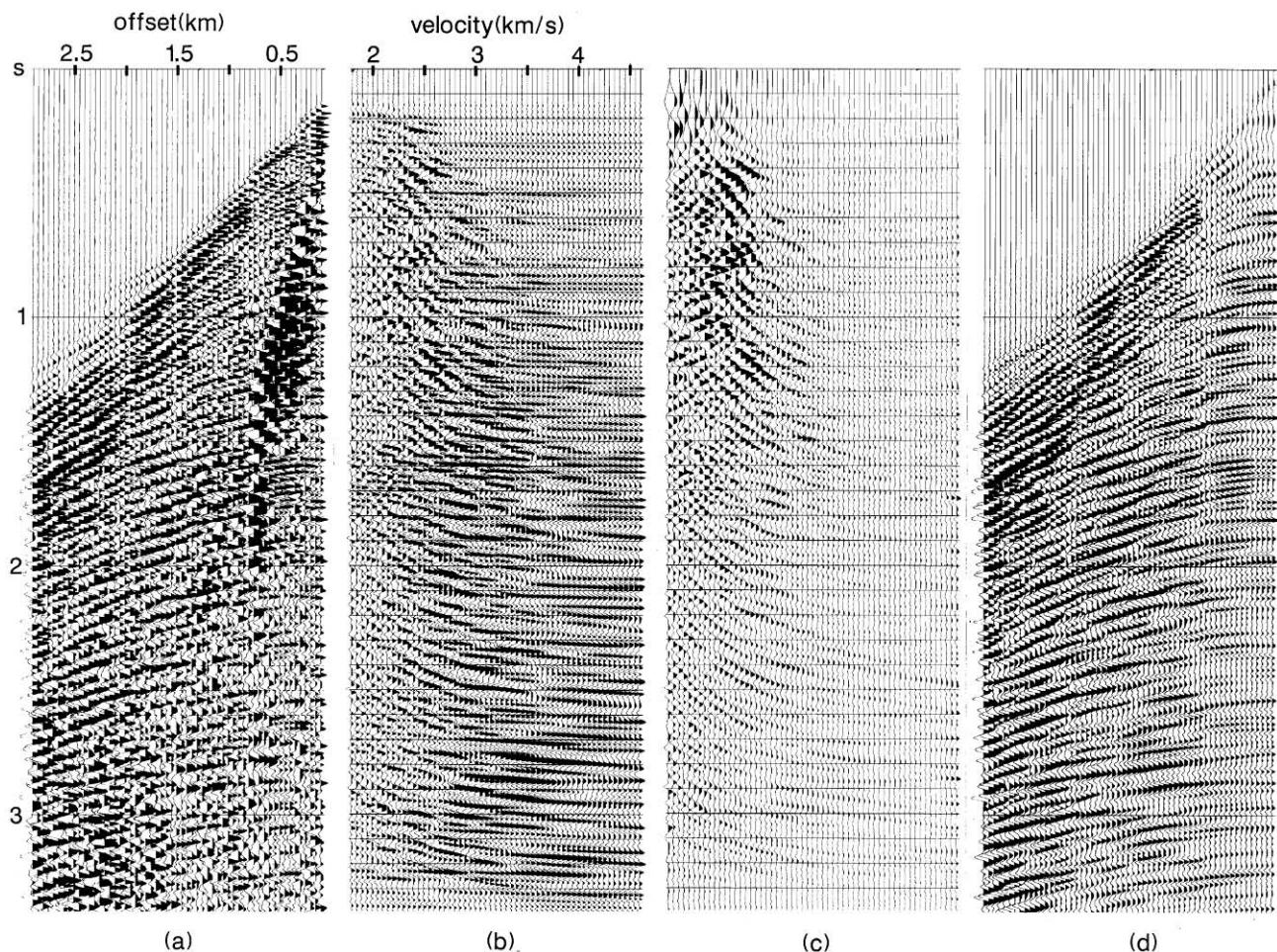


FIG. 6.4-17. (a) A shallow-water CMP gather with strong linear noise; (b) conventional velocity-stack gather; (c) proper velocity-stack gather; (d) the CMP gather reconstructed from (c). Compare with (a) and note that hyperbolic events are enhanced, and random and linear noise are suppressed. (Data courtesy Abu Dhabi National Oil Company.)

stack gathers computed by using the Radon transform. The lateral smearing has been reduced in the velocity space by the Radon transform as illustrated in Figure 6.4-4d.

Radon-Transform Multiple Attenuation

Consider the synthetic CMP gather in Figure 6.4-7a and the velocity-stack gather (Figure 6.4-7b) estimated from it using the discrete Radon transform. By including the entire velocity-stack gather in the summation in equation (6-10b), we get the fully reconstructed CMP gather shown in Figure 6.4-7c. That result is reproduced in Figure 6.4-19a. Aside from the loss of high-frequency energy at early times, this modeled CMP gather is a close approximation to the original CMP gather (Figure 6.4-7a).

Instead of including the entire velocity-stack gather (Figure 6.3-15b) in the summation in equation (6-10b), a CMP gather with only multiples (Figure 6.4-19b) or only primaries (Figure 6.4-19c) can be reconstructed by simply assigning suitable pass-reject zones over the velocity-stack gather. Compare the modeled multiples-only and primaries-only CMP gathers (Figures 6.4-19b,c) with the actual CMP gathers shown in Figures 6.4-2b,a. (The modeled shallow primary in Figure 6.4-19c corresponds to the primary in Figure 6.4-2b.) It appears that, although insignificant, the multiples-only gather (Figure 6.4-19b) contains some residual primary energy, and the primaries-only gather (Figure 6.4-19c) contains some residual multiple energy. In practice, it often is desirable to model the multiples and subtract the result from the actual CMP gather (Hampson, 1986). One reason for this is the necessity to retain in CMP data some of the nonhyperbolic energy, such

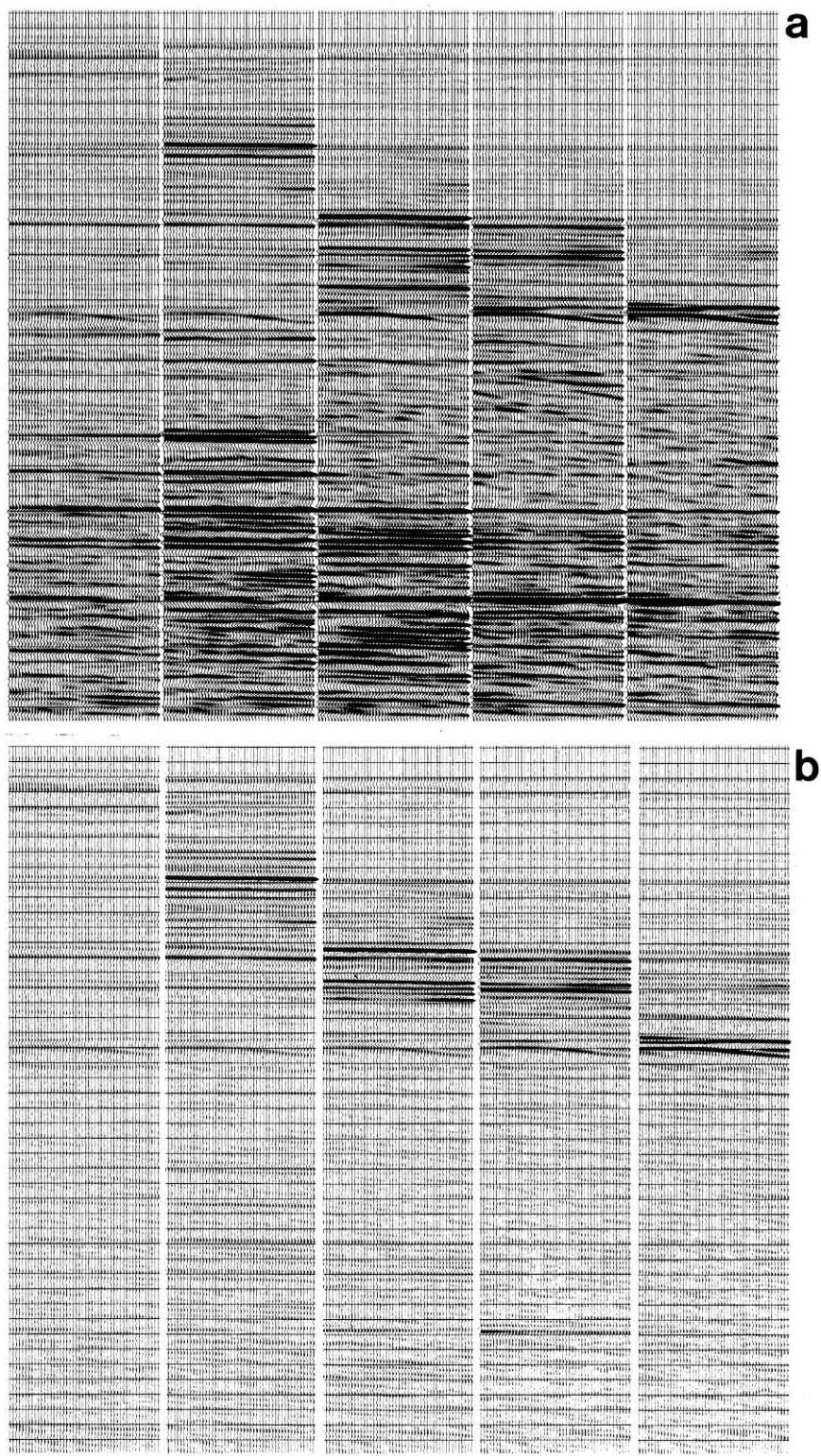


FIG. 6.4-18. Constant-velocity-stacks using five constant velocities. Panels in (a) are based on conventional velocity stacking and panels in (b) are based on proper velocity stacking using the Radon transform. The constant velocities fall in the range that corresponds to the primary velocity trend. Note the multiple contamination of the panels created from conventional velocity stacking (top).

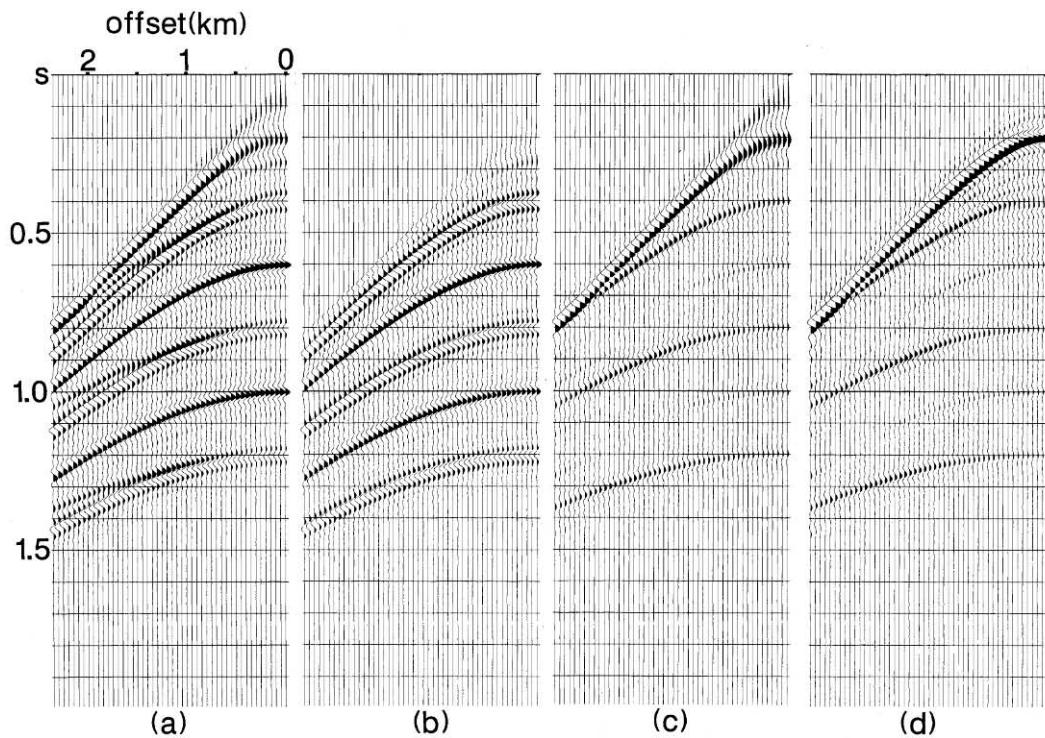


FIG. 6.4-19. (a) Reconstruction of the noise-free CMP gather in Figure 6.4-7a using (a) the entire velocity-stack gather in Figure 6.4-7b; (b) allowing only the multiple energy; (c) allowing only the primary energy; (d) subtraction of (b) from Figure 6.4-7a.

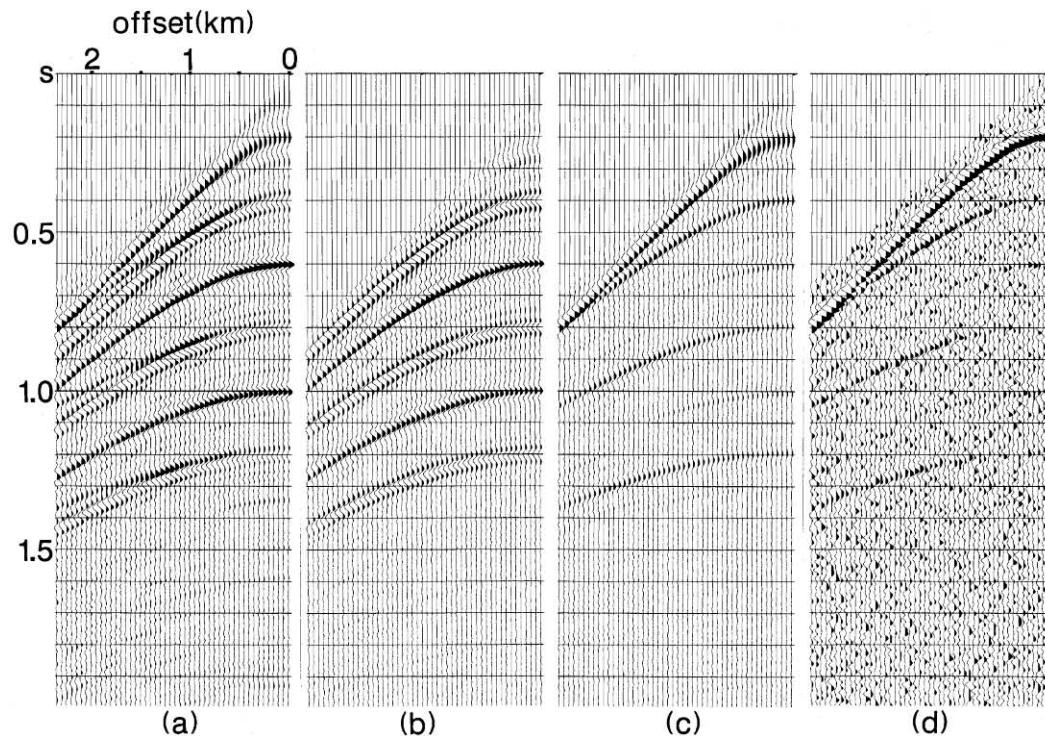


FIG. 6.4-20. Reconstruction of the noise-contaminated CMP gather in Figure 6.4-8b using (a) the entire velocity-stack gather in Figure 6.4-8d; (b) allowing only the multiple energy; (c) allowing only the primary energy; (d) subtraction of (b) from Figure 6.4-8b. Aside from the muted zone, the noise in the original gather (Figure 6.4-8b) is retained.

as diffractions. In the present example, Figure 6.4-19d shows the difference between the original CMP gather (Figure 6.4-7a) and the modeled multiples-only CMP gather (Figure 6.4-19b). When compared with Figure 6.4-19c, the subtraction result shown in Figure 6.4-19d shows differences at early times due to the t^2 -stretching artifacts.

The subtraction actually tends to retain the original texture of the data; this is demonstrated with the noise-contaminated CMP gather in Figure 6.4-8b. Using the entire velocity-stack gather (Figure 6.4-8d) associated with this CMP gather, we get the fully reconstructed CMP gather shown in Figure 6.4-20a. Note that this modeled CMP gather is a close approximation to the noise-free CMP gather (Figure 6.4-7a). Also, compare the modeled multiples-only and primaries-only CMP gathers (Figures 6.4-20b,c) with the corresponding results from the noise-free CMP gather (Figures 6.4-19b,c). Figure 6.4-20d shows the difference between the original CMP gather (Figure 6.4-8b) and the modeled multiples-only CMP gather (Figure 6.4-20b). When compared with Figure 6.4-20c, the subtraction result shown in Figure 6.4-20d retains the original noise component present in the data (Figure 6.4-8b).

Now consider a field data example for separation of primaries and multiples by the discrete Radon transform. Shown in Figure 6.4-21 are the deep-water CMP gather, and the reconstructed primaries-only, multiples-only, and the subtraction gathers. Corresponding velocity spectra in Figure 6.4-22 clearly show that multiples largely have been removed from the input CMP gather. Nevertheless, a complete separation of multiples from primaries is not achievable. As an example, note the residual primary energy especially visible above 4 s in the multiples-only CMP gather (Figure 6.4-21c). Accordingly, the subtraction result (Figure 6.4-21d) inevitably will have some remnant multiple energy. This is especially apparent in the corresponding velocity spectrum (Figure 6.4-22d); note the small coherency peaks in the multiple zone below 4 s.

Since the Radon-transform multiple attenuation using velocity-stack gathers exploits the velocity discrimination between primaries and multiples, it is appropriate to compare the technique with other methods that also are based on the same criterion. Figure 6.4-23 shows the synthetic CMP gather with multiple attenuation using the Radon transform, model-based (Section 6.1) and frequency-wavenumber filtering (Section 6.2) methods. Note that the model-based method fails to preserve the amplitude characteristics of the input data (Figure 6.4-23c). This is a direct consequence of the problems in creating model traces for multiples as was referred to in Section 6.1. The frequency-wavenumber filtering method has caused attenuation of primaries at near offsets — an effect similar to inside-trace muting (Figure 6.4-23d). Among the three approaches, the

Radon transform method appears to best preserve amplitude and phase characteristics of the input data (Figure 6.4-23b).

Further comparisons between the three methods based on velocity discrimination can be made using the noise-contaminated CMP gather in Figure 6.4-24. Again, the Radon transform yields the most desirable result. In fact, whenever data, which require multiple attenuation, are used for amplitude inversion to estimate acoustic impedance or amplitude variation with offset (AVO) analysis, the preferred technique for multiple attenuation most often is the Radon transform.

A challenging data example with short-period interbed multiples is shown in Figure 6.4-25. The velocity spectra computed from the original CMP gather (Figure 6.4-25a) and the gather with multiples removed (Figure 6.4-25d) are shown in Figure 6.4-26. Portions of CMP stacked sections with and without velocity-stack processing for multiple suppression are shown in Figure 6.4-27. An important observation in Figure 6.4-27a is the apparent lateral continuity caused by the multiples. This continuity is replaced, in Figure 6.4-27b, with features that are perhaps geologically more detailed and plausible. Note the presence of a subtle structural closure at 1.5 s in Figure 6.4-27b; this feature is completely disguised among the multiples in Figure 6.4-27a. Unfortunately, because of the unavailability of well logs, no definite assessment can be made about the details in the CMP stacked section processed for multiple suppression (Figure 6.4-27b).

We now demonstrate application of the Radon transform to moveout-corrected CMP gathers (Hampson, 1986). Figures 6.4-28 shows a CMP stack without multiple attenuation. Water-bottom and peg-leg multiples dominate the lower half of the sections and interfere with primary reflections of interest. Strong multiple reflections also are seen on the selected CMP gather in Figure 6.4-29a. Most of the multiples — water-bottom and the peg-legs associated with the depositional sequence boundary at 2 s, are long-period.

Hampson's implementation of the Radon transform requires input CMP gathers to be moveout-corrected using a primary velocity function (Figure 6.4-29b). The aim is to make the moveout of events — primaries and multiples, approximately parabolic. Prior to Radon transformation, spatial interpolation of the data may be needed to make the trace interval sufficiently small (Figure 6.4-29c). The Radon transformation itself is done using the moveout at a reference offset, instead of velocity, as the variable for the horizontal axis (Figure 6.4-29d).

Multiple attenuation in the transform domain is achieved by rejecting a zone that includes the primaries

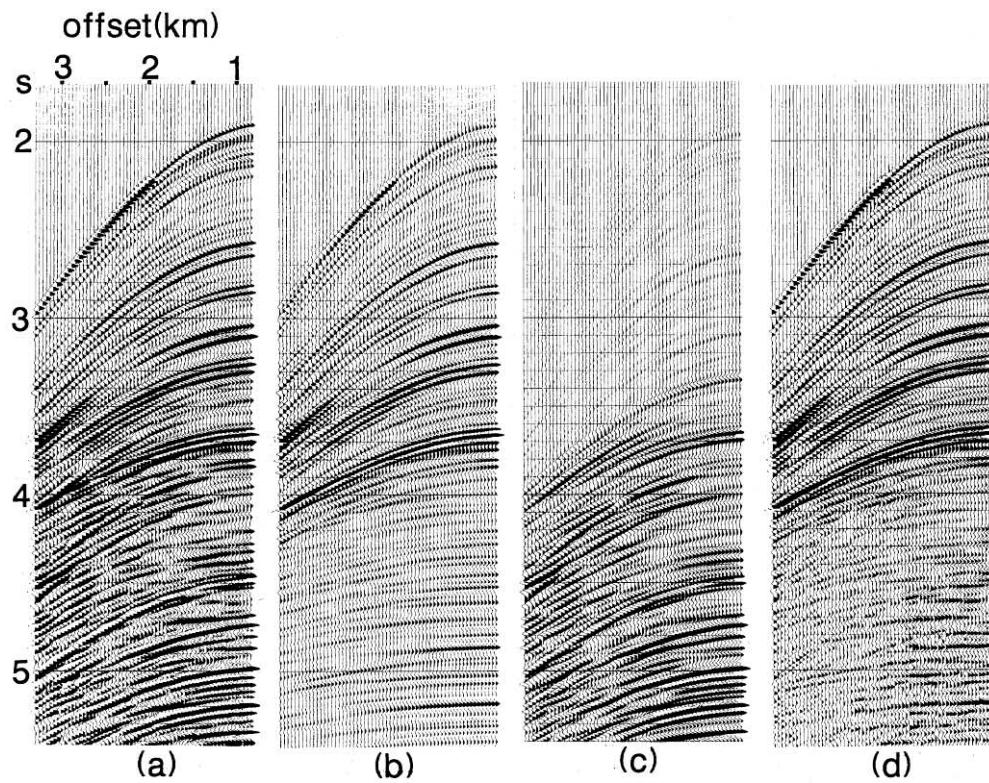


FIG. 6.4-21. (a) A deep-water CMP gather; (b) full reconstruction from the proper velocity-stack gather; (c) multiples-only reconstruction; (d) difference between (a) and (c). (Data courtesy Abu Dhabi National Oil Company.)

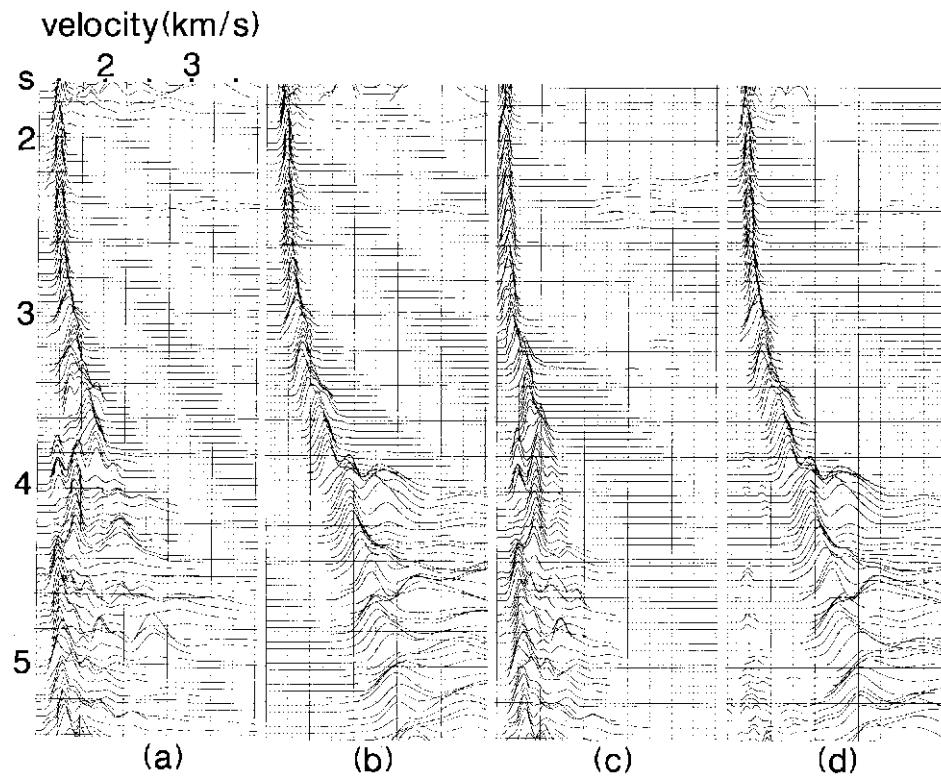


FIG. 6.4-22. Velocity spectra associated with the CMP gathers in Figure 6.4-21.

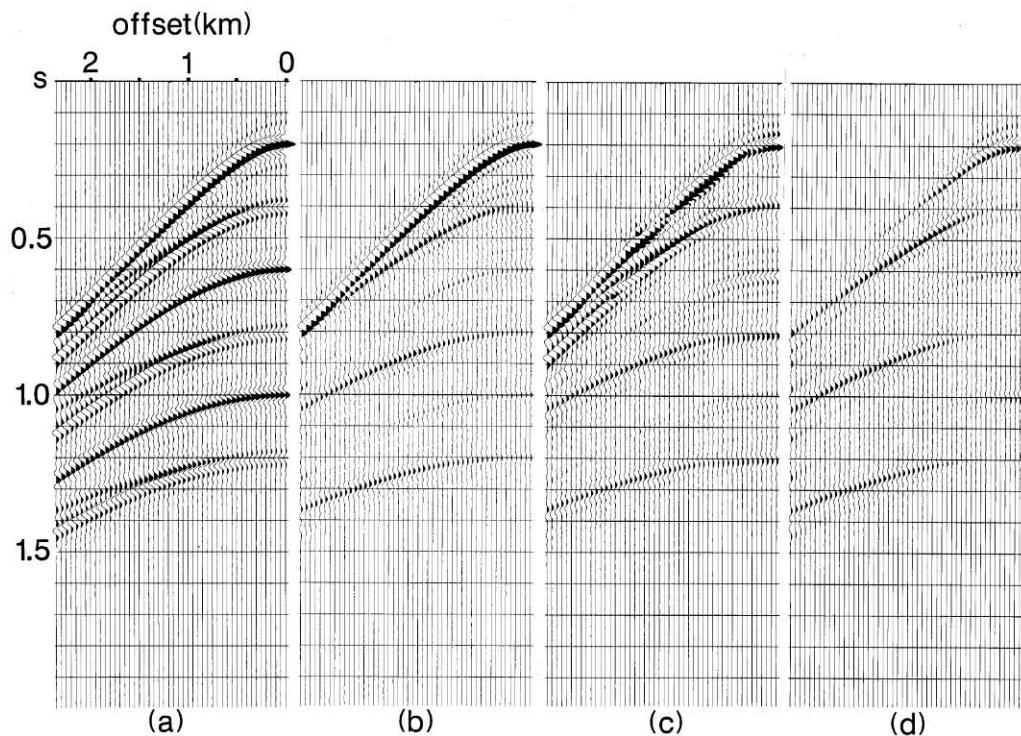


FIG. 6.4-23. (a) Synthetic CMP gather as in Figure 6.4-2c; after multiple attenuation using (b) the Radon transform, (c) the modeling of multiples in $t - x$ domain (Section 6.1), and (d) the $f - k$ method (Section 6.2).

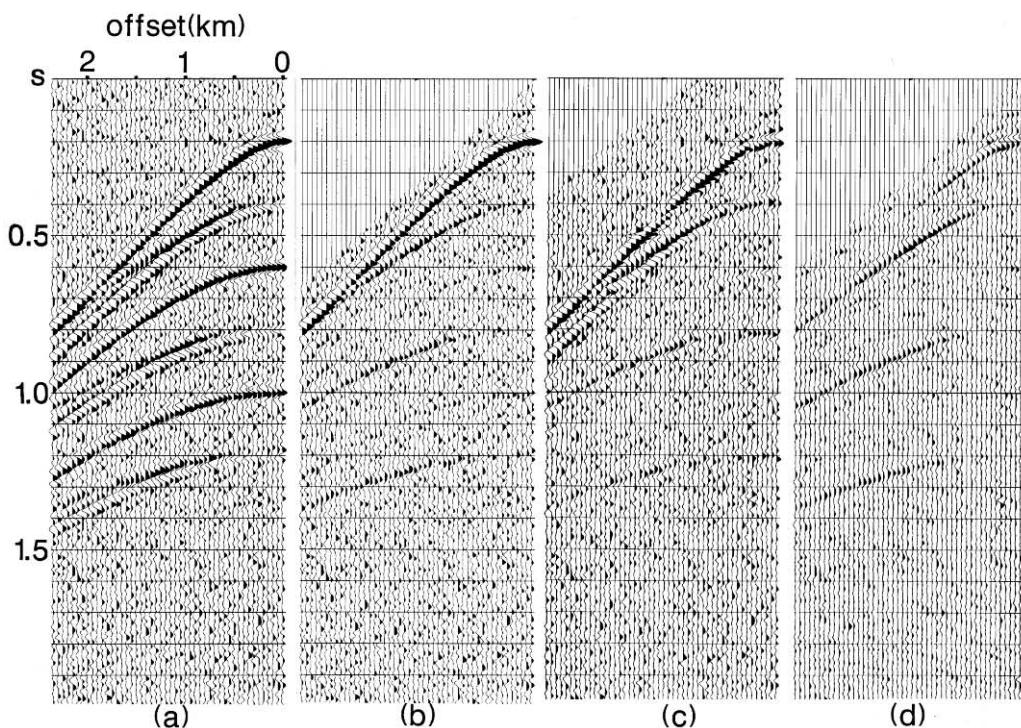


FIG. 6.4-24. (a) Synthetic CMP gather as in Figure 6.4-2c with added band-limited random noise; after multiple attenuation using (b) the Radon transform, (c) the modeling of multiples in $t - x$ domain (Section 6.1), and (d) the $f - k$ method (Section 6.2).

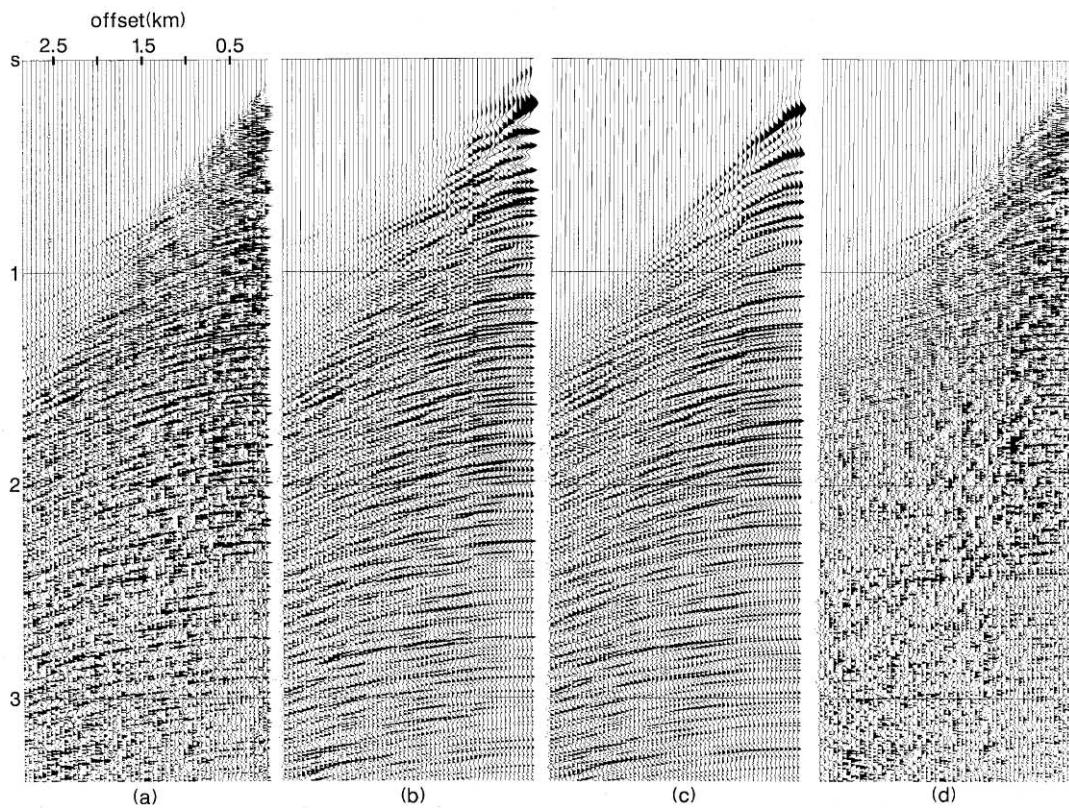


FIG. 6.4-25. (a) A shallow-water CMP gather; (b) full reconstruction from the proper velocity-stack gather; (c) multiples-only reconstruction; (d) difference between (a) and (c). (Data courtesy Abu Dhabi National Oil Company.)

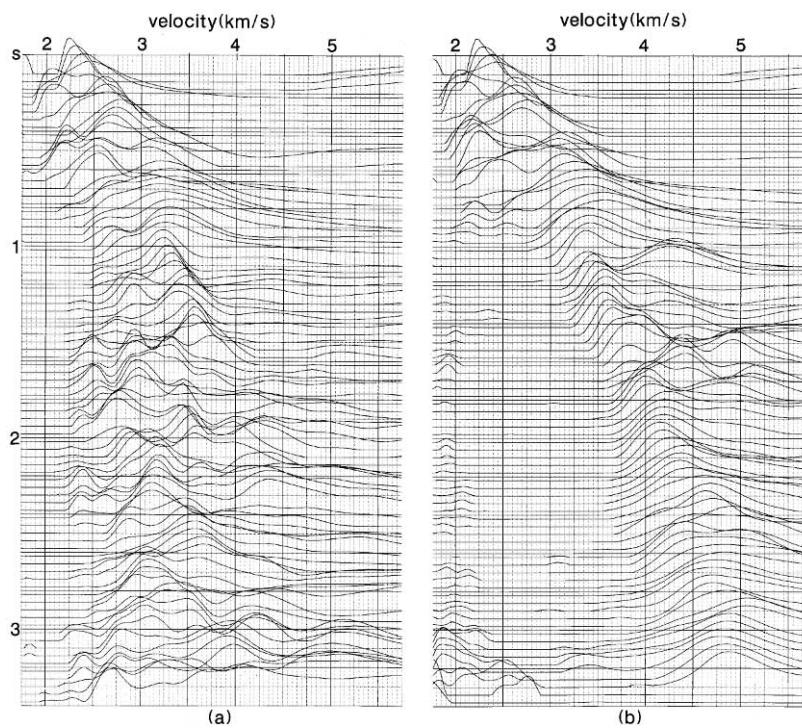


FIG. 6.4-26. Velocity spectra associated with (a) the CMP gather in Figure 6.4-25a; (b) the CMP gather in Figure 6.4-25d.

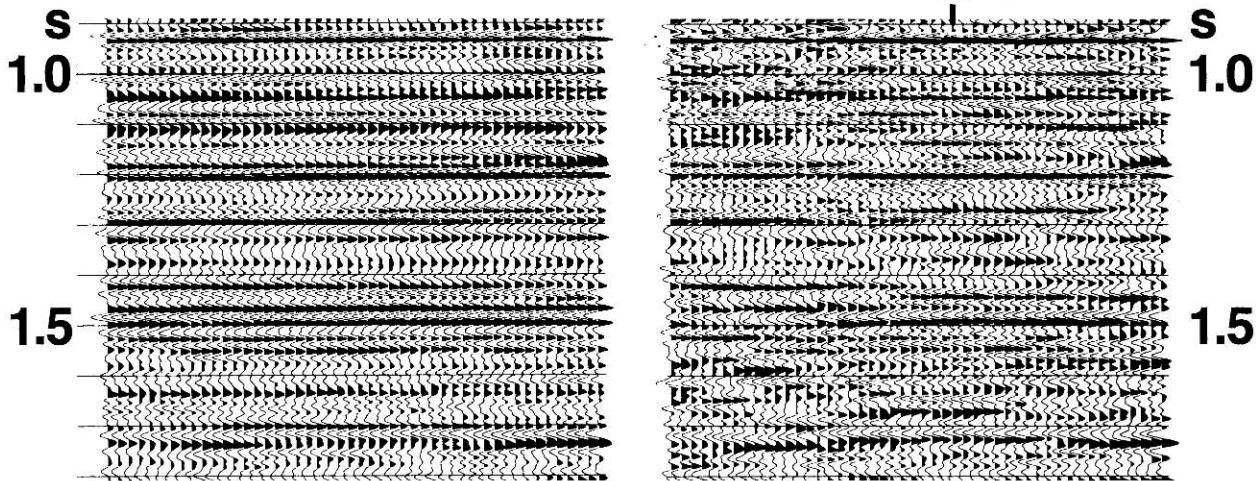


FIG. 6.4-27. (a) A portion of the CMP stacked section associated with the CMP gather in Figure 6.4-25a with short-period multiples; (b) same portion of the CMP stacked section associated with the CMP gather in Figure 6.4-25d with velocity-stack processing for multiple suppression. Note the apparent lateral continuity caused by the short-period multiples in (a); this false continuity is removed in (b), thereby uncovering a probable subtle structural feature at 1.5 s below midpoint A. (Data courtesy Abu Dhabi National Oil Company.)

(Figure 6.4-30a). The inverse transform yields the reconstructed gather that contains presumably only multiples (Figure 6.4-30b). Again, to preserve data characteristics, rather than modeling the primaries by reconstruction, it is preferred to model the multiples (Figure 6.4-30b) and subtract the modeled gather from the original (Figure 6.4-29c). The difference gather should contain the primaries (Figure 6.4-30c). Finally, traces which were generated during trace interpolation (Figure 6.4-29c) are dropped (Figure 6.4-30d). Compare Figure 6.4-30d — the gather after multiple attenuation, with Figure 6.4-29b — the gather before multiple attenuation. Aside from a residual of the water-bottom multiples, much of the energy associated with multiples has been removed.

Figure 6.4-31 shows the CMP stack after Radon-transform multiple attenuation. Note that multiple attenuation has uncovered the primary event at 3.5 s associated with an unconformity. Multiple attenuation also helps migration to yield an improved image as shown in Figure 6.4-32.

6.6 LINEAR UNCORRELATED NOISE ATTENUATION

Random noise uncorrelated from trace to trace abounds in recorded data and retains its presence at almost all

steps in a processing sequence. CMP stacking reduces the uncorrelated noise in the data significantly (Section 1.5). Noise that remains in the stacked data can have adverse effect on reflection continuity.

While time-variant filtering (Section 1.1) reduces noise in the temporal direction, it does not necessarily attenuate the noise uncorrelated from trace to trace. Although a number of multichannel signal enhancement techniques has been practiced, the one that best preserves relative amplitudes and retains the signal character without amplitude distortion is based on spatial prediction filtering invented by [Canales \(1984\)](#). Mathematical details of this uncorrelated noise attenuation technique is provided in Section F.5.

To understand the conceptual basis for spatial prediction filtering, first, recall from Section 2.3 the prediction filtering in the temporal direction. A recorded seismic trace is represented by a time series with two components — a predictable part that relates to the multiple reflections and an unpredictable part that relates to the primary reflections. The prediction process involves estimating some future value of the input series defined by the prediction lag from the past values of the input series. For the prediction process to work on a seismic trace, strictly, it must represent a zero-offset seismogram recorded over a horizontally layered earth so as to preserve periodicity of multiples. Assuming this

(text continues on p. 966)

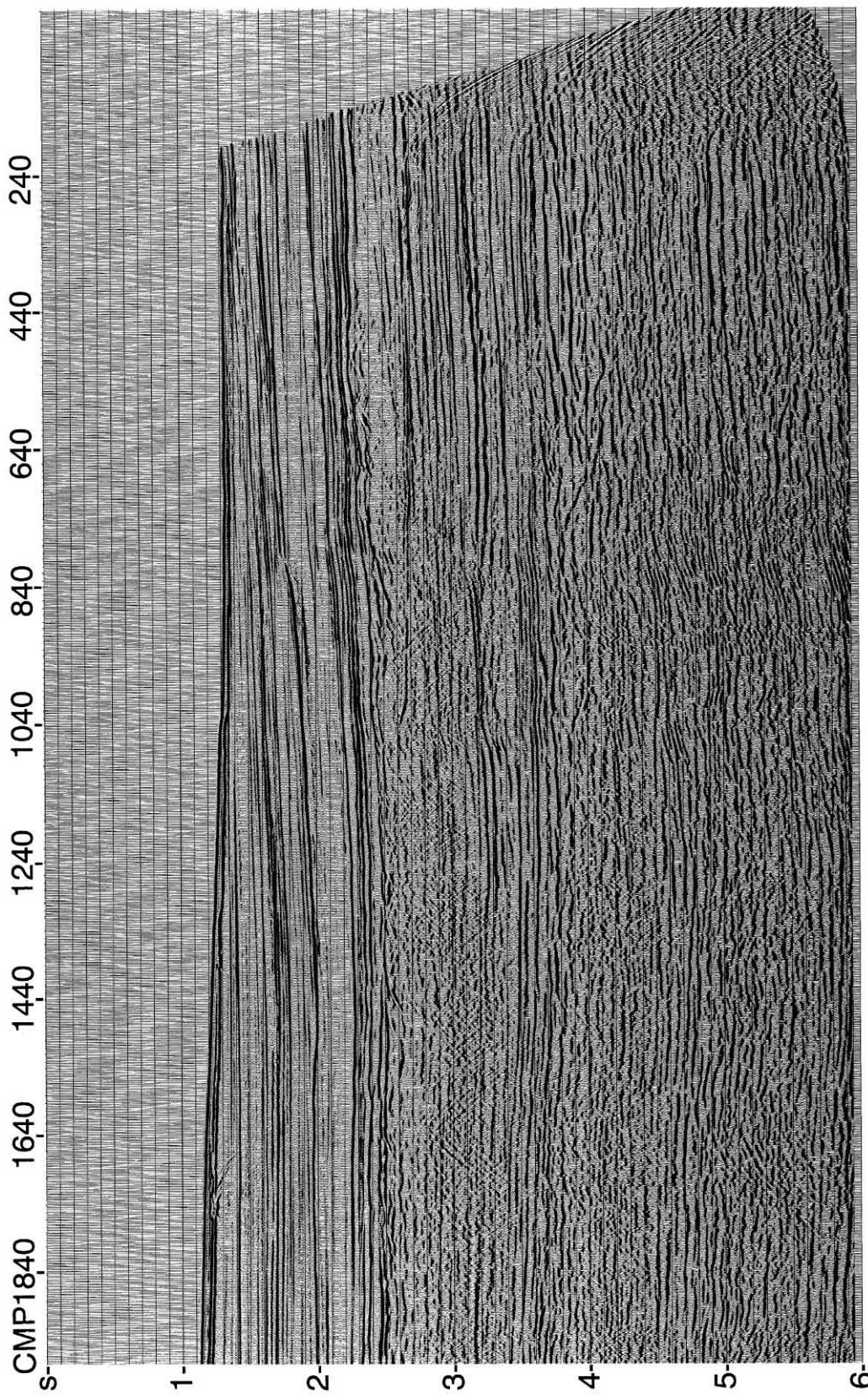


FIG. 6.4-28. A CMP-stacked section without multiple attenuation. (Data courtesy BP-Amoco and Shell.)

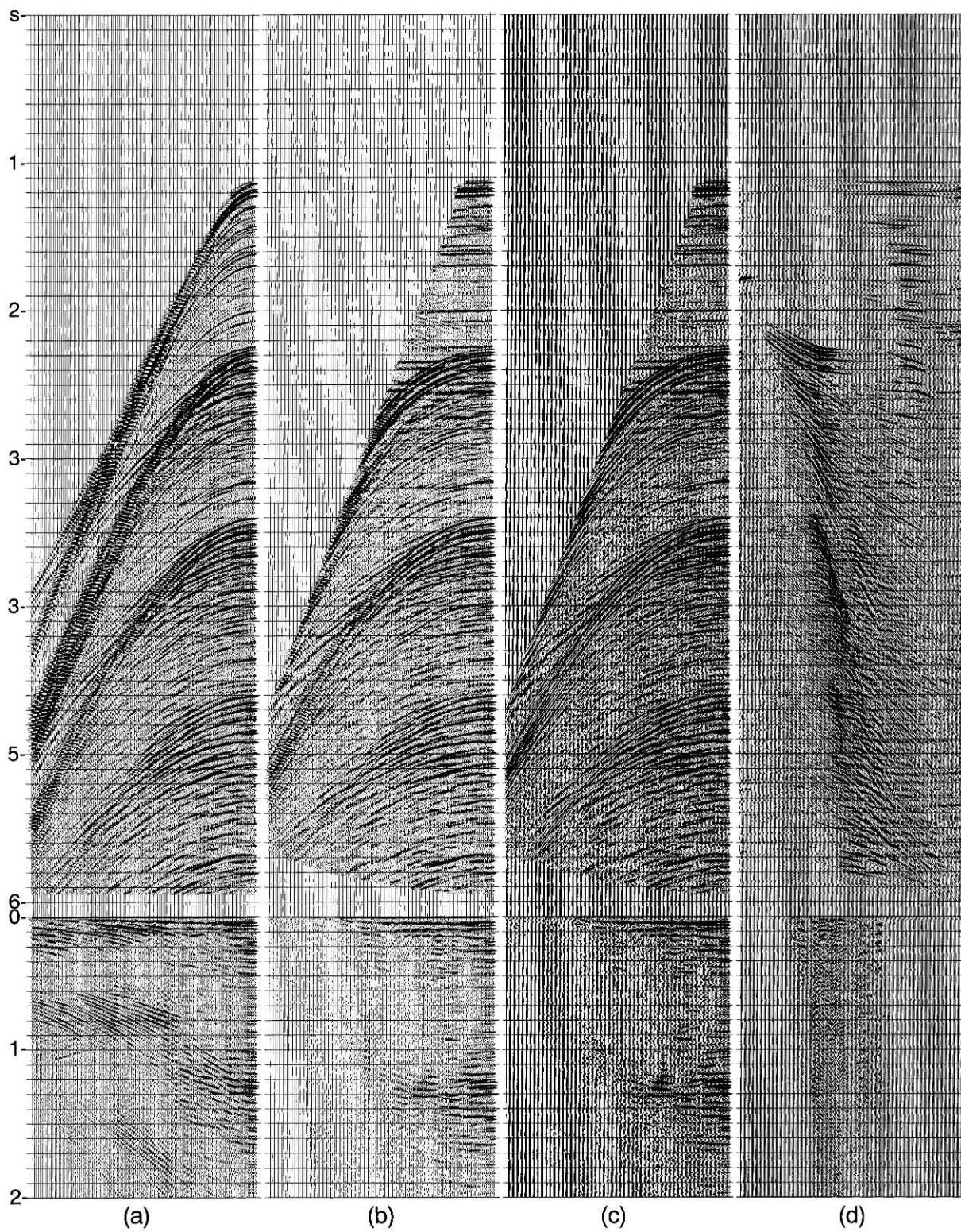


FIG. 6.4-29. (a) A CMP gather associated with the stacked section in Figure 6.4-28; (b) after moveout correction using primary velocities; (c) after trace interpolation using the $f - x$ method (Section G.1); (d) the parabolic Radon transform of (c). Shown beneath each panel is the autocorrelogram.

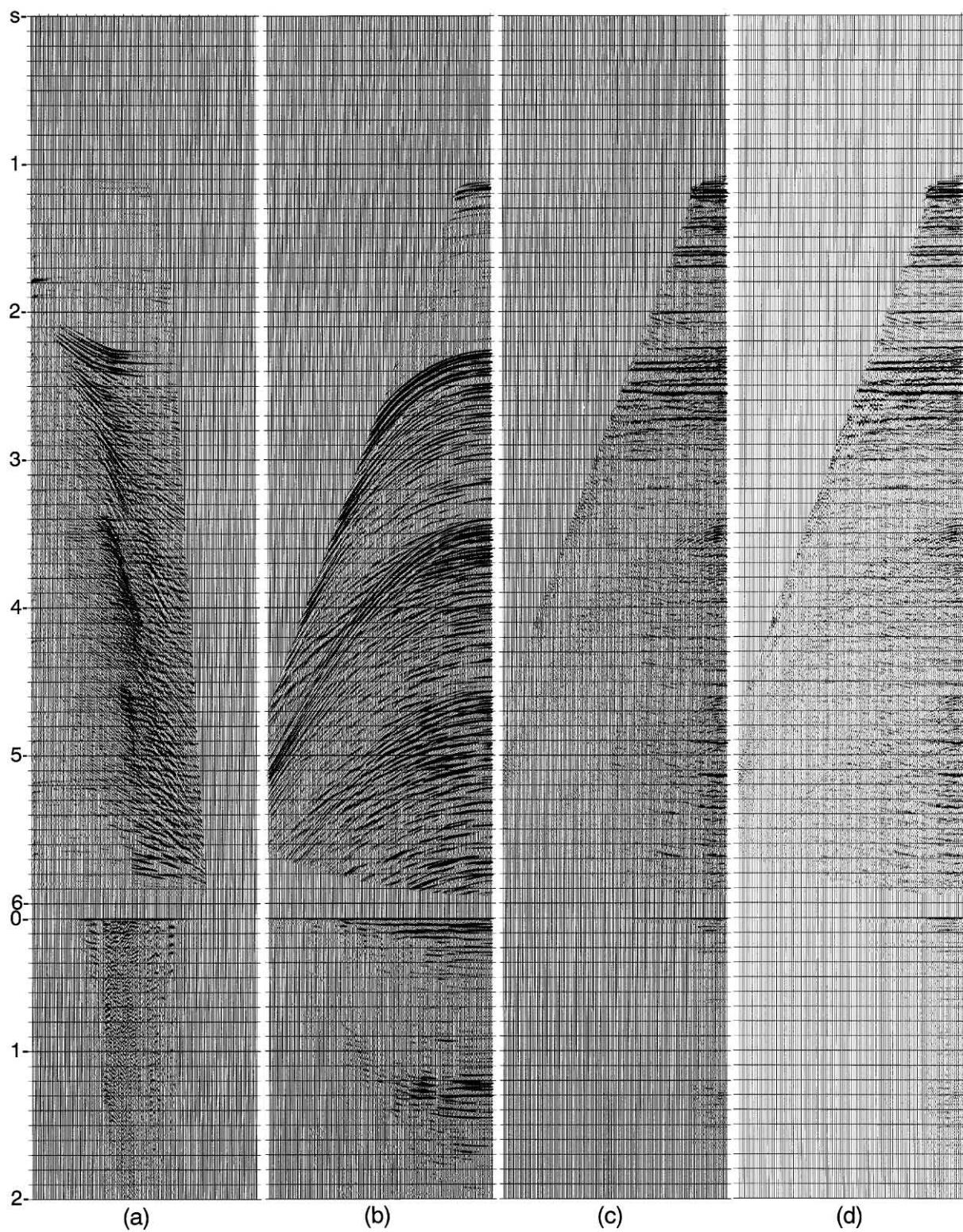


FIG. 6.4-30. (a) The Radon transform as in Figure 6.4-29d after muting the primary zone; (b) the reconstructed gather that contains only multiples; (c) the difference gather obtained by subtracting (b) from Figure 6.4-29c; (d) the same gather as in (c) but retaining every other trace with offsets as in Figure 6.4-29b. Compare (d) — the gather after multiple attenuation, with Figure 6.4-29b — the gather before multiple attenuation.

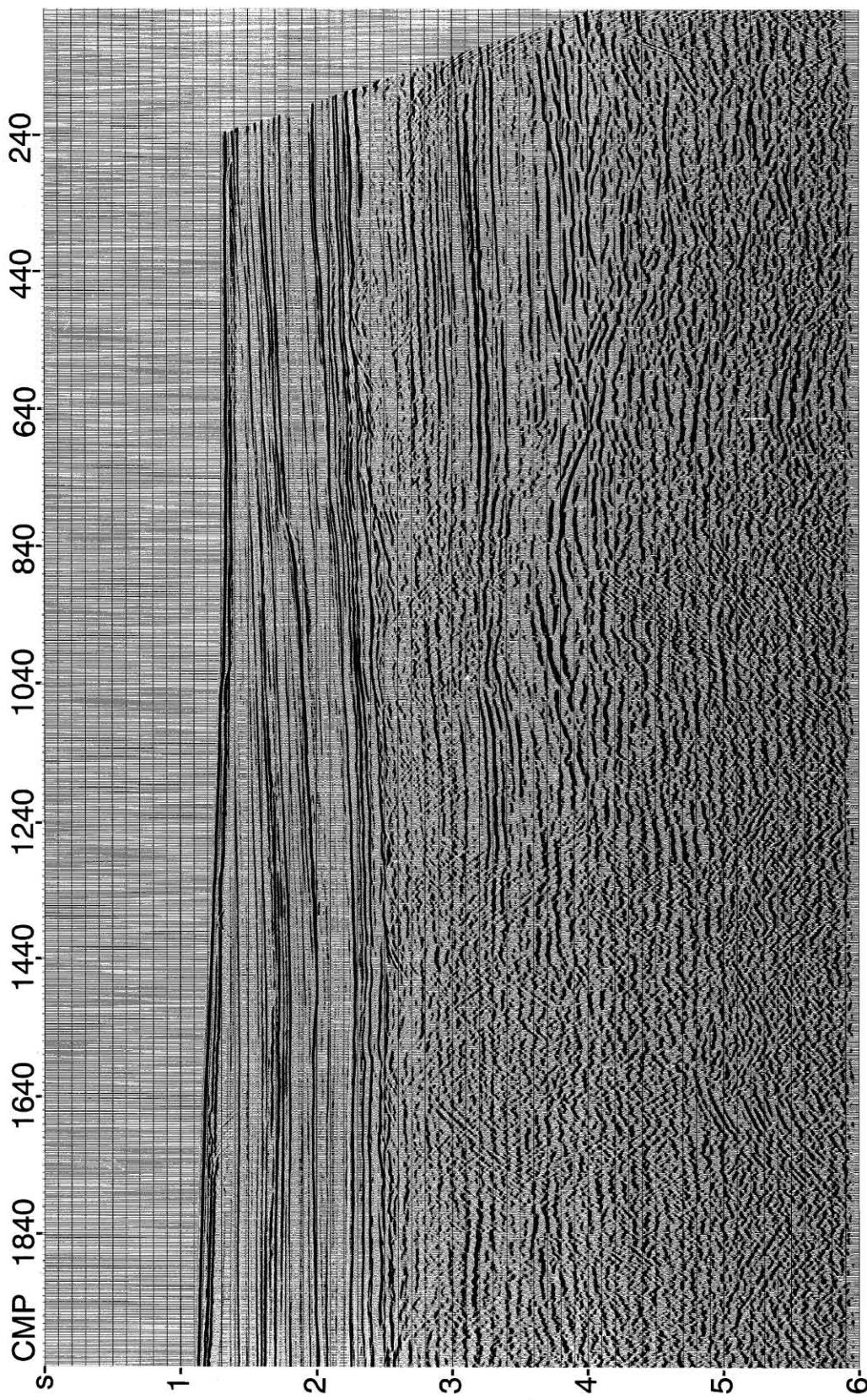


FIG. 6.4-31. The CMP-stacked section as in Figure 6.4-28 after multiple attenuation.

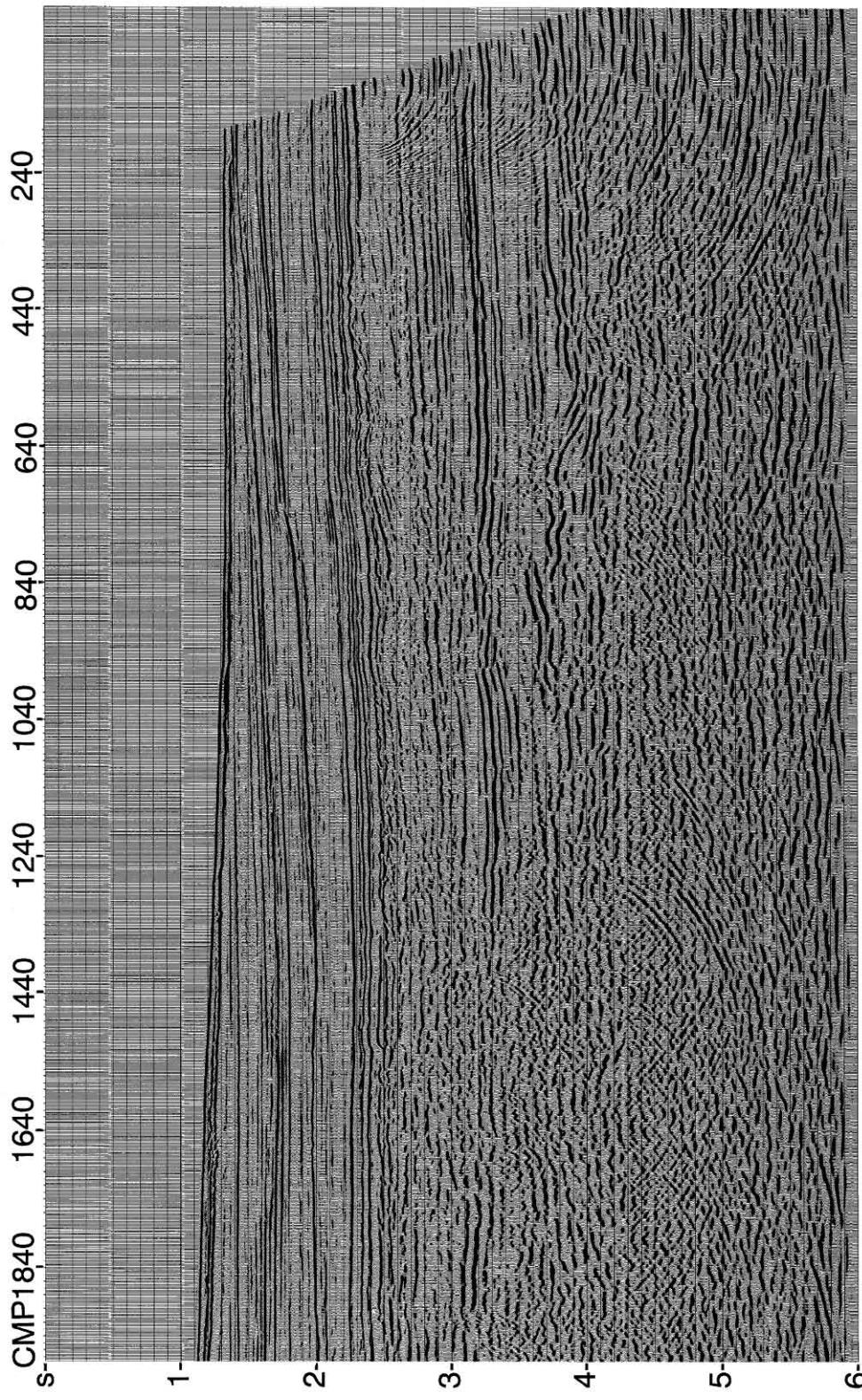


FIG. 6.4-32. The CMP-stacked section as in Figure 6.4-31 after migration.

to be the case, another fundamental assumption in predictive deconvolution is that the reflectivity series that contains the primaries is random. Hence, a prediction filter, when applied to the recorded seismic trace produces an estimate of the predictable part — the multiple reflections. The error in the prediction process then represents the random reflectivity series — the primary reflections.

Now consider the prediction process in the spatial direction. A spatial prediction filter, when applied to a stacked section, produces an estimate of the predictable part — the coherent signal. The error in the prediction process represents the noise uncorrelated from trace to trace. Whereas, the prediction lag for the temporal prediction filter is specified according to the period of the multiples, for the spatial application, a unit prediction lag is used. Since predictive deconvolution with a unit prediction lag is equivalent to spiking deconvolution, a spatial prediction filter is of the form of a spiking deconvolution operator.

Design of Spatial Prediction Filters

Spatially random noise is uncorrelated from trace to trace independent of temporal frequency. Therefore, spatial prediction filters can be conveniently designed and applied in the frequency-space domain. As such, spatial prediction filtering has come to be known in practice by the term $f - x$ deconvolution. While the theoretical review of the filter design and application is provided in Section F.5, below is a step-by-step procedure for $f - x$ deconvolution.

- (a) Start with the CMP-stacked section $P(x, t)$ and apply Fourier transform in the time direction to obtain the complex matrix $P(x, \omega)$.
- (b) Transpose the complex matrix $P(x, \omega)$, so that, for each frequency component, $P(x, \omega)$ is represented by the n -length complex vector $\mathbf{P} : (P_0, P_1, P_2, \dots, P_{n-1})$, where n is the number of traces in the stacked section.
- (c) For each frequency ω within a specified bandwidth, design a complex prediction filter $F(x)$ with unit prediction lag (Section F.6) represented by the m -length complex vector $\mathbf{F} : (F_0, F_1, F_2, \dots, F_{m-1})$, where m is the number of coefficients in the filter.
- (d) Apply the complex filter $F(x)$ to the input data component $P(x, \omega)$.
- (e) Repeat steps (c) and (d) for all frequency components within the specified bandwidth, combine the results, and transpose to trace format.

- (f) Inverse Fourier transform to obtain the filtered stacked section.

In practice, the prediction filter is designed using a group of stacked traces rather than the entire stacked section itself. The filter length m usually is chosen between 7-21 points, and the typical length n of the input complex vector \mathbf{P} is set to ten times the filter length. Starting at one end of the stacked section, say from the left-hand side, the filter is applied to output one predicted sample at $(m + 1)$ st trace for each frequency component. The design gate is then moved one trace to the right by dropping the first trace within the design window on the left and picking up the next trace on the right. The design gate is slid from one end of the section to the other one trace at a time. The prediction filter may be designed and applied in two opposite directions, and the outputs from the two applications may be averaged.

Field Data Examples

Although $f - x$ deconvolution usually is applied to stacked data, it also may be applied to moveout-corrected common-offset sections or CMP gathers. Figure 6.5-1 shows a CMP-stacked section before and after $f - x$ deconvolution. Both the input and output sections have been displayed using the same display gain. Note the significant reduction of the noise and enhancement of the coherent signal in the section.

A way to assess the effectiveness of noise attenuation is by examining the $f - k$ spectrum of the data before and after $f - x$ deconvolution as shown in Figure 6.5-2. The $f - k$ spectrum of the input section shows that the bandwidth of the data is approximately 10-70 Hz. It also shows the presence of random noise in the stacked section which maps over a rectangular area in the $f - k$ plane. Specifically, band-limited random noise contains energy at all wavenumbers for all frequencies within the passband. After $f - x$ deconvolution, note that the energy in the $f - k$ spectrum is limited to the region of coherent signal in the vicinity of the frequency axis.

If a time-variant scaling is applied to the output of $f - x$ deconvolution, the residual noise in the data is boosted. Figure 6.5-3 shows the stacked section as in Figure 6.5-1 after $f - x$ deconvolution and AGC scaling. Compare the sections in Figures 6.5-1b and 6.5-3b and note that AGC has scaled up the random noise. Nevertheless, by comparing sections in Figures 6.5-3a,b, note that the relative signal-to-noise ratio of the data has increased after $f - x$ deconvolution.

(text continues on p. 976)

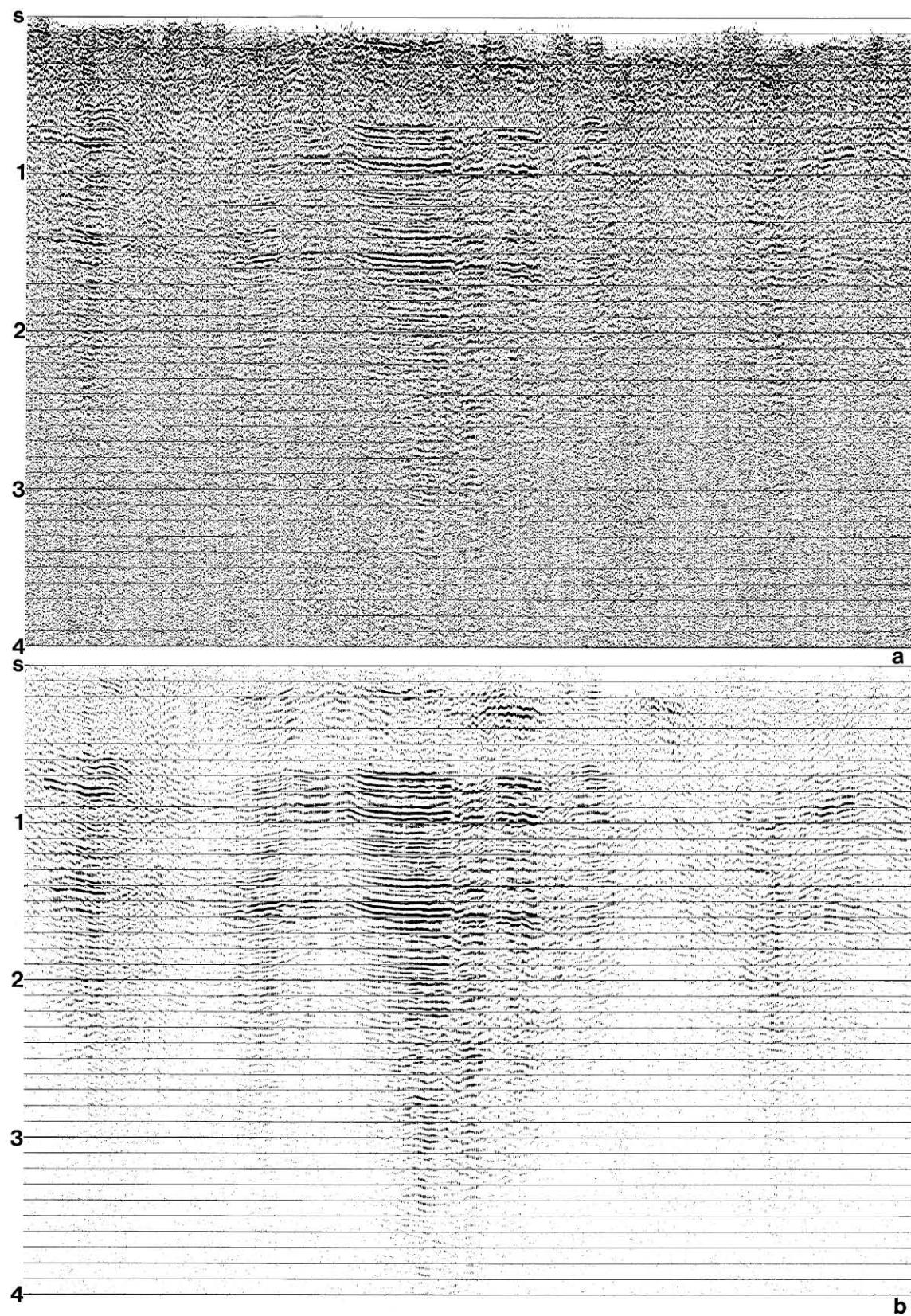


FIG. 6.5-1. A CMP-stacked section (a) before, and (b) after $f - x$ deconvolution.

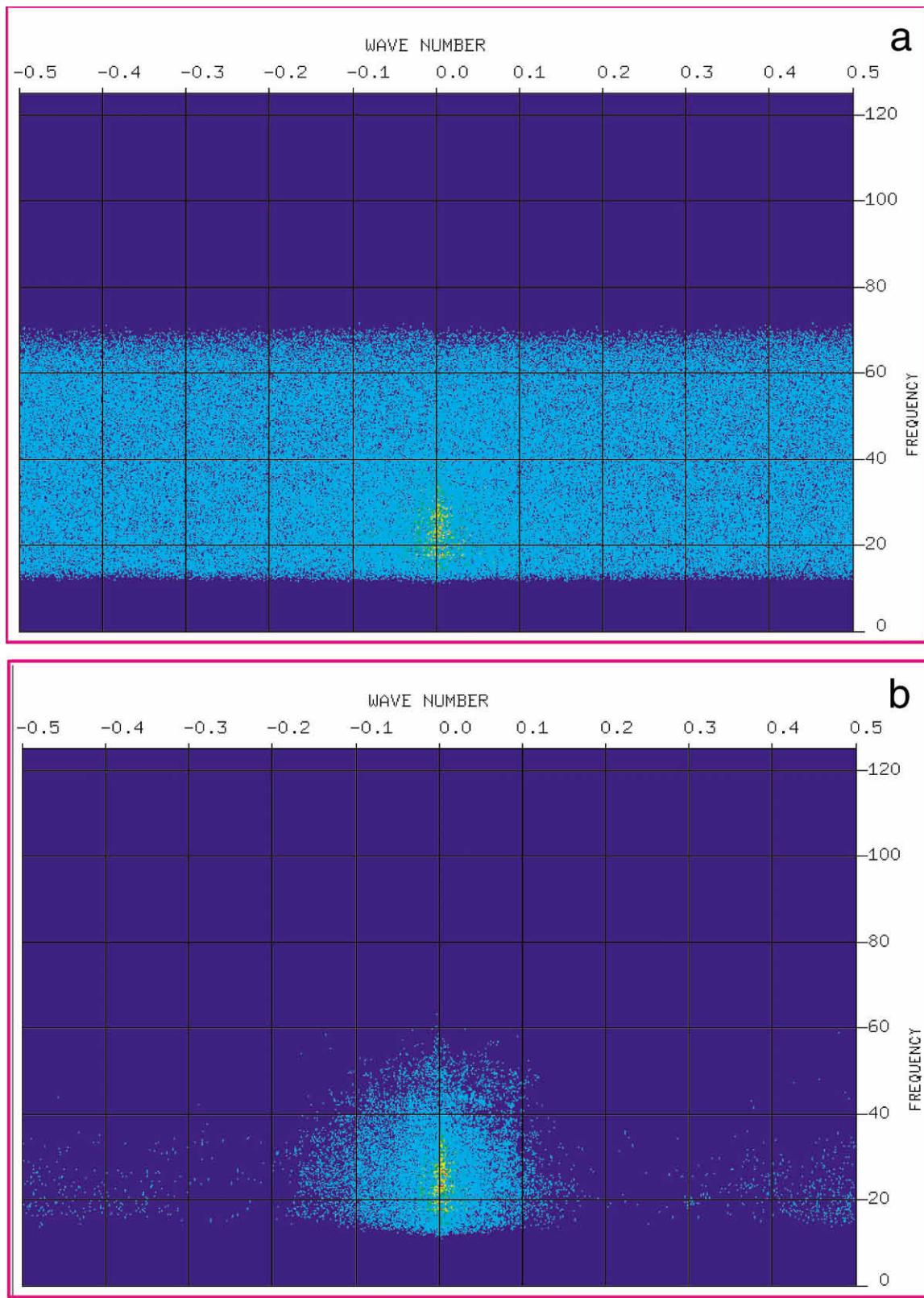


FIG. 6.5-2. The $f - k$ spectra of the stacked section as in Figure 6.5-1 9a) before, and (b) after $f - x$ deconvolution.

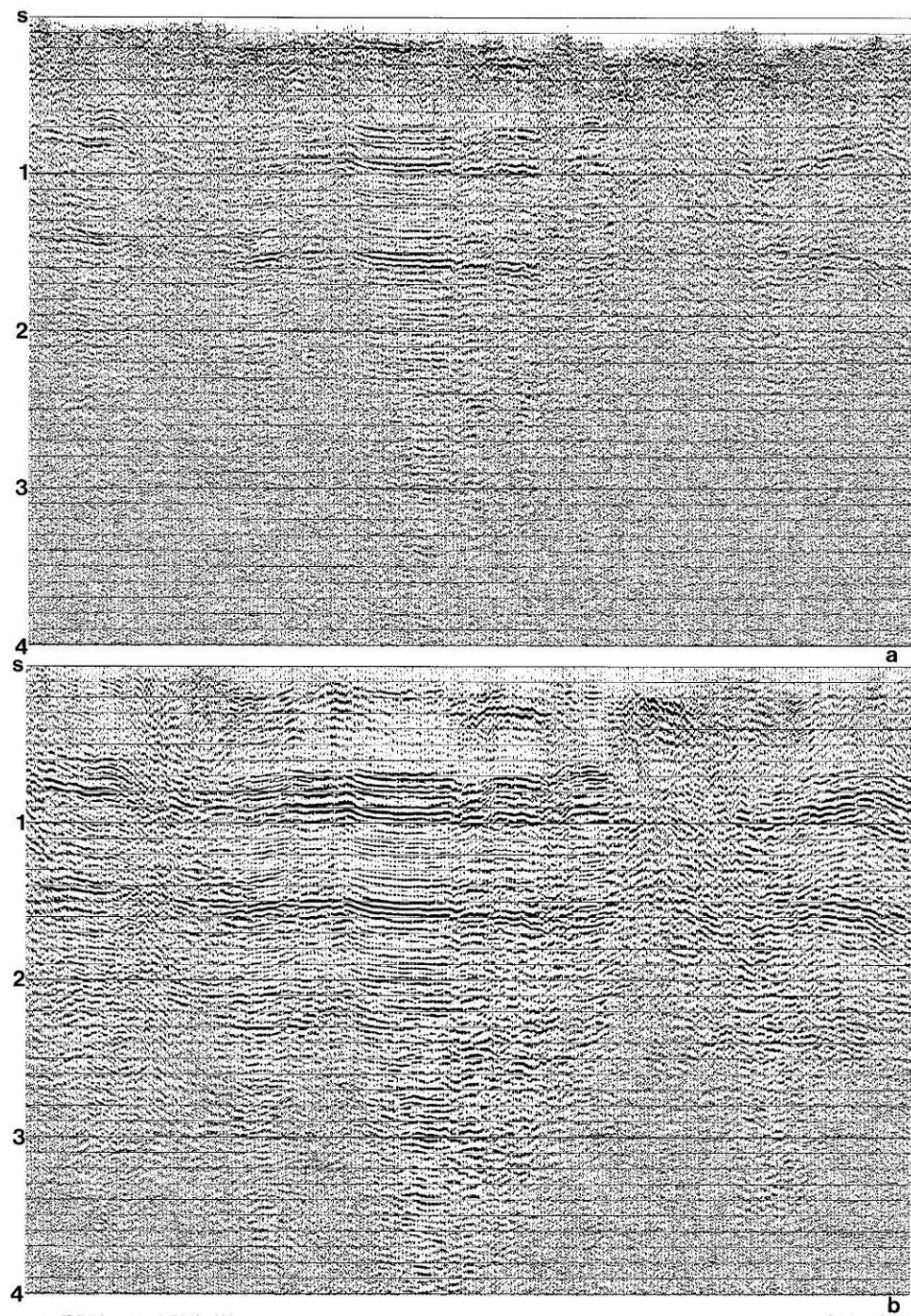


FIG. 6.5-3. (a) The CMP-stacked section as in Figure 6.5-1a, and (b) after $f - x$ deconvolution and AGC scaling.

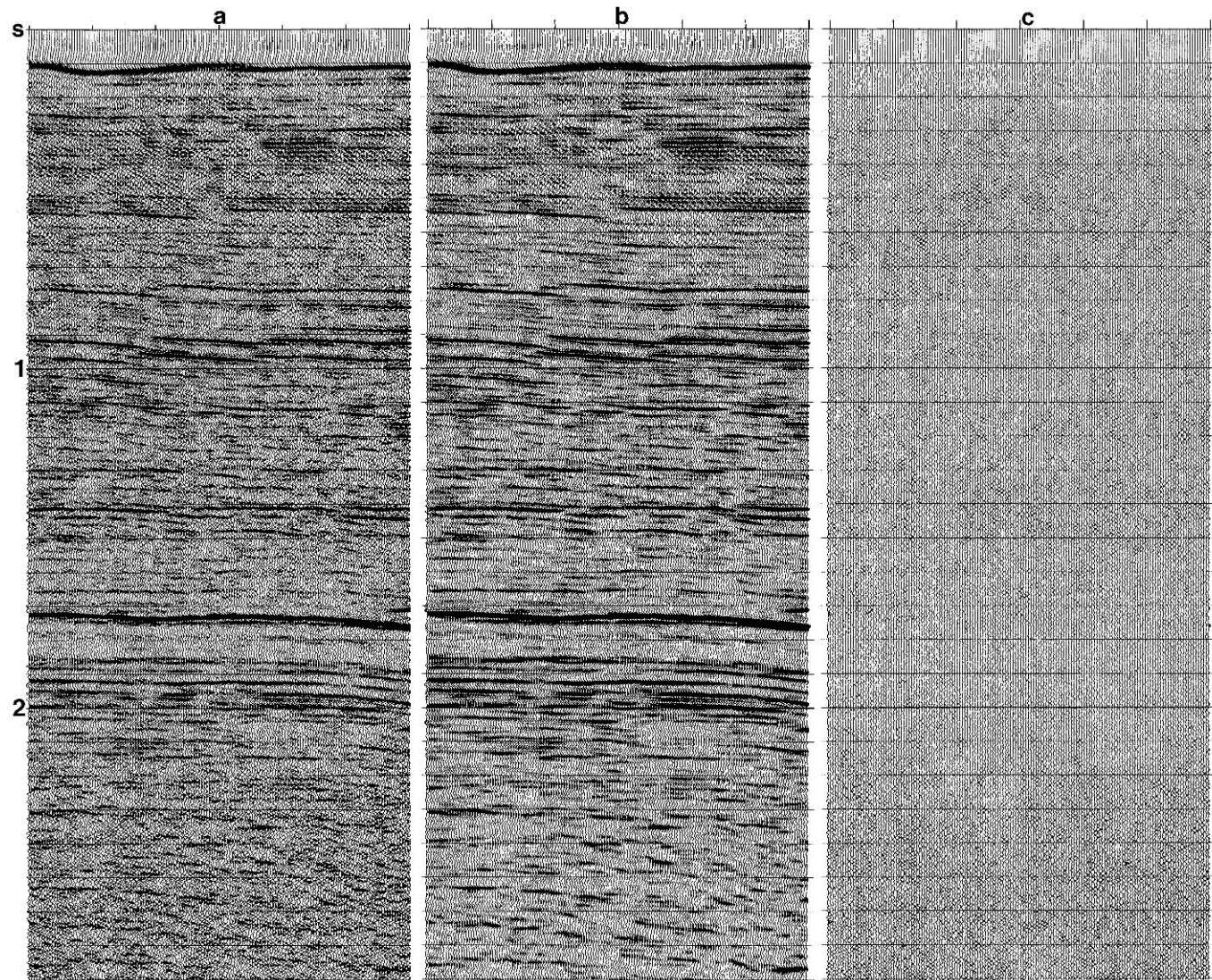


FIG. 6.5-4. A portion of a CMP-stacked section (a) before, and (b) after $f - x$ deconvolution with no addback, (c) the difference between (a) and (b).

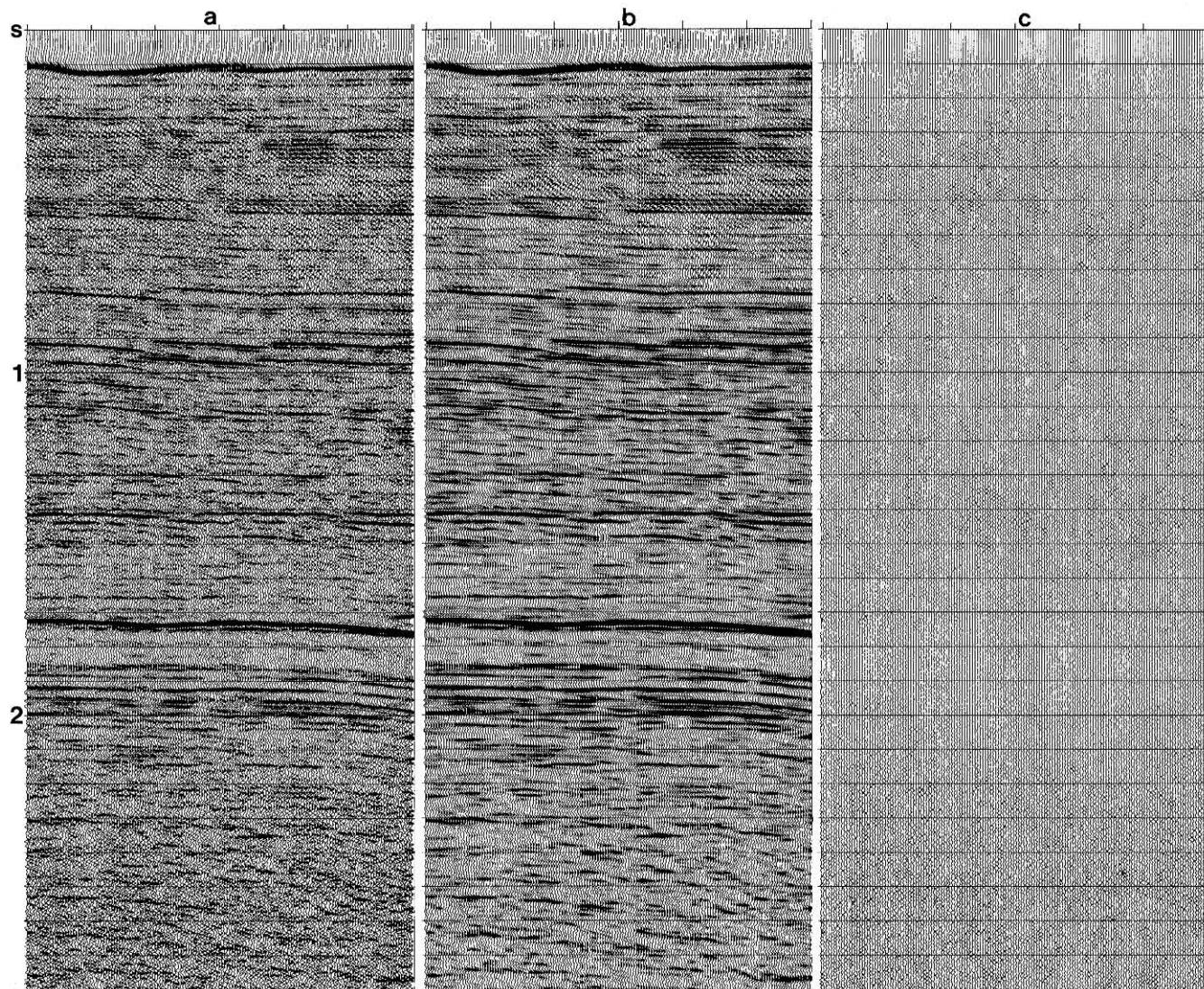


FIG. 6.5-5. A portion of a CMP-stacked section (same as in Figure 6.5-4a) (a) before, and (b) after $f - x$ deconvolution with 20 percent add-back, (c) the difference between (a) and (b).

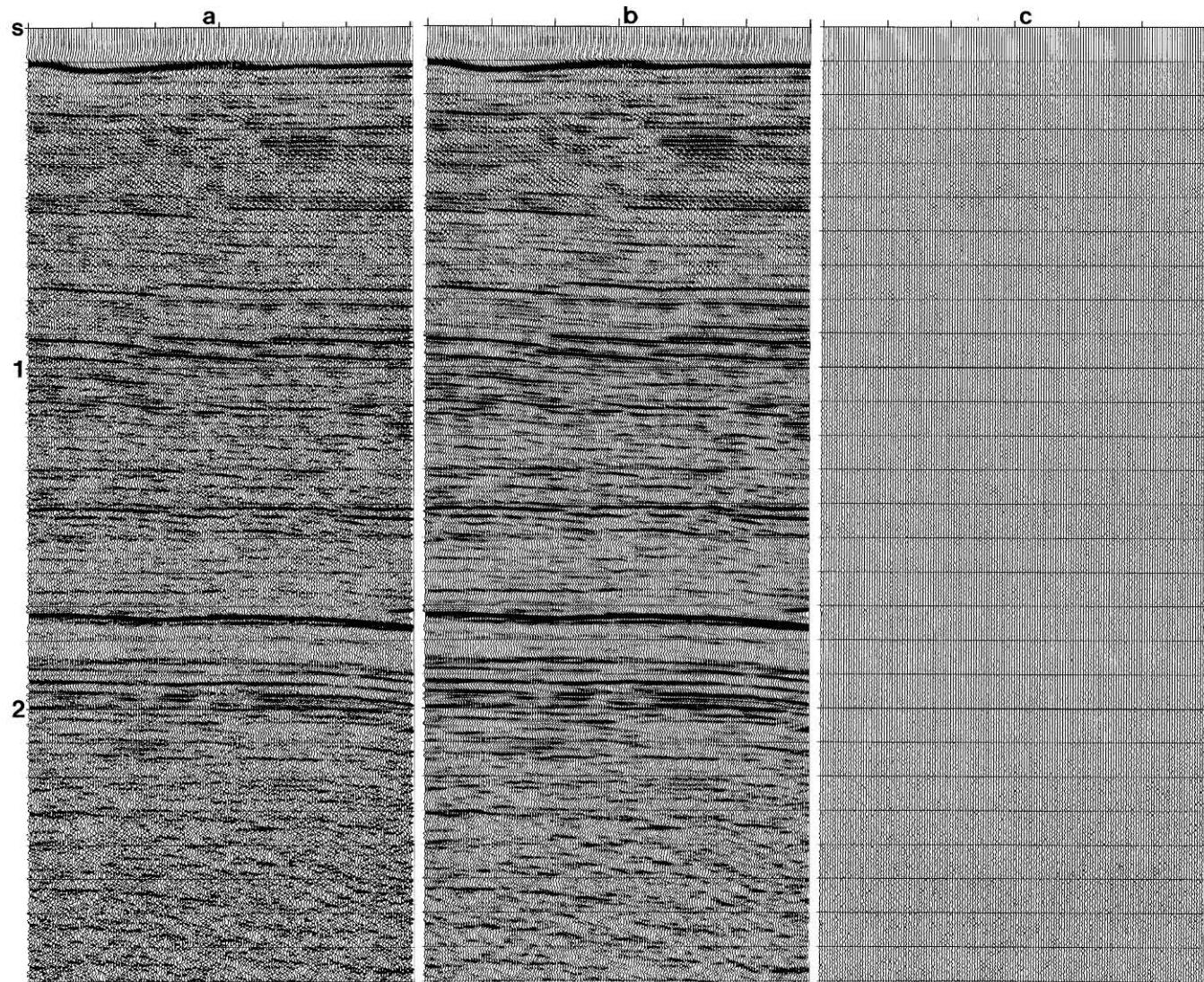


FIG. 6.5-6. A portion of a CMP-stacked section (same as in Figure 6.5-4a) (a) before, and (b) after $f - x$ deconvolution with 40 percent add-back, (c) the difference between (a) and (b).

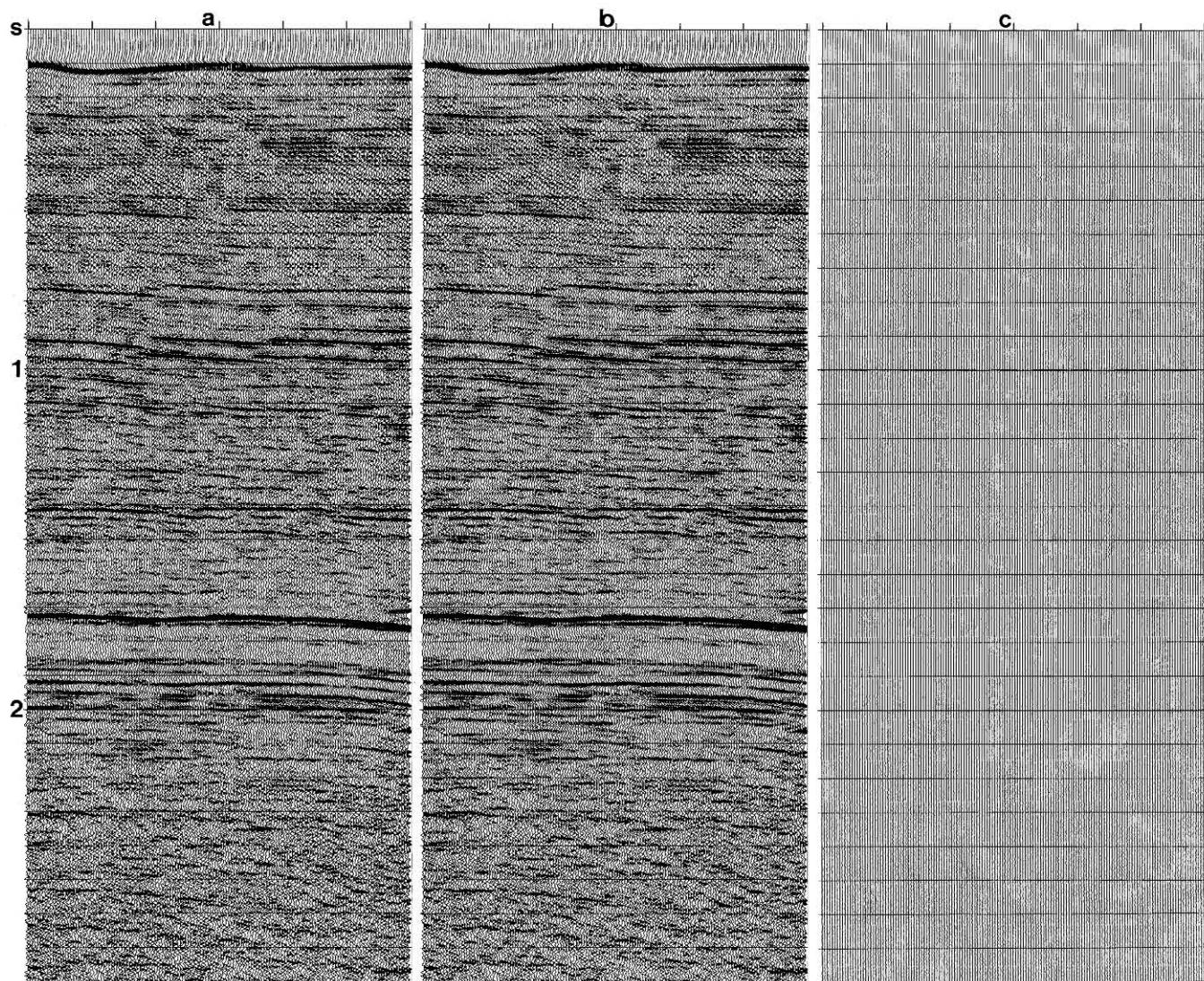


FIG. 6.5-7. A portion of a CMP-stacked section (same as in Figure 6.5-4a) (a) before, and (b) after $f - x$ deconvolution with 80 percent add-back, (c) the difference between (a) and (b).

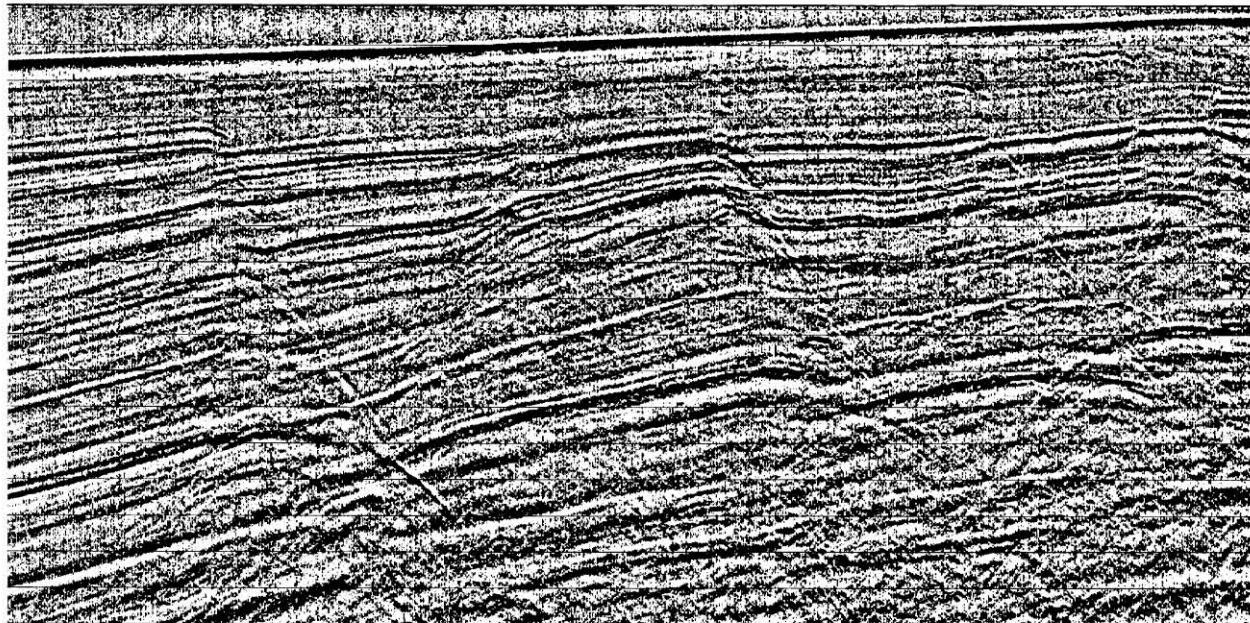
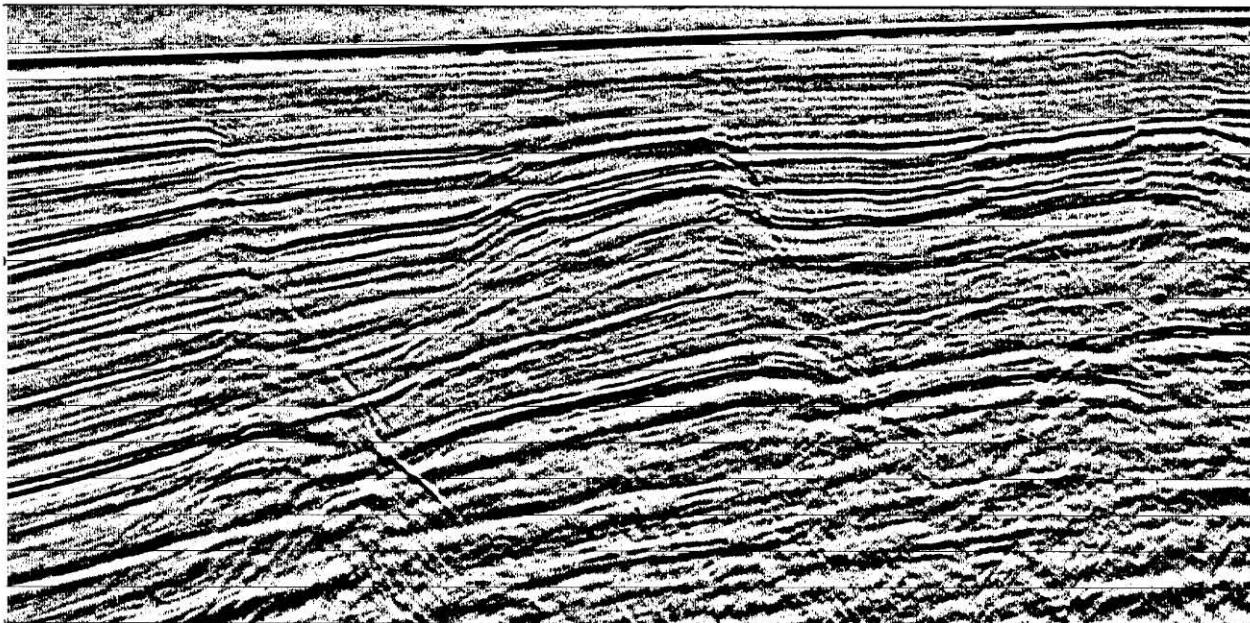
**a****b**

FIG. 6.5-8. A CMP-stacked section (a) before, and (b) after $f - x$ deconvolution.

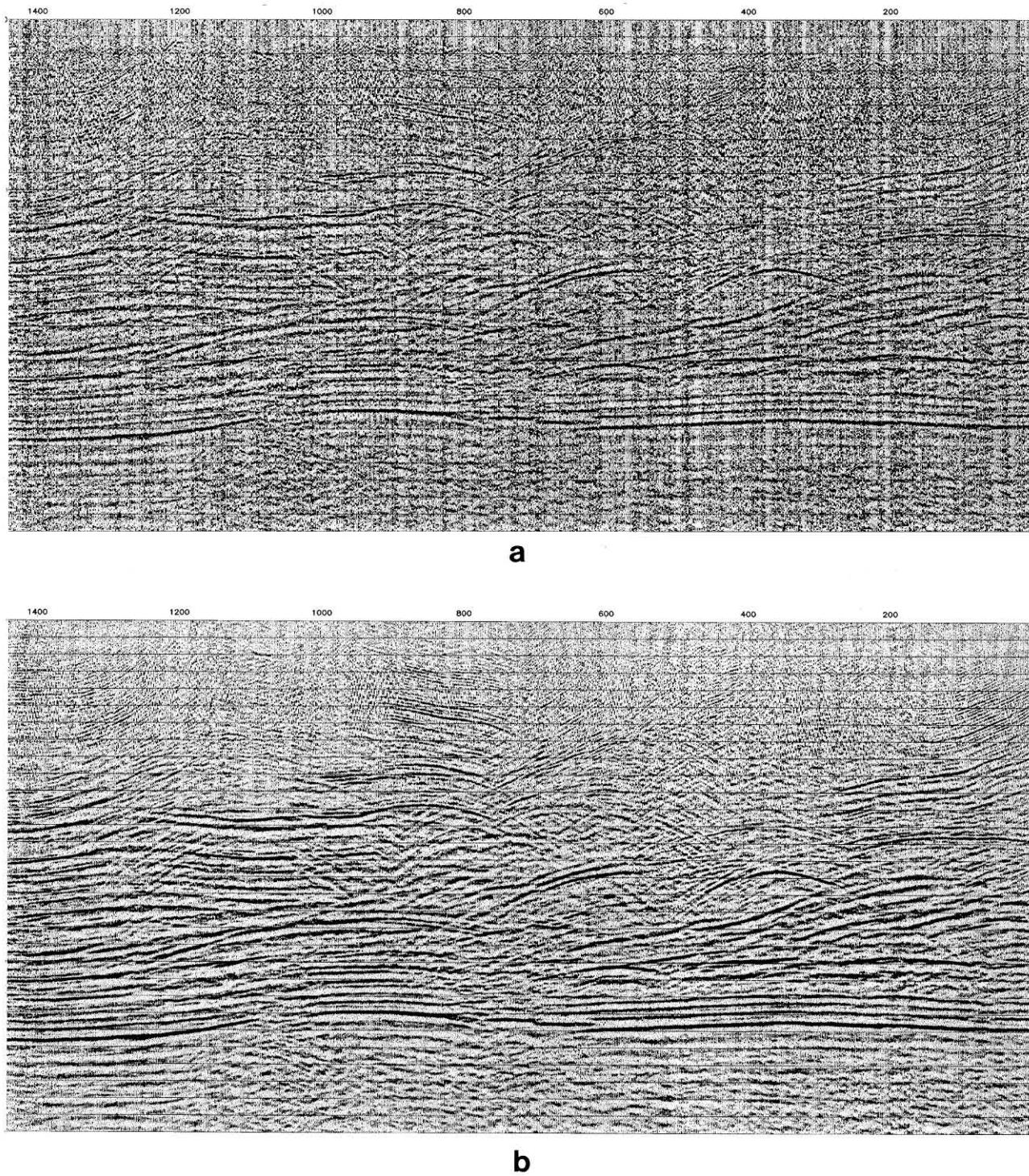


FIG. 6.5-9. A CMP-stacked section (a) before, and (b) after $f - x$ deconvolution.

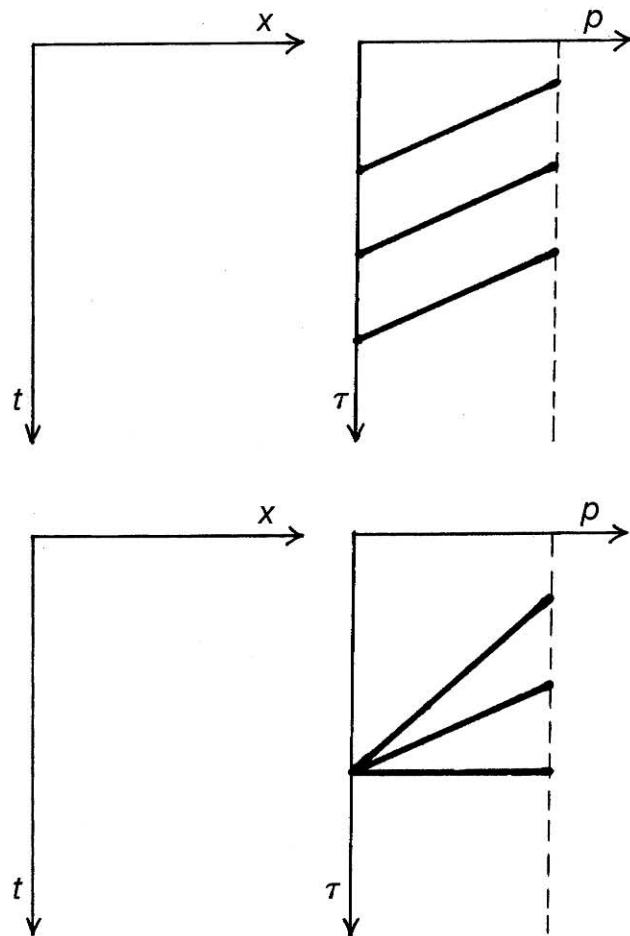


FIG. 6.E-1. Linear events in the p -gather are mapped onto points in the $x - t$ domain (see Exercise 6-2).

We now test $f - x$ deconvolution for noise attenuation in case of a CMP stack that contains near-horizontal reflections as shown in Figure 6.5-4a. The section after $f - x$ deconvolution is shown in Figure 6.5-4b, and the difference between the input (Figure 6.5-4a) and the output (Figure 6.5-4b) is shown in Figure 6.5-4c. The difference section represents the error in the prediction process, and as such, it contains the noise uncorrelated from trace to trace. All three sections in Figure 6.5-4 are shown with the same display gain.

Note in the shallow portion of the filtered section in Figure 6.5-4b above 1 s the zipper effect of the coherent linear noise which has remained in the data after stacking. The spatial prediction filter predicts coherent signal which includes primary and multiple reflections, diffractions, and coherent linear noise. Therefore, it should not

be surprising to observe a pronounced coherent linear noise trend in the data after $f - x$ deconvolution.

To circumvent the smeared appearance of the data after $f - x$ deconvolution, sometimes a portion of the difference section is added back to the output. Figures 6.5-5, 6.5-6 and 6.5-7 show the results of 20, 40, and 80 percent add-back. As the percent add-back is increased, the texture of the output from $f - x$ deconvolution resembles that of the input section more closely. In practice, typical add-back value varies between 0-40 percent.

Now consider a stacked data set with moderate structural complexity as shown in Figure 6.5-8. Note that a significant portion of the random noise has been attenuated by $f - x$ deconvolution, while diffractions at fault locations and reflections have been preserved.

Finally, Figure 6.5-9 shows a stacked section with a complex structure. Following $f - x$ deconvolution, coherent signal — reflections and diffractions, has largely been preserved. Hence, $f - x$ deconvolution for noise attenuation is a robust process even in the presence of a complex pattern of coherent signal as in Figure 6.5-9. The application of $f - x$ deconvolution to land data from areas with complex structures such as those associated with overthrust tectonics can improve the stack quality significantly. Also, land data from areas with near-surface complexity that causes poor penetration of the source energy into the subsurface can benefit from application of $f - x$ deconvolution.

EXERCISES

Exercise 6-1. Prove that a hyperbola in the offset domain (x, t) maps onto an ellipse in the slant-stack domain (τ, p).

Exercise 6-2. Refer to Figure 6.E-1. What would the $t - x$ domains look like?

Exercise 6-3. Consider constructing the slant-stack gather from offset data that consists of a reflection hyperbola. Does equal increment in p , the ray parameter, cause undersampling or oversampling of the steep dips? Of the gentle dips? What happens when an equal increment in $1/p$ is used? What happens when an equal increment in θ is used, where θ is related to p by $p = \sin \theta/v$?

Exercise 6-4. Identify event E in Figure 6.2-1.

Exercise 6-5. What procedure does CMP stacking correspond to in the $f - k$ domain?

Appendix F MULTICHANNEL FILTERING TECHNIQUES FOR NOISE AND MULTIPLE ATTENUATION

F.1 Analysis of Guided Waves

Marine data often are contaminated by guided waves that travel horizontally within the water layer or in the layers beneath the water layer. These waves exhibit characteristics that depend on water depth and on the geometry and material properties of the substrata. Modeling these pressure waves traveling within the water layer can lead to a better understanding of certain aspects of the field data and sometimes may even result in inferences about the strata below the water layer.

The well-known normal mode theory provides a way to laterally extrapolate acoustic and elastic waves (Pekeris, 1948; Press and Ewing, 1950). In this section, a normal mode procedure is applied to model shot profiles recorded over a water layer on top of a homogeneous elastic half space. Raypaths corresponding to multiple reflections, direct arrivals, refracted arrival, and its multiples are included in the normal mode theory.

The seismic waveguide effect of a surface layer is well known. Wave propagation in a surface layer, in particular guided waves, can be described by using the normal mode theory (Pekeris, 1948). Pekeris' model consists of a liquid layer over an acoustic (liquid) half space. More general models, which consist of a liquid layer on top of an elastic half space, were investigated by Press and Ewing (1950). The most complete summary of work in the field in the classic work by Ewing et al. (1957).

Guided waves are dispersive. This means each frequency component travels at a different speed; namely, the horizontal phase velocity. The dispersive character of guided waves is most pronounced in shallow water environments (less than 100 m). Depending on various water-bottom conditions, such as a mud layer with variable thickness or a hard bottom, the character of these waves may vary from shot to shot (Figure 6.0-3). They also can cause linear noise on stacked data (Figure 6.2-8a) and are easily confused with the linear noise that is associated with side scatterers (Figure 6.0-4).

McMechan and Yedlin (1981) proposed a way to obtain phase velocity information from field data. Their approach is based on a wavefield transformation. The shot record first is transformed into the slant-stack domain. Fourier transforming (in time) each trace of the slant-stack gather then yields phase velocity as a function of frequency. This two-step process is demonstrated with the field data example in Figure F-1a. Line CC' refers to the critical angle of propagation with a large reflection energy. To the right of this line is the supercritical propagation. The slant-stack gather is shown in Figure F-1b, and its 1-D amplitude spectrum is shown in Figure F-1c. Note that the horizontal axis in the slant-stack domain is the ray parameter, that is, the inverse of the horizontal phase velocity. Therefore, in Figure F-1c, we see the variation of the horizontal phase velocity as a function of frequency. Each curve corresponds to a particular *normal mode* propagating in the water layer. The phase velocities of the normal mode components asymptotically approach that of the water velocity v_w at the high-frequency end of the spectrum.

Consider the recording geometry depicted in Figure F-2 with a source and a receiver cable, and subsurface model that consists of a water layer on top of an elastic half space. The source is at a certain depth below the water surface, so the two raypaths — primary and ghost, must be considered.

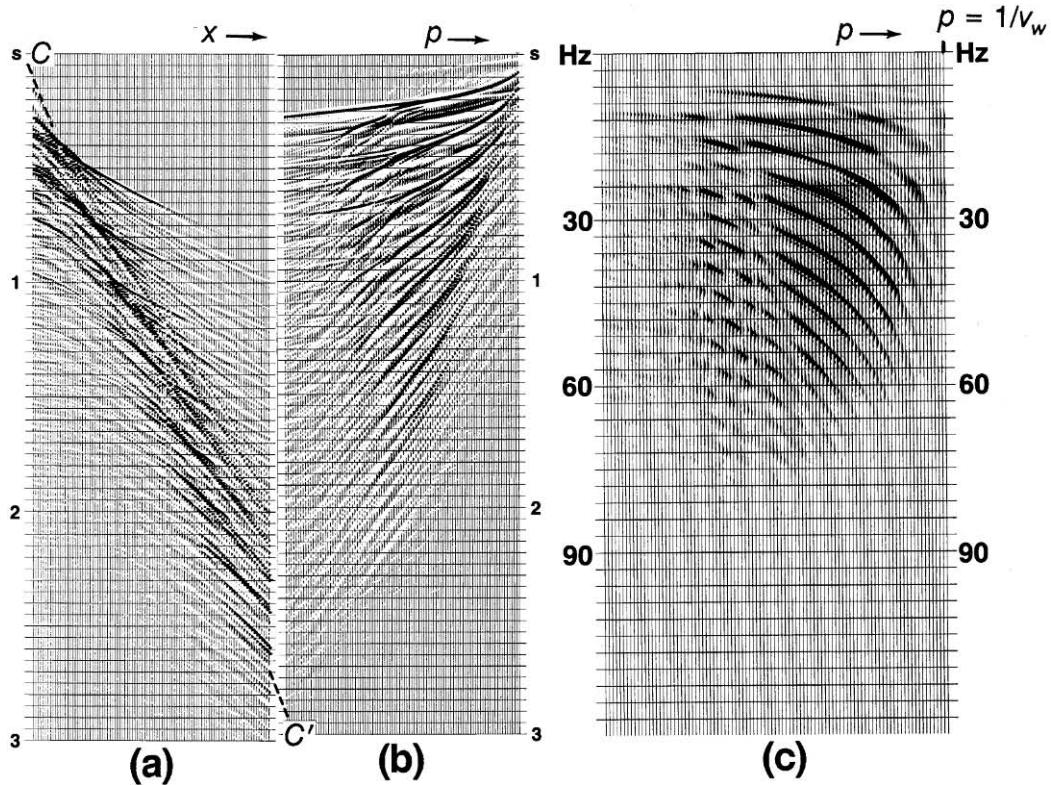


FIG. F-1. (a) A shot gather containing the strong reflected and refracted multiples associated with hard water-bottom conditions. Here, CC' = critical-angle energy. (b) The slant-stack gather derived from this shot gather. (c) The $\omega - p$ gather derived from the $\tau - p$ gather in panel (b). The inverse of p is the horizontal phase velocity. This figure demonstrates the dispersive nature of guided waves; that is, phase velocity is a function of frequency for all propagating normal mode components. These modes are represented by the curved trajectories on panel (c).

The normal mode theory of Ewing et al. (1957) provides an analytic expression for phase velocity as a function of frequency (the so-called characteristic equation or dispersion relation) for a given surface-layer model. The characteristic equation for the geometry in Figure F-2 is given by

$$\tan(k_x H r_1) = \frac{\rho_2 \beta_2^4 r_1}{\rho_1 c^4 r_2} [4r_2 s_2 - (1 + s_2^2)^2], \quad (F-1)$$

where k_x is the horizontal wavenumber, which is equal to $p\omega$ via equation (6-7), H is water depth, ρ_1 and ρ_2 are the water and substratum densities, respectively, β_2 is the S -wave velocity of the substratum, and c is the phase velocity of the guided waves in the water layer. Finally, the normalized variables are

$$r_1 = \sqrt{\frac{c^2}{\alpha_1^2} - 1}, \quad (F-2a)$$

$$r_2 = \sqrt{\frac{c^2}{\alpha_2^2} - 1}, \quad (F-2b)$$

$$s_2 = \sqrt{\frac{c^2}{\beta_2^2} - 1}, \quad (F-2c)$$

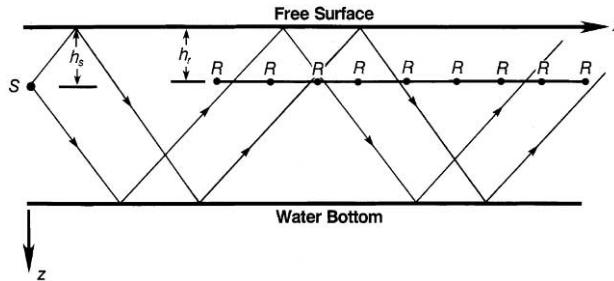


FIG. F-2. The geometry for normal-mode modeling of the guided waves illustrated in Figure F-3. Here, S = the source, R = receivers, h_s = source depth, and h_r = receiver depth.

where α_1 is the P -wave velocity in the water layer and α_2 is the P -wave velocity in the substratum. Because of the periodic nature of the tangent, equation (F-1) has a multiple-valued function on the left side and a single-valued function on the right side. To explicitly state the ambiguity, equation (F-1) can be rewritten as

$$k_x H r_1 + n\pi = \tan^{-1} B, \quad (F - 3)$$

where B is the right-hand side of equation (F-1), and the integer $n = 0, 1, 2, \dots$, defines the mode number. By carefully examining equations (F-1) and (F-3), note that phase velocity c is a function of frequency ω ; hence, guided waves are dispersive. Equation (F-3) yields real values of k_x for $\alpha_1 \leq c \leq \alpha_2$. (Here, we assume that $\alpha_1 < \beta_2 < \alpha_2$.) Table F-1 gives a summary of the phase-velocity regions and types of rays associated with each region. Note that we get a wide range of wave types propagating each with a certain phase velocity or a range of phase velocities.

Only in the supercritical region, $\alpha_1 < c < \beta_2$, are waves totally trapped within the water layer. These waves often form the major contribution to normal-mode propagation at longer offsets as in the field data example in Figure F-1a, where the supercritical region is to the right of line CC' . In the subcritical region, energy leaks into the substratum (thus, the name *leaky modes*). The contribution of this region to energy arriving at longer offsets is relatively weak.

The recorded pressure wavefield for the supercritical region at various receiver locations (Figure F-2) is given by

$$P(x, z = h_r, t) = 4 \sum_n \int d\omega \{ \omega^2 A(\omega) \sin(k_x r_1 h_s) \sin(k_x r_1 h_r) \exp[i\omega(t - x/c)] \}, \quad (F - 4)$$

where $A(\omega)$ is the amplitude spectrum of the source. Yilmaz (1981) modified this expression to account for the ghost effect. Note that reciprocity is satisfied here — the product of the sinusoidal factors that modulate the source spectrum $A(\omega)$ is unchanged if h_r and h_s are interchanged.

Table F-1. Regions of phase velocity and associated ray types.

Phase Velocity	Ray Type
$\alpha_1 < c < \alpha_2$	supercritical P -waves (wide-angle reflections)
$\beta_1 < c < \alpha_2$	supercritical, partially reflected P -waves
$c > \alpha_2$	subcritical P -waves
$c = \beta_2$	critically refracted S -wave
$c = \alpha_2$	critically refracted P -wave

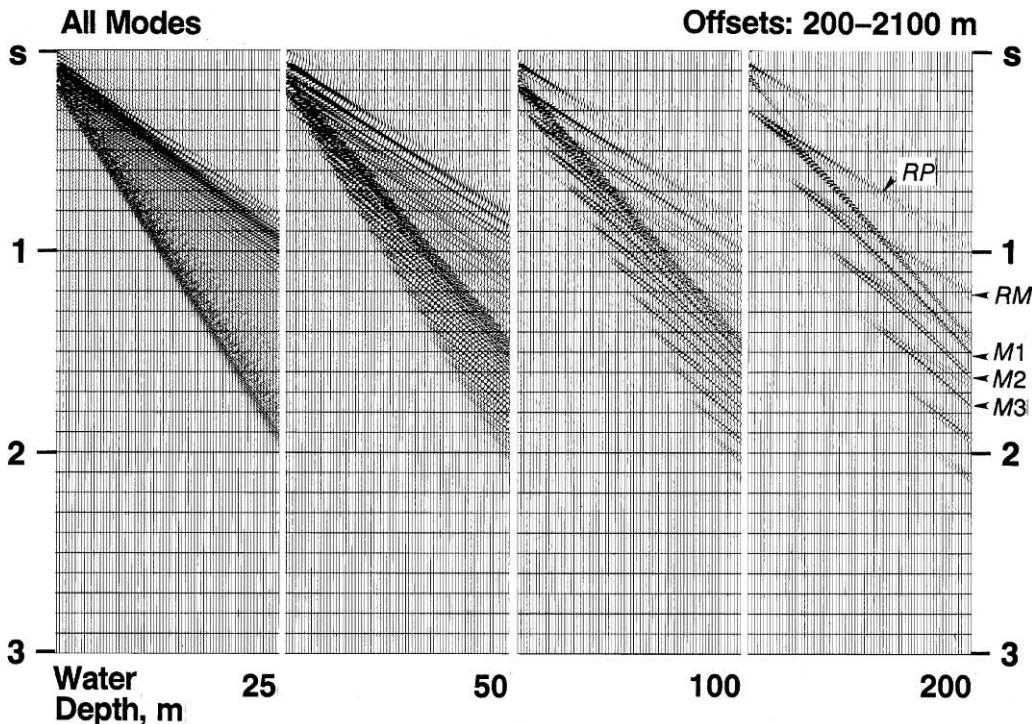


FIG. F-3. Superposition of all modes in water layers of different thicknesses. The depth model is shown in Figure F-2. Ghost effects are included in the modeling. Refer to the text for description of the labeled events.

We now consider modeling of normal modes using equation (F-4), including the ghost effect, for a range of water depths. The model parameters are: $\alpha_1 = 1500 \text{ m/s}$, $\beta_2 = 2\alpha_1$, $\alpha_2 = 1.6\beta_2$, and $\rho_2/\rho_1 = 2.2$. All the experimental results represent impulse responses of guided waves — that is, $A(\omega) = 1$ in equation (F-4). Guided waves in Figure F-3 manifest themselves with a complex interfering wave pattern at shallow water, then gradually separate into simple water-bottom multiples at increasing water depths. The dispersive character of the guided waves is prominent, especially for shallow water depths. In Figure F-3, the guided waves are simulated in the supercritical region. The elastic substratum, which is equivalent to the hard water-bottom case, supports the early refraction energy RP, its multiple RM, and the reflected water-bottom multiples M1, M2, and M3. The acoustic substratum ($\beta_2 = 0$, equivalent to the soft water-bottom case), yields only the reflected water-bottom multiples. Acoustic behavior of the substratum implies that no P -to- S conversion occurs. The phase velocity curves in Figure F-4 verify the existence of a number of propagating modes for each case. Note the cable truncation effect (CT).

F.2 Wavefield Extrapolation in the $\tau - p$ Domain

In Section 6.3, we discussed slant-stack transformation of a wavefield from midpoint-offset to midpoint-ray-parameter coordinates. This transformation is done by applying linear moveout and summing over the offset range for each value of the ray-parameter. From the results in Section D.1, the double square-root operator can be specialized for migration before stack in midpoint-ray-parameter coordinates (Ottolini, 1982). To derive the extrapolation equation in the slant-stack domain, we start with the relationships between the transform-domain variables:

$$p = \frac{\sin \theta}{v} \quad (F-5a)$$

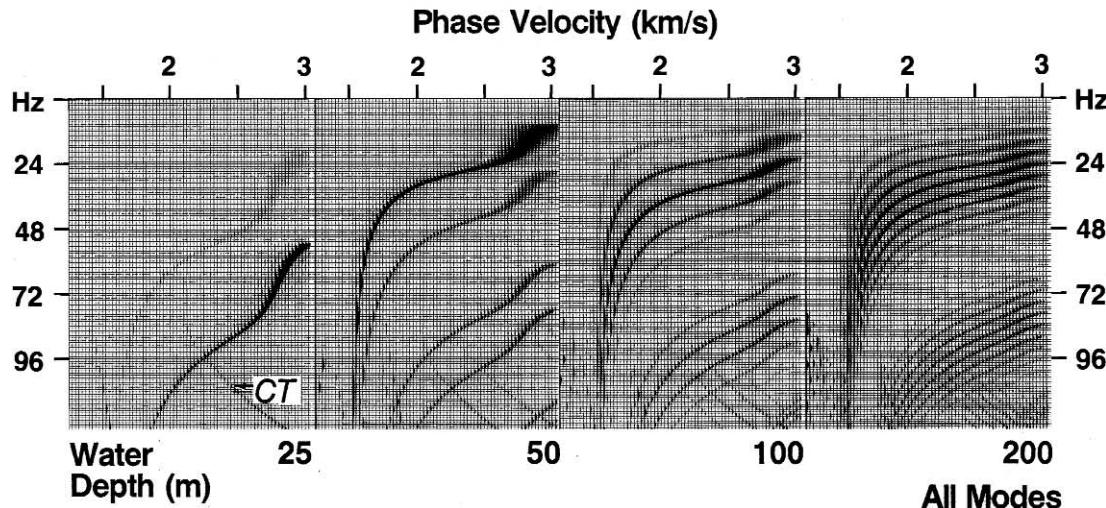


FIG. F-4. Phase velocity as a function of frequency for the cases shown in Figure F-3. Here, CT denotes the cable truncation artifact.

and

$$\frac{vk_h}{2\omega} = \sin \theta, \quad (F-5b)$$

where k_h is the offset wavenumber, ω is the temporal frequency, p is the ray parameter, v is the propagation velocity, and θ is the angle of propagation measured from the vertical. The normalized offset wavenumber H is defined as (Section D.1)

$$H = \frac{vk_h}{2\omega}. \quad (F-5c)$$

Combining the relationships given by equations (F-5a,b) with the definition given by equation (F-5c), we get

$$H = pv. \quad (F-6)$$

We rewrite the double square-root equation from Section D.1

$$DSR(Y, H) = \sqrt{1 - (Y + H)^2} + \sqrt{1 - (Y - H)^2}, \quad (F-7)$$

and substitute the definition of H in terms of p from equation (F-6) to get

$$DSR(Y, pv) = \sqrt{1 - (Y + pv)^2} + \sqrt{1 - (Y - pv)^2}. \quad (F-8)$$

Ottolini (1982) used this operator for migration before stack in midpoint-ray-parameter coordinates. The procedure is described in Figure F-5.

Clayton and McMechan (1981) adapted equation (F-8) to zero-dip case which is equivalent to setting $Y = 0$:

$$DSR(Y = 0, H = pv) = 2\sqrt{1 - p^2v^2}. \quad (F-9)$$

They then used this operator to downward continue refracted waves on CMP or shot gathers. The objective of inversion of a refraction profile is to estimate a velocity profile in depth, $v(z)$. The procedure is outlined in Figure F-6. The final step yields a profile, $P(p, z)$, of horizontal phase velocity $1/p$ as a function of depth z . Two issues must be kept in mind. First, the procedure is based on a layered earth assumption. Second, the procedure requires knowledge of the medium velocity to extrapolate the wavefield in depth. To get around this second problem, the process must be iterated until the phase velocity profile converges to the velocity function used in the extrapolation. It usually takes up to three iterations to achieve convergence.

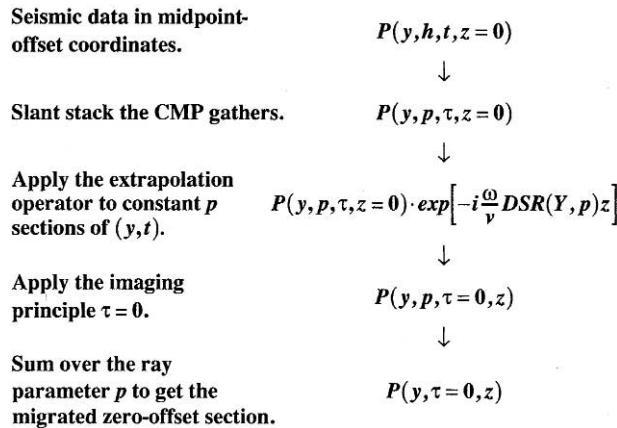


FIG. F-5. Flowchart for migration before stack in midpoint-ray-parameter coordinates.

F.3 Mathematical Foundation of the Discrete Radon Transform

The forward Radon transform $u(r, \tau)$ of a 2-D continuous function $d(h, t)$ is given by the integral expression (Beylkin, 1987)

$$u(r, \tau) = \int_{-\infty}^{\infty} d[h, t = \tau + \phi(r, h)] dh, \quad (F-10a)$$

where h and t are the input variables, and r and τ are the transform variables. The integration is along trajectories expressed as linear functions of traveltimes t and τ .

The inverse Radon transform given by the integral expression

$$d(h, t) = \int_{-\infty}^{\infty} \rho(\tau) * u[r, \tau = t - \phi(r, h)] dr \quad (F-10b)$$

incorporates convolution of $u(r, \tau)$ with the rho filter $\rho(\tau)$ prior to integration. For the 2-D data type $d(h, t)$, the Fourier transform of the rho filter is of the form $\sqrt{\omega} \exp(i\pi/4)$.

In practice, of course, we do not deal with continuous functions; instead, we have discretely sampled data in time and space. So we need to replace the integrals with discrete summations in equations (F-10a,b). We can use the least-squares technique to compute the discrete

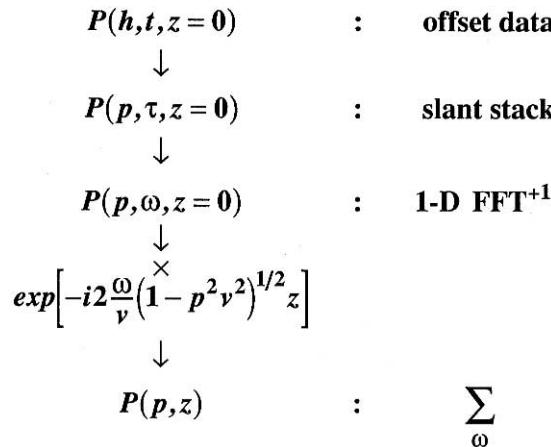


FIG. F-6. Processing flow for inversion of refraction profiles.

Radon transform (Beylkin, 1987) and account for the effects of discrete sampling and finite cable length. We shall consider three different forms of the function $\phi(r, h)$ in equation (F-10a) and, accordingly, define discrete hyperbolic (Thorson and Claerbout, 1985; Yilmaz, 1989; Foster and Mosher, 1992), parabolic (Hampson, 1986), and linear (Thorson and Claerbout, 1985) Radon transforms.

First, we shall discuss the discrete hyperbolic Radon transform. The transform variable r of the function $\phi(r, h)$ in equation (F-10a) represents stacking velocity v . The discrete transformation of the CMP data from the offset domain to the velocity domain is achieved by hyperbolic moveout correction and summing over offset

$$u(v, \tau) = \sum_h d(h, t = \sqrt{\tau^2 + 4h^2/v^2}), \quad (F - 11a)$$

where t is the two-way traveltime, τ is the two-way zero-offset time, and h is the half-offset. The inverse transform from the velocity domain back to the offset domain is achieved by inverse hyperbolic moveout correction and summing over velocity

$$d'(h, t) = \sum_v u(v, \tau = \sqrt{t^2 - 4h^2/v^2}). \quad (F - 11b)$$

The relationship between (h, t) and (v, τ) coordinates is given by the hyperbolic moveout equation:

$$t^2 = \tau^2 + \frac{4h^2}{v^2}. \quad (F - 12a)$$

To comply with the linear form of the Radon transform defined by equation (F-11a), apply stretching in the time direction by setting $t' = t^2$ and $\tau' = \tau^2$. Equation (F-12a) then takes the form

$$t' = \tau' + \frac{4h^2}{v^2}. \quad (F - 12b)$$

Also in the stretched coordinates, equations (F-11a,b) take the forms

$$u(v, \tau') = \sum_h d(h, t' = \tau' + 4h^2/v^2) \quad (F - 13a)$$

and

$$d'(h, t') = \sum_v u(v, \tau' = t' - 4h^2/v^2). \quad (F - 13b)$$

Now, consider equation (F-13b) in matrix notation:

$$\mathbf{d}' = \mathbf{L}\mathbf{u}. \quad (F - 14)$$

The matrix operator \mathbf{L} maps each point in $\mathbf{u} : u(v, \tau')$ onto a parabola in $\mathbf{d}' : d'(h, t')$, the modeled CMP gather in the stretched coordinates.

The objective is to estimate a $\mathbf{u} : u(v, \tau')$ such that the difference $\mathbf{e} : (h, t')$ between the actual CMP gather $\mathbf{d} : d(h, t')$ and the modeled CMP gather $\mathbf{d}' : d'(h, t')$ is minimum in the least-squares sense. Using the matrix notation and equation (F-14), \mathbf{e} is defined as

$$\mathbf{e} = \mathbf{d} - \mathbf{L}\mathbf{u}. \quad (F - 15)$$

To distinguish from the *conventional* velocity-stack gather defined by equation (F-11a) with amplitude smearing, we shall refer to \mathbf{u} in equation (F-14) as the Radon transform of \mathbf{d} in the stretched coordinates. By the Radon transform, parabolas in the offset domain (h, t') with the stretched coordinate t' (or, equivalently, hyperbolas in the offset domain h, t) with the unstretched coordinate t are represented by points in the velocity domain (v, τ) .

Following Lines and Treitel (1984), the least-squares solution for equation (F-14) is determined, first, by expressing the cumulative squared error S as

$$S = \mathbf{e}^T \mathbf{e}. \quad (F - 16a)$$

where \mathbf{T} is for transpose. By substituting for \mathbf{e} from equation (F-15), we get

$$S = (\mathbf{d} - \mathbf{Lu})^T(\mathbf{d} - \mathbf{Lu}). \quad (F - 16b)$$

Minimization of S with respect to \mathbf{u} yields the desired least-squares solution:

$$\mathbf{u} = (\mathbf{L}^T \mathbf{L})^{-1} \mathbf{L}^T \mathbf{d}, \quad (F - 17)$$

where \mathbf{T} denotes transpose of the matrix \mathbf{L} , and $(\mathbf{L}^T \mathbf{L})^{-1} \mathbf{L}^T$ is the least-squares (also called generalized) inverse of \mathbf{L} .

In equation (F-17) \mathbf{d} is a column vector containing all the data points from the actual CMP gather in the stretched coordinates. Its length is $n_h n_t$, where n_h is the number of offsets and n_t is the number of time samples in t' . Also, \mathbf{u} is a column vector containing all the points from the velocity stack-gather; its length is $n_v n_\tau$, where n_v is the number of velocities and n_τ is the number of time samples in τ' . The elements of the matrix operator \mathbf{L} are delta functions in the velocity domain; its dimensions are $n_h n_t \times n_v n_\tau$. For a typical field data set, $n_h = 60$, $n_t = 1000$, $n_v = 60$ and $n_\tau = 1000$; this implies an \mathbf{L} matrix of dimension $60\,000 \times 60\,000$.

The minimum error \mathbf{e} of equation F-15 associated with the least-squares solution \mathbf{u} of equation (F-17) should be interpreted as being the CMP gather that contains only the nonhyperbolic events, such as random or linear noise, that may be present in the original CMP gather \mathbf{d} . The velocity-stack gather \mathbf{u} obtained from equation (F-17) is one form of the discrete Radon transform of \mathbf{d} (Beylkin, 1987).

Direct solution for \mathbf{u} of equation (F-17) requires computing the inverse of the matrix $\mathbf{L}^T \mathbf{L}$ which may have dimensions of $60\,000 \times 60\,000$ for a typical field data set. Inverting such a large matrix is quite impractical. To circumvent solving a problem that involves a very large matrix \mathbf{L} , Fourier transform the CMP gather $d(h, t')$ in the direction of the stretch variable t' . Correspondingly, apply Fourier transform to equation (F-13b) with respect to t' given by

$$d'(h, \omega') = \sum_v u(v, \omega') \exp(-i\omega' 4h^2/v^2), \quad (F - 18)$$

where ω' is the Fourier dual of t' . For each ω' component of $d'(h, \omega')$ and $u(v, \omega')$, equation (F-18) can be written in the matrix form of equation (F-15), where \mathbf{L} now is a complex matrix of the form

$$\mathbf{L} = \begin{pmatrix} e^{-i\omega' 4h_1^2/v_1^2} & e^{-i\omega' 4h_2^2/v_2^2} & \dots & e^{-i\omega' 4h_m^2/v_n^2} \\ e^{-i\omega' 4h_2^2/v_1^2} & e^{-i\omega' 4h_3^2/v_2^2} & \dots & e^{-i\omega' 4h_m^2/v_n^2} \\ \vdots & \vdots & \ddots & \vdots \\ e^{-i\omega' 4h_m^2/v_1^2} & e^{-i\omega' 4h_m^2/v_2^2} & \dots & e^{-i\omega' 4h_m^2/v_n^2} \end{pmatrix}, \quad (F - 19)$$

with dimensions $m \times n = n_h \times n_v$, where n_h is the number of offsets, n_v is the number of velocities, and \mathbf{d}' and \mathbf{u} are complex vectors of lengths n_h and n_v , respectively. Note that the elements of the \mathbf{L} matrix depend on the geometry of the input CMP gather and the range of velocities used in constructing the velocity-stack gather.

We now restate our objective in solving for \mathbf{u} of the matrix equation (F-14) within the context of the Fourier transform domain: For each ω' , estimate the complex vector $\mathbf{u} : u(v, \omega')$ such that the difference $\mathbf{e} : e(v, \omega')$ between the complex vector of the actual CMP gather $\mathbf{d} : d(h, \omega')$ and that of the modeled CMP gather $\mathbf{d}' : d'(h, \omega')$ is minimum in the least-squares sense.

As for equation (F-17), follow the steps involving equations (F-14) through (F-16) to derive the least-squares solution in the Fourier transform domain as

$$\mathbf{u} = (\mathbf{L}^{T*} \mathbf{L})^{-1} \mathbf{L}^{T*} \mathbf{d}, \quad (F - 20)$$

where the asterisk denotes complex conjugate.

Equation (F-20) gives the unconstrained least-squares solution for \mathbf{u} . To avoid singularities or near singularities in the matrix $\mathbf{L}^{T*} \mathbf{L}$, the solution is constrained by incorporating a damping

factor β (also called the Lagrange multiplier) into equation (F-20) (Lines and Treitel, 1984):

$$\mathbf{u} = (\mathbf{L}^T \mathbf{L} + \beta \mathbf{I})^{-1} \mathbf{L}^T \mathbf{d}. \quad (F - 21)$$

Because of the near-singular character of the complex matrix \mathbf{L} , especially for small values of ω' , the solution given by equation (F-21) is best reformulated in terms of the singular-value decomposition (SVD) of the matrix \mathbf{L} (Press et al., 1986). This procedure factors \mathbf{L} into a product of three matrices:

$$\mathbf{L} = \mathbf{U} \mathbf{\Lambda} \mathbf{V}^T. \quad (F - 22)$$

By using this factorized form of the matrix \mathbf{L} , the constrained solution given by equation (F-21) takes the form

$$\mathbf{u} = \mathbf{V} [(\mathbf{\Lambda}^2 + \beta \mathbf{I})^{-1} \mathbf{\Lambda}] \mathbf{U}^T \mathbf{d}, \quad (F - 23)$$

where

$$(\mathbf{\Lambda}^2 + \beta \mathbf{I})^{-1} \mathbf{\Lambda} = \begin{pmatrix} \Gamma_1 & 0 & \dots & 0 \\ 0 & \Gamma_2 & \dots & 0 \\ \vdots & \vdots & \ddots & \vdots \\ 0 & 0 & \dots & \Gamma_{n_v} \end{pmatrix}, \quad (F - 24)$$

and $\Gamma_i = \lambda_i / (\lambda_i^2 + \beta)$, with λ_i as the positive square roots of the eigenvalues λ_i^2 of $\mathbf{L}^T \mathbf{L}$. Recall that the damping factor β is a scalar that prevents the solution (equation F-23) from becoming unstable.

We now summarize the method for computing the Radon transform represented by a velocity-stack gather:

- (1) Start with a CMP gather $d(h, t)$ and apply the t^2 -stretching, $d(h, t' = t^2)$.
- (2) Fourier transform in the t' direction, $d(h, \omega')$.
- (3) For a specific value of ω' :
 - (a) Set up the \mathbf{L} matrix (equation F-19) based on the geometry of the CMP gather.
 - (b) Set up the \mathbf{d} vector by transposing the data set $d(h, \omega')$.
 - (c) Apply singular-value decomposition to \mathbf{L} equation (F-22), and compute \mathbf{U} , $\mathbf{\Lambda}$ and \mathbf{V}^T , hence \mathbf{U}^T and \mathbf{V} .
 - (d) Specify a value for the damping factor β and set up the diagonal matrix of equation (F-24).
 - (e) Finally, solve for \mathbf{u} (equation F-23).
 - (f) Repeat (3) for all ω' values and accumulate the results in $u(v, \omega')$.
- (4) Inverse Fourier transform to get $u(v, \tau')$.
- (5) Undo the t^2 -stretching to get $u(v, \tau)$; this is the desired result, namely the velocity-stack gather with reduced amplitude smearing, which is a special form of the discrete Radon transform of $d(h, t)$.
- (6) The inverse mapping back to the offset domain to get the modeled CMP gather is done using equation (F-11b).

An important practical question is the sampling along the velocity axis in the transform domain. Specifically, in equation (F-19), one may consider sampling in terms of Δv or $1/\Delta v^2$. This will affect the quality of the velocity stack gather and the reconstructed gather. When $1/\Delta v^2$ sampling is used, the structure of the \mathbf{L} matrix in equation (F-19) becomes Toeplitz (Kostov, 1990). Hence, one can use Levinson recursion to solve equation (F-20) and thus obtain the Radon transform \mathbf{u} .

Figure F-7 shows a comparison of the performance of the various solutions to equation (F-20). The input is a synthetic CMP gather with band-limited noise. The velocity-stack gather was computed using the SVD approach described here with Δv and $1/\Delta v^2$ sampling criteria

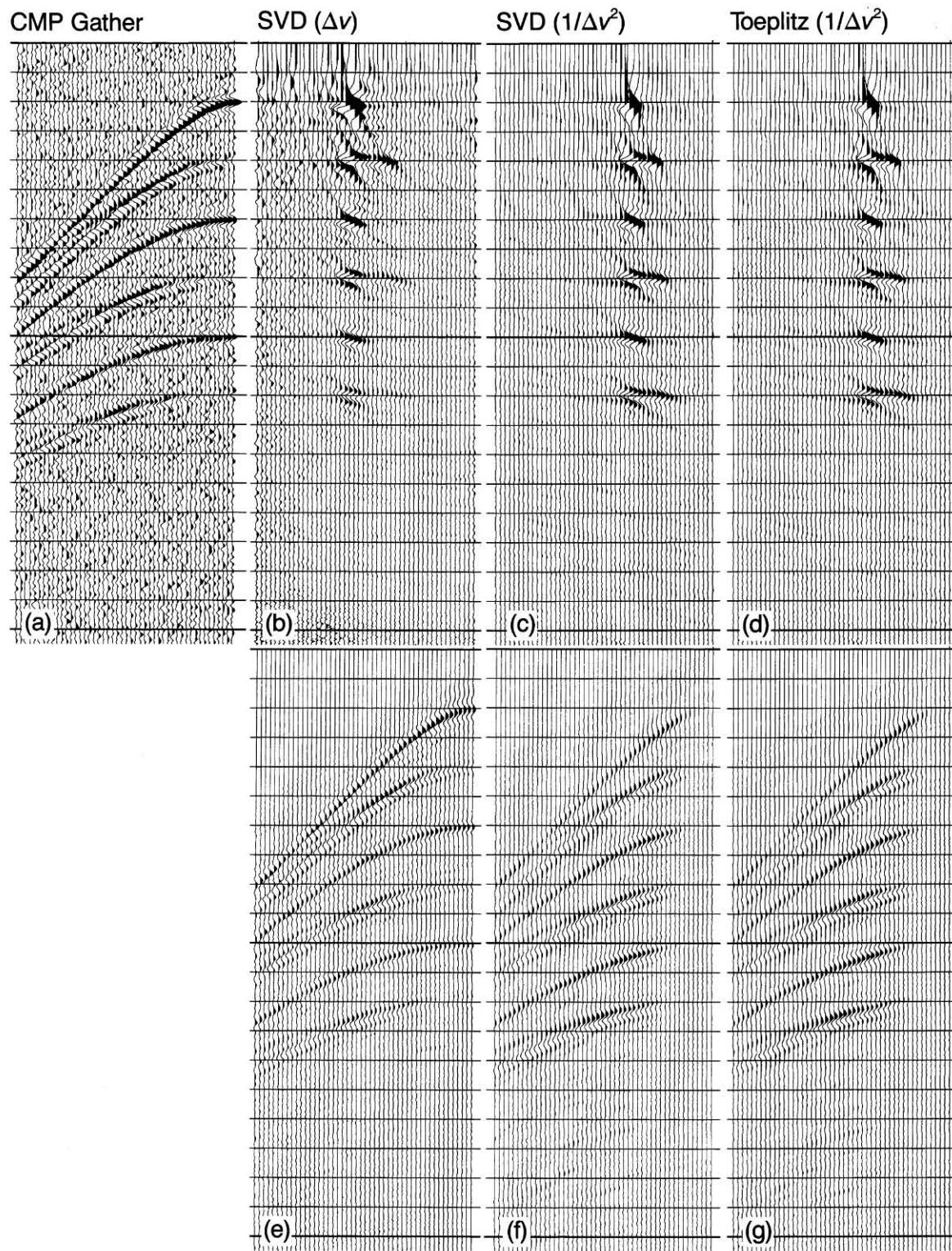


FIG. F-7. Solutions to equation (F-20) using SVD and Toeplitz procedures with two different sampling criteria — Δv and $1/\Delta v^2$. (a) A synthetic CMP gather as in Figure 6.4-2c with band-limited noise; (b), (c) and (d) the velocity-stack gathers using three combinations of sampling and procedure as indicated on top of each panel; and (e), (f) and (g) reconstructed gathers from (b), (c) and (d), respectively.

and the Toeplitz solution with the $1/\Delta v^2$ sampling criterion. Figure F-7 also shows the reconstructed gathers using equation (F-11b). Results indicate that the SVD approach with the Δv sampling criterion best preserves the amplitudes at all offsets. The $1/\Delta v^2$ sampling causes loss of amplitudes at near offsets.

We now set up the least-squares problem to perform the discrete parabolic Radon transform (Hampson, 1986, 1987). As an alternative to stretching in the time direction as defined by equation (F-12b) to comply with the linear form of the Radon transform (equation F-11a), consider the application of normal moveout correction to input CMP data (equation F-12a) using a velocity function v_n :

$$t_n = \sqrt{t^2 - \frac{4h^2}{v_n^2}}, \quad (F-25)$$

such that hyperbolic events in the original gather $d(h, t)$ can be approximately represented by parabolic events with the traveltime equation

$$t_n = \tau + qh^2, \quad (F-26)$$

where t_n is the time after NMO corection, v_n is the hyperbolic moveout correction velocity function, τ is the two-way zero-offset time, and q is the parameter that defines the curvature of the parabolic trajectory described by equation (F-26).

In the coordinates of the NMO-corrected gather $d(h, t_n)$, equations (F-11a,b) take the forms

$$u(q, \tau) = \sum_h d(h, t_n = \tau + qh^2) \quad (F-27a)$$

and

$$d'(h, t_n) = \sum_q u(q, \tau = t_n - qh^2). \quad (F-27b)$$

We want to find an estimate of \mathbf{u} such that when inverse transformed, the difference between the modeled moveout-corrected CMP gather $d'(h, t_n)$ and the original moveout-corrected CMP gather $d(h, t_n)$, which is the desired output, is minimum in the least-squares sense.

A practical estimation of \mathbf{u} based on the least-squares scheme can be achieved, again, by first Fourier transforming equation (F-26b) as

$$d'(h, \omega_n) = \sum_q u(q, \omega_n) \exp(-i\omega_n qh^2), \quad (F-28)$$

where ω_n is the Fourier dual of t_n . For each ω_n component of $d'(h, \omega_n)$ and $u(q, \omega_n)$, equation (F-28) can be written in the matrix form of equation (F-14), where \mathbf{L} is a complex matrix of the form:

$$\mathbf{L} = \begin{pmatrix} e^{-i\omega_n q_1 h_1^2} & e^{-i\omega_n q_2 h_1^2} & \dots & e^{-i\omega_n q_n h_1^2} \\ e^{-i\omega_n q_1 h_2^2} & e^{-i\omega_n q_2 h_2^2} & \dots & e^{-i\omega_n q_n h_2^2} \\ \vdots & \vdots & \ddots & \vdots \\ e^{-i\omega_n q_1 h_m^2} & e^{-i\omega_n q_2 h_m^2} & \dots & e^{-i\omega_n q_n h_m^2} \end{pmatrix}, \quad (F-29)$$

with dimensions $m \times n = n_h \times n_q$, where n_h is the number of offsets, and n_q is the number of q parameters for which the Radon transform $u(q, \tau)$ is to be estimated. As for the hyperbolic Radon transform (equation F-19), note that the elements of the \mathbf{L} matrix depend only on the geometry of the input CMP gather.

Aside from the \mathbf{L} matrix, for each frequency component ω_n , define the vectors for the input gather $\mathbf{d} : d(h, t)$, the unknown transform $\mathbf{u} : u(q, \tau)$, and the modeled CMP gather $\mathbf{d}' : d'(h, t)$. As for equation (F-18), for each frequency component ω_n , equation (F-28) is written in the matrix form of equation (F-14), where \mathbf{L} is the complex matrix given by equation (F-29). Using this new form of the \mathbf{L} matrix, follow the same procedure starting with equation (F-20) to obtain the solution expressed by equation (F-23).

Finally, we set up the least-squares problem to perform the discrete linear Radon transform. The transform variable r of the function $\phi(r, h)$ in equation (F-11a) represents the ray parameter p . The relationship between (h, t) and (p, τ) coordinates is given by the parabolic moveout equation

$$t = \tau + 2ph. \quad (F - 30)$$

The transformation of the CMP data from the offset domain to the ray-parameter domain is achieved by applying linear moveout correction and summing over offset

$$u(p, \tau) = \sum_h d(h, t = \tau + 2ph), \quad (F - 31a)$$

where t is the two-way traveltimes, τ is the intercept time at $p = 0$, and h is the half-offset. The inverse transform from the ray-parameter domain back to the offset domain is achieved by inverse linear moveout correction and summing over velocity

$$d'(h, t) = \sum_p u(v, \tau = t - 2ph). \quad (F - 31b)$$

We want to estimate $\mathbf{u} : u(p, \tau)$ such that when inverse transformed back to the offset domain, the difference between the modeled CMP gather $\mathbf{d}' : d'(h, t)$ and the original CMP gather $\mathbf{d} : d(h, t)$ is minimum in the least-squares sense.

A practical estimation of \mathbf{u} based on the least-squares scheme can be achieved, once again, by first Fourier transforming equation (F-31b) as

$$d'(h, \omega) = \sum_p u(p, \omega) \exp(-i\omega 2ph). \quad (F - 32)$$

For each ω component of $d'(h, \omega)$ and $u(p, \omega)$, equation (F-32) can be written in the matrix form of equation (F-14), where \mathbf{L} is a complex matrix of the form

$$\mathbf{L} = \begin{pmatrix} e^{-i\omega 2p_1 h_1} & e^{-i\omega 2p_2 h_1} & \dots & e^{-i\omega 2p_n h_1} \\ e^{-i\omega 2p_1 h_2} & e^{-i\omega 2p_2 h_2} & \dots & e^{-i\omega 2p_n h_2} \\ \vdots & \vdots & \ddots & \vdots \\ e^{-i\omega 2p_1 h_m} & e^{-i\omega 2p_2 h_m} & \dots & e^{-i\omega 2p_n h_m} \end{pmatrix}, \quad (F - 33)$$

with dimensions $m \times n = n_h \times n_p$, where n_h is the number of offsets, and n_p is the number of ray parameters p for which the Radon transform $u(p, \tau)$ is to be estimated. As for the hyperbolic and parabolic cases, the elements of the \mathbf{L} matrix depend only on the geometry of the input CMP gather.

Aside from the \mathbf{L} matrix, for each frequency component ω , define the vectors for the input gather $\mathbf{d} : d(h, t)$, the unknown transform $\mathbf{u} : u(p, \tau)$, and the modeled CMP gather $\mathbf{d}' : d'(h, t)$. As for the hyperbolic and parabolic cases, for each frequency component ω , equation (F-32) is written in the matrix form of equation (F-14), where \mathbf{L} is the complex matrix given by equation (F-33). Using this new form of the \mathbf{L} matrix, follow the same procedure starting with equation (F-20) to obtain the solution expressed by equation (F-23).

Figure F-8 shows a CMP gather and the modeled CMP gathers computed by inverse transforming the velocity-stack and slant-stack gathers that were themselves estimated using the respective discrete Radon transforms. The reconstruction based on the velocity-stack gather restores that component of the original gather associated with the hyperbolic events. The reconstruction based on the slant-stack transformation, when implemented as a special form of the discrete Radon transform, restores virtually all of the data characteristics of the original gather.

There exists an affinity between slant-stack transformation (Section 6.3) and the discrete linear Radon transform discussed here. To compute the slant-stack gather, recall from Section (6.3) that we applied linear moveout to input data and summed over the offset axis (equation 6-5). That operation is equivalent to applying the \mathbf{L}^T matrix on the input vector \mathbf{d} in equation (F-23). We then applied the rho filter to compensate for the attenuation of high frequencies

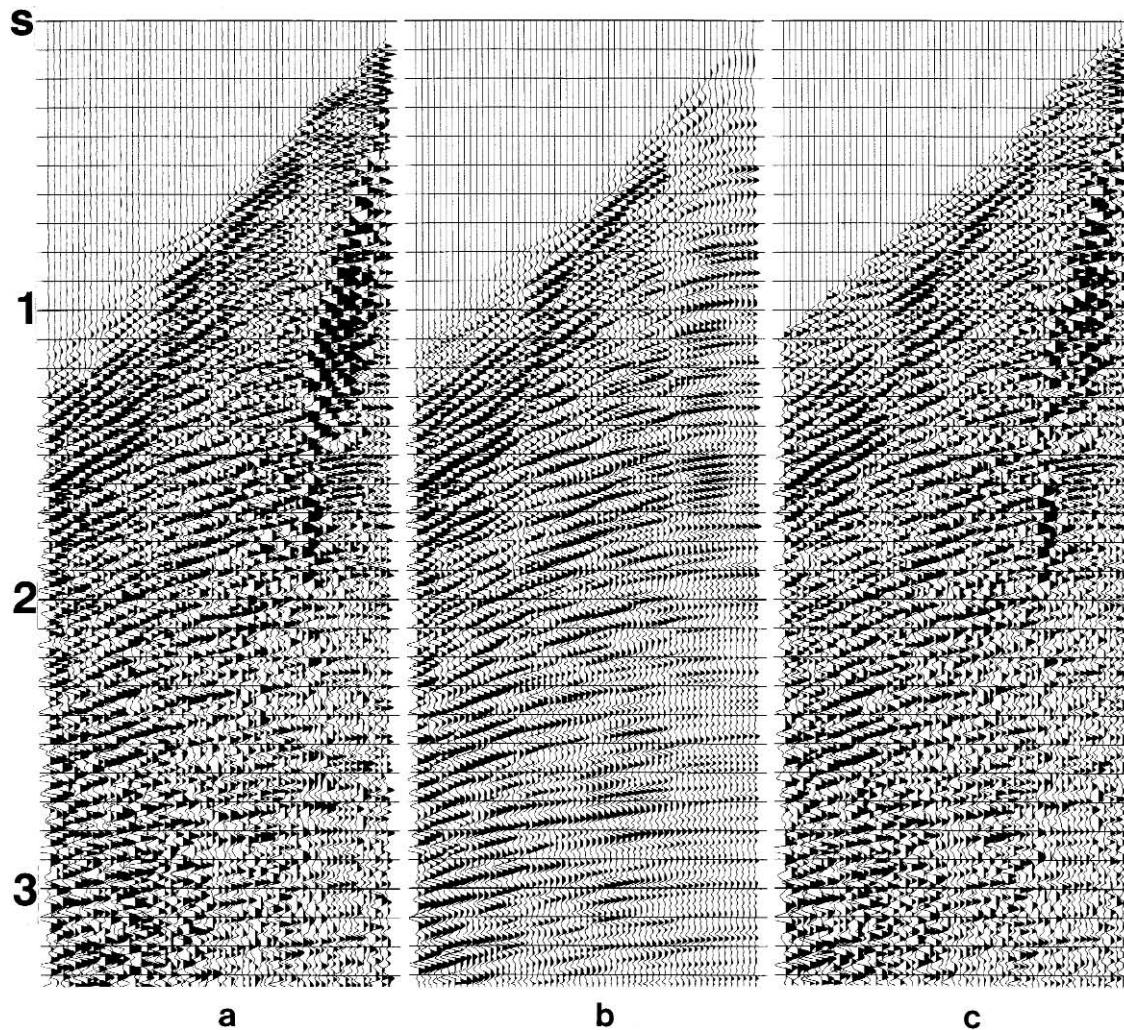


FIG. F-8. (a) A CMP gather; (b) reconstructed CMP gather by way of velocity-stack transformation; (c) reconstructed CMP gather by way of slant-stack transformation. Both velocity-stack and slant-stack transforms are special forms of the discrete Radon transform.

during the summation over the offset axis. Applying the rho filter is to some extent equivalent to applying the additional matrix operator $(\mathbf{L}^T * \mathbf{L})^{-1}$ of equation (F-20). Actually this 2-D operator does more than what the 1-D rho filter does — it accounts for the discrete sampling along the spatial axis and the finite cable length. Nevertheless, in practice, it turns out that just applying the rho filter in lieu of applying this computationally more involved operator yields a reasonably accurate slant-stack gather.

F.4 Free-Surface Multiple Attenuation

Refer to the raypath configurations for the various types of multiples depicted in Figure 6.0-18. Most significant multiples involve one or more bounces from the free surface. Figure 6.0-18a shows the first- and second-order water-bottom multiples, and Figure 6.0-18b shows the first- and second-order free-surface multiples associated with a deeper reflector. Figure 6.0-18c shows the peg-leg multiples associated with a primary reflection and intrabed multiple reflection, and Figure 6.0-18d shows the first- and second-order *intrabed* multiple reflections. Finally, Figure 6.0-18e shows the first- and second-order *interbed* multiple reflections.

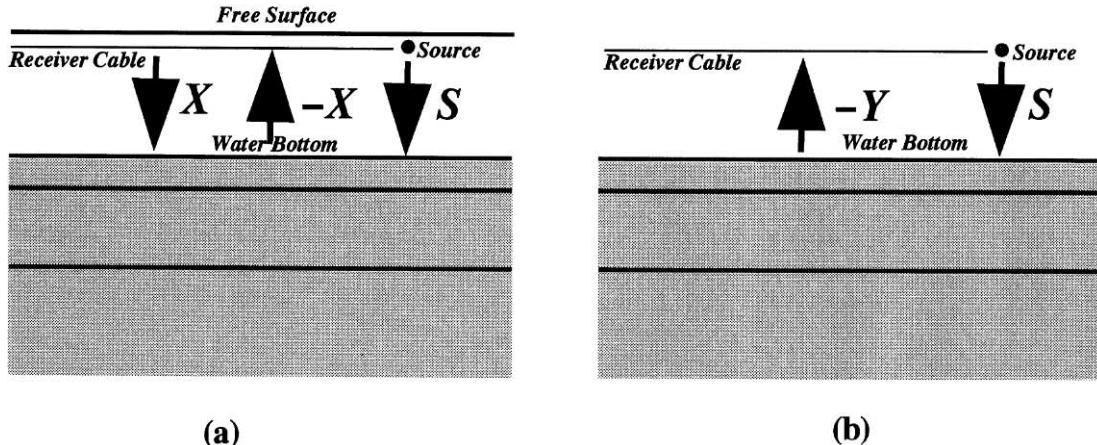


FIG. F-9. (a) Marine recording geometry, (b) Noah's geometry. S is the vertically downgoing source wavefield, X is the recorded upcoming wavefield with and Y is the wavefield without free-surface multiples. All wavefields are assumed to be plane waves. (Adapted from Riley and Claerbout, 1976.)

Shown in Figure 6.0-18 are but a limited subset of a countless group of multiples that are normally present in recorded marine data. Rather than attempting to attenuate all multiples, it makes sense to develop a technique aimed at attenuating the most significant set of multiples—those associated with the free surface. Riley and Claerbout (1976) developed an elegant theory for free-surface multiple attenuation applicable to 1-D seismograms. They also extended their ideas to 2-D recorded data to attenuate diffracted multiples. The free-surface multiple attenuation theory by Riley and Claerbout (1976) was reworked and widely publicized later by Kennett (1979), Verschuur (1991), Verschuur et al. (1992), Carvalho et al. (1991), Dragoset and McKay (1993), Verschuur and Berkhou (1994), and Berkhou and Verschuur (1995). Applications to field data were reported by Dragoset and McKay (1993), Verschuur et al. (1995), Kelamis and Verschuur (1996), and Dragoset and Jericevic (1998). Here, we shall develop the theory of free-surface multiple attenuation based on the work by Riley and Claerbout (1976), then review the work by Verschuur et al. (1992).

Consider the 1-D earth model in Figure F-9a and recording using a source represented by a vertically downward traveling plane wave W . If the free surface were removed from the earth model (Figure F-9b), then the associated multiples would also be removed from the recorded 1-D seismogram. The hypothetical recording geometry that facilitates removal of the free surface is called Noah's geometry by Riley and Claerbout (1976), and the technique to remove the free-surface multiples based on Noah's geometry is called Noah's deconvolution. Note that in Noah's geometry the recording cable now is being towed by a submarine rather than a surface vessel since the water level has risen as a result of the flood.

Whether you record with Noah's geometry (Figure F-9b) or the actual geometry at the same datum level (Figure F-9a), the earth's response $E(z)$ to the same source $S(z)$ defined in the z -transform domain should be the same. The earth's response $E(z)$ can be described by the ratio of the upcoming waves $U(z)$ to the downgoing waves $D(z)$:

$$E(z) = \frac{U(z)}{D(z)}. \quad (F-34a)$$

From Figure (F-9a), the upcoming wave is $U(z) = -X(z)$, the recorded seismogram, and the downgoing wave is $D(z) = S(z) + X(z)$. Here, we assume that the reflection coefficient of the free surface is -1 . From Figure F-9b, the upcoming wave is $U(z) = -Y(z)$, the seismogram that

is free of surface multiples, and the downgoing wave is $D(z) = S(z)$. Hence, the earth's response $E(z)$ defined by equation (F-34a) for the geometry of Figure F-9a is

$$E(z) = -\frac{X(z)}{S(z) + X(z)}, \quad (F-34b)$$

and for the geometry of Figure (F-9b) is

$$E(z) = -\frac{Y(z)}{S(z)}. \quad (F-34c)$$

Combine equations (F-34b,c) to obtain

$$\frac{Y(z)}{S(z)} = \frac{X(z)}{S(z) + X(z)}. \quad (F-35)$$

Assume that the source waveform is minimum phase (Section 2.2) and define its inverse $F(z) = S^{-1}(z)$. Then, solve equation (F-35) for the seismogram $Y(z)$ free of surface multiples as

$$Y(z) = \frac{X(z)}{1 + F(z)X(z)}. \quad (F-36)$$

Equation (F-38) is the basis for Noah's deconvolution described by Riley and Claerbout (1976). A practical perspective on the use of equation (F-36) is gained by the series expansion of the right-hand side:

$$Y(z) = X(z)[1 - F(z)X(z) + F^2(z)X^2(z) - \dots], \quad (F-37)$$

where it is assumed that $F(z)X(z) \ll 1$.

Equation (F-37) can be put into the convolutional form

$$y(t) = x(t) - x(t) * [f(t) * x(t)] + x(t) * [f(t) * x(t)] * [(f(t) * x(t))] - \dots \quad (F-38)$$

An iterative scheme to estimate the seismogram $y(t)$ free of surface multiples can be devised based on equation (F-38). First, write the following recursive relation:

$$y_{i+1}(t) = x(t) - x(t) * [f(t) * y_i(t)], \quad i = 0, 1, 2, \dots \quad (F-39)$$

where $y_0(t) = x(t)$.

The recursive relation described by equation (F-39) yields the truncated form of the series on the right-hand side of equation (F-38). To see this, set $i = 0$ in equation (F-39):

$$y_1(t) = x(t) - x(t) * [f(t) * x(t)], \quad (F-40a)$$

which corresponds to the first two terms of the series in equation (F-39). Next, set $i = 1$ in equation (F-39) and substitute equation (F-40a) for y_1 to get

$$y_2(t) = x(t) - x(t) * [f(t) * x(t)] + x(t) * [f(t) * x(t)] * [(f(t) * x(t))], \quad (F-40b)$$

which corresponds to the first three terms in equation (F-38).

Thus, by recursive application of equation (F-39) for a specified number of iterations, an estimate of the seismogram $y(t) \approx y_{i+1}(t)$ that is free of most of the surface-related multiples can be obtained. Specifically, equation (F-39) states that the output $y_{i+1}(t)$ of the next iteration is the difference between the input trace $x(t)$ and the input trace convolved with the inverse of the source wavelet $f(t)$ convolved with the output of the previous iteration $y_i(t)$. The number of iterations in practice often is no more than three.

While the recursive scheme described here based on the work by Riley and Claerbout (1976) is designed for a zero-offset seismogram $x(t)$ associated with a 1-D earth model, the theory has been extended to handle nonzero-offset data associated with a 2-D earth model by the same authors, and subsequently by Verschuur (1991), Verschuur and Berkhout (1994), and Dragoset and McKay (1993). In fact, the recursive relation given by equation (F-39), with a group of shot records as input, is the same as the update formula given by Verschuur and Berkhout (1994).

To attenuate free-surface multiples caused by reflectors with complex geometry, in theory, you need all of the shot records along the seismic line as one single input to equation (F-39) (Dragoset and McKay, 1993). In practice, however, assumptions are made about the subsurface complexity to be able to use individual CMP gathers as input (Kelmanis and Verschuur, 1996). Also, assuming that spiking deconvolution has been applied to the input CMP gather prior to free-surface multiple attenuation, the inverse of the source wavelet $f(t)$ in equation (F-39) may be set to a unit spike at $t = 0$. Then, it follows that

$$P_{i+1}(h, t) = P_0(h, t) - P_0(h, t) * P_i(h, t), \quad (F - 41)$$

where $P_0(h, t)$ is the input CMP gather and $P_i(h, t)$ is the gather after free-surface multiple attenuation, and h and t are the offset and time variables, respectively.

The recursion described by equation (F-41) requires 2-D convolution of the input gather $P_0(h, t)$ with the result of the previous iteration $P_i(h, t)$. For computational efficiency, the recursion can be performed in the space-frequency ($h - \omega$) domain

$$P_{i+1}(h, \omega) = P_0(h, \omega) - P_0(h, \omega)P_i(h, \omega), \quad (F - 42)$$

where $P_0(h, \omega)$ is the input CMP gather and $P_i(h, \omega)$ is the gather after free-surface multiple attenuation, both in the $h - \omega$ domain.

In practice, there are two issues that hinder the effectiveness of the free-surface multiple attenuation technique discussed here. First is the problem of an accurate estimate of the source wavelet $s(t)$. Actually, it is the inverse of the source wavelet $f(t)$ that is needed in the recursive relation described by equation (F-39). Deterministically, the source wavelet may be assumed equivalent to the recorded far-field signature (Section 2.5). Statistically, it may be assumed to be the minimum-phase inverse of the spiking deconvolution operator (Section 2.2). It is this latter viewpoint that is often taken in practice. As such, the input to the recursive estimate of the surface-related multiples in equation (F-41) is the CMP gather with spiking deconvolution.

The second issue is the missing near offsets. Attenuation of free-surface multiples using the recursive relation of equation (F-41) involves predicting multiples from the primaries. The free-surface multiples generated by a primary reflection that occurs within the near-offset range that is not recorded then are not attenuated. In fact, the problem of missing near-offset data has the most significant detrimental impact on the ability of the technique to attenuate all possible surface-related multiples (Dragoset and Jericevic, 1998). The Radon transform provides a theoretically appealing way to estimate the unrecorded near offsets (Section 6.4).

Figure F-10 shows a field data example of free-surface multiple attenuation. The free-surface multiples in the shot record (Figure F-10a) include the water-bottom multiples and the peg-leg multiples associated with the top-salt and base-salt reflections. The same record after free-surface multiple attenuation (Figure F-10b) exhibits some residual of these multiples, primarily because of the practical issues discussed above. The free-surface multiples heavily contaminate the subsalt reflections (Figure F-10c). After multiple attenuation, the subsalt region is largely free of surface-related multiples.

F.5 Water-Bottom Multiple Attenuation

A subset of surface-related multiples is water-bottom multiples. Based on the work by Morley (1982), Wiggins (1988) formulated a technique to attenuate water-bottom multiples associated with a complex water-bottom geometry. As for the free-surface multiple attenuation technique, this method also predicts multiples from the primaries contained in the recorded data within the cable length. To develop the conceptual basis, here, we shall review the technique for the special case of flat water bottom.

Refer to the raypath configuration in Figure F-11. Assume a horizontally layered earth model and treat a CMP gather a single wavefield equivalent to a shot record. The downgoing wavefield $D(h, z_W, \omega)$ at the water bottom is given by

$$D(h, z_W, \omega) = P_0(h, z_R, \omega) \exp [ik_z(z_W + z_R)], \quad (F - 43)$$

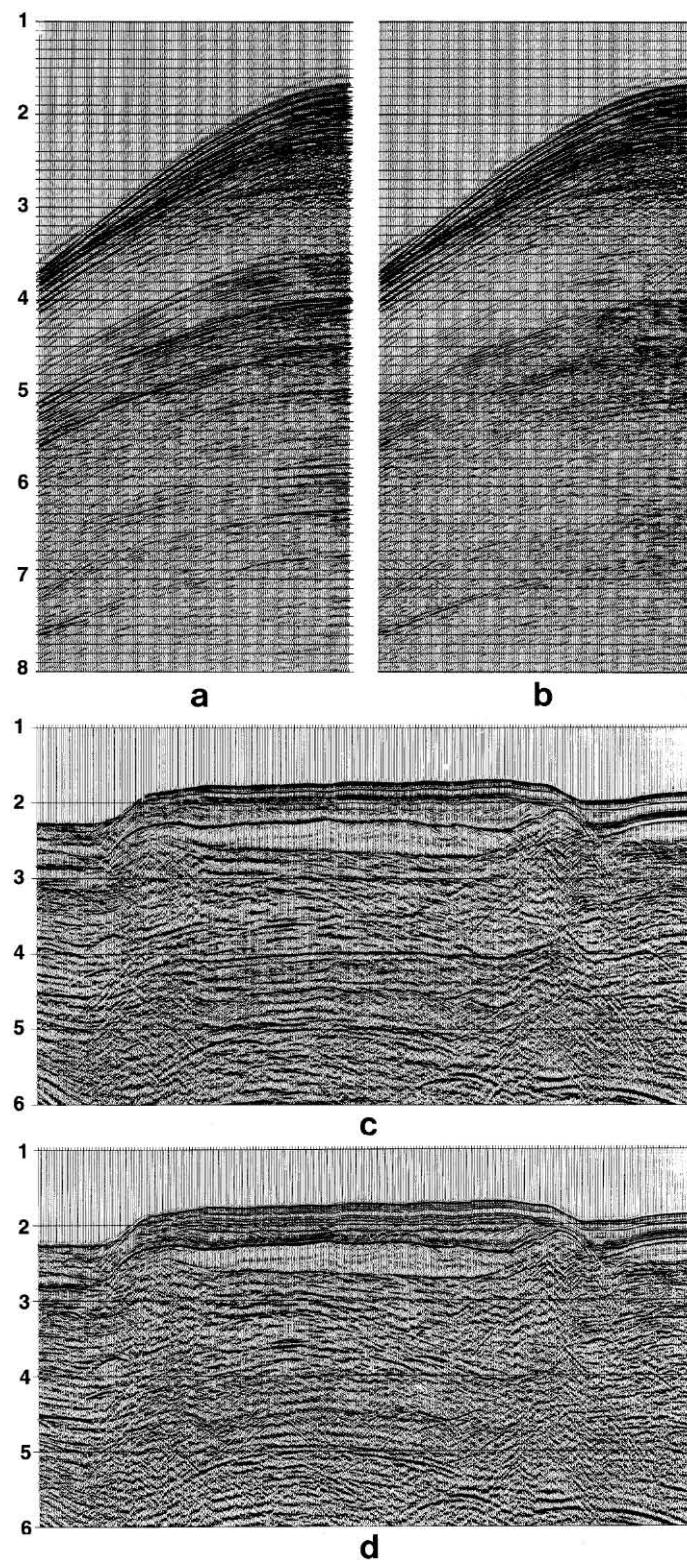


FIG. F-10. (a) A shot record with strong water-bottom multiples, (b) the same record after water-bottom multiple attenuation, (c) a portion of the stacked section associated with the data as in (a) that exhibits surface-related multiples, (d) a portion of the stacked section associated with the data as in (b) after free-surface multiple attenuation. (Dragoset and McKay, 1993.)

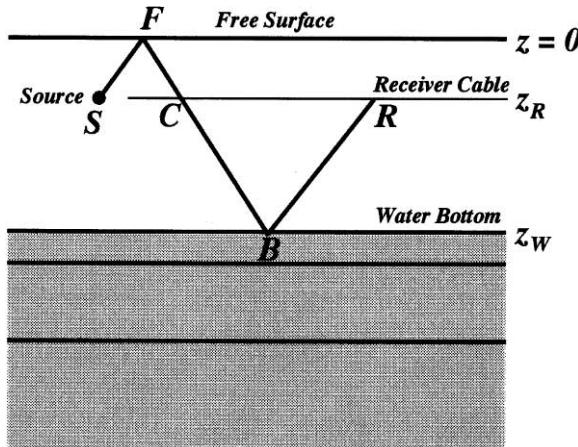


FIG. F-11. Raypath geometry associated with up- and downgoing waves at the water bottom.

where $P_0(h, z_R, \omega)$ is the CMP gather that represents the recorded wavefield at the receiver depth z_R , h is the offset variable, z_W is the water depth, ω is the temporal frequency and k_z is the vertical wavenumber. The upcoming wavefield $U(h, z_W, \omega)$ at the water bottom is given by

$$U(h, z_W, \omega) = P_0(h, z_R, \omega) \exp[-ik_z(z_W - z_R)]. \quad (F-44)$$

In equations (F-43) and (F-44), the sign convention defined in Section D.1 for wavefield extrapolation is used.

The CMP gather $P_p(h, z_W, \omega)$ free of water-bottom multiples defined at the water bottom is given by (Wiggins, 1988)

$$P_p(h, z_W, \omega) = U(h, z_W, \omega) - r_W(\omega)D(h, z_W, \omega), \quad (F-45)$$

where $r_W(\omega)$ is the water-bottom reflectivity.

Substitute equations (F-43) and (F-44) into equation (F-45) and simplify to get

$$P_p(h, z_W, \omega) = P_0(h, z_R, \omega) \{ \exp[-ik_z(z_W - z_R)] - r_W(\omega) \exp[ik_z(z_W + z_R)] \}. \quad (F-46)$$

The CMP gather $P_p(h, z_R, \omega)$ free of water-bottom multiples defined at the receiver depth is computed by extrapolating the CMP gather $P_p(h, z_W, \omega)$ defined at the water bottom:

$$P_p(h, z_R, \omega) = P_p(h, z_W, \omega) \exp[ik_z(z_W - z_R)]. \quad (F-47)$$

Now substitute equation (F-46) into (F-47) and simplify to get

$$P_p(h, z_R, \omega) = P_0(h, z_R, \omega) [1 - r_W(\omega) \exp(ik_z 2z_W)]. \quad (F-48)$$

Finally, rewrite this equation as

$$P_p(h, \omega) = P_0(h, \omega) - r_W(\omega)P_0(h, \omega) \exp(ik_z 2z_W), \quad (F-49)$$

where z_R has been omitted for simplicity. Equation (F-49) states that the gather $P_p(h, \omega)$ with water-bottom multiple attenuation is computed by taking the difference of the input gather $P_0(h, \omega)$ and the input gather scaled by the water-bottom reflectivity $r_W(\omega)$ and upward extrapolated by a depth interval twice the water depth z_W .

Equation (F-49) applies to data for which CMP assumptions are acceptable. For complex water-bottom multiples, the horizontal layer assumption no longer holds and therefore input data must be the entire set of shot records along the seismic line (Wiggins, 1988). As for free-surface multiple attenuation, however, computational efficiency in practice usually mandates use of individual CMP gathers in equation (F-49).

In practice, there are several limitations of the water-bottom multiple attenuation technique discussed here. First is the problem of an accurate estimate of the water-bottom reflectivity

$r_W(\omega)$ that is needed in equation (F-49). While attempts have been made to obtain an accurate and stable estimate of the water-bottom reflectivity (Wiggins, 1988), the problem remains as a major obstacle to the success of the technique in practice.

Additional issues arise in relation to spatial aliasing of the CMP data and missing near-offset data. As for the free-surface multiple attenuation, these problems may be circumvented by trace interpolation and extrapolation to zero offset using the Radon transform.

Perhaps the most serious limitation of the technique is the computational requirements to handle complex water-bottom geometry. In that case, the prediction and subtraction of multiples cannot be performed by the use of equation (F-49) based on phase-shift extrapolation. Instead, equation (F-45) needs to be employed wherein wave extrapolation has to be performed using the Kirchhoff integral to handle the irregular water-bottom geometry (Section 8.1). The water-bottom geometry itself can be determined by migrating the stacked section using the constant-velocity Stolt migration (Section 4.1) and converting the picked time horizon associated with the water-bottom reflection to depth as for the layer replacement (Section 8.1).

Figure F-12 shows a field data example of attenuation of complex water-bottom multiples (Wiggins, 1988). The shot record in Figure F-12a exhibits strong multiples associated with a dipping water bottom. After the application of the technique based on equation (F-49), water-bottom multiples have been largely attenuated as shown in Figure F-12b. The stacked section shown in Figure F-12c associated with the shot record as in Figure F-12a contains complex water-bottom multiples. Any remaining multiples after multiple attenuation (Figure F-12d) may be attributed to the limitations in an accurate estimate of the water-bottom reflectivity and the adverse effect of the missing near-offset data.

F.6 Spatial Prediction Filter

Consider a CMP-stacked data set $P(x, t)$, where x is the CMP axis and t is the two-way zero-offset time axis. Apply Fourier transform in the t direction to decompose this 2-D data set to its frequency components $P(x, \omega)$. For each frequency component, define a complex vector $\mathbf{P} : P(x, \omega)$ in the x direction.

We want to design a *complex* Wiener prediction filter $\mathbf{F} : F(x)$, such that, when applied to the input data vector $\mathbf{P} : P(x, \omega)$, it yields an estimate of the input vector $\mathbf{D} : D(x + \alpha, \omega)$, at $x + \alpha$, where \mathbf{D} is the desired output vector and α is the prediction lag. For the specific problem of attenuating random noise uncorrelated from trace to trace, we shall consider the unit prediction lag $\alpha = 1$. The output of the spatial prediction filtering is the predictable component of the input data vector that can be treated as the coherent signal, and the error in the prediction process is the random noise contained in the input data (Canales, 1984).

The prediction filtering is expressed by the following convolutional relation:

$$Y(x) = P(x, \omega) * F(x), \quad (F - 50)$$

where $Y(x)$ represents the actual output from prediction filtering. We want to compute a complex prediction filter $F(x)$ such that the difference $E(x)$ between the actual output $Y(x)$ and the desired output $D(x)$ is minimum in the least-squares sense. Consider the discrete form of equation (F-50), with $F(x)$ represented by the m -length complex vector $\mathbf{F} : (F_0, F_1, F_2, \dots, F_{m-1})$, $P(x, \omega)$ represented by the n -length complex vector $\mathbf{P} : (P_0, P_1, P_2, \dots, P_{n-1})$, and $Y(x)$ represented by the $(m + n - 1)$ -length complex vector $\mathbf{Y} : (Y_0, Y_1, Y_2, \dots, Y_{m+n-1})$. Equation (F-50) can then be expressed in the following matrix form:

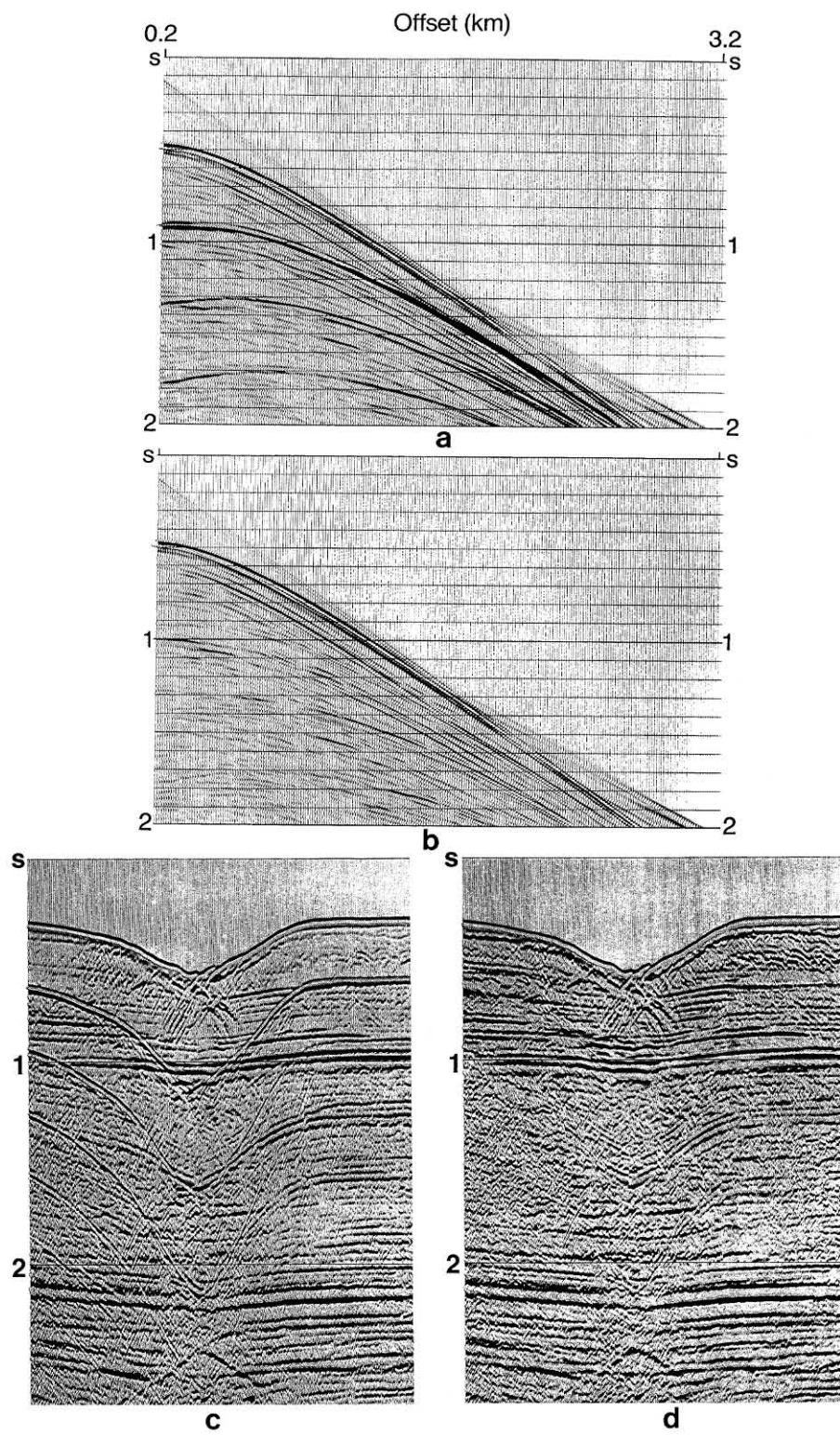


FIG. F-12. (a) A shot record with strong water-bottom multiples, (b) the same record after water-bottom multiple attenuation, (c) a portion of the stacked section associated with the data as in (a) that exhibits complex water-bottom multiples, (d) a portion of the stacked section associated with the data as in (b) after water-bottom multiple attenuation. (Wiggins, 1988.)

$$\begin{pmatrix} Y_0 \\ Y_1 \\ Y_2 \\ \vdots \\ Y_{m+n-1} \end{pmatrix} = \begin{pmatrix} P_0 & 0 & \dots & 0 \\ P_1 & P_0 & \dots & 0 \\ P_2 & P_1 & P_0 & \vdots \\ \vdots & P_2 & P_1 & P_0 \\ P_{m-1} & \vdots & P_2 & P_1 \\ 0 & P_{m-1} & \vdots & P_2 \\ \vdots & \dots & P_{m-1} & \vdots \\ 0 & 0 & \dots & P_{m-1} \end{pmatrix} \begin{pmatrix} F_0 \\ F_1 \\ F_2 \\ \vdots \\ F_{n-1} \end{pmatrix}. \quad (F-51)$$

This is the equation for complete transient convolution. Define the $(m + n - 1) \times (m + n - 1)$ coefficient matrix on the right-hand side by \mathbf{L} . Equation (F-51) takes the compact form

$$\mathbf{Y} = \mathbf{LF}. \quad (F-52)$$

The error vector $\mathbf{E} : (E_0, E_1, E_2, \dots, E_{m+n-1})$ is defined as the difference between the desired output $\mathbf{D} : (D_0, D_1, D_2, \dots, D_{m+n-1})$ and the actual output $\mathbf{Y} : (Y_0, Y_1, Y_2, \dots, Y_{m+n-1})$:

$$\mathbf{E} = \mathbf{D} - \mathbf{Y}. \quad (F-53)$$

By substituting equation (F-52) into equation (F-53), we obtain

$$\mathbf{E} = \mathbf{D} - \mathbf{LF}. \quad (F-54)$$

The energy of the error vector is

$$S = \mathbf{E}^T \mathbf{E}, \quad (F-55)$$

where T denotes matrix transpose and $*$ denotes complex conjugate. Now, substitution of equation (F-54) into the definition defined by equation (F-55) yields:

$$S = (\mathbf{D} - \mathbf{LF})^T \mathbf{E} \quad (F-56)$$

Expand the right-hand side:

$$S = \mathbf{D}^T \mathbf{D} - \mathbf{F}^T \mathbf{L}^T \mathbf{D} - \mathbf{D}^T \mathbf{L} \mathbf{F} + \mathbf{F}^T \mathbf{L}^T \mathbf{L} \mathbf{F}. \quad (F-57)$$

We want to estimate a prediction filter vector \mathbf{F} such that the quantity S is minimum. This condition leads to setting the derivative of S with respect to \mathbf{F} to zero. Differentiate both sides of equation (F-57) with respect to \mathbf{F} and observe the requirement for least-squares minimization that $\partial S / \partial \mathbf{F} = 0$:

$$-\mathbf{D}^T \mathbf{L} + \mathbf{F}^T \mathbf{L}^T \mathbf{L} = \mathbf{0}. \quad (F-58)$$

Apply matrix transpose and rearrange the terms:

$$(\mathbf{L}^T \mathbf{L})^T \mathbf{F} = \mathbf{L}^T \mathbf{D}. \quad (F-59)$$

Now define

$$\mathbf{G} = \mathbf{L}^T \mathbf{D} \quad (F-60a)$$

and

$$\mathbf{R} = \mathbf{L}^T \mathbf{L}, \quad (F-60b)$$

which yields the relation

$$\mathbf{R}^T = \mathbf{R}, \quad (F-60c)$$

thus making \mathbf{R} a Hermitian matrix of the size $(m + n - 1) \times (m + n - 1)$.

Use the relations given by equations (F-60a,b,c), to rewrite equation (F-58) in the form

$$\mathbf{RF} = \mathbf{G}, \quad (F-61)$$

which can be rewritten by using equations (F-60a,b) as follows:

$$\mathbf{F} = (\mathbf{L}^T \mathbf{L})^{-1} \mathbf{L}^T \mathbf{D}. \quad (F - 62)$$

This solution is of the same form as the generalized linear inverse form of the discrete Radon transform represented by equation (F-20). As for the latter application, singular-value decomposition technique based on equation (F-23) can be used to solve for the complex Wiener filter coefficients $\mathbf{F} : (F_0, F_1, F_2, \dots, F_{m-1})$.

An efficient recursive algorithm to solve for the complex Wiener prediction filter coefficients \mathbf{F} in equation (F-61) is described by [Treitel \(1974\)](#). The technique makes use of the Hermitian property (equation F-60c) of the autocorrelation matrix \mathbf{R} . Write this matrix in terms of its real \mathbf{R}_r and imaginary \mathbf{R}_i components as

$$\mathbf{R} = \mathbf{R}_r + i\mathbf{R}_i. \quad (F - 63a)$$

Similarly, write the complex Wiener filter \mathbf{F} and the crosscorrelation matrix \mathbf{G} in the same form:

$$\mathbf{F} = \mathbf{F}_r + i\mathbf{F}_i \quad (F - 63b)$$

and

$$\mathbf{G} = \mathbf{G}_r + i\mathbf{G}_i. \quad (F - 63c)$$

Substitute equations (F-63a,b,c) into equation (F-61) and equate the real and imaginary parts of both sides of the resulting expression to get

$$\mathbf{R}_r \mathbf{F}_r - \mathbf{R}_i \mathbf{F}_i = \mathbf{G}_r \quad (F - 64a)$$

and

$$\mathbf{R}_i \mathbf{F}_r + \mathbf{R}_r \mathbf{F}_i = \mathbf{G}_i. \quad (F - 64b)$$

Finally, write equations (F-64a,b) in matrix form:

$$\begin{pmatrix} \mathbf{R}_r & -\mathbf{R}_i \\ \mathbf{R}_i & \mathbf{R}_r \end{pmatrix} \begin{pmatrix} \mathbf{F}_r \\ \mathbf{F}_i \end{pmatrix} = \begin{pmatrix} \mathbf{G}_r \\ \mathbf{G}_i \end{pmatrix}. \quad (F - 65)$$

The square matrix on the left-hand side of this equation is a block Toeplitz matrix ([Robinson, 1967](#); [Robinson and Treitel, 1980](#)). This property leads to an efficient recursive algorithm that does not require complex arithmetic to solve for the complex prediction filter coefficients \mathbf{F} ([Treitel, 1974](#)).

REFERENCES

- Alam, A. and Austin, J., 1981, Multiple attenuation using slant stacks: Tech. Rep., Western Geophysical Company.
- Alam, A. and Lasocki, L., 1981, Slant stack and applications: Presented at the 41st Ann. Eur. Assoc. Expl. Geophys. Mtg.
- Al-Yahya, K., 1991, [Application of the partial Karhunen-Loeve transform to suppress random noise in seismic sections: Geophys. Prosp.](#), **39**, 77-93.
- Berkhout, A. J. and Verschuur, E. J., 1995, [Estimation of multiple scattering by iterative inversion, Part 1: Theoretical considerations: 55th Ann. Internat. Mtg., Soc. Expl. Geophys., Expanded Abstracts](#), 715-718.
- Beylkin, G., 1987, [Discrete Radon transform: IEEE Trans. on Acoustics, Speech and Signal Processing](#), **AASP-35**, 162-172.
- Canales, L., 1984, [Random noise reduction: 54th Ann. Internat. Mtg., Soc. Expl. Geophys., Expanded Abstracts](#), 525.

- Claerbout, J. F., 1978, Snell waves: Stanford Exploration Project Report No. **15**, 57-72, Stanford University.
- Claerbout, J. F., 1985, Imaging the earth's interior: Blackwell Scientific Publications.
- Clayton, R. W. and McMechan, G., 1981, Inversion of refraction data by wave-field extrapolation: *Geophysics*, **46**, 860-868.
- Carvalho, P. M., Weglein, A. B. and Stolt, R. H., 1991, Examples of a nonlinear inversion method based on the **T** matrix of scattering theory: Application to multiple suppression: 61st Ann. Internat. Mtg., Soc. Expl. Geophys., Expanded Abstracts, 1319-1322.
- Diebold, J. B. and Stoffa, P. L., 1981, The traveltime equation, $\tau - p$ mapping and inversion of common midpoint data: *Geophysics*, **46**, 238-254.
- Doicin, D. and Spitz, S., 1991, Multichannel extraction of water-bottom peg-legs pertaining to high-amplitude reflection: 61st Ann. Internat. Mtg., Soc. Expl. Geophys., Expanded Abstracts, 1439-1442.
- Dragoset, W. H. and Jericevic, Z., 1998, Some remarks on surface multiple elimination: *Geophysics*, **63**, 772-789.
- Dragoset, W. H. and MacKay, S., 1993, Surface multiple elimination and subsalt imaging: *Expl. Geophys.*, **24**, 463-472.
- Ewing, M., Jardetsky, W. S., and Press, F., 1957, Elastic waves in layered media: McGraw-Hill Book Co.
- Foster, D. J. and Mosher, C. C., 1992, Suppression of multiple reflections using the Radon transform: *geophysics*, **57**, 386-395.
- Gonzalez-Serrano, A., 1982, Wave-equation velocity analysis: Ph.D. thesis, Stanford University.
- Hampson, D., 1986, Inverse velocity stacking for multiple elimination: *J. Can. Soc. Expl. Geophys.*, **22**, 44-55.
- Hampson, D., 1987, The discrete Radon transform: A new tool for image enhancement and noise suppression: 57th Ann. Internat. Mtg., Soc. Expl. Geophys., Expanded Abstracts, 141-143.
- Hubral, P. and Krey, T., 1980, Interval velocities from seismic reflection time measurements: *Soc. Expl. Geophys.*
- Jones, I. F. and Levy, S., 1987, Signal-to-noise ratio enhancement in multichannel seismic data via the Karhunen-Loeve transform: *Geophys. Prosp.*, **35**, 12-32.
- Kelamis, P. G. and Mitchell, A. R., 1989, Slant-stack processing: *First Break*, **7**, 43-54.
- Kelamis, P. G. and Verschuur, D. J., 1996, Multiple elimination strategies for land data: Eur. Assoc. Expl. Geophys. Mtg., Extended Abstracts.
- Kennett, B. L. N., 1979, The suppression of surface multiples on seismic records: *Geophys. Prosp.*, **28**, 584-600.
- Kostov, C., 1990, Toeplitz structure in slant-stack inversion: 60th Ann. Internat. Mtg., Soc. Expl. Geophys., Expanded Abstracts, 1618-1621.
- Levin, F. K. and Shah, P. M., 1977, Peg-leg multiples and dipping reflectors: *Geophysics*, **42**, 957-981.
- Lines, L. R. and Treitel, S., 1984, Tutorial: A review of least-squares inversion and its application to geophysical problems: *Geophys. Prosp.*, **32**, 159-186.
- McMechan, G. and Yedlin, M., 1981, Analysis of dispersive waves by wavefield transformation: *Geophysics*, **46**, 869-879.
- Morley, L., 1982, Predictive techniques for marine multiple suppression: Ph. D. dissertation, Stanford Univ.
- Ottolini, R., 1982, Migration of seismic data in angle-midpoint coordinates: Ph.D. thesis, Stanford University.
- Pekeris, C. L., 1948, Theory of propagation of explosive sounds in shallow water: *Geol. Soc. Am. Mem.* **27**.
- Press, F. and Ewing, M., 1950, Propagation of explosive sound in a liquid layer overlying a semi-infinite elastic solid: *Geophysics*, **15**, 111-148.
- Press, W. H., Flannery, B. P., Teukolsky, S. A. and Vetterling, W. T., 1986, Numerical Recipes: The Art of Scientific Computing: Cambridge University Press.
- Riley, D. C. and J. F. Claerbout, 1976, 2-D multiple reflections: *Geophysics*, **41**, 592-620.

- Robinson, E. A., 1967, Multichannel time series analysis with digital computer programs: Holden-Day.
- Robinson, E. A. and Treitel, S., 1980, Geophysical signal analysis: Prentice-Hall, Inc.
- Ryu, J. V., 1980, Decomposition of seismic gathers into velocity components by a space-time filter: Presented at the 50th Ann. Internat. Mtg. Soc. Expl. Geophys.
- Schlitz, P. S. and Claerbout, J. F., 1978, Velocity estimation by wavefront synthesis: *Geophysics*, **43**, 691-712.
- Sengbush, R.L., 1983, Seismic exploration methods: Internat. Human Res. Dev. Corp., Boston.
- Sherwood, J. W. C. and Poe, P. H., 1972, Constant-velocity stack and wavelet processing: *Geophysics*, **37**, 769-787.
- Taner, M. T., 1977, Simplan – plane-wave stacking: Presented at the 37th Ann. Eur. Assoc. Explor. Geophys. Mtg.
- Taner, M. T., 1980, Long-period sea-floor multiples and their attenuation: *Geophys. Prosp.*, **28**, 30-48.
- Thorson, J., 1978, Reconstruction of slant stacks: Stanford Exploration Project Report No. 14, 83-91, Stanford University.
- Thorson, J. R. and Claerbout, J. F., 1985, Velocity-stack and slant-stack stochastic inversion: *Geophysics*, **50**, 2727-2741.
- Treitel, S., 1974, The complex Wiener filter: *Geophysics*, **39**, 169-173.
- Treitel, S., Gutowski, P. R., and Wagner, D. E., 1982, Plane-wave decomposition of seismograms: *Geophysics*, **47**, 1375-1401.
- Ulrych, T. J., Freire, S. L. and Siston, P., 1988, Eigenimage processing of seismic sections: 58th Ann. Internat. Mtg., Soc. Expl. Geophys., Expanded Abstracts, 1261-1265.
- Verschuur, D. J., 1991, Surface-related multiple elimination, an inversion approach: Ph. D. thesis, Delft Univ. of Tech.
- Verschuur, D. J. and Berkhouit, A. J., 1994, Multiple technology, part 1: Estimation of multiple reflections: 64th Ann. Internat. Mtg., Soc. Expl. Geophys., Expanded Abstracts, 1493-1496.
- Verschuur, D. J., Berkhouit A. J., and Kelamis, P. G., 1995, Estimation of multiple scattering by iterative inversion — part II: examples of marine and land data: 65th Ann. Internat. Mtg., Soc. Expl. Geophys., Expanded Abstracts, 1470-1473.
- Verschuur, D. J., Berkhouit, A. J. and Wapenaar, C. P. A., 1992, Adaptive surface-related multiple elimination: *Geophysics*, **57**, 1166-1177.
- White, R. E., 1984, Signal and noise estimation from seismic reflection data using spectral coherence methods: *Proc. IEEE*, **72**, 1340-1356.
- Wiggins, J. W., 1988, Attenuation of complex water-bottom multiple by wave-equation-based prediction and subtraction: *Geophysics*, **53**, 1527-1539.
- Yilmaz, O., 1981, Modeling guided waves in an irregular water layer: Presented at the 51st Ann. Internat. Mtg. Soc. Expl. Geophys.
- Yilmaz, O., 1989, Velocity-stack processing: *Geophys. Prosp.*, **37**, 357-382.